Universiteit Gent
Faculteit Wetenschappen
Vakgroep Subatomaire en Stralingsfysica
Voorzitter Prof. Dr. K. Heyde

Search for two-phonon states in nuclei in the tin region using the photon scattering technique

Johan Bryssinck

Our job in physics is to see things simply, to understand a great many complicated phenomena, in terms of a few simple principles.

Steven Weinberg

Proefschrift ingediend tot het behalen van de academische graad
van Doctor in de Wetenschappen : Natuurkunde
Academiejaar 2000 – 2001
promotoren : Prof. Dr. E. Jacobs en Prof. Dr. C. Wagemans

Vooraf

Na vier jaar voorbereiding van deze doctoraatsthesis, ben ik verheugd zovele mensen te kunnen danken die bijdroegen tot het welslagen van dit werk. Sterker nog, zonder deze steun zou dit werk nooit tot een goed einde gebracht zijn. Het is dan ook aan hen dat ik deze "vooraf" opdraag.

Op de eerste plaats wens ik mijn promotoren Prof. Dr. E. Jacobs en Prof. Dr. C. Wagemans, alsook Prof. Dr. D. De Frenne en Prof. Dr. K. Heyde te danken voor de kans die zij mij boden om vier jaar lang experimenteel onderzoek te verrichten in de kernstructuur en nucleosynthese groep van de vakgroep voor Subatomaire en Stralingsfysica. Hun enthousiasme en ervaring in het fundamenteel onderzoek hielpen mij op weg doorheen het kluwen van allerhande spectra en data en de interpretatie ervan. Verder ben ik Prof. Dr. E. Jacobs erkentelijk voor het grondig nalezen van mijn werk en de vele aanbevelingen die hier uit voort kwamen.

All the experimental results in this work have been obtained at the NRF facility installed at the 4.3 MV Dynamitron accelerator of the Stuttgart University. Therefore, I would like to acknowledge Prof. Dr. U. Kneissl and Dr. H. H. Pitz for the smooth running accelerator, for many interesting discussions and for the kind hospitality during my several stays in Stuttgart. Their continuous interest in the progress of this work, stimulated me very much. I'm also grateful to my colleagues from the NRF group in Stuttgart (directed by Prof. Dr. U. Kneissl): O. Beck, D. Belic, T. Eckert, C. Kohstall, H. Maser, A. Nord, M. Scheck, F. Stedille and the NRF group in Köln (directed by Prof. Dr. P. von Brentano): C. Fransen, R.-D. Herzberg, N. Pietralla, and V. Werner. They shared with me the day and night shifts during the experiments. In particular, I thank D. Belic for the analysis of the data obtained with the Compton polarimeters.

The target material for this work was provided by the Kurchatov Institute in Moscow. I had the opportunity to collaborate with Dr. Govor from this institute, which ment for me a great stimulating help in the analysis and interpretation of the data. To support the interpretation of the NRF data, theoretical calculations have been performed within the framework of the quasiparticle phonon model by Dr. V. Yu. Ponomarev from the Joint Institute for Nuclear Research in Dubna (Russia). He learned me about the basics of this model. I will remember our Russian collaborators not only as excellent scientists, but also as close friends.

Verder wens ik ook een woordje van dank te richten aan mijn collega's F. Bauwens, H. De Witte, M. Hagemann en J. Heyse met wie het aangenaam samenwerken was.

Tenslotte dank ik de heren R. Verspille en D. Van Waerbeke voor het verzorgde teken-, copieer- en inbindwerk.

Nederlandse samenvatting

Het voorliggende doctoraatswerk behandelt de zoektocht naar $[2_1^+ \otimes 3_1^-]_{1^-}$ tweefonontoestanden in even-even en onevenmassa kernen uit het Z = 50 gebied: de ^{116,118,120,122,124}Sn, ^{117}Sn en ^{121,123}Sb isotopen. Dit onderzoek werd uitgevoerd met behulp van de nucleaire resonantie fluorescentie (NRF) opstelling aan het 4.3 MV Dynamitron in Stuttgart (Duitsland) in samenwerking met de NRF groepen uit Stuttgart (o.l.v. Prof. Dr. U. Kneissl) en Keulen (o.l.v. Prof. Dr. P. von Brentano) en met Dr. L. Govor. Met de NRF opstelling in Stuttgart kunnen kernniveaus onderzocht worden met een maximum excitatieënergie van 4 MeV. De bekomen experimentele resultaten in dit werk werden vergeleken met theoretische berekeningen uitgevoerd door Dr. Ponomarev binnen het quasideeltje fonon model (QPM) [Solo92]. Het Kurchatov Instituut in Moskou zorgde voor het aangerijkte trefplaatmateriaal. De NRF methode, opstelling en analyse van de data worden voorgesteld in de hoofdstukken 2 en 3. De bekomen experimentele resultaten worden gepresenteerd in hoofdstuk 4 en aan een discussie onderworpen in hoofdstuk 5.

De semimagische even-even Sn kernen, met een afgesloten protonenschil, zijn alle sferisch. Het lageënergie niveauschema wordt gedomineerd door quadrupool en octupool oppervlakte vibraties waarvan de eigenschappen in theoretische modellen beschreven worden aan de hand van fononen [Bohr75]. De laagste 2_1^+ en 3_1^- niveaus worden bijgevolg éénfonontoestanden genoemd. Wanneer dergelijke collectieve vibrationele modes gekoppeld worden, verkrijgt men een multiplet van zogenaamde tweefonontoestanden. Zo is het $[2_1^+ \otimes 2_1^+]$ triplet een voorbeeld van goed gekende tweefonontoestanden in het lage energiegebied van heel wat sferische even-even kernen. De koppeling van de laagste vibrationele 2_1^+ en 3_1^- niveaus levert op haar beurt een gemengd tweefonon $[2_1^+ \otimes 3_1^-]$ quintuplet op, bestaande uit de negatieve pariteitsniveaus met $J^\pi = 1^-, \ldots, 5^-$. De resonante verstrooiing van reële fotonen aan sferische kernen laat toe om het 1^- lid uit dit $[2_1^+ \otimes 3_1^-]$ quintuplet nauwkeurig te bestuderen.

De nucleaire resonantie fluorescentie techniek, die gebruik maakt van de resonante verstrooiing van reële fotonen aan de kern, laat toe om op een model onafhankelijke wijze kernspektroscopisch onderzoek uit te voeren. Aangezien fotonen massaloze deeltjes zijn, is de impulsoverdracht klein en blijft dit onderzoek beperkt tot nucleaire toestanden die bereikbaar zijn vanaf de nucleaire grondtoestand via dipool en elektrische quadrupool excitaties. Deze hoge spin selectiviteit laat toe om zware kernen, zoals de Sn kernen, met een hoge densiteit aan energieniveaus te bestuderen. De klassieke fotonenbron bij uitstek toegepast in NRF experimenten, is bremsstralhung, die ontstaat door afremming van een elektronenbundel in een trefplaat. Het continue remstralingsspectrum laat toe alle toestanden met een voldoende grondtoestand overgangsbreedte Γ_0 simultaan te exciteren. Bovendien worden problemen te wijten aan de terugstootenergie van

de geëxciteerde kern vermeden. De verstrooide fotonen worden gedetecteerd met hyperzuivere Ge detectoren. De moderne Ge detectoren hebben een hoge resolutie en zijn zeer efficient in de detectie van fotonen. Het meest complete geheel van kernspectroscopische informatie kan bekomen worden in het geval van even-even kernen. Zij omvat:

- excitatieënergie
- totale verstrooiingswerkzame doorsnede I_S
- spin J
- pariteit π
- verhouding van de overgangssterktes Γ_0^2/Γ
- gereduceerde overgangswaarschijnlijkheid $B(\pi L)\uparrow$

van het aangeslagen niveau. Aangezien enkel gesteund wordt op de theorie van de elektromagnetische wisselwerking, kan de analyse van de experimentele data volledig model onafhankelijk gebeuren.

Een spinbepaling van de geëxciteerde niveaus in een even-even kern kan bekomen worden aan de hand van de gemeten hoekdistributie van de resonant verstrooide fotonen. Hierbij wordt gesteund op de karakteristieke verschillen in de hoekdistributies van dipool en quadrupool straling in $0-1-0$ en $0-2-0$ spin cascades zoals geïllustreerd in Fig. 2.2. Deze verschillen zijn het meest duidelijk voor de verstrooiingshoeken $90°$ en $127°$ waaronder de Ge detectoren opgesteld staan. In het geval van een onevenmassa kern leidt de halftallige grondtoestandsspin tot quasi isotrope hoekverdelingen van de resonant verstrooide fotonen (zie Fig. 2.3 voor het geval van een onevenmassa kern met grondtoestandsspin 5/2). Dit verhindert de bepaling van de spin van het aangeslagen niveau. Enkel in het specifiek geval van een onevenmassa kern met een grondstoestandsspin 1/2, kan een beperkte spin informatie afgeleid worden.

Een pariteitsbepaling van de geëxciteerde niveaus is noodzakelijk voor een volledige karakterisatie van de niveaus en om een vergelijking te kunnen maken met resultaten bekomen uit theoretische kernmodellen. De NRF groep in Stuttgart beschikt over twee comptonpolarimeters waarmee de pariteit van de geëxciteerde niveaus in even-even kernen kan bepaald worden. Resonant verstrooide fotonen aan een even-even kern onder een verstrooiingshoek van $90°$ zijn 100% lineair gepolariseerd waarbij de richting van de elektrische veldvector ten opzichte van het reactievlak afhankelijk is van het elektrisch of magnetisch karakter van de transitie (en dus ook van de pariteit van het aangeslagen niveau). Bij excitatieënergieën beneden ongeveer 5 MeV, is het comptoneffect een goede analysator van de lineaire polarisatie van de resonante verstrooide fotonen. In het comptoneffect wordt het foton preferentieel verstrooid in een vlak loodrecht op zijn elektrische veldvector. Een comptonpolarimeter bestaat dan ook uit een verstrooier, waarin het resonant verstrooide foton comptonverstrooiing ondergaat en een aantal absorbers die in coincidentie het verstrooide foton detecteren (zie Fig. 2.8). De gemeten asymmetrie tussen de absorberdetectoren laat toe de lineaire polarisatie van het resonant verstrooide foton en dus de pariteit van het aangeslagen niveau te bepalen. De comptonpolarimeters die gebruikt werden in

de NRF opstelling in Stuttgart, zijn viervoudig gesectoreerde HP Ge detectoren (zie Fig. 3.3). De werking hiervan wordt uitvoerig beschreven in hoofdstuk 3.

Een aantal belangrijke voorafgaande onderzoeksresultaten vormen de basis van dit werk. Zo werd het bestaan van $[2_1^+ \otimes 3_1^-]_{1^-}$ tweefonontoestanden reeds opgemerkt door Metzger in zijn NRF pionierswerk aan de semimagische kernen ^{142}Nd [Metz78] en ^{144}Sm [Metz76]. Meer recent, werd het voorkomen van $[2_1^+ \otimes 3_1^-]_{1^-}$ tweefonontoestanden in de N = 82 isotonen ^{138}Ba, ^{140}Ce, ^{142}Nd en ^{144}Sm [Herz95b] systematisch onderzocht. In NRF experimenten uitgevoerd aan de linac in Gent, waarbij de kernen ^{116}Sn en ^{124}Sn [Gova98] werden onderzocht tot aan de deeltjesgrens, werden 1^- niveaus waargenomen met een onderliggende $[2_1^+ \otimes 3_1^-]$ tweefononstructuur.

In Fig. 4.1 werden de opgenomen NRF spectra aan ^{116,118,120,122,124}Sn afgebeeld voor excitatieënergieën gelegen tussen 2.6 en 3.6 MeV. Elk van deze spectra wordt duidelijk gedomineerd door één resonantiepiek gelegen bij een excitatieënergie tussen 3.0 en 3.3 MeV. Uit de gemeten hoekdistributie (zie Fig. 4.2 en Ref. [Gova94b]) kan met grote nauwkeurigheid afgeleid worden dat het hier telkens gaat om de excitatie van een niveau met spin 1. In het geval van ^{116}Sn en ^{124}Sn werd de pariteit van de 3334 en 3490 keV niveaus bepaald met behulp van "off-axis" gedeeltelijk lineair gepolariseerde fotonen aan de 15 MeV linac in Gent [Gova94b]. De meting van de lineaire polarisatie van de resonant verstrooide fotonen met behulp van de comptonpolarimeters in Stuttgart liet toe om ondubbelzinnig de pariteit van de 3270 en 3359 keV niveaus in ^{118}Sn en ^{122}Sn te bepalen (zie Fig. 4.3) [Beli00]. Al deze pariteitsmetingen leiden tot de conclusie dat het telkens een 1^- niveau betreft. Op basis van deze analoge resultaten werd ook een negatieve pariteit voor het 3279 keV niveau in ^{120}Sn aangenomen. Voor al deze 1^- niveaus wordt een onderliggende $[2_1^+ \otimes 3_1^-]_{1^-}$ tweefononconfiguratie aangenomen, steunend op de volgende experimentele vaststellingen :

- excitatieënergie nabij de som $E(2_1^+) + E(3_1^-)$
- verhoogde gereduceerde overgangswaarschijnlijkheid $B(E1)\uparrow$
- vervalpatroon
- correlatie tussen de $B(E1; 1_1^- \rightarrow 0_{g.s.}^+)$ en $B(E1; 3_1^- \rightarrow 2_1^+)$ gereduceerde overgangswaarschijnlijkheden

Deze vier argumenten worden hierna kort toegelicht.

Indien men aanneemt dat er een volledige harmonieuze koppeling plaatsgrijpt tussen de 2_1^+ en 3_1^- éénfonontoestanden, valt de excitatieënergie van het $[2_1^+ \otimes 3_1^-]_{1^-}$ tweefononniveau samen met de somenergie $E(2_1^+) + E(3_1^-)$. In Fig. 5.4a) worden de excitatieënergieën van de 1^- niveaus in ^{116,118,120,122,124}Sn vergeleken met deze somenergie. Er werd vastgesteld dat de excitatieënergieën van deze 1^- niveaus (zwarte kruisen in Fig. 5.4a)) zeer nauw aansluiten bij deze somenergie (open kruisen), met een gemiddelde energieverhouding $R_E = [E_x(1^-)]/[E_x(2_1^+) + E_x(3_1^-)]$ van 92.6%. Dit betekent dat de anharmoniciteit in deze $[2_1^+ \otimes 3_1^-]_{1^-}$ toestanden zeer klein is. Dit wordt verklaard in het QPM aan de hand van de fermionstructuur van de individuele fononen en de driefononbijmengingen in de golffunctie. In Fig. 5.4b) worden de afgeleide gereduceerde overgangswaarschijnlijkheden $B(E1)\uparrow$ weergegeven. Hierbij werd vastgesteld dat deze nagenoeg constant blijven in de Sn massaketen ($B(E1)\uparrow \approx 7.0 \cdot 10^{-3} \cdot e^2 fm^2$) met een maximum

bij ^{120}Sn. Deze gereduceerde overgangswaarschijnlijkheden zijn "verhoogd" vergeleken met wat men kan verwachten op basis van een extrapolatie van de staart van de $E1$ reuzeresonantie (GDR). Deze $E1$ excitaties vormen een verboden overgang in een zuiver bosonenformalisme voor deze $[2_1^+ \otimes 3_1^-]_{1^-}$ toestand [Pono98a]. In het QPM zijn deze $E1$ overgangen mogelijk dankzij de fermionstructuur van de constitutionele fononen en een klein percentage éénfononbijmengingen afkomstig uit de $E1$ reuzeresonantie (destructief). De resultaten bekomen uit de QPM-berekeningen voor de excitatieënergieën en de gereduceerde overgangswaarschijnlijkheden $B(E1)\uparrow$ van de $[2_1^+ \otimes 3_1^-]_{1^-}$ toestanden in de even-even Sn kernen worden vergeleken met de experimentele resultaten in tabel 5.3. Er is een goede overeenkomst tussen de theoretische en experimentele resultaten. Echter in het geval van ^{122}Sn en ^{124}Sn wordt een dalende theoretische $B(E1)\uparrow$ overgangswaarschijnlijkheid bekomen in tegenstelling tot de experimentele resultaten die nagenoeg constant zijn. Dit kan te wijten zijn aan de dalende $B(E2)\uparrow$ en $B(E3)\uparrow$ overgangswaarschijnlijkheden van de 2_1^+ en 3_1^- éénfonontoestanden die als inputparameters gebruikt werden in het QPM. Indien deze waarden echter constant zouden blijven, zouden ook de bekomen theoretische $B(E1)\uparrow$ overgangswaarschijnlijkheden constant blijven.

De meest voor de hand liggende en directe manier om een $[2_1^+ \otimes 3_1^-]_{1^-}$ tweefononconfiguratie voor de 1^- niveaus in de Sn kernen experimenteel aan te tonen, is het opmeten van het vervalpatroon zoals geïllustreerd in Fig. 5.5. In een tweefononconfiguratie voor het 1^- niveau zal de $B(E2)\uparrow$ overgangswaarschijnlijkheid in de $[2_1^+ \otimes 3_1^-]_{1^-} \rightarrow 3_1^-$ transitie dezelfde zijn als in de $2_1^- \rightarrow 0_{g.s.}^+$ transitie, aangezien in beide gevallen hetzelfde fonon verdwijnt. In het geval van de $[2_1^+ \otimes 3_1^-]_{1^-} \rightarrow 2_1^+$ en de $3_1^- \rightarrow 0_{g.s.}^+$ transities, moet de sterkte van de $E3$ componente telkens gelijk zijn. In dit laatste geval treedt het probleem op dat in de $[2_1^+ \otimes 3_1^-]_{1^-} \rightarrow 2_1^+$ transitie, de $E3$ componente experimenteel niet waarneembaar is door de bijhorende snellere $E1$ componente. Verder is het in NRF experimenten niet mogelijk om deze zwakke inelastische overgangen te detecteren, aangezien zij in een energiegebied van het spectrum gelegen zijn ($[2_1^+ \otimes 3_1^-]_{1^-} \rightarrow 3_1^- \cong$ 1 MeV en $[2_1^+ \otimes 3_1^-]_{1^-} \rightarrow 2_1^+ \cong$ 2 MeV) waar de continue achtergrond reeds hoog is, te wijten aan niet resonante verstrooiing van de fotonen in de NRF trefplaat. Er kan wel een bovengrens bepaald worden voor de verhouding in de transitie breedtes $\Gamma_{1^- \rightarrow 2^+}/\Gamma_0$. De aldus bekomen bovengrens wordt in tabel 5.1 vergeleken met de resultaten volgens het QPM. In inelastische protonen verstrooiingsexperimenten $(p, p'\gamma)$ aan ^{142}Nd en ^{144}Sm [Wilh96, Wilh98] werd aangetoond dat in beide kernen de $E2$ sterkte in het inelastische verval $[2_1^+ \otimes 3_1^-]_{1^-} \rightarrow 3_1^-$ binnen de statistische nauwkeurigheid gelijk is aan de $E2$ sterkte van de $2_1^+ \rightarrow 0_{g.s.}^+$ transitie. Dit zijn de enige twee gevallen waarbij op een directe manier een $[2_1^+ \otimes 3_1^-]$ tweefononconfiguratie werd aangetoond. Verder kon in deze $(p, p'\gamma)$ experimenten de vertakking $[2_1^+ \otimes 3_1^-]_{1^-} \rightarrow 2_1^+$ waargenomen worden, waarvan de verhouding in de transitie breedtes $\Gamma_{1^- \rightarrow 2^+}/\Gamma_0$ overeenstemt met de gevonden bovengrenzen in de Sn kernen in dit werk.

Recent werd door Pietralla [Piet99a] een correlatie gevonden tussen de $B(E1; 1_1^- \rightarrow 0_{g.s.}^+)$ en de $B(E1; 3_1^- \rightarrow 2_1^+)$ gereduceerde overgangswaarschijnlijkheden. Dit wordt aangetoond in Fig. 5.6 waar de $B(E1; 3_1^- \rightarrow 2_1^+)$ overgangswaarschijnlijkheid getekend werd versus de $B(E1; 1_1^- \rightarrow 0_{g.s.}^+)$ overgangswaarschijnlijkheid in een grote varieteit aan even-even kernen. Ondanks het feit dat beide grootheden met meer dan één grootte orde variëren, blijft de verhouding

van beide nagenoeg constant:

$$R = \frac{B(E1; 1_1^- \rightarrow 0_{g.s.}^+)}{B(E1; 3_1^- \rightarrow 2_1^+)} \cong 1 \ .$$

Merk hierbij op dat de resultaten bekomen in dit werk voor de even-even Sn kernen (rode punten in Fig. 5.6) perfect in deze systematiek passen. Bij theoretische berekeningen uitgevoerd in het interagerend bosonen model (IBM) door Pietralla werd een afschatting van R bekomen [Piet99a]:

$$R = \frac{B(E1; 1_1^- \rightarrow 0_{g.s.}^+)}{B(E1; 3_1^- \rightarrow 2_1^+)} = \frac{7}{3} \ .$$

Deze afschatting van R kon verbeterd worden door eerste orde QPM-berekeningen door Ponomarev, waarbij een waarde van 0.9 werd gevonden [Pono99c]. Hierbij werd aangetoond dat elk theoretisch model gebaseerd op de quasiparticle random phase approximation (QRPA) en dat bijgevolg rekening houdt met de interne fermionstructuur van de fononen voor R resulteert in [Pono99c] :

$$0 < R < \frac{7}{3} \ .$$

De waarde 0 correspondeert met niet collectieve fononen en vormt de beneden grens. De verhouding 7/3 komt overeen met extreem collectieve fononen en is bijgevolg een onbereikbare bovengrens. In een tweefononbeeld kan de sterke correlatie tussen de $B(E1; 1_1^- \rightarrow 0_{g.s.}^+)$ en de $B(E1; 3_1^- \rightarrow 2_1^+)$ gereduceerde overgangswaarschijnlijkheden als volgt verklaard worden : in beide transities $[2_1^+ \otimes 3_1^-]_{1^-} \rightarrow 0_{g.s.}^+$ en $3_1^- \rightarrow 2_1^+$ is het onderliggende mechanisme een uitwisseling van dezelfde twee éénfonontoestanden 2_1^+ en 3_1^-.

Na een systematische studie van de $[2_1^+ \otimes 3_1^-]_{1^-}$ tweefonontoestanden in de even-even Sn kernen, rees de vraag hoe de verhoogde $B(E1)\uparrow$ overgangswaarschijnlijkheid zou fragmenteren in de oneven nabuurkernen ^{117}Sn en ^{121,123}Sb. In een eenvoudig model waarbij men het ongepaarde nucleon koppelt aan de even-even nabuurkern, zal ieder niveau van het $[2_1^+ \otimes 3_1^-]$ quintuplet opsplitsen in een aantal niveaus met elk een deeltje$\otimes[2_1^+ \otimes 3_1^-]$ structuur (zie ook Fig. 5.8). Daarbij verwacht men dat de gesommeerde $B(E1)\uparrow$ sterkte van de niveaus uit het deeltje$\otimes[2_1^+ \otimes 3_1^-]$ multiplet die bereikbaar zijn via $E1$ excitaties gelijk is aan de $B(E1)\uparrow$ sterkte van de $[2_1^+ \otimes 3_1^-]_{1^-}$ toestand uit de even-even nabuur. Deze fragmentatie van de elektromagnetische sterkte in een onevenmassa kern wordt bepaald door de halftallige grondtoestandsspin J_0. Dipool excitaties kunnen plaatsgrijpen naar niveaus met een spin gelegen tussen $J_0 - 1$ en $J_0 + 1$. Niveaus met een spin gelegen tussen $J_0 - 2$ en $J_0 + 2$ kunnen geëxciteerd worden via quadrupool transities. Verder wordt de fragmentatie ook bepaald door de locatie van het ongepaarde nucleon. Indien het ongepaarde nucleon zich net buiten een afgesloten schil bevindt, verwacht men dat de $E1$ sterkte geconcentreerd blijft in een klein aantal niveaus. Bevindt het ongepaarde nucleon zich in het midden tussen twee schillen, dan zal de fragmentatie sterker zijn vanwege het grotere aantal vrijheidsgraden. Het meest duidelijke voorbeeld van een deeltje$\otimes[2_1^+ \otimes 3_1^-]$ multiplet werd gevonden in ^{143}Nd [Zilg93, Herz95a], met een ongepaard neutron in het $f_{7/2}$ orbitaal net buiten de afgesloten N = 82 schil, waarbij tussen 2.7 en 4.0 MeV een klein aantal overgangen werden waargenomen waarvan de gesommeerde $B(E1)\uparrow$ gereduceerde overgangswaarschijnlijkheid binnen de statistische fout overeenkomt met de $B(E1)\uparrow$ sterkte van de $[2_1^+ \otimes 3_1^-]_{1^-}$ toestand in

^{142}Nd. Echter bij latere NRF experimenten aan ^{139}La en ^{141}Pr [Herz95b, Herz95d], waarbij de ongepaarde protonen tussen de twee afgesloten schillen Z = 50 en Z = 82 gelegen zijn, bedroeg de gesommeerde gereduceerde overgangswaarschijnlijkheid tussen 2.7 en 4.0 MeV slechts ongeveer 40% van de $B(E1)\uparrow$ sterkte in de even-even naburen ^{138}Ba en ^{140}Ce. Hierbij dient opgemerkt te worden aangezien noch een spinbepaling noch een pariteitsbepaling voor de geëxciteerde niveaus in een onevenmassa kern mogelijk is in NRF, er aangenomen werd dat alle excitaties in het energiegebied tussen 2.7 en 4.0 MeV een $E1$ karakter hadden. Men kan in deze studies dus werkelijk spreken van een "zoektocht" naar $[2^+_1 \otimes 3^-_1]$ tweefononexcitaties in onevenmassa kernen.

De eerste onevenmassa kern die in dit werk werd onderzocht, is ^{117}Sn waarin het ongepaarde neutron zich in een $3s_{1/2}$ orbitaal bevindt halverwege de N = 50 en N = 82 schillen. Deze lage halftallige spin van het ongepaarde neutron heeft als voordeel dat de verwachte fragmentatie van de elektromagnetische sterkte relatief klein zal blijven. Zo kunnen dipool excitaties enkel plaatsgrijpen naar toestanden met een spin 1/2 en 3/2, terwijl toestanden met een spin 3/2 of 5/2 bereikbaar zijn via quadrupool excitaties. De koppeling van het ongepaarde $3s_{1/2}$ neutron aan het $[2^+_1 \otimes 3^-_1]$ quintuplet in de even-even ^{116}Sn kern resulteert slechts in drie toestanden die bereikbaar zijn via $E1$ excitaties vanuit de grondtoestand. In Fig. 4.4 wordt het opgenomen NRF spectrum aan ^{117}Sn weergeven tezamen met de ^{116}Sn en ^{118}Sn naburen. Men stelt duidelijk een sterke fragmentatie vast van de elektromagnetische sterkte in de omgeving van de $[2^+_1 \otimes 3^-_1]_{1^-}$ tweefonontoestanden in ^{116}Sn en ^{118}Sn. Deze fragmentatie is zeker sterker dan wat men kan verwachten op basis van een eenvoudig koppelingsmodel. In totaal werden meer dan 50 transities gedetecteerd waarvan de meeste nog niet gekend zijn in de literatuur. Uit de gemeten hoekdistributies kon voor enkele geëxciteerde niveaus een suggestie gegeven worden voor de spin. Deze resultaten worden uitvoerig toegelicht in hoofdstuk 4. Voor de overgrote meerderheid van alle toestanden echter is de spin onbekend en pariteiten kunnen niet bepaald worden met de huidige statistische nauwkeurigheid van de NRF metingen.

Om op basis van de experimentele resultaten een idee te krijgen of al dan niet fragmenten van het $3s_{1/2} \otimes [2^+_1 \otimes 3^-_1]$ deeltje tweefononmultiplet werden waargenomen, zullen we aannemen dat alle waargenomen transities een zuiver $E1$ karakter hebben. Daarbij wordt de gesommeerde gereduceerde overgangswaarschijnlijkheid $B(E1)\uparrow$ van de geëxciteerde niveaus in een energiegebied rond de $[2^+_1 \otimes 3^-_1]_{1^-}$ tweefonontoestand in de even nabuur vergeleken met de $B(E1)\uparrow$ sterkte van deze 1^- tweefonontoestand. Dit geeft een indicatie of al dan niet fragmenten van het deeltje$\otimes[2^+_1 \otimes 3^-_1]$ multiplet werden waargenomen. In Fig. 5.9 wordt de fragmentatie van de totale verstrooiingswerkzame doorsnede I_S vergeleken met de even naburen ^{116}Sn en ^{118}Sn en met resultaten bekomen uit QPM-berekeningen. Aan de hand van de experimentele resultaten in Fig. 5.9b) kan men vaststellen dat er een "resonantie" werd waargenomen in het energiegebied tussen 2.7 en 3.6 MeV gecentreerd rond de $[2^+_1 \otimes 3^-_1]_{1^-}$ tweefonontoestanden in ^{116}Sn en ^{118}Sn. De gesommeerde $B(E1)$ sterkte in dit energiegebied bedraagt 5.59 (64) $10^{-3} \cdot e^2fm^2$ of correspondeert met 85(13) – 77(14)% van de $B(E1)\uparrow$ tweefononsterkte in ^{116}Sn en ^{118}Sn. Een directe verificatie of een niveau al dan niet behoort tot een deeltje$\otimes[2^+_1 \otimes 3^-_1]$ multiplet, kan bereikt worden door bijvoorbeeld de $E2$ sterkte in de transitie $3s_{1/2} \otimes [2^+_1 \otimes 3^-_1]_{1/2^-} \rightarrow [3s_{1/2} \otimes 3^-_1]_{5/2^-}$ op te meten. Dergelijke inelastische overgangen zijn echter dermate zwak, dat zij niet kunnen geobserveerd worden in NRF experimenten.

Door het gebrek aan spin- en pariteitsinformatie voor de geëxciteerde niveaus in ^{117}Sn in onze NRF experimenten en gegevens uit de literatuur, is het noodzakelijk om de bekomen experimentele resultaten te vergelijken met QPM-berekeningen om een beter inzicht te krijgen. Deze QPM-berekeningen werden voor de eerste maal uitgevoerd in een volledige configuratieruimte waarbij $[qp \otimes Nph]$-configuraties, met N = 0,1,2 en 3, in de golffunctie van de grondtoestand en de geëxciteerde niveaus in acht werden genomen. De resultaten van deze QPM-berekeningen worden vergeleken met de experimentele resultaten in Fig. 5.9b) en c). Hierbij valt op dat er een goede overeenkomst is tussen beide wat de fragmentatie van de elektromagnetische sterkte betreft. Deze QPM-berekeningen tonen aan dat de $E1$ sterkte inderdaad dominant is beneden een excitatieënergie van 4 MeV, maar $M1$ en $E2$ contributies in het excitatiespectrum mogen echter niet verwaarloosd worden. De totale gesommeerde berekende verstrooiingswerkzame doorsnede I_S bedraagt 152 eVb en komt binnen de 15% overeen met de experimentele waarde van 133(21) eVb. De theoretische bijdragen van $E1$, $M1$ en $E2$ transities bedraagt respectievelijk 73, 37 en 42 eVb. De QPM-resultaten tonen aan dat een groot gedeelte van de $[3s_{1/2} \otimes [2_1^+ \otimes 3_1^-]_{1^-}]_{1/2^-,3/2^-}$-configuraties geconcentreerd is in een aantal $3/2^-$ toestanden bij 3.04, 3.55 en 3.56 MeV en in een aantal $1/2^-$ toestanden bij 3.00 en 3.63 MeV. De fragmentatie van de elektromagnetische sterkte is te wijten aan interacties met $[qp \otimes 1ph]$ en $[qp \otimes 2ph]$-configuraties met dezelfde spin en pariteit in de nabijheid van de $[3s_{1/2} \otimes [2_1^+ \otimes 3_1^-]_{1^-}]_{1/2^-,3/2^-}$-configuraties.

In Fig. 5.11b) en d) worden de gemeten totale verstrooiingswerkzame doorsnedes in ^{121}Sb en ^{123}Sb en in de even-even ^{120}Sn (Fig. 5.11a)), ^{122}Sn (Fig. 5.11c)) en ^{124}Sn (Fig. 5.11e)) naburen weergegeven. In ^{121}Sb en ^{123}Sb bevindt het ongepaarde proton zich net buiten de afgesloten Z = 50 schil in respectievelijk het $2d_{5/2}$ en het $2d_{7/2}$ orbitaal. De koppeling van het ongepaarde $2d_{5/2}$ proton in ^{121}Sb aan het tweefonon $[2_1^+ \otimes 3_1^-]$ quintuplet in de even-even kern ^{120}Sn leidt tot een multiplet bestaande uit 26 niveaus waarvan 14 niveaus kunnen geëxciteerd worden via $E1$ excitaties. Het $2d_{7/2} \otimes [2_1^+ \otimes 3_1^-]$ multiplet in ^{123}Sb bestaat uit 31 niveaus waarvan 15 kunnen geëxciteerd worden via $E1$ excitaties. Bij de analyse van de NRF data verkregen voor ^{121}Sb en ^{123}Sb werd onverwacht een zeer grote fragmentatie van de elektromagnetische sterkte vastgesteld. In ^{121}Sb en ^{123}Sb werden respectievelijk 164 en 83 overgangen gedetecteerd. Als gemakshalve opnieuw het energiegebied tussen 2.7 en 3.6 MeV in ^{121}Sb beschouwd wordt en aangenomen wordt dat alle gedetecteerde transities een zuiver $E1$ karakter hebben, bedraagt de totale gesommeerde $B(E1)\uparrow$ sterkte 6.38 (128) $10^{-3}e^2fm^2$ of 84 (23) – 89 (25)% van de tweefonon $B(E1)\uparrow$ sterkte in ^{120}Sn en ^{122}Sn. Dit resultaat is gelijklopend met wat gevonden werd in het geval van ^{117}Sn. In ^{123}Sb echter bedraagt de totale $B(E1)\uparrow$ sterkte in hetzelfde energiegebied slechts 2.88 (54) $10^{-3}e^2fm^2$ of 40 (11) – 47 (14)% van de even-even ^{122}Sn en ^{124}Sn naburen. Dit is mogelijk te wijten aan de hogere halftallige grondtoestandsspin in ^{123}Sb, wat tot een sterkere fragmentatie leidt. Een gedeelte van de elektromagnetische sterkte kan gemist worden wanneer de sterkte van de individuele fragmenten beneden de detectielimiet valt van de NRF opstelling. Hierbij dient opgemerkt te worden dat in de NRF experimenten uitgevoerd aan ^{123}Sb de eindpuntsenergie bij 3.8 MeV lag, te wijten aan technische problemen met het Dynamitron. Door deze lagere eindpuntsenergie werden er geen niveaus boven 3.5 MeV waargenomen, waardoor een gedeelte van de elektromagnetische sterkte gemist werd.

Tot slot is het interessant om de bekomen resultaten voor ^{117}Sn en ^{121,123}Sb te vergelijken

met deze voor ^{139}La, ^{141}Pr en ^{143}Nd [Herz95b, Herz95d, Zilg93, Herz95a]. Hierbij kunnen twee groepen onderscheiden worden : in ^{117}Sn, ^{139}La en ^{141}Pr bevindt het ongepaarde nucleon zich tussen twee gesloten schillen terwijl in ^{121,123}Sb en ^{143}Nd het ongepaarde nucleon gesitueerd is net buiten een afgesloten schil.

In de NRF experimenten uitgevoerd aan ^{139}La en ^{141}Pr werd slechts 44% van de naburige tweefonon $B(E1)\uparrow$ sterkte teruggevonden, terwijl dit in het geval van ^{117}Sn ongeveer het dubbele was (mits aanname dat alle transities in deze onevenmassa kernen een zuiver $E1$ karakter hebben !). Hierbij dient echter opgemerkt te worden dat de detectielimiet in de NRF experimenten uitgevoerd aan ^{139}La en ^{141}Pr ongeveer een orde slechter was dan in ^{117}Sn. Als dezelfde sensitiviteit voor ^{117}Sn wordt toegepast als in de ^{139}La en ^{141}Pr experimenten, wordt slechts 59 (11)% van de naburige $B(E1)\uparrow$ sterkte in ^{116}Sn en ^{118}Sn teruggevonden. Het feit dat deze waarde nog iets hoger is dan de 44% gevonden in ^{139}La en ^{141}Pr, kan te wijten zijn aan de lagere waarde van de halftallige grondtoestandsspin in ^{117}Sn. In dit opzicht kan men stellen dat de resultaten in ^{117}Sn, ^{139}La en ^{141}Pr gelijklopend zijn. Bovendien werd aangetoond in QPM-berekeningen dat de $E1$ sterkte in ^{117}Sn rond 3.0 MeV inderdaad afkomstig is van de excitatie van niveaus met een dominante deeltje tweefononstructuur.

Bij een vergelijking tussen ^{121,123}Sb en ^{143}Nd vallen er een aantal markante verschillen op. In ^{143}Nd werden in het energiegebied tussen 2.9 en 4.0 MeV 13 niveaus waargenomen, waarvan 6 overeenkomen met een totale verstrooiingswerkzame doorsnede van meer dan 10 eVb en een maximale waarde van 35.6 eVb. In het energiegebied tussen 2.7 en 3.6 MeV, bedraagt de maximale waarde van de totale verstrooiingswerkzame doorsnede 4.19 en 6.32 eVb in ^{121}Sb en ^{123}Sb. Indien dezelfde detectielimiet in het geval van ^{143}Nd wordt toegepast voor ^{121}Sb, wordt slechts 34.3% van de naburige $B(E1)\uparrow$ sterkte in ^{120}Sn en ^{122}Sn teruggevonden. Dit betekent dat de situatie in ^{121,123}Sb duidelijk verschillend is van ^{143}Nd. Ook wordt hiermee duidelijk aangetoond dat de voorwaarde van gelijke $E1$ sterktes in onevenmassa en even-even nabuurkernen, zoals ze in dit werk werd toegepast, een *nodige* voorwaarde is, maar zeker niet *voldoende* !

Contents

Chapter 1

Introduction and motivation

Nuclei, as finite composite systems of nucleons, are well known to exhibit excited states which are characterised by an excitation energy, spin, and parity, a certain excitation and de-excitation probability, and decay properties to other lower lying nuclear levels. The complex composite structure of the nuclear system is reflected in its wave function and the properties of the system are determined by the detailed structure of this wave function. The study of these properties challenges both the experimental and theoretical approaches. Although nowadays, in modern nuclear physics, the interest mainly goes to the study of nuclei under extreme conditions, such as high energies, high spins or deformations, high isospins, ... this work focuses on the most elementary excitations of nuclei: dipole excitations. The nuclear resonance fluorescence (NRF) technique, as chosen in this work, is an ideal probe to investigate these dipole excitations.

The history of NRF starts in the first half of the past century with a long period of scrutinizing possible techniques to establish resonance fluorescence (which was known from optics and atomic physics) in nuclei. Details of it can be found in [Knei96]. In 1946, the best solution was finally found by Schiff [Schi46], who proposed to use electron bremsstrahlung as a continuous photon source. The main advantage is that the produced continuous bremsstrahlung allows to excite simultaneously all nuclear levels with a sufficient ground state transition width. Due to the low momentum transfer of the massless photons in the scattering process, a high spin selectivity is obtained. As a consequence of this spin selectivity, only levels can be studied which are excitable from the ground state via dipole or electric quadrupole excitations. A lot of pioneering nuclear spectroscopy work using photon scattering off nuclei was performed by Metzger in the 1960's and 70's. However, in his investigations, Metzger was hindered by the low duty cycle of the accelerators at that time and the low detection efficiency and resolution of his γ spectrometers.

The big breakthrough of the (NRF) technique came in the 1980's with the advent of high duty cycle electron accelerators and Ge detectors with high efficiency and excellent energy resolution. The revival of NRF was initiated by the discovery of the $M1$ scissors mode in (e,e') experiments at the Darmstadt S-DALINAC by Richter and his coworkers [Rich83, Bohl84] which opened a new field of magnetic dipole excitations to be studied extensively.

Since the last two decades, an enormous attention has been paid to the investigation of electric and magnetic dipole excitations in heavy nuclei. The obtained results can be divided in two groups. A first group of phenomena comprises the study of the existence of the $M1$ scissors

mode in deformed nuclei and the study of low energy electric dipole and quadrupole excitations at the NRF facilities of the Stuttgart (Germany) [Knei96] and Darmstadt (Germany) [Mohr99] Universities. These NRF experiments can be carried out with a maximum end point energy of 4.0 MeV. The second group consists of investigations up to the particle binding energies as performed at the NRF facilities in Giessen (Germany) [Berg87], Gent (Belgium) [Gova94a], and Darmstadt. In the nearest future a new NRF facility, also enabling experiments up to the particle binding energies, will become available as part of the ELBE project in the Forschungszentrum Rossendorf (Germany).

In Fig. 1.1, an overview is given of the dipole excitations studied in heavy nuclei below an excitation energy of 4 MeV. Strong magnetic dipole excitations were for the first time found in the rigid deformed rare earth nucleus ^{156}Gd in (e,e') experiments by Richter and coworkers [Rich83, Bohl84]. Their existence was established subsequently in NRF experiments on ^{156,158,160}Gd [Pitz89, Fried94] at the Stuttgart Dynamitron accelerator. These $M1$ excitations were predicted a few years before by Lo Iudice and Palumbo in a macroscopic two-rotor-model [Iudi78, Iudi79]. The detected $M1$ excitation mode corresponds to a scissors-like oscillation of the proton and neutron fluids of the rigid deformed nuclear body around a common axis (see Fig. 1.1a)). It is therefore denoted as the "scissors mode". The main characteristics of this $M1$ scissors mode can be summarized as:

- a mean excitation energy $E_x \cong 66 \cdot \delta \cdot A^{-1/3}$ MeV (δ deformation parameter, A mass number)
- a total $B(M1)\uparrow$ strength of about 3 μ_N^2 in the mid shell rare earth nuclei

The discovery of this new orbital $M1$ mode resulted in a huge experimental and theoretical activity. Since the discovery of the scissors mode in the Gd nuclei, this excitation mode has been systematically investigated in the rare earth nuclei ^{160,162,164}Dy [Wess88], ^{172,174,176}Yb [Zilg90b], ^{164,166,168,170}Er [Mase96a], ... A detailed discussion on the $M1$ scissors mode is out of the scope of this introduction. However, a summary of the most important outcomes is presented here.

In systematic NRF investigations on the ^{148,150,152,154}Sm shape transitional nuclei with increasing nuclear deformation parameters δ, Ziegler et al. [Zieg90] found that the total orbital $M1$ strength is linearly proportional to δ^2 (so called δ^2-law). The same relation was independently observed in the shape transitional ^{142,144,146,148,150}Nd nuclei [Marg93, Ecke97].

In a survey on the $M1$ scissors mode strength observed in the even-A rare earth nuclei for A = 140 – 190, a correlation with the $B(E2; 0_1^+ \rightarrow 2_1^+)$ strength (which exhausts more than 90% of the whole $E2$ strength in these nuclei) was found by Pietralla et al. [Piet95b]:

$$B(M1)_{Sc}[\text{s.p.u}(M1)] = \frac{10.6}{Z^2} B(E2)[\text{s.p.u}(E2)]$$

Single particle units are used to exclude mass dependence. Secondly, the saturation behaviour of the total orbital $M1$ strength was investigated. If the total scissors mode $M1$ strength is plotted versus the P factor which scales the proton neutron interaction ($P = N_p N_n/(N_p + N_n)$, the product of the valence proton and neutron numbers divided by there sum), two distinct

Figure 1.1: Overview on dipole excitations studied in heavy nuclei below an excitation energy of 4 MeV.

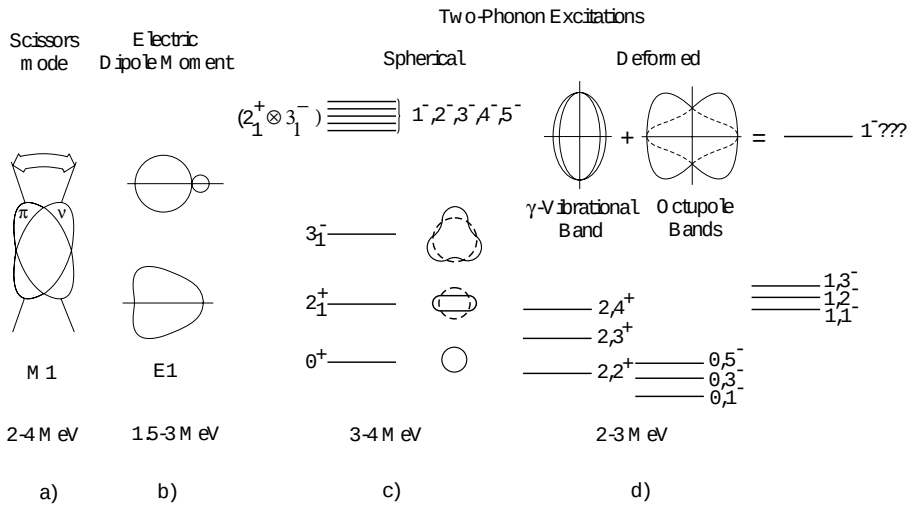

tracks are obtained [Piet95b]: for nuclei with a mass number $A \leq 170$ (group I) and nuclei with $A > 170$ (group II). In group I the total $M1$ strength increases with increasing mass number (going from spherical to deformed nuclei) and saturates in the mid shell nuclei. The total $M1$ strength in nuclei from group II increases with decreasing mass number (going from γ-soft rotors to rigid deformed nuclei) but does not reach saturation (see Fig. in ref. [Piet95b]). The same behaviour was observed for the $B(E2; 0_1^+ \rightarrow 2_1^+)$ strength which again points to the correlation with the total $M1$ strength.

The observation of $M1$ transitions belonging to the excitation of a scissors mode is not restricted to rare earth nuclei. It has also been observed in the actinide nuclei: ^{232}Th [Heil88], ^{238}U [Heil88], and ^{236}U [Marg90]. Further systematic investigations in this region were not possible due to a lack of enriched target material. The high proton number of these nuclei increases the continuous background in the NRF experiments and makes the observation of the fragmentation of the scissors mode a though challenge. Fragments of the scissors mode in a γ soft nucleus have been first observed by von Brentano et al. [Bren96] in NRF experiments on ^{196}Pt. These fragments could be detected thanks to the use of a cluster detector consisting of seven HP Ge detectors. Each Ge detector has an efficiency of 60% (relative to a 3 x 3 in^2. NaI(Tl) detector). By adding off-line the coincident pulses of neighbouring segments, the cluster detector behaves like a single Ge detector with an efficiency of 600%. This was the first NRF experiment in which a cluster detector was used. The fragmentation of the scissors mode strength was found to be comparable to the fragmentation observed in the rare earth nuclei, but the total strength amounts to only 25% compared to the latter and fits into the systematics presented in [Piet95b]. Subsequent NRF measurements on ^{134}Ba [Mase96b], ^{178,180}Hf [Piet97] and ^{190,192}Os [Fran99] established the existence of the $M1$ scissors mode in γ soft nuclei.

As more and more experimental information about the fragments of the scissors mode in even-even deformed nuclei became available, the question was addressed whether the scissors mode found in even-even deformed nuclei, also exists in odd-mass nuclei as common phenomenon. It is expected from theoretical calculations that the scissors mode will further fragment in the odd-mass nuclei due to the different couplings of the unpaired nucleon to each of the orbital $M1$ excitations in the even-even core and due to the mixing with single particle levels. As a result, the observation of the scissors mode in odd-mass nuclei will be hampered by the disappearance of the resonant scattering peaks in the continuous background in the NRF spectra. If the strength of the individual excitations is too low, the corresponding γ transitions will be hidden in the background. Furthermore, the nearly isotropic angular distributions and nearly vanishing linear polarization of the resonantly scattered photons off odd-mass nuclei with a half integer ground state spin prohibits the determination of the spin and parity of the excited levels. A first attempt to observe fragments of the scissors mode in ^{165}Ho [Huxe92] failed. The first successful observation of the scissors mode in an heavy odd-mass nucleus was achieved in NRF experiments on ^{163}Dy [Baus93]. Later on, it could be confirmed in ^{161}Dy [Marg95]. In both odd-mass nuclei, a similar excitation pattern was found, exhibiting a smooth trend with the mass number for the mean excitation energy which fits perfectly in the systematics of the scissors mode in the even-even Dy nuclei. In contradiction, this smooth systematics is completely broken in the odd-mass ^{157}Gd [Marg95] and ^{155}Gd nuclei [Nord96]. No concentration of dipole strength could be observed in the energy region of the scissors mode: the excitations are equally spread over the entire investigated energy region. Intermediate cases have been found in ^{159}Tb [Schi95] and ^{167}Er [Schl95]. As a common result, the detected $M1$ scissors mode strength in the odd-mass nuclei was found to be reduced by a factor of three compared to the even-even neighbours. An answer to the question: "Where is the scissors mode strength in odd-mass nuclei ?" was delivered by Enders et al. [Ende97]. From a fluctuation analysis of the continuous background in NRF spectra it was concluded that: *"the strength of the scissors mode in odd-mass nuclei is comparable to the even-even neighbours, but is so fragmented that a significant part lies below the experimental detection thresholds"*. However, at present, the experimental sensitivity of the Stuttgart NRF setup has been improved and is about one order of magnitude better. Recently, new NRF experiments performed on ^{163}Dy resolved much weaker γ transitions and a comparable $M1$ scissors mode strength with the even-even neighbours could be detected [Bren99].

In complex atomic nuclei, the $E1$ strength is mainly concentrated in the high-lying unbound giant dipole resonance (GDR). Low-lying electric dipole transitions are forbidden if one assumes a homogeneous charge distribution and a reflection symmetric shape. As a result, $E1$ transitions between low-lying states are very weak: they represent only a few milli Weiskoppf units while the GDR strength corresponds to several Weiskoppf units. Nevertheless, enhanced $E1$ transitions (compared to values obtained from an extrapolation of the tail of the GDR) have been observed in nuclei. A survey on the systematics of low lying $E1$ excitations in the A $\simeq$ 130 – 200 mass region is presented in [Fran98]. Iachello [Iach85] predicted enhanced electric dipole transitions between 1.5 and 3.5 MeV to occur in heavy nuclei where the global isospin symmetry is reduced to a local symmetry (see Fig. 1.1b)). This can be achieved in nuclei which clusterize in fragments with a different charge to mass ratio (Z/A): for instance α-clustering. Secondly, in nuclei with

a permanent octupole deformation, the protons tend to have a higher density in the tip of the pear shape in order to reduce the Coulomb potential. In both cases, the center of mass does not coincide anymore with the center of charge, resulting in a dipole moment of which the magnitude can not be neglected. Therefore, enhanced electric dipole transitions are expected to occur in nuclei with a static or dynamic clusterization and/or octupole deformation. Iachello suggested ^{150}Nd, ^{154}Sm, and ^{154}Gd (unfortunately unstable) as good candidates to observe these enhanced electric dipole transitions [Iach85]. NRF experiments on ^{156}Gd and ^{160}Gd [Pitz89] revealed two enhanced electric dipole transitions in ^{156}Gd and one in ^{160}Gd. The theoretical predictions of the electric dipole strength assuming α-clustering or octupole deformation are in good agreement with the experimental values, however the NRF technique does not allow to distinguish between both excitation mechanisms. In contrast to the Gd isotopes, not a single enhanced electric dipole transition compared to an extrapolation of the GDR was found in ^{150}Nd in [Pitz90]. Later on, linear polarization measurements on ^{150}Nd and ^{162}Dy [Fried92] revealed an enhanced $E1$ excitation near 2.5 MeV. The prediction of the $B(E1)\uparrow$ strengths on the basis of α-clustering or octupole deformation are of the same order of the experimental values.

Enhanced electric dipole transitions below an excitation energy of 4 MeV can also emerge from a coupling between collective modes in heavy spherical and deformed nuclei. In spherical semimagic nuclei, the low-lying level scheme is dominated by strong collective surface quadrupole and octupole vibrations (see Fig. 1.1c)), described in theory as phonons [Bohr75]. If one couples such a quadrupole and an octupole phonon, a quintuplet of negative parity states ($J^\pi = 1^- \ldots 5^-$) is obtained, so-called two-phonon states, of which the 1^- member can ideally be investigated in NRF experiments (see Fig. 1.1c)). Isolated enhanced electric dipole excitations have been found in the N = 82 isotones (^{138}Ba, ^{140}Ce, ^{142}Nd, and ^{144}Sm) [Herz95b] which could be interpreted as being two-phonon $[2^+_1 \otimes 3^-_1]_{1^-}$ states. Actually, Metzger stated already the existence of two-phonon 1^- states in his pioneering NRF work in the 1970's (see e.g. ^{88}Sr [Metz75], ^{144}Sm [Metz76], and ^{142}Nd [Metz78]). The observation of 1^- states with a two-phonon character in ^{116,124}Sn [Gova94b] forms the onset of this work in which the systematics of these two-phonon excitations have been studied in the even-even ^{116,118,120,122,124}Sn isotopes. Similar to the studies of the scissors mode, it will be questioned how the two-phonon $B(E1)\uparrow$ strength observed in the even-even Sn mass chain fragments and distributes in the adjacent odd-mass neighbours ^{117}Sn and ^{121,123}Sb. These studies are of extreme interest for theoretical calculations, because the enhanced electric dipole strength of these two-phonon states are delicately influenced by small admixtures of the GDR. Hence, the quality of the applied theoretical model can be tested in its capacity to reproduce the fragmentation and distribution of the electric dipole strength in even-even and odd-mass nuclei. The improved sensitivity of the present NRF facility of the Stuttgart University should allow to overcome some of the problems encountered in the studies of the scissors mode in heavy odd-mass nuclei. More details will be discussed in Chapter 5.

In quadrupole deformed nuclei, rotational bands are built on top of the ground state and on the γ or β quadrupole vibrations of the nuclear shape. The γ and β bands are characterised by their K-quantum number, the projection of the angular momentum on the symmetry axis of the nucleus. In NRF, these K-quantum numbers can be determined from a comparison of

the measured decay branching ratios to the first excited 2^+ state and to the ground state with the expected values within the validity of the Alaga rules [Alag55]. The available experimental data as well as the IBA-2 model suggest that $J = 1$, $K = 0$ states should have a negative parity [Zilg91]. States with $J = 1$ and $K = 1$ can have a positive or negative parity.

The rotational bands formed on top of the octupole vibrations coupled to the quadrupole deformed core leads to the so-called octupole vibrational bands. In Fig. 1.1d), the $J^\pi = 1^-$ bandheads with $K = 0$ or $K = 1$ are shown. NRF experiments on the rare earth nuclei revealed that the $K^\pi = 0^-$ electric dipole strength is mainly concentrated in one or two transitions near 1.5 MeV and with a total strength $\sum B(E1)\uparrow$ of $20 \cdot 10^{-3} \cdot e^2fm^2$ [Zilg91]. The detected correlation of the energies of these $K = 0$, $J^\pi = 1^-$ states with the energies of closely lying $J^\pi = 3^-$ states, allows to interpret them as the bandhead of the $K^\pi = 0^-$ octupole vibrational band [Zilg91]. A second group of weaker $\Delta K = 0$ transitions is found to be distributed between 2 and 4 MeV.

In NRF experiments on the rare earth nuclei ^{164}Dy and ^{168}Er [Knei96], in which also parity assignments of the excited levels were obtained, no $\Delta K = 1$ $E1$ transitions in ^{164}Dy and only three weaker $E1$ transitions in ^{168}Er could be detected. The detection limit in these experiments was about $B(E1)\uparrow \approx 0.1 \cdot 10^{-3} \cdot e^2fm^2$.

In NRF investigations of well deformed nuclei out of the rare earth region, it was found that most observed levels obey the Alaga rules for their decay. However, a few exhibit decay properties lying in between the values expected for $\Delta K = 0$ and $\Delta K = 1$ transitions. The observed uncommon decay branching ratios give evidence for a possible K-mixing in these states [Zilg90a]. Further on, the level scheme contains one isolated strong $E1$ transition with an energy varying between 2.1 and 2.7 MeV. From energy considerations, these states are interpreted as a novel type of two-phonon excitations [Knei93]: the coupling of quadrupole γ vibrations ($J = 2^+$, $K = 2$) and octupole vibrations ($J = 3^-$, $K = 1$) (see Fig. 1.1d)). This coupling mechanism has already been introduced theoretically by Donner and Greiner [Donn66]. Some details of these states will be presented in Chapter 5, in comparison with the two-phonon excitations observed in even-even semimagic nuclei.

At the beginning of the 1980's, the NRF facility built at the 65 MeV linear electron accelerator (linac) of the Giessen University was the first setup which allowed to perform NRF experiments up to the particle thresholds in nuclei. Parities could be assigned to the excited levels by measuring the azimuthal asymmetry of resonantly scattered partially linearly polarized photons. These NRF studies focussed on the $M1$ spin-flip strength distribution in sd, fp and heavy nuclei. The occurrence of the $M1$ spin-flip resonance can be explained in the nuclear shell model by transitions between occupied and unoccupied members of the spin-orbit partners. In 1989, when the NRF facility in Giessen was closed, this kind of NRF experiments were taken over by our NRF group at the 15 MeV linac in Gent. The semimagic ^{116,124}Sn nuclei were chosen to study the $M1$ spin-flip resonance. However, only three tentative $M1$ transitions could be assigned in these nuclei [Gova96]. The lack of $M1$ excitations can be regarded as an indication for a considerable fragmentation of the $M1$ strength over a large number of relatively weak individual transitions which cannot be detected within the sensitivity of the NRF setup. This is in contrast with NRF experiments on ^{56}Fe and ^{58}Ni [Bauw00] where the number of observed $M1$

transitions almost equals the number of $E1$ transitions. An intermediate case was recently met in ^{92}Mo. It should be remarked that real photons are not the ideal probe to study $M1$ strengths (other probes such as electron and proton scattering are more suited), not only because real photon absorption is predominantly $E1$ absorption (the $M1$ absorption probability is some two orders of magnitude lower), but also $E1$ branching of the excited 1^+ to possible 1^- or 2^- levels will have a high probability compared to the $M1$ ground state transition probability. To study this mechanism, more sensitive $(p,p'\gamma)$-studies are planned on the Sn nuclei in our collaboration with the KVI in Groningen.

Besides the search for $M1$ spin-flip transitions, strong electric dipole transitions were observed in the Giessen NRF experiments on the fp shell nuclei ^{48}Ti [Dege90], ^{52}Cr [Berg81], ^{54,56}Fe, ^{58,60}Ni, the transitional nuclei ^{70,72,74,76}Ge [Jung95], and the N = 50 isotones ^{88}Sr and ^{90}Zr. In some cases, the observed electric dipole strengths are lying above the RUL (Recommended Upper Limit) of this mass region $45 \leq A \leq 90$ [Endt79]. In the NRF experiments on ^{116,124}Sn [Gova96] it was found that the $E1$ response between 5.0 and 8 MeV displays some fine structure superimposed on the smooth Lorentz tail of the GDR. This resonance is often referred to as "pigmy resonance" in analogy to the GDR. Such a concentration of electric dipole strength in some energy regions below the GDR received increased interest in the last few years. Iachello suggested that oscillations of a small portion of nuclear matter relative to the rest of the nucleus could be responsible for the observed enhancement of $E1$ strength in certain energy regions well below the $E1$ GDR [Iach97]. Van Isacker et al. [Isac91] discussed the possibility that nuclei with a reasonable neutron skin could exhibit pigmy-$E1$ resonances below the $E1$ GDR. Heyde et al. [Oros98] proposed a schematic two-group random-phase approximation (RPA) model to study the $E1$ strength and its location. They found that the model implies a concentration of local dipole strength in some region of the lower tail of the $E1$ GDR. Similar $E1$ "pigmy resonance" structures have been observed in ^{140}Ce [Herz97] and in the lighter nuclei ^{56}Fe and ^{58}Ni [Bauw00] were it is concentrated in a few states. In ^{138}Ba, the $E1$ strength was also found to be concentrated around 6 MeV, but the strongest transition observed turned out to have a likely $M1$ character [Herz99]. Recently, a close correlation between the occurrence of an $E1$ pigmy resonance and the neutron skin of a nucleus could be demonstrated in NRF studies on the doubly magic nuclei ^{40}Ca and ^{48}Ca [Hart00]. In these Ca nuclei, the N/Z ratio varies from 1.0 to 1.4. Only ^{48}Ca, with a neutron excess out of a N = Z core which form a neutron skin, was found to exhibit an $E1$ pigmy resonance.

The NRF experiments on the ^{116,124}Sn nuclei [Gova98] revealed a problem which may arise in NRF studies performed with high end point energies: the mechanism of feeding. This is caused by the inelastic decay of higher lying states in an intermediate level. In some cases, it was found that this mechanism of feeding exceeds the direct population of a level from the ground state by more than 200% leading to a severe overestimation of the real strength. The effects from feeding vary from level to level and is closely related with the underlying configuration. As a second consequence, this strong feeding prohibits a good detection of spin and parity observables. Indeed, in the case of dominant feeding of a level the angular distribution of the resonantly scattered photons becomes isotropic and in addition the measured azimuthal asymmetry in the $(\gamma,\vec{\gamma'})$ measurements is strongly reduced. Because of this feeding, the NRF experiments have to

be carried out in several steps with different end point energies, which is a very time consuming solution to the problem.

In the next chapters of this thesis, the NRF method will be presented (Chapter 2) as well as the experimental setup and the method of data analysis (Chapter 3). In Chapter 4 an overview is given on the experimental results obtained in this work which will be discussed in Chapter 5. The final conclusions and remarks are given in Chapter 6.

Chapter 2

Nuclear Resonance Fluorescence

In this chapter the nuclear resonance fluorescence (NRF) technique, applied throughout this work, will be presented. Different aspects of the NRF method will be covered as far as they are important for the understanding of this work. For more detailed descriptions and applications of this technique, the reader is referred to more extended review articles in the literature [Metz59, Fagg59, Skor75, Berg87, Knei96].

In a NRF experiment, the nucleus under investigation is irradiated with real photons from an external photon source (see Chapter 3). The *resonance* condition for the excitation of a certain level is fulfilled if the energy of a real photon, impinging on the nucleus, falls in the narrow energy interval $[E_x - \Gamma, E_x + \Gamma]$ determined by the excitation energy E_x and the total transition width Γ of this level. In NRF, photo-excited levels are studied for which the decay mode is preferentially a gamma ray transition to the ground state (*fluorescence*). This limits the NRF technique to the study of nuclear levels lying below the particle thresholds. Below these particle thresholds, alternative decay modes might be gamma ray cascades via intermediate lying states, but in general these are of lesser importance. This can be understood as the transition probability diminishes quickly with a decreasing energy of the γ transition. However, the detection of inelastic branchings can be crucial in the interpretation and determination of the underlying configuration of a level.

The aim of nuclear resonance fluorescence or the study of elastically scattered real photons off nuclei, is to gain spectroscopic information. Only levels which can be reached via a dipole or to a lesser extent electric quadrupole transition from the ground state, will be populated. This is due to the low momentum transfer of the massless photons. The high spin selectivity of the real photon probe allows to study the properties of nuclear levels, even in regions with high level densities as met in heavy or odd-mass nuclei. As the electromagnetic interaction is very well known, the data obtained in an NRF experiment can be analyzed in a completely model independent way. In the case of even-even nuclei, the most complete set of spectroscopic information can be determined:

- level excitation energy E_x
- total cross section I_S
- spin J

- parity π
- transition width ratio Γ_0^2/Γ
- $B(\pi L)\uparrow$ excitation probabilities.

Details about these nuclear properties and important differences between even-even and odd-mass nuclei will be explained further in this Chapter.

2.1 Total scattering cross section I_S

The cross section for the excitation of a level with an excitation energy E_x by a photon with an energy E and its subsequent de-excitation to an intermediate lying state by the emission of a γ ray at the scattering angle θ can be expressed in a Breit-Wigner form [Metz59, Skor75]:

$$\sigma(E,\theta) = \pi\lambda\!\!\!^{-2} \cdot \frac{2J+1}{2(2J_0+1)} \cdot \frac{\Gamma_0 \cdot \Gamma_f}{(E-E_x)^2 + \frac{1}{4}\Gamma^2} \cdot \frac{W(\theta)}{4\pi} \tag{2.1}$$

with J_0 the ground state spin and J the spin of the excited level. The parameters Γ_0, Γ_f and Γ denote the transition widths to the ground state and the intermediate level as well as the total transition width:

$$\Gamma = \Gamma_0 + \sum_f \Gamma_f$$

with f the sum over all intermediate levels. All these nuclear properties are schematically illustrated in Fig. 2.1. The total decay width and the lifetime τ of a level are connected via the Heisenberg uncertainty relation (under the best circumstances):

$$\tau \cdot \Gamma = \hbar \ .$$

In the case of elastic scattering, the intermediate level coincides with the nuclear ground state

Figure 2.1: Illustration of the excitation and de-excitation of a level in nuclear resonance fluorescence. The important spectroscopic quantities are denoted on the figure. Their physical meaning is explained in the text.

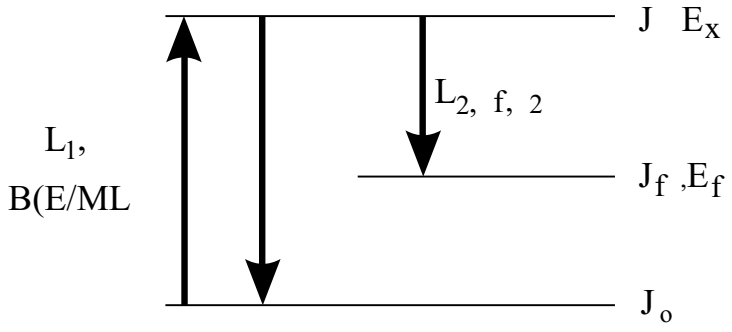

and the corresponding cross section becomes:

$$\sigma_{elas}(E,\theta) = \pi\lambda\!\!\!^{-2} \cdot \frac{2J+1}{2(2J_0+1)} \cdot \frac{\Gamma_0^2}{(E-E_x)^2+\frac{1}{4}\Gamma^2} \cdot \frac{W(\theta)}{4\pi} \ . \tag{2.2}$$

The total absorption cross section is obtained from a summation over all intermediate levels (including the ground state) in Eq. (2.1):

$$\sigma_{abs}(E,\theta) = \pi\lambda\!\!\!^{-2} \cdot \frac{2J+1}{2(2J_0+1)} \cdot \frac{\Gamma_0 \cdot \Gamma}{(E-E_x)^2+\frac{1}{4}\Gamma^2} \cdot \frac{W(\theta)}{4\pi} \ . \tag{2.3}$$

A detailed discussion about the influence of the angular correlation function $W(\theta)$ is postponed to the next section. The influence of the factor $W(\theta)$ can be omitted here by integrating over all scattering angles θ:

$$\sigma_{abs}(E) = \pi\lambda\!\!\!^{-2} \cdot \frac{2J+1}{2(2J_0+1)} \cdot \frac{\Gamma_0 \cdot \Gamma}{(E-E_x)^2+\frac{1}{4}\Gamma^2} \ .$$

The Doppler effect, due to the thermal velocity v of the nucleus, broadens the actual width of the Breit-Wigner functions. The energy E of the γ radiation is shifted by the velocity of the nucleus towards an energy E':

$$E' \approx E\left(1+\frac{v}{c}\right) \ . \tag{2.4}$$

For the nuclear velocities v, a Maxwellian distribution function is assumed [Metz59]:

$$w(v)dv = \sqrt{\frac{M}{2\pi kT}} \exp\left(-\frac{Mv^2}{2kT}\right) dv \tag{2.5}$$

with M the nuclear mass, k Boltzmann's constant and T the temperature of the target nuclei. Taking into account relations (2.4) and (2.5) the energy distribution for the γ radiation equals:

$$w(E')dE' = \frac{1}{\Delta\sqrt{\pi}} \exp\left(-\left[\frac{E'-E}{\Delta}\right]^2\right) dE'$$

with

$$\Delta = \left(\frac{E}{c}\right)\sqrt{\frac{2kT}{M}}$$

the Doppler width. The absorption cross section $\sigma_{abs}(E)$ has to be averaged over all the energies E' of the incident γ radiation:

$$\sigma_D(E) = \int_{-\infty}^{+\infty} \sigma_{abs}(E')w(E')dE' = \sigma_{max} \cdot \psi(x,t)$$

with

$$\begin{aligned}
\psi(x,t) &= \left[\frac{1}{2\sqrt{\pi t}}\right] \int_{-\infty}^{+\infty} \frac{\exp[-(x-y)^2/4t]}{1+y^2} dy \\
x &= \frac{2(E-E_x)}{\Gamma} \quad ; \quad y = \frac{2(E'-E_x)}{\Gamma} \\
t &= \left(\frac{\Delta}{\Gamma}\right)^2 \\
\sigma_{max} &= \pi \cdot \lambda\!\!\!^{-2} \, \frac{2(2J+1)}{2J_0+1} \cdot \frac{\Gamma_0}{\Gamma}
\end{aligned}$$

and $\sigma_D(E)$ is the "Doppler form" of the absorption cross section. For large values of t, $\psi(x,t)$ is approximated by [Metz59]:

$$\psi(x,t) = \frac{\sqrt{\pi}}{2\sqrt{t}} \exp\left[-\frac{x^2}{4t}\right] \ .$$

The Doppler width Δ of a 3 MeV photon impinging on a nucleus with mass number 120 at room temperature equals 2000 meV. The total decay width Γ represents only a few meV and consequently this condition is fulfilled. Hence, the Doppler form of the absorption cross section can be written as:

$$\sigma_D(E) = \sigma_{max} \left(\frac{\Gamma\sqrt{\pi}}{2\Delta}\right) \exp\left(-\left[\frac{E-E_x}{\Delta}\right]^2\right) \ .$$

Taking into account that the integral:

$$\int_{-\infty}^{+\infty} \frac{\sqrt{\pi}}{2\sqrt{t}} \exp\left(-\frac{x^2}{4t}\right) dx = \pi$$

independent of the value of t, the energy integration of the "Doppler form" over a single resonance equals:

$$\int_0^{+\infty} \sigma_D(E)dE = \sigma_{max} \cdot \pi \cdot \frac{\Gamma}{2} = \pi^2 \lambda\!\!\!^{-2} \frac{2J+1}{2J_0+1} \cdot \Gamma_0 \ . \tag{2.6}$$

From the Eqs. (2.2) and (2.3) it is learned that the elastic and absorption cross sections are connected by:

$$\sigma_{elas}(E) = \frac{\Gamma_0}{\Gamma} \cdot \sigma_{abs}(E) = Br \cdot \sigma_{abs}(E)$$

with Br the branching ratio Γ_0/Γ of the level. This relation can be used to deduce immediately the total elastic scattering cross section I_S integrated over a single resonance and over the complete solid angle from Eq. (2.6):

$$I_S = Br \cdot \int_0^{+\infty} \sigma_D(E)dE = \frac{2J+1}{2J_0+1} \left(\frac{\pi\hbar c}{E_x}\right)^2 \frac{\Gamma_0^2}{\Gamma} \ . \tag{2.7}$$

For convenience, the expression "total scattering cross section I_S" will be used throughout this work. The total scattering cross section doesn't depend on the Doppler width Δ and consequently can be determined independently of the target temperature.

Eq. (2.7) illustrates that the scattering cross section I_S depends linearly on the transition width ratio Γ_0^2/Γ. Hence, when the branching ratio Γ_0/Γ can be determined in an NRF experiment or is known from literature data, the ground state level width Γ_0 can be deduced from the measured scattering cross section I_S and the reduced excitation probability extracted [Knei96]:

$$B(\pi L)\uparrow = \ g \cdot \frac{L[(2L+1)!!]^2}{8\pi(L+1)} \left(\frac{\hbar c}{E_x}\right)^{2L+1} \cdot \Gamma_0 \ . \tag{2.8}$$

The statistical spin factor g depends on the ground state spin and the spin of the excited level:

$$g = \frac{2J+1}{2J_0+1} \ .$$

The reduced transition probabilities $B(\pi L)\uparrow$ (excitation) and $B(\pi L)\downarrow$ (de-excitation) relate as:

$$B(\pi L)\uparrow = \ g \cdot B(\pi L)\downarrow \ .$$

These reduced transition probabilities allow to compare the strength of the observed transitions with those observed in other nuclei and with results from theoretical calculations.

2.2 Spin determination and angular distribution functions

The angular distribution function $W(\theta)$ for resonantly scattered real photons is given by the following expression [Fagg59]:

$$W(\theta) = \sum_{\nu\ even}^{\min(2J,2L_1,2L_2)} A_\nu(1) \cdot A_\nu(2) \cdot P_\nu(\cos\theta) \tag{2.9}$$

with θ the scattering angle between the direction of the incident photon and the scattered photon and $P_\nu(\cos\theta)$ the Legendre functions. The coefficient $A_\nu(1)$ describes the photon in the entrance channel, with multipolarity L_1 or $L_1' = L_1 + 1$ and mixing ratio δ_1 for the involved transition, and similarly $A_\nu(2)$ takes into account the resonantly scattered photon (with multipolarity L_2 or $L_2' = L_2 + 1$ and mixing ratio δ_2 for the involved transition):

$$\begin{aligned} A_\nu(1) &= \left(\frac{1}{1+\delta_1^2}\right) \cdot \left\{F_\nu(L_1L_1J_0J) + 2\cdot\delta_1 \cdot F_\nu(L_1L_1'J_0J) + \delta_1^2 \cdot F_\nu(L_1'L_1'J_0J)\right\} \\ A_\nu(2) &= \left(\frac{1}{1+\delta_2^2}\right) \cdot \left\{F_\nu(L_2L_2J_fJ) + 2\cdot\delta_2 \cdot F_\nu(L_2L_2'J_fJ) + \delta_2^2 \cdot F_\nu(L_2'L_2'J_fJ)\right\} \ . \end{aligned} \tag{2.10}$$

The "F-coefficients" are given in Appendix A. The mixing ratio δ_1 (δ_2) is defined as [Fagg59]:

$$\delta_{1(2)} = \frac{\langle\psi_f|L'_{1(2)}|\psi_i\rangle}{\langle\psi_f|L_{1(2)}|\psi_i\rangle} \ .$$

In the case of elastic scattering $\delta_1 = \delta_2 = \delta$. For a further discussion it is needed to distinguish between even-even and odd-mass nuclei.

2.2.1 Even-even nuclei

Nuclei with even proton and neutron numbers always have a ground state spin and parity J_0^π of 0^+. As a consequence, only levels with a spin 1 or 2 can be excited in (γ,γ') measurements. In the case of elastic scattering, only the spin sequences $0-1-0$ and $0-2-0$ will occur corresponding to pure dipole and quadrupole transitions and the following expressions for the angular distribution functions $W(\theta)$ are obtained:

$$\begin{aligned} W(\theta)_D &= \frac{3}{4}(1+\cos^2\theta) \\ W(\theta)_Q &= \frac{5}{4}(1-3\cos^2\theta+4\cos^4\theta) \ . \end{aligned}$$

These angular distribution functions are plotted in Fig. 2.2. A clear distinction between both distributions exists, most prominent at the scattering angles of 90° and 127°. Thus, in the case of an even-even nucleus a measurement of the γ intensities at only two angles (90° and 127°) allows the determination of the multipolarity L and the spin J of the excited level. The ratio of the measured scattered γ intensities at 90° and 127° should result in one of the two expected values:

$$\frac{W(90°)_D}{W(127°)_D} = 0.73 \quad \text{or} \quad \frac{W(90°)_Q}{W(127°)_Q} = 2.28$$

Figure 2.2: Radial plot of the angular distribution functions for pure dipole ($W(\theta)_D$) and quadrupole ($W(\theta)_Q$) ground state transitions in even-even nuclei.

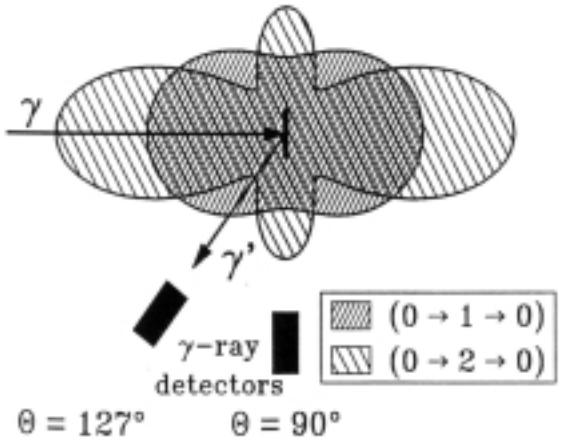

depending on the multipolarity of the involved γ transition. Once the spin of the excited level is determined, the statistical spin factor g is known and the reduced excitation probabilities are calculated using Eq. (2.8). The transition width ratio Γ_0^2/Γ is extracted from the measured total scattering cross sections I_S (Eq. (2.7)) and often it is assumed that the branching ratio $\Gamma_0/\Gamma = 1$. For dipole and quadrupole transitions in even-even nuclei the numerical relations hold:

$$B(E1)\uparrow = 2.866 \ \frac{\Gamma_0}{E_x^3} \qquad (10^{-3}e^2fm^2)$$

$$B(M1)\uparrow = 0.2598\frac{\Gamma_0}{E_x^3} \qquad (\mu_N^2)$$

$$B(E2)\uparrow = 6201 \ \frac{\Gamma_0}{E_x^5} \qquad (e^2fm^4)$$

with the ground state decay width Γ_0 in (meV) and the excitation energy E_x in (MeV). The determination of the electric or magnetic character of the transition requires the knowledge of the parity of the excited level (see further section 2.3).

2.2.2 Odd-mass nuclei

The half integer ground state spin in odd-mass nuclei leads usually to nearly isotropic angular distributions. With the nowadays NRF facilities, it is in general impossible to determine in this case the spins of the excited levels. However, in the favourable case of an odd-mass nucleus with a ground state spin J_0 of 1/2, the extraction of limited spin information is possible. In NRF, only transitions to levels with a spin J of 1/2, 3/2, and 5/2 can be observed due to the high spin selectivity of the real photon probe. For resonantly elastic scattering of real photons, the angular correlation functions $W(\theta)$ for the different spin sequences are (see Appendix B):

$\frac{1}{2} \rightarrow \frac{1}{2} \rightarrow \frac{1}{2}$

$$W(\theta) = 1$$

$\frac{1}{2} \rightarrow \frac{3}{2} \rightarrow \frac{1}{2}$

$$W(\theta) = 1 + \left(\frac{1}{1+\delta^2}\right)^2 \times (3\cos^2\theta - 1) \times \left(\frac{1}{8} - \frac{\sqrt{3}}{2}\delta + \frac{5}{4}\delta^2 + \frac{\sqrt{3}}{2}\delta^3 + \frac{\delta^4}{8}\right) \tag{2.11}$$

$\frac{1}{2} \rightarrow \frac{5}{2} \rightarrow \frac{1}{2}$

$$W(\theta) = 1 + \left(\frac{1}{1+\delta^2}\right)^2 \times \frac{(3\cos^2\theta - 1)}{14} \times \left(2 + 4\sqrt{2}\delta + 10\delta^2 + \frac{12}{\sqrt{2}}\delta^3 + \frac{9}{2}\delta^4\right) + \left(\frac{1}{1+\delta^2}\right)^2 \times \frac{(35\cos^4\theta - 30\cos^2\theta + 3)}{168} \times \left(8 - 40\sqrt{2}\delta + 96\delta^2 + \frac{20}{\sqrt{2}}\delta^3 + \frac{\delta^4}{2}\right) .$$

A graphical method can be used to obtain information on the spin of the excited level. In Fig. 2.3 the expected ratio of the angular correlation functions $W(90°)/W(150°)$ is plotted versus the ratio $W(90°)/W(127°)$ for different values of the mixing ratio δ and for the three possible induced spin sequences. A level with spin 1/2 can only be excited from the ground state via a pure dipole transition and hence no mixing of multipolarities is possible in a 1/2 – 1/2 – 1/2 spin cascade. Such a cascade has an isotropic angular distribution function W. The solid square in Fig. 2.3 represents the unique location in this figure where 1/2 – 1/2 – 1/2 spin sequences can be found.

Figure 2.3: Angular distribution ratio $W(90°)/W(150°)$ plotted versus $W(90°)/W(127°)$ for different values of the mixing ratio δ and for spin cascades in an odd-mass nucleus with a ground state spin J of 1/2. Detailed information on the solid line, square, triangle, and star can be found in the text.

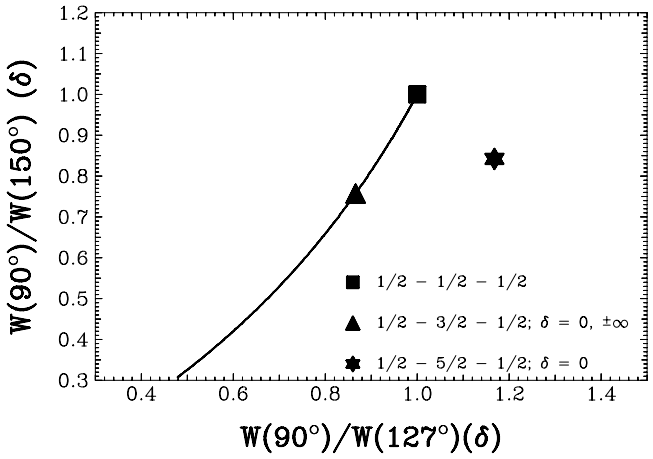

In the case of a 1/2 – 3/2 – 1/2 spin sequence, assuming a positive parity for the 1/2 ground state (as is the case in ^{117}Sn investigated in this work), a $E1/M2$ or $M1/E2$ mixing is theoretically possible depending on the parity of the excited 3/2 level. However, $M2$ transitions

can not be observed in NRF experiments. In this case, the mixing ratio δ of the transitions with multipolarities $L = 1$ and $L = 2$ influences the ratio between the angular distributions. This influence is illustrated in Fig. 2.3 by the solid line: when changing δ between -∞ and ∞ the point representing the ratio $W(90°)/W(150°)$ versus $W(90°)/W(127°)$ moves along the solid line. The extremes of this line (0.48, 0.30) and (1,1) are reached for mixing ratios δ equal to -0.57 and 0.27. The plotted line has been obtained by varying the mixing ratio δ in the corresponding angular distribution function of Eq. (2.11) between -0.57 and 0.27 (for smaller or higher values of δ the points are lying between the extreme values). For a pure $E1$ ($M1$) transition, corresponding to a mixing ratio $\delta = 0$, and also for a pure $M2$ ($E2$) transition, with mixing ratio $\delta = \pm\infty$, to the 3/2 level with a negative (positive) parity the same ratios of $W(90°)/W(127°)$ and $W(90°)/W(150°)$ are obtained from Eq. (2.11) which is represented by the solid triangle in Fig. 2.3. It has to be pointed out that if the mixing ratio δ in a 1/2 – 3/2 – 1/2 spin sequence takes the value of -3.73 or 0.27 the angular distribution function 1/2 – 3/2 – 1/2 spin sequence becomes isotropic as for a 1/2 – 1/2 – 1/2 spin sequence (remark that in Fig. 2.3 the solid square is one of the extremes of the solid line).

For a 1/2 – 5/2 – 1/2 spin sequence, transitions with multipolarities $L = 2$ and $L = 3$ are theoretically possible. However, $M2$, $E3$, and $M3$ excitations have scattering cross sections I_S far below the sensitivity of the setup. Therefore, only a pure $E2$ excitation to a 5/2 level can be observed. The solid star in Fig. 2.3 shows where these 1/2 – 5/2 – 1/2 spin sequences are expected.

For scattering angles corresponding to those typically used in the NRF experiments in this work and assuming no mixing of multipolarities, the following results are obtained:

$\frac{1}{2} \rightarrow \frac{1}{2} \rightarrow \frac{1}{2}$

$$W(90°) = W(127°) = W(150°) = 1$$

$\frac{1}{2} \rightarrow \frac{3}{2} \rightarrow \frac{1}{2}$

$$\frac{W(90°)}{W(127°)} = 0.866 \; \frac{W(90°)}{W(150°)} = 0.757; \quad \delta = 0, \pm\infty$$

$\frac{1}{2} \rightarrow \frac{5}{2} \rightarrow \frac{1}{2}$

$$\frac{W(90°)}{W(127°)} = 1.168 \; \frac{W(90°)}{W(150°)} = 0.842; \quad \delta = 0 \quad .$$

For the strongest transitions observed with a high statistical precision, the experimental uncertainties on the ratios $W(90°)/W(127°)$ and $W(90°)/(150°)$ will be small enough to suggest the induced half integer spin sequence (see section 4.2). In most cases the statistical accuracy will not allow to determine the spin sequence and hence the statistical spin factor g can not be determined.

With increasing half integer ground state spin values, all the angular distribution functions become nearly isotropic. This is illustrated in Fig. 2.4 for an odd-mass nucleus with a 5/2 ground state spin. In this figure, the angular distribution functions are plotted for pure dipole transitions in 5/2 – 3/2 – 5/2, 5/2 – 5/2 – 5/2, and 5/2 – 7/2 – 5/2 spin sequences (see also Appendix B). The present statistical accuracy of the NRF setup does not allow to distinguish between these different spin cascades.

Figure 2.4: Angular distribution functions plotted for pure electric dipole transitions for 5/2 – 3/2 – 5/2 (blue line), 5/2 – 5/2 – 5/2 (red line), and 5/2 – 7/2 – 5/2 (green line) spin sequences in an odd-mass nucleus with a ground state spin of 5/2.

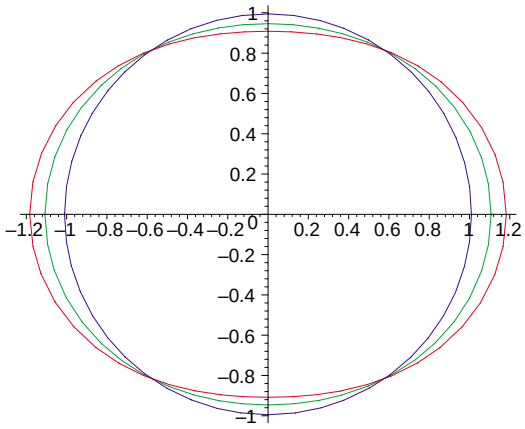

To conclude, for most of the levels in odd-mass nuclei, the statistical spin factor g will remain unknown. Therefore, only the product of the transition width ratio Γ_0^2/Γ with the spin factor g can be extracted form the total scattering cross section I_S. The reduced excitation probabilities depend linearly on the product $g \cdot \Gamma_0$ (see Eq. 2.8) and can be determined independently of the induced spin sequence. For example, the reduced electric dipole excitation probability equals (assuming a branching ratio $\Gamma_0/\Gamma = 1$):

$$B(E1)\uparrow = \frac{2.866}{3} \cdot \frac{g \cdot \Gamma_0}{E_x^3} \quad (10^{-3} e^2 f m^2)$$

with the ground state width Γ_0 in (meV) and the excitation energy E_x in (MeV).

2.3 Parity determination

A complete characterisation of the photo-excited levels is important for the comparison of the experimental results and data from theoretical nuclear structure models. Therefore also the parity of the involved levels has to be determined. Two experimental methods exist to assign parities:

- a measurement of the linear polarization of the resonantly scattered photons

- the scattering of (partially) linearly polarized off-axis bremsstrahlung

Both methods will be introduced here. Although they are physically completely different, they exhibit a lot of similarities.

2.3.1 Linear polarization of resonantly scattered photons

The linear polarization distribution of resonantly scattered photons is given by [Fagg59, Schl94]:

$$W(\theta,\varphi) = W(\theta) + (\pm)_{L_2'} \sum_{\nu\ even}^{\min(2J,2L_1,2L_2)} A_\nu(1)\cdot A'_\nu(2)\cdot P_\nu^{(2)}(\cos\theta)\cdot\cos(2\varphi)\ . \tag{2.12}$$

In this expression is θ the angle between the directions of the incoming and scattered photon and φ describes the angle between the electric vector $\vec{E}$ of the scattered photon and the reaction plane. The angular correlation function $W(\theta)$ was already introduced in Eq. (2.9). The coefficient $A_\nu(1)$ describes again the characteristics of the photon in the entrance channel (see Eq. 2.10). The coefficient $A'_\nu(2)$ equals [Fagg59, Schl94]:

$$A'_\nu(2) = \left(\frac{1}{1+\delta_2^2}\right) \quad \{ \quad -\kappa_\nu(L_2L_2)\cdot F_\nu(L_2L_2J_fJ) + 2\delta_2\cdot\kappa_\nu(L_2L_2')\cdot F_\nu(L_2L_2'J_fJ) \\ +\delta_2^2\cdot\kappa_\nu(L_2'L_2')\cdot F_\nu(L_2'L_2'J_fJ)\}$$

with κ_ν the polarization coefficient [Fagg59] depending on the multipolarities of the radiation and $P_\nu^{(2)}(\cos\theta)$ the unnormalized associated Legendre polynomial. The polarization distribution distinguishes between electric and magnetic transitions:

$$(\pm)_{L_2'} = \begin{cases} + & L_2' \quad \text{electric transition} \\ - & L_2' \quad \text{magnetic transition.} \end{cases}$$

The linear polarization degree of photons scattered under an angle θ is defined as the normalized difference between the cross sections $\sigma_\parallel$ (electric vector parallel with the reaction plane) and $\sigma_\perp$ (electric vector perpendicular to the reaction plane):

$$P_\gamma(\theta) = \frac{\sigma_\parallel - \sigma_\perp}{\sigma_\parallel + \sigma_\perp} = \frac{W(\theta,\varphi=0°) - W(\theta,\varphi=90°)}{W(\theta,\varphi=0°) + W(\theta,\varphi=90°)}$$

or after substituting Eqs. (2.9) and (2.12)

$$P_\gamma(\theta) = \frac{(\pm)_{L_2'}\sum_{\nu\ even} A_\nu(1)\cdot A'_\nu(2)\cdot P_\nu^{(2)}(\cos\theta)}{\sum_{\nu\ even} A_\nu(1)\cdot A_\nu(2)\cdot P_\nu(\cos\theta)\ .} \tag{2.13}$$

For a further discussion it is again necessary to distinguish between γ transitions in even-even and odd-mass nuclei.

2.3.1.1 Even-even nuclei

The linear polarization degree of the resonantly scattered photons in $0-1-0$ and $0-2-0$ spin cascades in even-even nuclei can be calculated using Eq. (2.13) and is equal to:

$$\begin{aligned} 0-1-0 \qquad & P_\gamma(\theta) \ = \ (\pm)_{L_2'}\frac{\sin^2\theta}{1+\cos^2\theta} \\ 0-2-0 \qquad & P_\gamma(\theta) = -(\pm)_{L_2'}\frac{1-5\cos^2\theta+4\cos^4\theta}{1-3\cos^2\theta+4\cos^4\theta}\ . \end{aligned}$$

The dependence of the photon linear polarization degree P_γ on the scattering angle θ is plotted in Fig. 2.5. For both spin sequences, $0-1-0$ and $0-2-0$, the polarization degree of the scattered

Figure 2.5: Plot of the dependence of the photon linear polarization degree on the scattering angle θ for $0-1-0$ and $0-2-0$ spin sequences in even-even nuclei. The linear polarization degree reaches a maximum under a scattering angle of 90°.

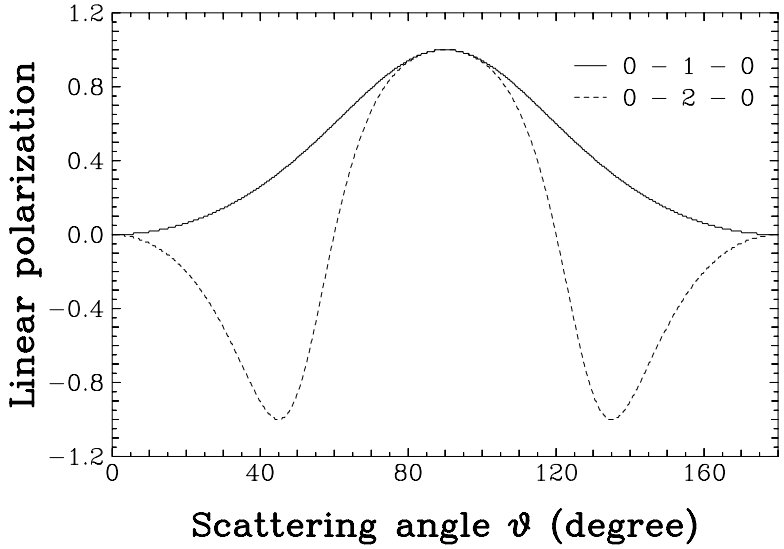

photons reaches its maximum value $|P_\gamma| = 1$ for a scattering angle of 90°. As a consequence, photons scattered at 90° are completely polarized. In summary, for photons resonantly scattered at 90° off even-even nuclei, the linear polarization degree equals:

$$P_\gamma(90°) = \begin{cases} -1 & E1 \\ +1 & M1, E2 \end{cases} .$$

An example is given in Fig. 2.6 for the case of an electric dipole transition: the electric vector of the resonantly scattered photon under the scattering angle of 90° is standing perpendicular on the NRF reaction plane ($\varphi = 90°$). Similarly, the electric vector will be parallel to the NRF reaction plane in the case of an $M1$ or $E2$ transition. In conclusion, a measurement of the photon linear polarization would allow to determine unambiguously and model independently the parity of the photo-excited levels in even-even nuclei.

2.3.1.2 Odd-mass nuclei

In the case of odd-mass nuclei, the linear polarization of the scattered photons will nearly vanish due to the half integer spins. Therefore, it is impossible to determine the parity of an excited level in an odd-mass nucleus in photon scattering experiments.

2.3.2 Compton scattering as polarization analyzer

In Compton scattering, photons are scattered off free or quasifree electrons. The Compton scattering process is sensitive to the linear polarization of the incident photon, so the process

Figure 2.6: Linear polarization of resonantly scattered photons in the case of a pure electric dipole transition in an even-even nucleus. At a scattering angle of 90°, the photons are completely vertically polarized for an horizontal NRF reaction plane.

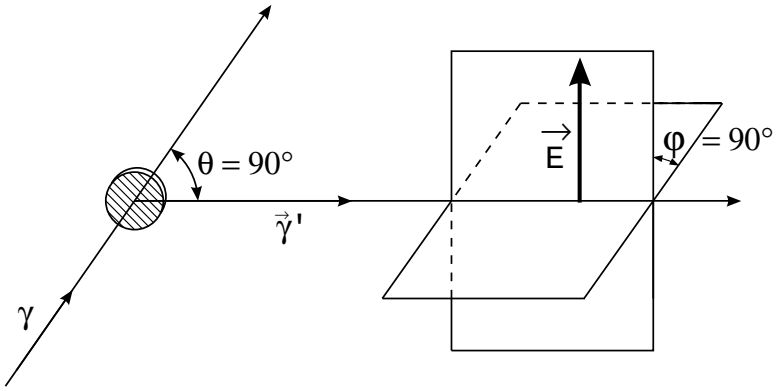

can be used to determine the linear polarization of resonantly scattered photons off nuclei.

Taking into account energy and momentum conservation in a scattering process, the energy $E_{\gamma'}$ of the Compton scattered photon is determined to:

$$E_{\gamma'} = \frac{E_\gamma}{1 + \alpha(1 - \cos\vartheta)} \ ,$$

with E_γ the energy of the incident photon and $\alpha = E_\gamma / m_0 c^2$ with $m_0 c^2$ the electron rest mass. The scattering angle ϑ is the angle between the directions of the incident and Compton scattered photon. The kinematics of the Compton scattering process is illustrated in Fig. 2.7. The differential cross section for Compton scattering is given by the Klein-Nishina formula:

$$\frac{d\sigma}{d\Omega} = \frac{1}{2} r_0^2 \frac{E_{\gamma'}^2}{E_\gamma^2} \left(\frac{E_{\gamma'}}{E_\gamma} + \frac{E_\gamma}{E_{\gamma'}} - 2\sin^2\vartheta\cos^2\phi \right)$$

where r_0^2 is the classical electron radius. The angle ϕ expresses the angle between the polarization plane of the incident photon and the Compton scattering plane (see also Fig. 2.7). For constant energies, the differential cross section reaches a maximum if ϕ equals to 90°. It can be concluded that Compton scattering events will predominantly take place in a plane perpendicular to the electric vector of the incoming photon.

This feature of the Compton scattering process will be used to determine the linear polarization of the resonantly scattered photons in the NRF process. If the NRF reaction plane is again taken as reference plane for the linear polarization $P_\gamma(\theta)$, the counting rates $N_\perp$ and $N_\parallel$ of Compton scattering events perpendicular and parallel to this plane can be considered. The counting rates $N_\perp$ and $N_\parallel$ depend on the Compton scattering differential cross sections $d\sigma/d\Omega(\vartheta, \phi)$ and the linear polarization distribution $W(\theta, \varphi)$:

$$\begin{aligned} N_\perp &= W(\theta, \varphi = 0°) \frac{d\sigma}{d\Omega}(\vartheta, \phi = 90°) + W(\theta, \varphi = 90°) \frac{d\sigma}{d\Omega}(\vartheta, \phi = 0°) \\ N_\parallel &= W(\theta, \varphi = 0°) \frac{d\sigma}{d\Omega}(\vartheta, \phi = 0°) + W(\theta, \varphi = 90°) \frac{d\sigma}{d\Omega}(\vartheta, \phi = 90°) \ . \end{aligned} \qquad (2.14)$$

Figure 2.7: Kinematics of the Compton scattering process.

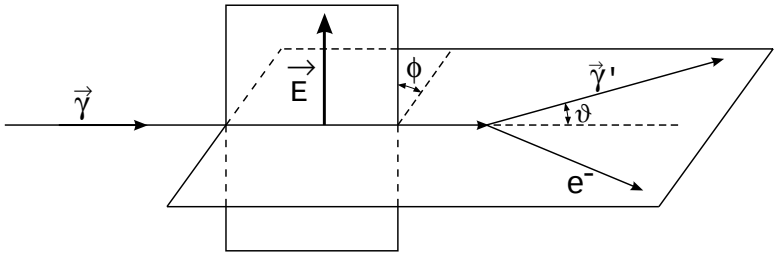

An important quantity is the azimuthal asymmetry ϵ which is defined as the relative difference of the counting rates $N_\perp$ and $N_\parallel$:

$$\epsilon = \frac{N_\perp - N_\parallel}{N_\perp + N_\parallel} \ .$$

Including the expressions for the counting rates $N_\perp$ and $N_\parallel$ results in:

$$\epsilon = \frac{\frac{d\sigma}{d\Omega}(\vartheta, \phi = 90°) - \frac{d\sigma}{d\Omega}(\vartheta, \phi = 0°)}{\frac{d\sigma}{d\Omega}(\vartheta, \phi = 90°) + \frac{d\sigma}{d\Omega}(\vartheta, \phi = 0°)} \cdot \frac{W(\theta, \varphi = 0°) - W(\theta, \varphi = 90°)}{W(\theta, \varphi = 0°) + W(\theta, \varphi = 90°)}$$

or

$$\epsilon = \Sigma(\vartheta, E_\gamma) \cdot P_\gamma(\theta)$$

and the factor $\Sigma(\vartheta, E_\gamma)$ denotes the analyzing power and is defined as:

$$\Sigma(\vartheta, E_\gamma) = \frac{\frac{d\sigma}{d\Omega}(\vartheta, \phi = 90°) - \frac{d\sigma}{d\Omega}(\vartheta, \phi = 0°)}{\frac{d\sigma}{d\Omega}(\vartheta, \phi = 90°) + \frac{d\sigma}{d\Omega}(\vartheta, \phi = 0°)} \ . \tag{2.15}$$

The azimuthal asymmetry can be determined experimentally using a three detector setup as shown in Fig. 2.8. The two detectors (A) perpendicular and parallel to the NRF reaction plane act like absorbers for the Compton scattered photons in the central detector (S), also called the scatterer. Consider the case of a scattered photon corresponding to an electric dipole transition in the nucleus. As stated in paragraph 2.3.1.1, the electric vector of the scattered photon will be perpendicular to the reaction plane ($\varphi = 90°$ in Fig. 2.8). Due to the polarization sensitivity of the Compton scattering process, the counting rate $N_\parallel$ will be higher than $N_\perp$, resulting in a negative asymmetry ϵ. Analogously, a positive asymmetry will be measured in the case of $M1$ or $E2$ transitions. In conclusion, the measurement of the azimuthal asymmetry allows to determine the parity of the excited level in an unambiguously model independent way.

In the case of point like scatterer and absorbers the analyzing power $\Sigma(\vartheta, E_\gamma)$ (Eq. (2.15)) equals:

$$\Sigma(\vartheta, E_\gamma) = \frac{\sin^2 \vartheta}{\frac{E'_\gamma}{E_\gamma} + \frac{E_\gamma}{E'_\gamma} - \sin^2 \vartheta}$$

In Fig. 2.9 the analyzing power is plotted for different photon energies. The maximum analyzing power $\Sigma(\vartheta, E_\gamma)$ corresponds to photon energies $E_\gamma \to 0$. The analyzing power decreases with increasing photon energy and the optimal photon scattering angle shifts to Compton scattering angles $\vartheta < 90°$. Due to the decreasing analyzing power with higher photon energies, the

Figure 2.8: Three detector setup as Compton polarimeter. The photons are compton scattered in the central detector (S) and depending on their linear polarization predominantly detected in one of the two absorber detectors (A).

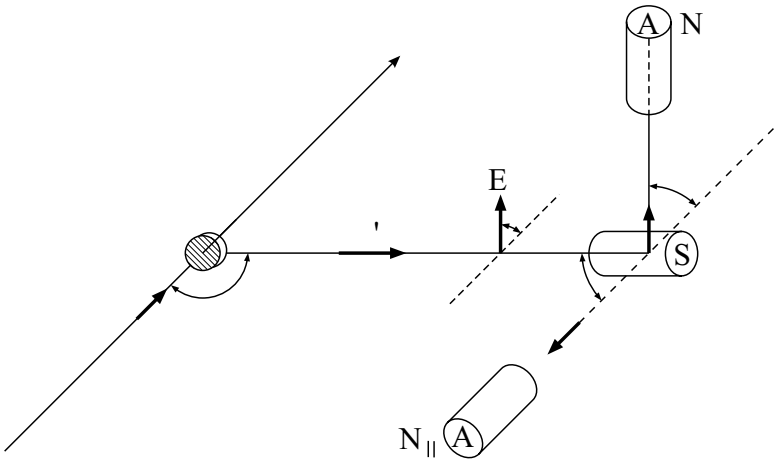

determination of the linear polarization of the resonantly scattered photons will be limited to excitation energies in the nucleus below about 5 MeV. Hence, the determination of the parities of excited levels using the Compton polarimetry method is limited to an excitation energy of about 5 MeV.

In this paragraph, the principles of measuring the linear polarization of photons has been illustrated using a classical three detector setup. Nowadays, more efficient Compton polarimeters are available as will be shown in Chapter 3.

2.3.3 Partially linearly polarized off-axis bremsstrahlung

A second method to determine the parity of photo-excited levels uses partially linearly polarized off-axis bremsstrahlung in the entrance channel. This technique was applied at the linear electron accelerators of the Giessen [Berg87] and Gent [Gova94a] Universities. The partially linearly polarized photons are obtained by selecting only a part of the bremsstrahlung cone [Berg87, Gova94a]. The angular distribution for the scattering of linearly polarized photons is given by [Fagg59]:

$$W(\theta,\varphi) = W(\theta) + (\pm)_{L_1'} \sum_{\nu even}^{\min(2J,2L_1,2L_2)} A_\nu'(1)\cdot A_\nu(2)\cdot P_\nu^{(2)}(\cos\theta)\cdot\cos(2\varphi) \qquad (2.16)$$

with $W(\theta)$ the angular distribution corresponding to the scattering of unpolarized photons, φ the angle between the electric vector of the incoming photon and the NRF reaction plane. The

Figure 2.9: The analyzing power of the Compton scattering process as a function of the Compton scattering angle ϑ. With increasing energy of the incident photons, the maximum of the analyzing power decreases and shifts to lower Compton scattering angles.

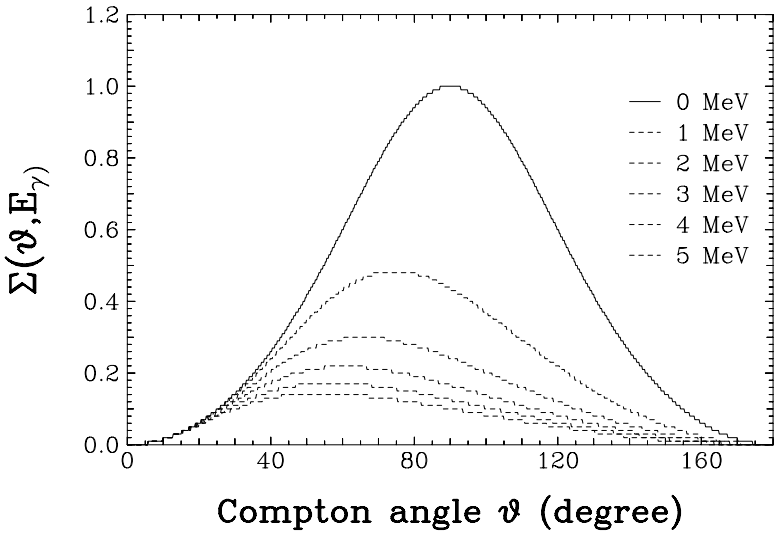

coefficient $A'_\nu(1)$ describes the incoming linearly polarized photon:

$$A'_\nu(1) = \left(\frac{1}{1+\delta_1^2}\right) \quad \{ \quad -\kappa_\nu(L_1L_1)\cdot F_\nu(L_1L_1J_fJ) + 2\delta_1\cdot\kappa_\nu(L_1L'_1)\cdot F_\nu(L_1L'_1J_fJ) \\ +\delta_1^2\cdot\kappa_\nu(L'_1L'_1)\cdot F_\nu(L'_1L'_1J_fJ)\}$$

and $A_\nu(2)$ the resonantly scattered photon (see Eq. (2.10)). The angular distribution function for the scattering of linearly polarized photons leads to an azimuthal asymmetry ϵ of the scattered photons which can be measured with a four detector setup. The detectors are placed at the same scattering angle θ and at the azimuthal angles φ of 0°, 90°, 180°, and 270° around the incident γ beam axis. This allows to determine the counting rates $N_\perp$ and $N_\parallel$ of scattered photons perpendicular and parallel to the polarization plane of the incoming photons. The azimuthal asymmetry $\epsilon(\theta, E_\gamma)$ is defined as:

$$\epsilon(\theta, E_\gamma) = \frac{N_\perp - N_\parallel}{N_\perp + N_\parallel} \ .$$

The azimuthal asymmetry can also be factorized as [Gova94a]:

$$\epsilon(\theta, E_\gamma) = \Sigma(\theta)\cdot P_\gamma(E_\gamma) \ .$$

The factor $P_\gamma(E_\gamma)$ represents the linear polarization degree of the incoming photons while the analyzing power $\Sigma(\theta)$ is defined as:

$$\Sigma(\theta) = \frac{W(\theta,\varphi=90°) - W(\theta,\varphi=0°)}{W(\theta,\varphi=90°) + W(\theta,\varphi=0°)} \ .$$

Figure 2.10: Angular distribution of scattered linearly polarized photons in $M1$ and $E1$ transitions. The angular distribution is calculated for a polarization degree of 33% of the incident photon beam.

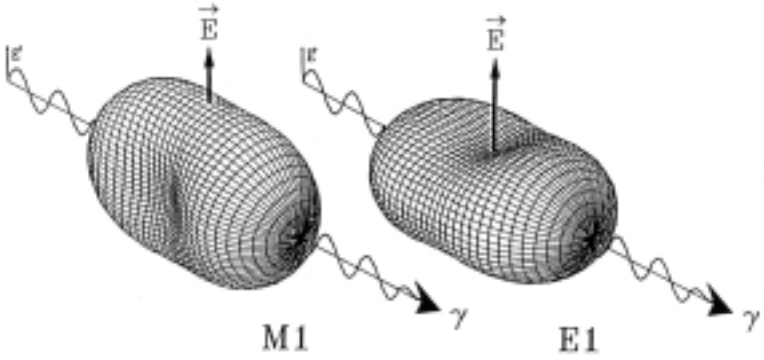

The analyzing power expresses how the scattered photons will be divided among the four detectors. Substituting the expression for the angular distribution (Eq. 2.16) results for the analyzing power $\Sigma(\theta)$ in:

$$\Sigma(\theta) = -\frac{(\pm)_{L_1'} \sum_{\nu\ even} A_\nu'(1) \cdot A_\nu(2) \cdot P_\nu^{(2)}(\cos\theta)}{\sum_{\nu\ even} A_\nu(1) \cdot A_\nu(2) \cdot P_\nu(\cos\theta)} \ .$$

This expression is similar to Eq. (2.13). For even-even nuclei, the analyzing power $\Sigma(\theta)$ reaches its maximum at the scattering angle of 90° and it is equal to:

$$\Sigma(90^\circ) = \begin{cases} +1 & E1 \\ -1 & M1, E2 \ . \end{cases}$$

Therefore, the four detectors will be placed at the scattering angle of 90°. According with the analyzing power, photons stemming from an $E1$ transition will be detected in the perpendicular detectors while photons corresponding to $M1$ or $E2$ transitions will be detected in the parallel detectors. However, in practice this clear distinction is influenced by the limited polarization degree of the incoming photons. This is illustrated in Fig. 2.10 where the actual angular distribution of the resonantly scattered photons is plotted for a polarization degree of 33% of the incident photon beam. In odd-mass nuclei the analyzing power $\Sigma(\theta)$ nearly vanishes due to the half integer spins of the ground and excited states.

This method of parity determination was applied for several years at the Giessen [Jung95] and Gent [Gova94a, Gova98, Bauw00] linacs in nuclear structure investigations of even-even nuclei up to the particle thresholds.

2.3.4 Comparison between Compton polarimetry and the scattering of linearly polarized photons

Compton polarimetry and the scattering of partially linearly polarized photons represent two useful and complementary techniques to determine the parities of photo-excited levels in even-

even nuclei. Below an excitation energy of about 5 MeV, the Compton polarimetry technique is superior. The analyzing power (or better the polarization sensitivity Q (see Chapter 3)) is sufficient to extract the parities of the measured azimuthal asymmetries ϵ. However, above an excitation energy of about 5 MeV the decreasing analyzing power prohibits an unambiguous measurement of the azimuthal asymmetry.

The technique making use of partially linearly polarized photons in the entrance channel is hampered by the limited polarization degree of the produced γ beam. In these experiments the end point energy of the incident γ beam is typically chosen at 12 MeV because the polarization degree increases towards lower energies and vanishes at the end point energy. In this case an average polarization degree of 16% between 5 and 12 MeV is obtained [Gova98]. This allows to measure the azimuthal asymmetries between about 5 MeV and the particle threshold in heavy nuclei. Below an excitation energy of 5 MeV, the measured azimuthal asymmetries are disturbed by feeding effects from higher lying states [Gova94b, Gova98] and nearly vanish. This inhibits parity assignments to levels with an excitation energy too far from the end point energy of the γ beam.

Chapter 3

Experimental setup and data analysis

The photon scattering experiments in this work were performed at the bremsstrahlung NRF facility installed at the 4.3 MV Dynamitron accelerator [Knei96] of the Institute für Strahlenphysik of the Stuttgart University (Germany). Bremsstrahlung produced by the deceleration of electrons in a radiation converter forms the most classical photon source. It has several advantages: the continuous bremsstrahlung spectrum allows to excite all levels with a sufficient ground state transition width Γ_0 simultaneously and problems related to the recoil of the excited nucleus, are avoided. The energy of the scattered photons can be determined precisely using highly efficient γ spectrometers with a good energy resolution which are available nowadays. The relatively low end point energy of 4.1 MeV limits the overestimation of the measured cross sections due to feeding from higher lying levels. One of the main drawbacks of the use of bremsstrahlung as photon source is the huge continuous background in the lower energy part of the recorded spectra. Due to mainly nonresonant scattering events in the NRF target, the background increases drastically to lower energies. This continuous background can hamper the observation of weak γ transitions or inelastic transitions which are crucial in a complete characterisation of a level.

In this Chapter some technical details of the Dynamitron accelerator, the production of bremsstrahlung, the NRF setup and the data acquisition systems will be discussed. The second part of this Chapter is devoted to the model independent analysis of the (γ, γ') data.

3.1 Dynamitron accelerator

The Dynamitron accelerator of the Stuttgart University is a single-end electrostatic generator which can be used to accelerate electrons as well as positive ions [Hamm75a, Hamm79]. This accelerator represents a modified and improved high voltage accelerator as was built for the first time by Cockroft and Walton in the Cavendish Laboratory of the Cambridge University (UK) in 1932 [Kran88].

An electron source can be obtained by leading a high electric current through a tungsten (W) wire. Electrons will leave the wire because of thermal evaporation. The maximum electron current which can be achieved is 4 mA with a maximum energy of 4.1 MeV. To obtain a positive

ion source the principles of Duoplasmatron, Penning sources, and high frequency sources are applied. The maximum ion current is 2 mA and a maximum energy of qV, with q the electric charge of the ions and V the high voltage of the terminal. To avoid scattering of the accelerated particles off the air molecules, the accelerator tube and the beam transport system are evacuated to a vacuum of 10^{-6} – 10^{-7} mbar.

3.2 Production of bremsstrahlung

In Fig. 3.1 the whole experimental facility consisting of the Dynamitron accelerator, the beam transport system (for details see [Hamm75a, Hamm79]) and the NRF setup is depicted. The electron beam delivered by the Dynamitron accelerator is deflected in an analyzing magnet over 120° into the beam line at which the NRF setup is placed. Bremsstrahlung is produced in high pressure water cooled gold (Au) radiator target. The gold radiator target has a thickness of 4 mm in which the electrons are completely stopped. Gold was chosen as basic material for the radiator target because of its high Z value which makes it very efficient in the production of bremsstrahlung and for its good thermal conductivity characteristics. Part of the electron energy is converted into γ rays, the other part of the energy is converted into heat. Therefore, the radiator target is water cooled with a pressure of 50 bar. The thermal capacity of the gold radiator target limits the electron beam current to about 250 μA for 4.1 MeV electrons (typical electron energy in a NRF experiment). In the gold radiator target very intense γ beams are produced with a flux of typically 10^6 photons/keV/second for 3 MeV photons. Before entering the experimental room, the continuous bremsstrahlung spectrum is hardened by a lead absorber (reducing the intensity of low energy photons) and collimated in a 1 m lead tube with a diameter of 10 mm.

3.3 NRF setup

The experimental room is separated from the generator room where the Dynamitron accelerator is located by a concrete wall of 2 m thickness. This avoids γ ray background in the experimental room stemming from the accelerator and beam transport system. The highly collimated γ beam enters an evacuated tube (vacuum of 10^{-3} – 10^{-4} bar), to avoid scattering of the γ beam off air molecules, which contains the NRF targets under investigation (see Fig. 3.1). Due to the high quality of the intense γ beam, two NRF setups can be operated simultaneously.

A first setup is used to perform angular distribution (γ, γ') measurements. This setup consists of three HP Ge detectors placed at the scattering angles of 90°, 127°, and 150°. Nowadays, large volume HP Ge detectors with an efficiency of 100% (relative to a 3 x 3 in^2. NaI(Tl) scintillation crystal) and a good energy resolution of about 2.0 keV at 1.33 MeV (γ ray produced by the radioactive ^{60}Co nucleus) are available. Typical measuring times at this setup are about 2 days for even-even nuclei and 4 days in the case of odd-mass nuclei. These extreme short measuring times are due to the high counting rates of about 5 kHz.

At the second setup a combination of angular distribution (γ, γ') and photon linear polarization $(\gamma, \vec{\gamma})$ measurements is carried out. This setup consists of two Compton polarimeters,

Figure 3.1: The NRF facilities at the 4.3 MV Dynamitron accelerator of the Stuttgart University. Two NRF facilities are placed at the 120° beam line. The first setup is used to perform angular distribution measurements, while at the second one angular distribution and linear polarization measurements of the resonantly scattered photons are carried out simultaneously.

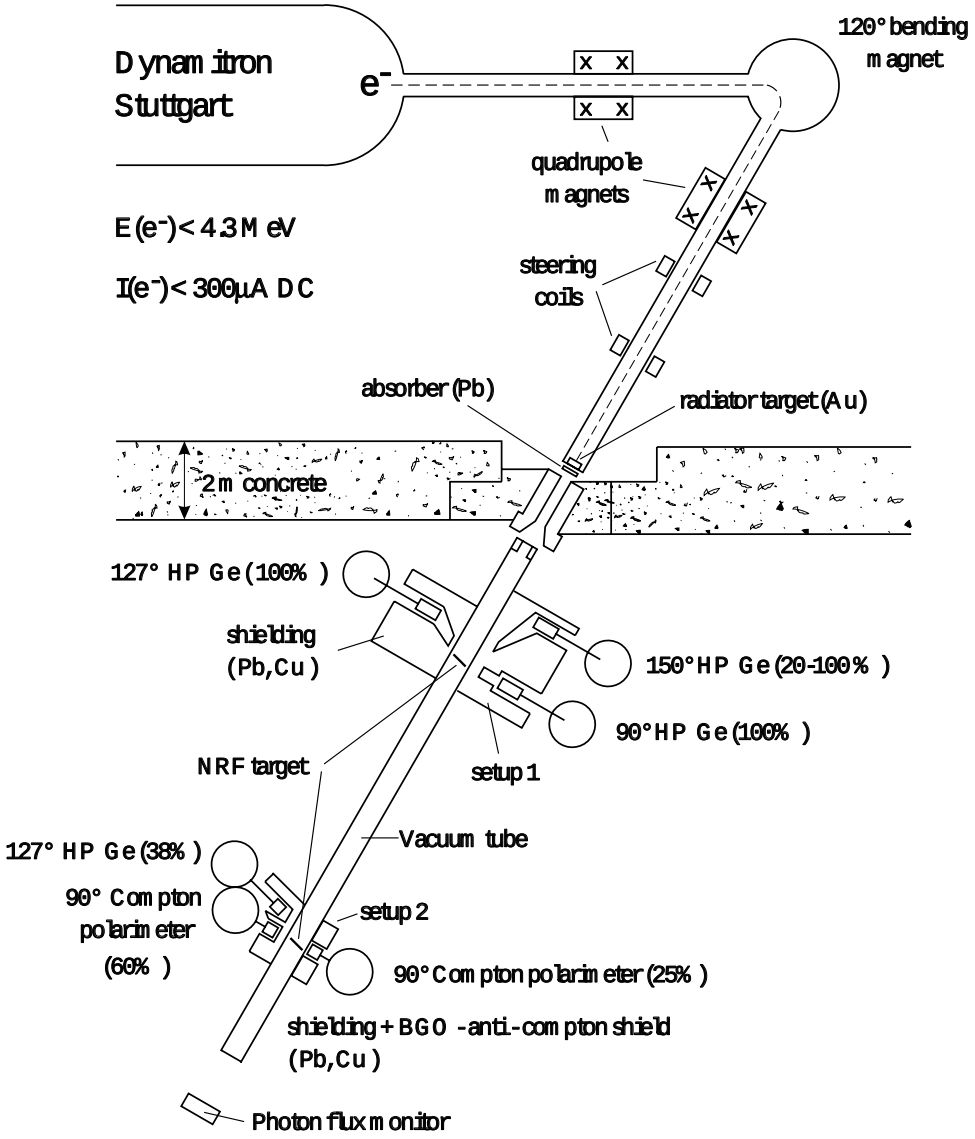

placed at slightly backward scattering angles of 95° and an additional HP Ge detector located at 127°. The Compton polarimeters are used to determine the linear polarization of the resonantly scattered photons enabling to deduce the parities of the excited levels (see Chapter 2). As the signal from the core of the Compton polarimeter carries already the full energy information of the detected γ rays, angular distribution measurements can be performed simultaneously at this setup. More technical details of the operation of the Compton polarimeters will be given in paragraph 3.3.2. At this setup, only even-even nuclei are studied because it is impossible to determine parities of levels in odd-mass nuclei (see Chapter 2). The accumulation of experimental data with sufficient statistical accuracy requires measuring times of 3 to 4 weeks.

In front of each Ge detector or Compton polarimeter a lead filter is placed to reduce the intensity of low energy photons (mainly with energies below 1 MeV). Otherwise, the large flux of these low energy photons can cause pile-up problems in the data acquisition system. The counting rate in the detectors should not exceed 10 kHz. Each Ge detector is surrounded with a lead shield to suppress the γ background.

3.3.1 Germanium γ ray spectrometers

The detection of γ rays critically depends on the number of electron-hole pairs created in the interaction with the detector material. The most important interaction processes of photons with matter are photo-electric absorption, Compton scattering and pair production. In all of these processes free electrons are created in the detector material. Commonly, semiconductors are used in which the primary electron created in the interaction produces secondary electron-hole pairs. The collection of these charge carriers is achieved by putting a voltage over the semiconductor and measuring the current collected at the electrodes. For a good charge collection, semiconductors with zones free of charge carriers are needed ("depleted zones"). Due to the penetrating characteristics of the incident γ radiation, semiconductor materials with thick depletion depths are required. In normal semiconductor materials a maximum depletion depth of only 2 – 3 mm can be achieved by applying an inverse bias voltage near the breakdown level. In the 1960's larger depletion depths became available in silicon and germanium crystals (the only two natural semiconductor materials) by lithium ion drifting. The interstitial lithium donor atoms compensate the acceptor impurities in the silicon and germanium crystals. This allows the creation of depletion depths with a thickness of 2 cm. At the end of the 1970's new techniques were found to grow germanium crystals with very low impurity concentrations of approximately 10^{10} atoms/cm^3. Nowadays, these intrinsic germanium or high-purity germanium (HP Ge) detectors are widespread because they are much easier to handle than lithium ion drifted detectors. For instance, they can be warmed up to room temperature when they are not in use, while the lithium ion drifted detectors should be maintained at low temperature.

In the case of γ ray spectroscopy at high energies detectors are needed with a large active volume. This can be fulfilled in a cylindrical or coaxial geometry. In this case, one electrode is fabricated at the outer cylindrical surface (see Fig. 3.2) of a long germanium cylindrical crystal, while a second inner cylindrical contact is obtained by removing the core of the crystal. The HP Ge detectors used in the Stuttgart NRF facility have actually a closed-ended coaxial

Figure 3.2: Closed-ended HP Ge detector

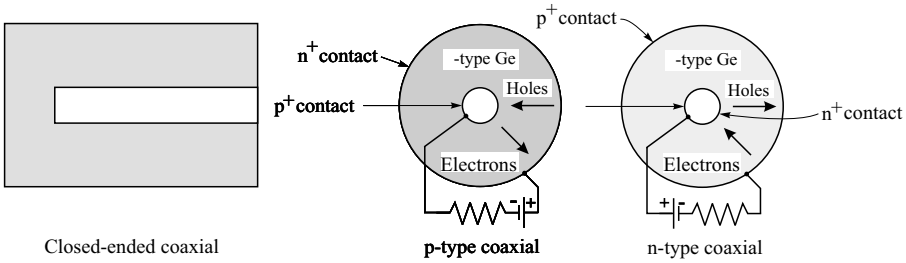

configuration in which only part of the central core has been removed. The outer electrode covers the outer cylindrical surface and one flat closed end of the crystal. The electrical properties of the HP Ge crystal depend on the remaining low-level impurities. In the case of remaining acceptor impurities, the HP Ge crystal will be p-type (similarly donor impurities give rise to a n-type HP Ge crystal). Reverse biasing requires that a positive voltage is applied to the n-contact with respect to the p-contact. During operation, the HP Ge detectors are cooled with liquid nitrogen to a temperature of 77° K to reduce the negative influence of thermal electronic noise (the band gap in Ge is 0.7 eV). The HP Ge detector is housed in a vacuum-tight cryostat to inhibit thermal conductivity between the crystal and the surrounding air. Secondly, a high over voltage is applied on the crystal to saturate the electron and hole drift velocities in the crystal in order to make the response time of the detector as short as possible.

The most outstanding characteristic of HP Ge detectors is their excellent energy resolution, allowing the separation of many close-spaced γ peaks which occur in NRF studies on heavy nuclei or odd-mass nuclei with high level densities. The energy resolution is determined by the statistical spread in the number of charge carriers, variation in the collection efficiency, and the contribution of the electronic noise. Generally, γ energies can be extracted from the recorded (γ, γ') spectrum with a precision better than 1 keV.

The response function of HP Ge detectors depends on the type of interaction of the γ rays with the Ge crystal. Photo-electric absorption, Compton scattering, and pair production contribute to the response function. In all these processes charge carriers are created which produce electron-hole pairs. Finally, the energy deposited in the crystal will be collected at the electrodes.

For the used HP Ge detectors, the photo-electric absorption process is dominating below incident photon energies of a few hundred keV. In photo-electric absorption, the energy of the incident photon is transfered into a photo-electron. The photo-electron has a kinetic energy which equals the difference of the photon energy and the binding energy of the electron. Due to the low energy of the photo-electrons, they will be completely absorbed in the crystal volume. A resulting single peak will be observed in the spectrum, the so-called photo-peak. In the energy region of interest between 1 and 4 MeV in the NRF experiments at the Stuttgart facility, photo-electric absorption plays a minor role. Photo-electric absorption will only occur at the end of multiple Compton scattering processes.

Compton scattering predominates in the region of 0.2 – 9 MeV [Knol89] incident photon energy. In Compton scattering a secondary photon is produced together with a Compton electron. The secondary photon can again undergo Compton scattering ("multiple Compton scattering") or can be completely absorbed by the photo-electric effect. Finally, if the complete incident γ ray energy is converted into charge carriers and if at the same time all the charged particle energy is absorbed within the detector volume, these events will again contribute to the photo-peak. In this case, the contribution to the photo-peak stems from a complete energy deposition of the incoming photon in the crystal after multiple scattering. Therefore, the photo-peak is also called full energy peak (FE). If the secondary photon escapes from the crystal, the Compton scattered electron will contribute to the Compton continuum. The Compton electrons have an energy distribution ranging between 0 and a certain maximum energy, the Compton edge. For a 3 MeV photon, the Compton edge is lying about 235 keV lower than the full energy peak. If photons stemming from multiple Compton scattering leave the detector, the Compton scattered electrons will give rise to a continuum between the Compton edge and the full energy peak.

Above 9 MeV, pair production is the dominating interaction process for photons with the Ge crystal. In the pair production process, the incident γ ray energy is used for the creation of an electron-positron pair. For this process a minimum energy of 1.02 MeV is required for the incident photon. The excess energy appears as kinetic energy of the electron-positron pair. Both the electron and positron will slow down quickly in the surrounding detector material. The positron is an unstable particle and annihilates with an electron, resulting in the creation of two 511 keV photons. If both the annihilation photons interact with the detector, the released incident photon energy will accumulate in the full energy peak. Incomplete absorption of one or both of the annihilation photons will result in a single escape peak (511 keV below the full energy peak) or a double escape peak (1022 keV below the full energy peak).

More details about radiation detection and the performances of Ge detectors as spectrometers can be found in [Debe88, Knol89]

3.3.2 Fourfold sectored Ge crystal as Compton polarimeter

In Chapter 2 the principle of measuring the linear polarization of resonantly scattered photons was illustrated with a three detector setup. One of the advantages of such a setup is that the Compton scattering angle can be optimized for a certain photon energy to compensate the shift in the maximum of the analyzing power towards smaller scattering angles (see Section 2.3.2). However, the small solid angle and the summation of energy signals from different detectors diminish the efficiency and energy resolution. Experiments with a five detector setup as Compton polarimeter have been carried out at the Stuttgart NRF facility [Heil90].

In Fig. 3.3 is shown how a large volume HP Ge detector can be used as Compton polarimeter. The outer electrode is divided into four electrodes electrically insulated from each other. Each of the four electrodes is connected with a separate amplifier. This procedure divides the crystal into four sectors which can individually detect γ rays. In Compton polarimetry measurements, the interest goes to events in which a γ ray is Compton scattered in one sector and absorbed in the neighbouring sector. Therefore the horizontal and vertical coincidence counting rates H

Figure 3.3: A fourfold sectored HP Ge crystal as Compton polarimeter. The usual outer electrode is replaced by four electrically insulated electrodes dividing the crystal into four sectors. The azimuthal asymmetry ϵ can be determined from a measurement of the horizontal (H) and vertical (V) coincidence counting rates

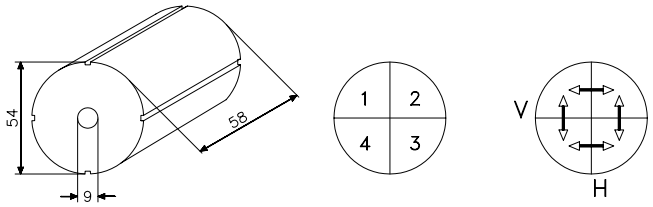

and V are determined:

$$H = (12\overline{3}\overline{4}) + (\overline{1}\overline{2}34)$$
$$V = (1\overline{2}\overline{3}4) + (\overline{1}23\overline{4}) \ .$$

In this case, each sector acts as Compton scatterer and absorber. Since Compton scattering occurs preferentially in a plane perpendicular to the electric vector, the linear polarization of the radiation incident on the Compton polarimeter will give rise to characteristic differences in the horizontal and vertical coincidence counting rates and an azimuthal asymmetry will be measured:

$$\epsilon = \frac{V - H}{V + H}$$

or

$$\epsilon = \frac{N_\perp - N_\parallel}{N_\perp + N_\parallel}$$

because the Compton polarimeter is placed in the horizontal plane (which coincides with the NRF reaction plane). In Section 2.3.2 it was shown that the azimuthal asymmetry ϵ equals $\Sigma(\vartheta, E_\gamma) \cdot P_\gamma(\theta)$. However, this relation was derived for point like scatterer and absorbers. In the case of a fourfold sectored HP Ge detector it should be replaced by [Schl94]:

$$\epsilon = Q(\vartheta, E_\gamma) \cdot P_\gamma(\theta)$$

with Q the polarization sensitivity of the Compton polarimeter. The polarization sensitivity can be parametrised as [But173]:

$$Q(\vartheta, E_\gamma) = \Sigma(\vartheta, E_\gamma) \cdot (a + bE_\gamma) \ .$$

This formula takes into account the large solid angle of the Compton polarimeter and the shift of the optimal Compton scattering angle to smaller angles for increasing energy of the incident photons. To be able to extract the photon linear polarization from the measured azimuthal asymmetry ϵ, the dependence of the polarization sensitivity Q on the photon energy should be determined precisely. Below an energy of 1 MeV this can be achieved in coincidence polarization-correlation measurements of nuclear $(\gamma - \gamma)$ cascades [Schl94, Beli97] in radioactive isotopes

Table 3.1: Characteristics of the two Compton polarimeters of the Stuttgart University

	polarimeter 1[a]	polarimeter 2[b]	
Energy resolution ΔE_γ	2.2 keV	$\cong$ 2.0 keV	at 1332 keV
Total detection efficiency ϵ_{total}	25%	60%	at 1332 keV
Coincidence efficiency ϵ_{coinc}	25%	30%	at 3 MeV
asymmetry	$< 1\%$	$<1\%$	
Polarization sensitivity Q	20%	25%	at 0.5 MeV
	9.5%	4.8%	at 4.4 MeV

[a] See Ref. [Schl94]

[b] See Ref. [Beli97]

with known linear polarization, e.g. ^{106}Pd. For the energy between 1 and 5 MeV $(p, p'\gamma)$-reactions on light nuclei are used, e.g. ^{12}C, ^{24}Mg, ^{28}Si, and ^{56}Fe. In these $(p, p'\gamma)$-reactions levels are populated which decay via γ transitions with known polarization [Schl94, Maie92, Beli97]. The polarization sensitivity Q can be improved by imposing a minimum energy on the Compton scattered photon in the absorber and on the Compton electron in the scatterer. For a certain incident photon energy, the energy of the Compton scattered photon and Compton electron depend on the Compton scattering angle. Hence, a minimum threshold on the Compton scattered photon will limit the maximum value of the Compton scattering angle. Vice versa the minimum value of the Comtpon scattering angle can be raised by putting an energy threshold on the detected Compton electron in the scatterer. In conclusion, the energy threshold applied in the scatterer and absorber narrows the interval of the Compton scattering angles around the optimal value. In the case of a fourfold sectored polarimeter, the roles of scatterer and absorber are interchanged. Therefore the same energy threshold is applied in all the sectors.

For the NRF facility in Stuttgart two Compton polarimeters are used of which the characteristics are summarized in Table 3.1. The energy resolution ΔE_γ and the total detection efficiency ϵ_{total} are given for the 1332 keV γ produced in the decay of the radioactive isotope ^{60}Co. The coincidence efficiency is given by [Schl94]:

$$\epsilon_{coinc} = \frac{V + H}{N_S}$$

in which the total number of coincidence events $(V + H)$ is compared to the detected photo-peak events N_S (without any coincidence requirement). It is obvious that the coincidence efficiency will decrease with an increasing threshold applied in the Compton polarimeter sectors. An important quantity is the asymmetry of the Compton polarimeter which should be very low. For a perfect symmetric polarimeter, the azimuthal asymmetry for completely unpolarized radiation should vanish [Schl94]:

$$\begin{aligned} \epsilon(P_\gamma = 0) &= \frac{aV^{unpol.} - H^{unpol.}}{aV^{unpol.} + H^{unpol.}} = 0 \\ \Rightarrow a &= \frac{H^{unpol.}}{V^{unpol.}} \ . \end{aligned}$$

The asymmetry of the Compton polarimeter corresponds to 1 - a and can be determined in the energy region between 0 and 3.5 MeV using a ^{56}Co radioactive source (see Appendix C). Finally, a polarization sensitivity Q of about 20% at 0.5 MeV and 9.5% at 4.4 MeV allows to determine unambiguously and model independently the parities of photo-excited levels up to an excitation energy of 4 MeV with good accuracy [Heil90]. The energy threshold applied in the sectors of the Compton polarimeters is typically about 260 keV. To improve the response function of the Compton polarimeter with the lowest efficiency, it has been surrounded with an eightfold sectored BGO-anti-Compton shield [Knei96, Mase96a].

The use of a fourfold sectored HP Ge crystal as Compton polarimeter represents several advantages [Schl94]:

- The core-output delivers the total energy signal deposited in the crystal. There is no energy summation needed to determine the energy of the incident photons.
- The sectored polarimeter has a high coincidence efficiency $\epsilon_{coinc} = (V + H)/N_s$ due to the narrow geometry and the large solid angle.
- The large volume of the crystal results in a high total detection efficiency.
- The sectored polarimeter offers a nearly full symmetry. The asymmetry is very small.
- The polarimeter is rather compact and can be easily shielded by a passive shielding (lead) or active shielding like a BGO-anti-Compton shield.

One of the latest developments in Compton polarimeters was achieved in the proposal to use a Euroball-cluster detector for Compton polarimetry measurements [Weis96]. A Euroball-cluster contains seven encapsulated Ge detectors with a relative efficiency of 60% each. The hexagonal shapes of the Ge detectors allow a close packing into a cluster arrangement (see Fig. 3.4). The Euroball-cluster is part of the European project to build a Euroball spectrometer with a very high efficiency for nuclear spectroscopy studies [Simp97]. The main difference with the aforementioned Compton polarimeters (three detector setup and sectored Ge crystal) is the angle between the scatterer and absorber which is equal to 60° and not 90° as usual ("nonorthogonal Compton polarimeter"). For such an arrangement the azimuthal asymmetry is determined to [Weis96]:

$$\epsilon = \frac{N_{90^\circ} - c(N_{30^\circ} + N_{150^\circ})}{N_{90^\circ} + c(N_{30^\circ} + N_{150^\circ})} ,$$

with N_{90°, N_{30°, and N_{150° the coincidence counting rates in the three possible directions of scatter-absorber combinations. The factor c normalises the pair of scatter-absorber coincidences and amounts to 0.5. The Euroball-cluster detector was already used to determine the parities of levels observed in ^{138}Ba [Herz99] and ^{88}Sr [Kaub00]. The main drawbacks of such a Compton polarimeter are the lower polarization sensitivity Q (due to the lower angle between the scatter and the absorber) and the lower coincidence efficiency (due to the large volume of the Ge crystals). However, numerical simulations [Garc95] and experimental [Weis96] tests show that the figure of merit of the cluster detector can be somewhat larger at high γ energies than that of fourfold sectored Compton polarimeters.

Figure 3.4: Cluster detector consisting of seven HP Ge detectors used as Compton polarimeter. This is an example of a nonorthogonal Compton polarimeter since the different scatter-absorber pairs make an angle of 60°

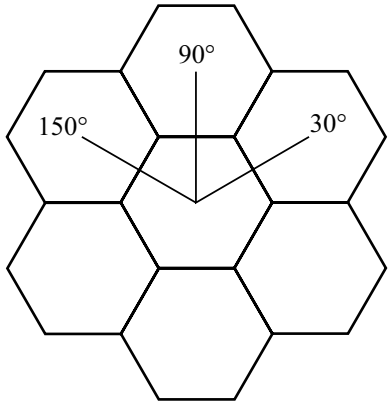

For more details about Compton polarimeters and their performances, the reader is referred to the extensive literature [Bass79, Simp83, Heil90, Schl94] and reference therein.

3.4 Data acquisition

Due to the different kind of measurements performed at the first and second setup, each setup has its own data acquisition system.

3.4.1 Data acquisition system at the first setup

The data acquisition system developed for NRF measurements at the first setup is depicted in Fig. 3.5. After the interaction of the incoming photon with the Ge crystal, the electric signal from the electrodes is amplified and shaped in a preamplifier (PA) and a main amplifier (MA) (Silena 7612). The preamplifier is incorporated as part of the cryostat package. This allows to build a close-fitting lead shielding around the detector. The input stages of the preamplifier are cooled together with the Ge crystal by liquid nitrogen to reduce the influence of electronic noise. The main amplifier gives a gaussian shape to the signal. The signal is transported through a 50 m cable to a separate air conditioned room. In this room, the ADC's (Analog to Digital Converter, Silena 7411) which convert the analog signal into a binary value are placed. Each binary value corresponds to a memory address in a TMCA-card (Target Multi Channel Analyser) in which a number of counts is accumulated. This card is plugged into a computer and every 8 hours the accumulated spectra recorded in the TMCA-card are stored on a hard disk and a floppy disk. The use of a TMCA-card allows to check the recorded spectra online and to correct for too long dead times or shifts in the ADC's. However, the air conditioning guarantees a longtime temperature stability of the ADC's. After the completion of the measurements, the format of

Figure 3.5: Data acquisition system for angular distribution measurements at the first setup.

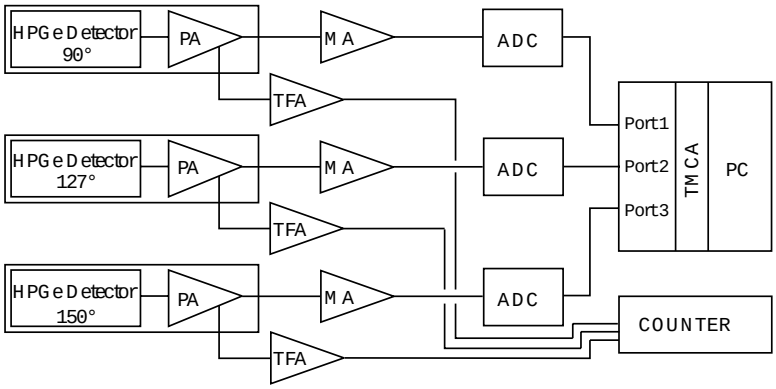

the TMCA pulls height spectra is converted and transmitted to a VAX 3100 station (with a VMS operating system). This VAX station contains a complete set of analysis software.

3.4.2 Data acquisition system at the second setup

The situation at the second setup is much more complex. In the case of the Compton polarimeter surrounded with the BGO-anti-Compton shield the following energy and time signals need to be stored:

- core-signal of the polarimeter
- four energy signals from each sector of the polarimeter
- four time signals from each sector of the polarimeter
- four time signals of the BGO-anti-Compton shielding

In Fig. 3.6 a flow diagram is given of the Compton polarimeter electronics. The five detector signals (core + four sectors) are amplified and shaped in a preamplifier (PA) and a main amplifier (MA) resulting in a gaussian shape for the energy signals. The energy signals are sent through 50 m cables towards the air conditioned room and stored in the ADC's. The five time signals of the Compton polarimeter are amplified and transformed in fast timing signals in the TFA's (Time Filter Amplifier). The CFD (Constant Fraction Discriminator) converts the signals from the TFA's into a logic pulse. For the time signals of the BGO-anti-Compton shield FTA's (Fast Time Amplifiers) are used. The time signals of the eightfold BGO-anti-Compton shield are taken two by two. In order to obtain good time resolutions, the threshold is as low as possible, about 30 mV. The logic pulse from the core of the polarimeter is used as start pulse ("event-trigger") to the TDC (Time to Digital Converter). Under these conditions, the counting rate of the start signal is typically about 5000 – 6000 counts/second. In the energy spectra, the continuous background increases quickly towards lower energies, due to the shape of the produced bremsstrahlung spectrum. The huge background below excitation energies of 1.5 MeV

prevents the observation of resonant scattering peaks in the (γ, γ') spectrum. Therefore, a second CFD is used for the time signals from the core of the polarimeter which allows to reject the storage of events corresponding to incoming photons with an energy lower than 1.5 MeV. In this procedure, the counting rate of the start signal decreases to 15 – 20 counts/second. For the second Compton polarimeter without BGO-anti-Compton shielding, the electronic measuring chain is very similar.

All the signals created in the ADC's and TDC's need to be stored to a hard disk or tape. The solution for this problem was found in the implementation of a high speed list mode data acquisition system [Mase96c] (see Fig. 3.7). The hardware of this system is very similar to a list mode system used at the Institut für Kernphysik of the University of Cologne. The heart of this system is a MC68030 CPU (Motorola, 25Mhz, 16Mbyte RAM) with the Lynx Os. Connected to the VME bus are a CAMAC-bus and FERA-bus. The CAMAC-system is a widespread standard to link different electronic modules together. The CBD 8110 acts as interface between the VME-bus and the CAMAC-bus. The CAMAC bus is used to initialize and program the modules. It is also used to read the single spectra out of the NFI (NIM Fera Interface). The ADC's and TDC's are read out by a FERA-bus (Fast Encoding and Readout ADC) with a speed of 10 Mwords/s. The FERA-bus stores the data in two HSM's 8170 (High Speed Memory) of 1 Mb RAM which act as buffer between the Fast FERA-system and the slower VME-bus. These two HSM's are operated in a "flip-flop" mode. If one of the two HSM's is full, the other one will be filled with data. The VME-bus always reads data from the HSM which was completely filled. This method allows to reduce the dead time in the case of high data rates. The VME computer stores the recorded data on a hard disk which can be reached from other computers via the Ethernet.

At this setup, angular distribution measurements are performed simultaneously with the linear polarization measurements. For the angular distribution measurements the core signals of the Compton polarimeter and the detection signal of a third HP Ge detector installed at the scattering angle of 127° is stored in a TMCA-card plugged in a PC (similar to the first setup). The TMCA spectra are again converted into another format and transmitted to a VAX station. These spectra are analysed in the same way as if they were taken at the first setup.

For more details about the list mode data acquisition system see [Mase96c, Mase98]

Figure 3.6: Electronic measuring chain behind a Compton polarimeter which is surrounded with a BGO-anti-Compton shield. For more explanations see text.

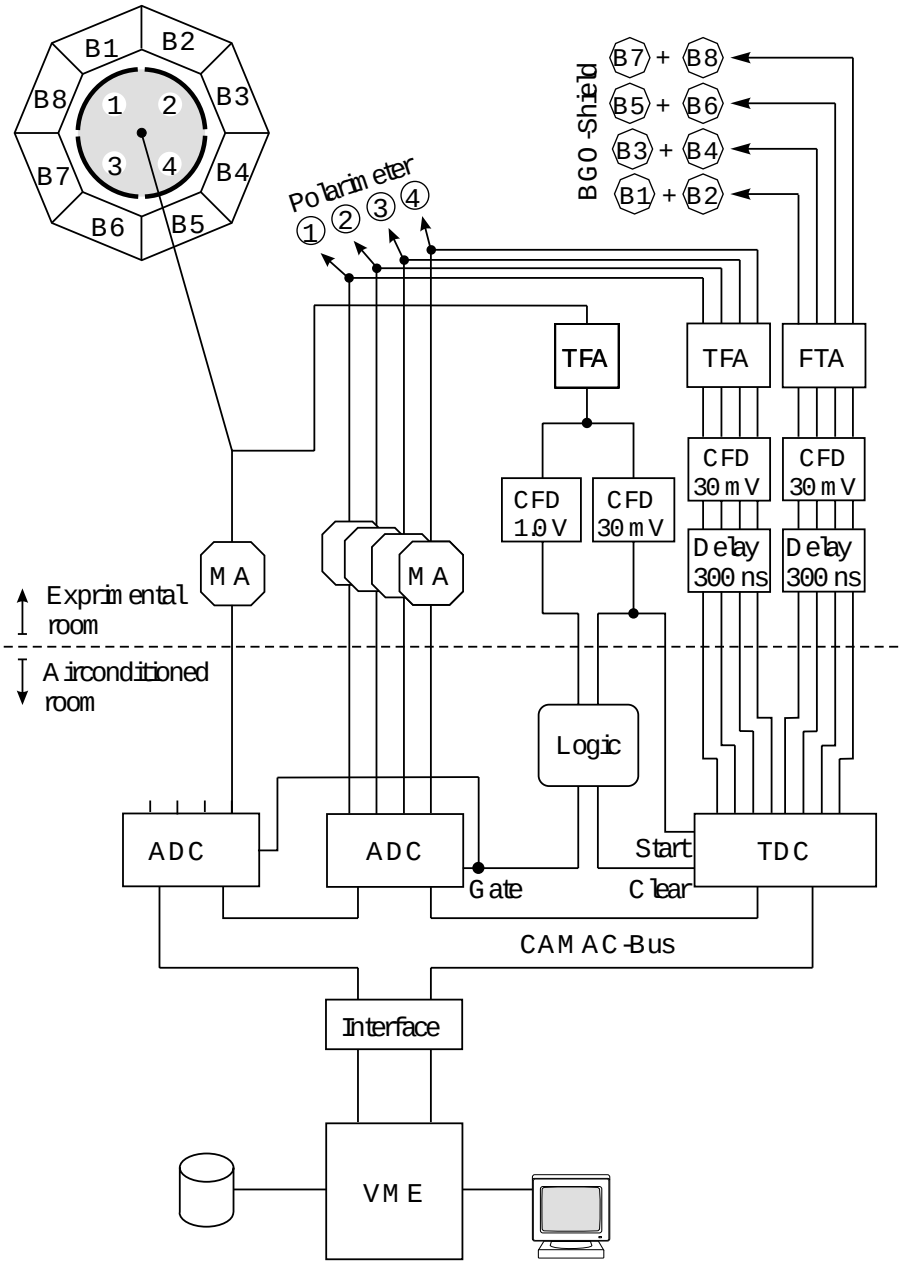

Figure 3.7: Implementation of a high speed list mode data acquisition system. Taken from [Mase96c].

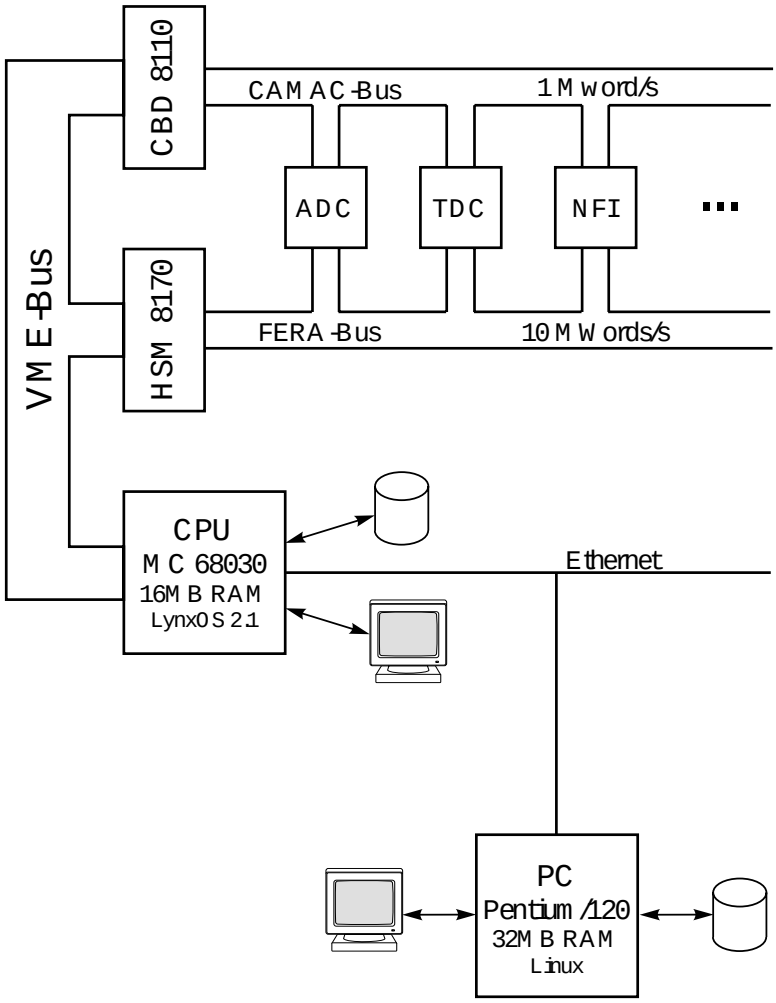

3.5 NRF spectra

An example of a recorded NRF spectrum on ^{121}Sb is shown in Fig. 3.8. The continuous γ background observed in the spectrum corresponds mainly to nonresonant scattering events in the NRF target. The background increases quickly to lower energies, because of the fast increasing γ flux at low energies. In addition, nonresonant scattering events in the NRF target lower the energy of the photons impinging on the HP Ge detector. A smaller fraction of the background is due to Compton background formed in the detector. As the cross sections of the nonresonant scattering events peak in the forward direction, the amount of background in a NRF spectrum diminishes with increasing scattering angles. In the recorded NRF spectrum, a huge peak will be found at 511 keV (not shown in Fig. 3.8) due to pair production and positron annihilation events in the NRF target and lead shielding.

Figure 3.8: Comparison between NRF spectra taken with a detector without (unsuppressed) and with a BGO-anti-Compton shield surrounding (suppressed). The suppression of the continuous background leads to a better peak-to-background ratio and SE and DE peaks are suppressed as can be seen in the second panel.

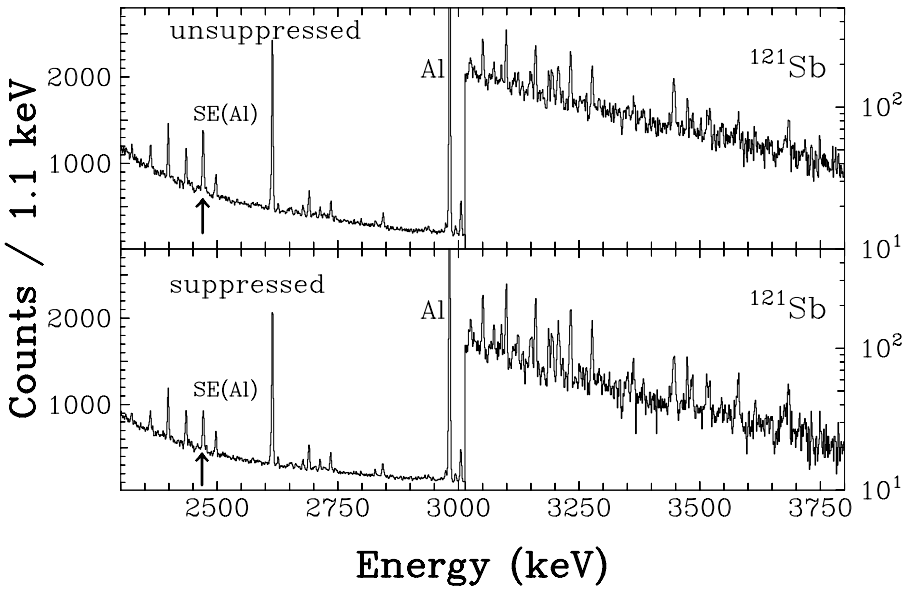

Superimposed on the continuous background, the "real" NRF spectrum is found with its characteristic resonant scattering peaks. The quality of the recorded NRF spectrum is determined by the efficiency and energy resolution of the γ spectrometer and the obtained peak-to-background ratio. The response function of the used HP Ge detectors can be further improved by surrounding the detector with an active BGO-anti-Compton shielding. The anti coincidence between pulses detected in the HP Ge detector and BGO shielding suppresses the Compton background in the NRF spectrum. The Compton background in the NRF spectrum stems from

Compton scattering events in which at least one secondary photon leaves the Ge crystal without detection. The influence of such an anti-Compton shielding is depicted in Fig. 3.8 where an unsuppressed spectrum (upper panel) is compared with a suppressed one (lower panel). Firstly, the suppression of the Compton background in the NRF spectrum leads to a better peak-to-background ratio. This effect is illustrated in the higher energy part (between 3 and 3.6 MeV) of Fig.3.8. In the suppressed spectrum, weaker γ transitions are better resolved. Secondly, the anti-Compton shielding reduces the single and double escape peaks observed in the spectrum. In the unsuppressed spectrum, the single escape peak of the 2981 keV transition in ^{27}Al is larger compared to the suppressed spectrum (^{27}Al is used to monitor the photon flux, see section 3.6.3). Single and double escape peaks are not completely suppressed due to the limited efficiency of the anti-Compton shielding and the fact that it can not surround the complete solid angle of the HP Ge detector. Finally, the anti-Compton shield forms also an active shield against room and cosmic ray background.

The response function of a HP Ge detector is also strictly related with its volume. With an increasing volume, the number of counts in the Compton continuum will decrease as well as the chance that one or two of the annihilation photons from the pair production process escapes the crystal. In Fig. 3.9, the ratios of full energy to single escape, full energy to double escape, and single escape to double escape peak efficiencies are given for different energies of the incident photon on a HP Ge detector with an efficiency of 100% at 1.33 MeV (relative to a 3 x 3 in^2. NaI(Tl) scintillation crystal). These ratios were determined to a maximum energy of 3.5 MeV by placing a ^{56}Co radioactive source (see Appendix C) in the position of the NRF target. The solid squares represent the ratios for an unsuppressed spectrum, the triangles for a suppressed one. It is clear from Fig. 3.9 that the suppression of the single and double escape peaks leads to a better ratio of the full escape peak to the single and double escape peaks. The ratio of the single to double escape peaks is constant in both spectra at all γ energies because it only depends on the volume of the Ge crystal. The peak ratios with the imperative energy difference of 511 keV are used to determine which peaks in the spectrum are single or double escape peaks. A reduction of the peak height in the suppressed spectrum, provides an additional evidence for its single or double escape nature.

3.6 Data analysis

At the end of a series of NRF measurements, the quality of the recorded NRF spectra is checked. Instabilities in the electronic measuring chain may cause shifts or even jumps in the position of the peaks in the spectra of different runs. As a consequence, the resolution of the peaks is poor or satellite peaks occur in the final spectrum. Therefore, the position and width of prominent peaks are compared between spectra of different runs. On the VAX station, a special program (SPEADD) runs that allows to correct for the shift in the position of the peaks (interpolation with a polynomial of third degree) and to add the spectra together.

For the analysis of the NRF spectra, a program called LEONE [Hane81, Albe88] was developed by the NRF group from Cologne. This program provides a graphical user interface showing the part of the spectrum that is currently analyzed. In a first step, the user can mark regions

Figure 3.9: The ratio of the full energy peak to single and double escape peaks and the ratio of the single escape peak to the double escape peak are shown for photon energies up to 3.5 MeV. The triangles correspond to a detector with a BGO-anti-Compton shield and the squares accord with a detector without anti-Compton shielding.

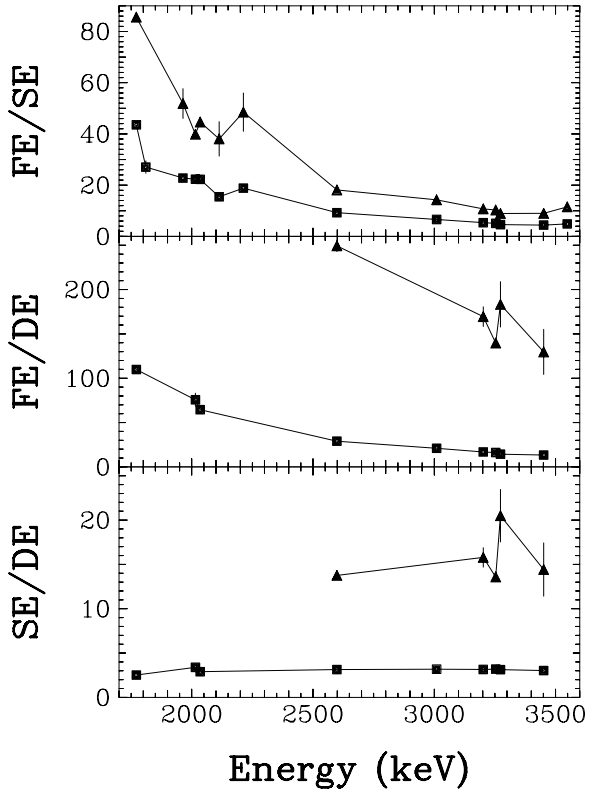

which are free of resonant scattering peaks. These regions are used to fit the continuous nonresonant γ background with a polynomial of second degree. Secondly, the resonant scattering peaks are marked. The area and the position of the resonant scattering peaks are determined from a least square fit to their gaussian shape. Due to the relative low energy increase per channel of 0.6 keV, the resonant scattering peaks show up with a left tail. This is caused by trapping of charge carriers in the Ge crystal which leads to an incomplete charge collection. Therefore, the peaks are fitted with a gauss function and a variable left tail. The advantage of this program is that it allows to check the quality of the fit visually. Attempts have been made to implement an automatic peak searching and analyzing program, but they all failed due to the complexity of the continuous gamma background.

Spectroscopic information of a photo-excited level (spin J, total scattering cross section I_S, transition widths, ...) can be extracted from the observed peak areas in the recorded (γ, γ') spectrum. For the determination of the parities π an additional measurement is needed.

3.6.1 Determination of excitation energies

For the calibration of the NRF spectra, a radioactive ^{56}Co source is used. In the β^+-decay of ^{56}Co to ^{56}Fe, 19 levels with an excitation energy between 0.6 and 3.6 MeV are populated (see Appendix C). This energy range almost covers the whole range of interest (maximum energy is 4.0 MeV). Between two different NRF measurements, a ^{56}Co source is placed in the position of the NRF targets and a ^{56}Co spectrum is recorded for each detector. The knowledge of the peak position of the known ^{56}Co lines and their energies allows the energy calibration of the detector. The use of a second degree polynomial is sufficient for a good calibration of the HP Ge detector:

$$E(x) = A_0 + A_1 \cdot x + A_2 \cdot x^2 \tag{3.1}$$

with x the channel number (peak position) and $E(x)$ the corresponding energy. The result of such a fit procedure is shown in Fig. 3.10. In the upper part of the figure, the residuum is plotted which is a measure for the deviation between the exact value and the fitted value. The maximum residuum amounts to 0.05 keV. In the lower part of Fig. 3.10, the deviation from a linear fit is shown. The observed quadratic deviation from a linear fit, indicates that the application of a second degree polynomial should be indeed sufficient.

The energies of the resonant scattering peaks in the NRF spectra can be determined from Eq. (3.1). To convert these energies into the excitation energy E_x of the level, the recoil energy of the nucleus should be taken into account. According with conservation of energy and momentum, the recoil energy amounts to:

$$E_r = \frac{E_\gamma^2}{2Mc^2}(1 - 2\cos\theta) \cong \frac{E_x^2}{2Mc^2}(1 - 2\cos\theta)$$

These recoil corrections are rather small in NRF studies on heavy nuclei: E_r amounts to 0.04 keV for a resonantly scattered 3 MeV photon off a nucleus with mass number 120 and a scattering angle of 90°.

The uncertainty on the excitation energies is determined by the statistical uncertainty of the peak position. The quality of the energy calibration is also checked by comparing the energy of the γ transitions in the ^{27}Al calibration standard deduced from Eq. (3.1) with the energies in the literature. The deviation between both values in the different energy regions was added linearly as systematic error.

Figure 3.10: Energy calibration of an HP Ge detector. The upper part shows the residuum of the calibration. The lower part presents the deviation from linearity.

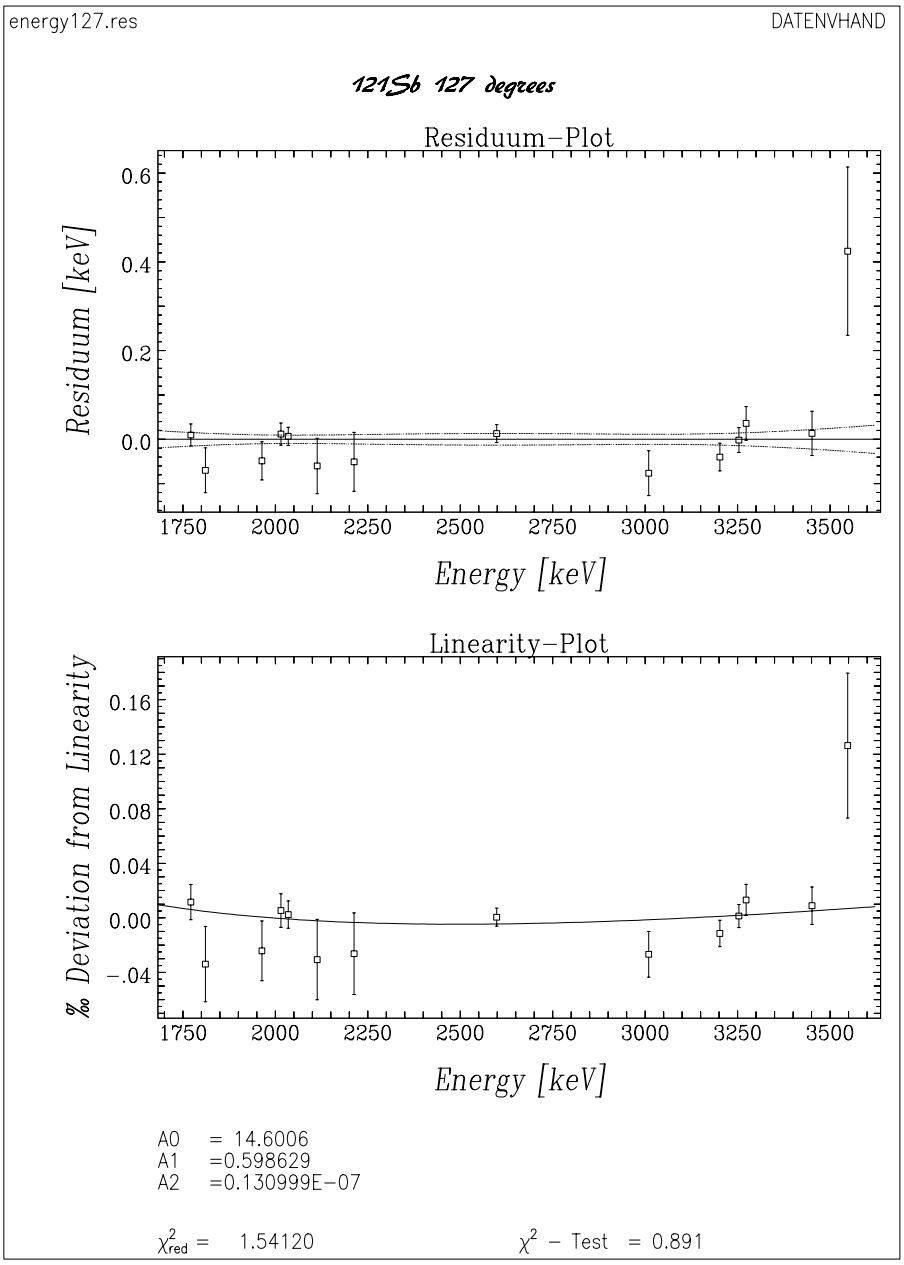

3.6.2 Spin assignment

The γ intensity detected at a scattering angle θ due to the excitation of a level depends on the photon flux N_γ, the detector efficiency ϵ, the number of target nuclei N_T (taking into account the isotopic enrichment), the "Doppler form" of the absorption cross section $\sigma_D(E)$ (see Section 2.1) and the angular correlation function $W_T(\theta)$:

$$A_T(E,\theta)\ dE = N_\gamma(E) \cdot \epsilon(E,\theta) \cdot N_T \cdot Br \cdot \sigma_{D,T}(E) \cdot \frac{W_T(\theta)}{4\pi}\ dE\ . \tag{3.2}$$

The branching ratio Br has been added to take into account the specific decay mechanism of the photo-excited level. The majority of the observed transitions are transitions to the ground state and in this cases the factor Br equals Γ_0/Γ. The angular correlation function $W_T(\theta)$ depends on the induced spin sequence in the target nucleus. As the width of a NRF peak, due to the detector resolution, is on the order of 10^6 times the width of a nuclear resonance, only the total peak area of the Doppler form can be measured in NRF experiments. This total peak area (at a scattering angle θ) can be obtained by energy integrating Eq. (3.2) over a single resonance and reckoning with Eq. (2.7):

$$A_T(\theta) = \int_0^{+\infty} A_T(E,\theta)\ dE = N_\gamma(E) \cdot \epsilon(E,\theta) \cdot N_T \cdot I_{S,T} \cdot \frac{W_T(\theta)}{4\pi}\ . \tag{3.3}$$

The photon flux $N_\gamma(E)$ and the detector efficiency $\epsilon(E,\theta)$ can be treated as constants due to the narrow width of $\sigma_D(E)$. The factor $I_{S,T}$ represents the total scattering cross section of a level in the NRF target nucleus.

The shape of the detector efficiency function $\epsilon(E,\theta)$ can be determined for each detector from the recorded ^{56}Co spectra. The radioactive ^{56}Co source provides 19 γ transitions between 0.6 and 3.6 MeV with known relative γ intensities to the 847 keV transition (see Appendix C). Hence, the efficiency can be deduced relatively to the 847 keV transition, which is:

$$\epsilon_{Co}(\theta) = \frac{A_{Co}(\theta)}{I_\gamma}$$

with uncertainty

$$\frac{\Delta(\epsilon_{Co}(\theta))}{\epsilon_{Co}(\theta)} = \frac{\Delta(I_\gamma)}{I_\gamma} + \frac{\Delta(A_{Co}(\theta))}{A_{Co}(\theta)}\ .$$

The ^{56}Co spectra are recorded with a ^{56}Co source with the same dimensions as the NRF target and exactly in the target position. The advantage of this procedure is that the obtained efficiency curve takes into account the solid angle of the detector and the thickness of the lead absorber in front. The absolute detector efficiency $\epsilon(E,\theta)$ differs only by a constant factor F from the deduced relative efficiency:

$$\epsilon(E,\theta) = F \cdot \epsilon_{Co}(E)\ .$$

The factor F is the same for each detector. The shape of the relative efficiency curve can be fitted using the formula:

$$\epsilon_{Co}(E) = (a \cdot E + \frac{b}{E}) \cdot \exp(c \cdot E + \frac{d}{E})\ .$$

Figure 3.11: Relative efficiency of an HP Ge detector determined with a radioactive ^{56}Co source at the position of the NRF target.

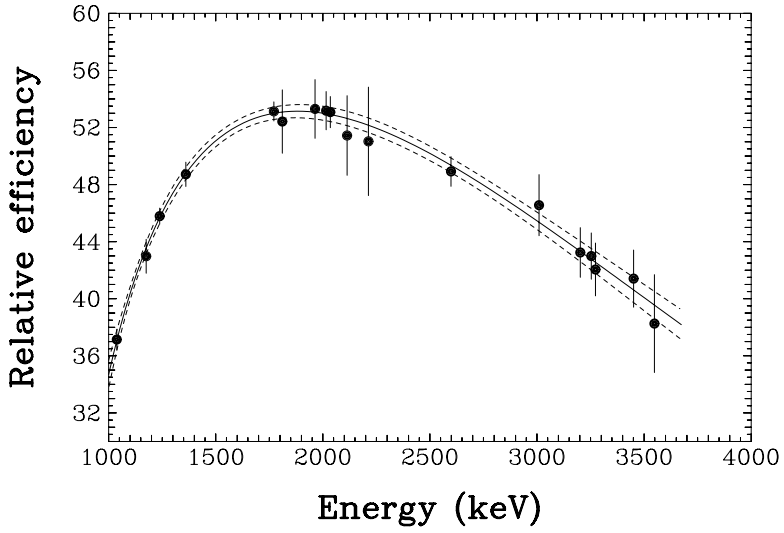

The first factor reckons with the energy dependence of the Compton scattering and pair production processes in the detector, while the exponential factor describes the influence of Compton scattering and pair production in the lead absorber in front. The result of such a fit procedure is shown in Fig. 3.11. The efficiency decreases below an energy of 2 MeV due to the influence of the lead absorber placed in front of the detector.

Spins can be assigned to the observed levels from a comparison of the detected γ intensities at different scattering angles:

$$\frac{W_T(90°)}{W_T(127°)} = \frac{A_T(90°) \cdot \epsilon_{Co}(127°)}{A_T(127°) \cdot \epsilon_{Co}(90°)} \; .$$

The uncertainty on this ratio is given by:

$$\Delta\left(\frac{W_T(90°)}{W_T(127°)}\right) = \left\{ \left[\frac{\Delta(A_T(90°)) \cdot \epsilon_{Co}(127°)}{A_T(127°) \cdot \epsilon_{Co}(90°)}\right]^2 + \left[\frac{A_T(90°) \cdot \Delta(\epsilon_{Co}(127°))}{A_T(127°) \cdot \epsilon_{Co}(90°)}\right]^2 + \left[\frac{A_T(90°) \cdot \epsilon_{Co}(127°) \cdot \Delta(A_T(127°))}{A_T(127°)^2 \cdot \epsilon_{Co}(90°)}\right]^2 + \left[\frac{A_T(90°) \cdot \epsilon_{Co}(127°)\Delta(\epsilon_{Co}(90°))}{A_T(127°) \cdot \epsilon_{Co}(90°)^2}\right]^2 \right\}^{1/2} .$$

Similar relations hold for the comparison of intensity ratios between other scattering angles. In even-even nuclei, a clear distinction exists between the ratios of the angular correlation functions for a pure dipole or quadrupole transition. Generally, in odd-mass nuclei the angular distribution functions $W_T(\theta)$ tend to be nearly isotropic and inhibit the determination of the spin of the excited level (see Section 2.2).

3.6.3 Determination of the total scattering cross section I_S

According with Eq. (3.3) the total scattering cross section I_S can be determined from the measured total γ peak area in each Ge detector. To deduce the total scattering cross section directly from the observed γ intensity, it is necessary to know the absolute values of the γ flux and the detector efficiency ϵ. This problem is solved by determining the total scattering cross section of the levels in the target nucleus relatively to the well known cross section of the 2981 keV transition in the ^{27}Al calibration standard (see Appendix D). This can be achieved by using mixed targets in which the NRF target is alternated with ^{27}Al calibration disks. The γ intensity of the 2981 keV transition obeys a similar relation:

$$A_{Al}(2981,\theta) = N_\gamma(2981)\cdot\epsilon(2981,\theta)\cdot N_{Al}\cdot I_{S,Al}\cdot\frac{W_{Al}(\theta)}{4\pi}\ . \tag{3.4}$$

The relative detector efficiency can be determined as described in the preceding paragraph. The spectral shape of the incoming photon flux $N_\gamma(E)$ can be fitted using the Schiff formula [Schi46] for thin radiator targets. Although the electron beam is completely stopped in the radiator target, the Schiff formula for a thin radiator target describes in an adequate way the bremsstrahlung spectrum [Piet95a]. The collimator used in the Stuttgart NRF facility has a total length of about 1 m and selects the extremely forward moving γ rays. The resulting highly collimated γ beam contains predominantly photons produced in single interaction events of electrons with the radiator target. Conclusively, the thickness of the bremsstrahlung production target can be neglected. The NRF group from Cologne developed a program (called SCHIFF) which interpolates the observed photon flux at the ^{27}Al calibration lines 2211, 2981, and 3956 keV (see Appendix D). The Schiff formula contains only two free parameters: a normalizing constant and the end point energy of the electron beam. The photon flux is normalized to the 2981 keV line (using the normalizing constant):

$$N_\gamma(E) = N_\gamma(2981)\cdot N_{\gamma,rel}(E)\ . \tag{3.5}$$

The SCHIFF program makes a fit of the relative photon flux $N_{\gamma,rel}(E)$. In Fig. 3.12 an example of such a fit of the relative photon flux $N_{\gamma,rel}(E)$ is given. It is seen that in a broad energy region around 3 MeV the photon flux $N_{\gamma,rel}(E)$ can be represented by a straight line as was done in former NRF experiments.

For convenience, also the relative detector efficiencies obtained from the ^{56}Co standard are normalized to the 2981 keV transition in the ^{27}Al calibration standard:

$$\epsilon(E,\theta) = F\cdot\epsilon_{Co}(2981)\cdot\epsilon_{rel}(E)\ . \tag{3.6}$$

From Eq. (3.4) it is learned that:

$$N_\gamma(2981)\cdot F\cdot\epsilon_{Co}(2981,\theta) = \frac{A_{Al}(2981,\theta)}{I_{S,Al}\cdot\frac{W_{Al}(\theta)}{4\pi}\cdot N_{Al}}\ , \tag{3.7}$$

and the relation (3.3) can be rewritten as:

$$A_T(\theta) = N_\gamma(2981)\cdot N_{\gamma,rel}(E)\cdot F\cdot\epsilon_{Co}(2981,\theta)\cdot\epsilon_{rel}(E,\theta)\cdot N_T\cdot I_{S,T}\cdot\frac{W_T(\theta)}{4\pi}\ .$$

Figure 3.12: Plot of the relative photon flux between 1.6 and 4.1 MeV. Known transitions in the ^{27}Al calibration standard are used to monitor the photon flux. The Schiff formula for thin targets is applied to fit the shape of the photon flux.

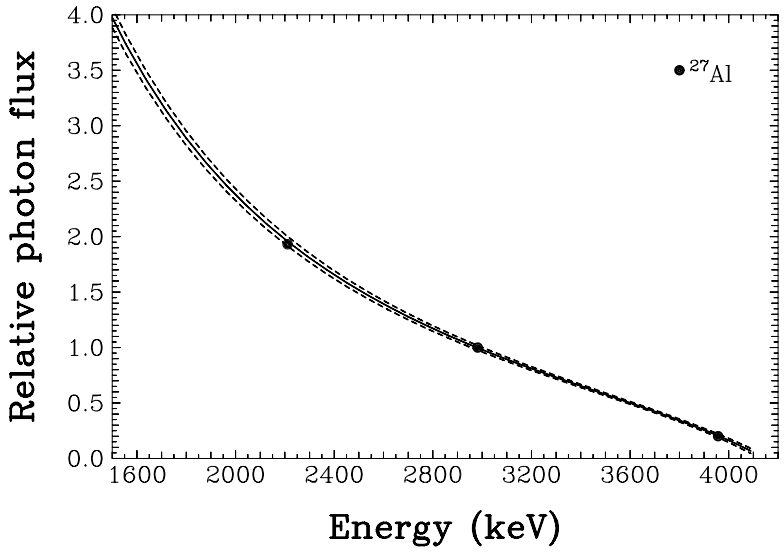

The unknown total scattering cross section $I_{S,T}$ can be finally determined from the latter equation and substituting Eq. (3.7):

$$I_{S,T} = C(\theta) \cdot \frac{A_T(\theta)}{N_{\gamma,rel}(E) \cdot \epsilon_{rel}(E,\theta) \cdot W_T(\theta)} \tag{3.8}$$

$$\Delta(I_{S,T}) = \frac{C(\theta)}{W_T(\theta)} \cdot \left\{ \left[\frac{\Delta(A_T(\theta))}{N_{\gamma,rel}(E) \cdot \epsilon_{rel}(E,\theta)} \right]^2 + \left[\frac{A_T(\theta) \cdot \Delta(N_{\gamma,rel}(E))}{N_{\gamma,rel}(E)^2 \cdot \epsilon_{rel}(E,\theta)} \right]^2 + \left[\frac{A_T(\theta) \cdot \Delta(\epsilon_{rel}(E))}{N_{\gamma,rel}(E) \cdot \epsilon_{rel}(E,\theta)^2} \right]^2 \right\}^2$$

$\Delta(I_{S,T})$ represents the statistical uncertainty. Remember that the value of $W_T(\theta)$ is known from the spin assignment as described in the previous paragraph. The constant $C(\theta)$ equals:

$$C(\theta) = \frac{I_{S,Al} \cdot W_{Al}(\theta)}{A_{Al}(2981,\theta)} \cdot \frac{N_{Al}}{N_T} \ .$$

At the NRF setup in Stuttgart, the total cross section can be determined at the scattering angles of 90°, 127°, and 150° and if possible a weighted average of the 3 values of the total scattering cross section is taken. However, to deduce the final accuracy a systematic uncertainty of the ^{56}Co and ^{27}Al calibration standards should be taken into account:

$$\frac{\Delta_{\text{fin}} I_{S,T}}{I_{S,T}} = \sqrt{\left(\frac{\Delta(A_{Al})}{A_{Al}}\right)^2 + \left(\frac{\Delta(I_{S,T})}{I_{S,T}}\right)^2} + 0.035 \ .$$

The contribution of 0.035 represents the average uncertainty on the γ intensities of the ^{56}Co source.

The transition widths Γ_0^2/Γ and the reduced excitation strengths $B(\pi L)\uparrow$ are determined using the equations given in paragraphs 2.2.1 and 2.2.2 and using the formulas for error propagation.

A second method to determine the relative photon flux and detector efficiency, makes a direct fit to the product $N_\gamma(E)\cdot\epsilon(E,\theta)$ for a calibration standard measured simultaneously with the target under investigation. This method is used in NRF experiments with higher end point energies, as no radioactive sources delivering γ transitions above 4 MeV to determine the relative detector efficiency are available. For this kind of NRF experiments, H_3BO_3 is often chosen as calibration standard [Gova98].

3.6.4 Parity assignment

Below an excitation energy of 5 MeV, parities can be ideally assigned to photo-excited levels using the Compton polarimetry technique. The main advantage of the list mode data acquisition system (for details see paragraph 3.3.2) is that it allows to construct the coincidence spectra $V+H$ and $V-H$ off line. It means that all parameters of influence on the coincidence spectra can be optimized after the measurement. Once the coincidence spectra have been constructed, the azimuthal asymmetry ϵ can be determined:

$$\epsilon = \frac{V+H}{V-H}$$

As deduced in paragraph 2.3.2, a negative asymmetry gives evidence for an $E1$ transition, a positive asymmetry points to an $M1$ or $E2$ transition. To obtain a conclusive decision about the parity of a level, the measured azimuthal asymmetry should be compared with the polarization sensitivity Q of the Compton polarimeter.

3.6.5 Corrections for atomic absorption and nuclear self absorption

In the energy integration of Eq. (3.2) over a single resonance, it was assumed that each nucleus in the target is irradiated by the same photon flux $N_\gamma(E)$. In practice, this is not true. Due to absorption processes in the target, the photon flux will be attenuated. The γ ray flux decreases exponentially with the path length a photon has to travel to "reach" a certain nucleus in the target. Two kind of absorption processes cause this reduction of the γ flux. At first, atomic interactions between the incoming photons and target matter, like photo-electric absorption, Compton scattering, and pair production give rise to a decrease of the photon flux. In photo-electric absorption, the photon disappears, while in Compton scattering a shift in energy and direction occurs. In the pair production interaction, two 511 keV photons are released. These atomic absorption processes may take place before or after a nuclear resonance fluorescence interaction. Secondly, nuclear self absorption further diminishes the γ flux. Nuclear self absorption occurs when an incoming γ ray is absorbed by a target nucleus. The photo-excited nucleus will decay to the ground state or an intermediate state. In the latter case, the released photon will be shifted over an energy distance of $E_{level} - E_{interm.level} - E_{recoil}$ and is clearly

out off the nuclear resonance condition. If the excited level decays to the ground state (case of elastic scattering), the re-emitted photon carries the difference in energy of the incoming photon and the recoil energy of the target nucleus ($E_{level} - E_{recoil}$). Recoil energies, typically a few electron volts, are at least three orders of magnitude larger than the nuclear transition widths of a few milli electron volts. Also in this case, the scattered photon is out off the nuclear resonance condition. Nuclear resonantly scattered photons can not undergo any further nuclear self absorption along their path trough the target. Therefore, it is sufficient to reckon with the amount of nuclear self absorption processes which have taken place before a nuclear resonance fluorescence scattering interaction.

All the aforementioned processes, atomic absorption and nuclear self absorption, lead to an effective decrease of the photon flux $N_\gamma(E)$ at a certain energy E. This effect can be studied by the calculation of the average amount of absorption in the target. At the present NRF facility with two experimental setups, different situations are met whether a target is placed at the first or second setup.

3.6.5.1 Absorption in a target at the first setup

To include the effects of the atomic absorption and nuclear self absorption in the target, Eq. (3.2) should be modified into:

$$\begin{aligned} A_T(E,\theta,x)\ dE\ dx &= \epsilon(E,\theta)\cdot\frac{W_T(\theta)}{4\pi}\cdot\frac{N_T}{d}\cdot N_\gamma(E)\cdot\exp\left[-\Sigma^{at}\cdot v(\varphi)\cdot\frac{x}{d}\right] \\ &\quad\cdot\exp\left[-x\cdot\frac{N_T}{S\cdot d}\cdot\frac{\sigma_{D,T}(E)}{\cos\varphi}\right]\cdot Br\cdot\sigma_{D,T}(E)\ dE\ dx \end{aligned} \tag{3.9}$$

Most quantities were already introduced in paragraph 3.6.2. The atomic absorption in the target of the incoming and outgoing radiation is described by the exponential function:

$$\frac{N_\gamma(E)}{N_{\gamma,0}(E)} = \exp\left[-\Sigma^{at}\cdot v(\varphi)\cdot\frac{x}{d}\right]$$

with Σ^{at} the total cross section for the interaction of photons with matter, φ the angle of the target measured perpendicular to the beam axis, x the path length along the X-axis and d the target thickness. Fig. 3.13 depicts schematically the important factors of influence. The angular function $v(\varphi)$ describes the path length measured relatively to the X-axis and depends on the position of the target and the detector:

$$\begin{aligned} v_{90^\circ}(\varphi) &= \frac{1}{\cos(\varphi)} + \frac{1}{\sin(\varphi)} \\ v_{127^\circ}(\varphi) &= \frac{1}{\cos(\varphi)} + \frac{1}{\sin(\varphi + 37^\circ)} \end{aligned}$$

The total photon absorption cross section for mixed targets can be calculated from the compilation of photon absorption cross sections in different materials by Storm and Israel [Stor70]:

$$\Sigma^{at} = \frac{N_{Al}\sigma_{Al} + N_T'\sigma_T}{S}$$

with S the area of the target, N_{Al} and N_T' the total number of ^{27}Al and target atoms (considering the complete isotopic distribution in the target) and σ_{Al} and σ_T the respective total

Figure 3.13: Depiction of a target placed at the first setup. The important factors to make an estimate of the atomic and nuclear self absorption are indicated.

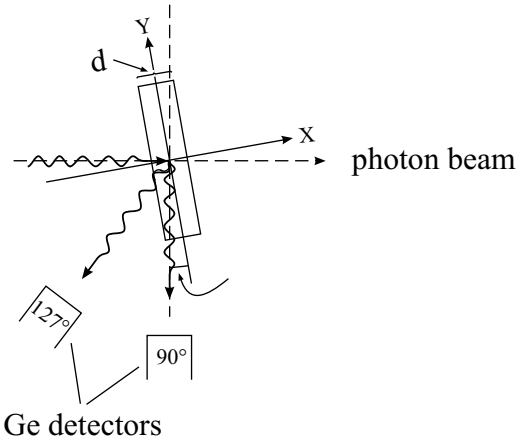

photon absorption cross sections for interaction with Al and target atoms. Also the nuclear self absorption process of the incoming radiation can be expressed in an exponential form:

$$\frac{N_\gamma(E)}{N_{\gamma,0}(E)} = \exp\left[-x \cdot \frac{N_T}{S \cdot d}\frac{\sigma_{D,T}(E)}{\cos\varphi}\right]$$

The Doppler form of the absorption cross section describes the complete nuclear self absorption process at one level in the target nucleus. Note that the amount of nuclear self absorption is independent of the detector position.

The total area $A_T(\theta)$ that will be observed in a Ge detector installed at the scattering angle θ, taking into account the influence of the atomic absorption and nuclear self absorption, can be found by integrating Eq. (3.9) over the target thickness d and a single nuclear resonance:

$$A_T(\theta) = \int_0^{+\infty}\int_0^d A(E,\theta,x)\ dE\ dx$$

In the calculation of this double integral, the exponential forms of the atomic and nuclear self absorption can be replaced by expansions up to second and first order respectively:

$$A_T(\theta) = N_\gamma(E)\cdot\epsilon(E,\theta)\cdot\frac{W(\theta)}{4\pi}\cdot\frac{N_T}{d} \cdot Br\int_0^{+\infty}\int_0^d\left[1-\Sigma^{at}\cdot v(\varphi)\cdot\frac{x}{d}+\frac{1}{2}\left(\Sigma^{at}\cdot v(\varphi)\cdot\frac{x}{d}\right)^2\right] \cdot\left[1-x\cdot\frac{N_T}{S\cdot d}\frac{\sigma_{D,T}(E)}{\cos\varphi}\right]\sigma_{D,T}(E)\ dE\ dx$$

Integrating this equation over the target thickness and taking into account the general integral:

$$\int_0^{+\infty}[\sigma_D(E)]^n\ dE = \left(\frac{I_S}{Br}\right)^n\frac{1}{\Delta^{(n-1)}\pi^{(n-1)/2}\sqrt{n}}$$

the relation is obtained:

$$A_T(\theta) = A_0(\theta) \cdot \Bigg[\quad 1 \quad -\frac{\Sigma^{at}}{2} \cdot v(\varphi) + \frac{(\Sigma^{at})^2}{6} \cdot v^2(\varphi) - \frac{N_T}{2 \cdot S} \cdot \frac{I_{S,T}}{Br} \cdot \frac{1}{\sqrt{2\pi}\Delta \cos\varphi}$$
$$+ \quad \Sigma^{at} \cdot v(\varphi) \frac{N_T}{3 \cdot S} \cdot \frac{I_{S,T}}{Br} \cdot \frac{1}{\sqrt{2\pi}\Delta \cos\varphi}$$
$$- \quad (\Sigma^{at})^2 \cdot v^2(\varphi) \cdot \frac{N_T}{8 \cdot S} \cdot \frac{I_{S,T}}{Br} \cdot \frac{1}{\sqrt{2\pi}\Delta \cos\varphi} \Bigg] \tag{3.10}$$

In this formula $A_0(\theta)$ represents the scattering intensity without any absorption processes in the target as deduced in Eq. (3.3). The obtained relation between $A_0(\theta)$ and the measured $A_T(\theta)$ holds for γ transitions in the NRF target and the ^{27}Al calibration target.

The correction of the measured peak areas corresponding to the γ transitions in the ^{27}Al calibration standard, can be immediately performed. The total cross sections I_S of the levels in ^{27}Al are well known from the literature (see Appendix D) and can be applied in Eq. (3.10).

To correct the measured peak areas $A_T(\theta)$ of each level observed in the nucleus under investigation, for the atomic absorption and nuclear self absorption, the knowledge of the total scattering cross sections I_S is needed. However, these quantities are unknown and should be determined from the peak areas $A_0(\theta)$ (see Eq. (3.8)) which need to be deduced from Eq. (3.10) with the knowledge of the cross sections I_S. As a consequence, the absorption corrections are performed recursively. Schematically, the following recursive chain is followed:

$$I^0_{S,T} = 0 \longrightarrow A^1_0(\theta) \longrightarrow I^1_{S,T} \longrightarrow A^2_0(\theta) \longrightarrow I^2_{S,T} \longrightarrow \ldots$$

In the first step, the influence of the nuclear self absorption is switched off by putting $I_{S,T} = 0$. After each correction of the peak area, a new $I_{S,T}$ value is determined according to Eq. (3.8). In practice, convergence is already reached after two or three steps, because the atomic absorption is dominating over the nuclear self absorption.

3.6.5.2 Absorption in a target at the second setup

At the second setup, the corrections for atomic absorption and nuclear self absorption are more complicated due to the influence of the NRF target placed at the first setup (see Fig. 3.14). In fact, the target of the first setup can be seen as an "absorber" and all quantities in this paragraph referring to it will be denoted with an "ab" tag. At the second setup, the γ transitions in the target nucleus and the γ transitions in the ^{27}Al calibration standard can not be treated equally as was the case for the corrections performed at the first setup.

Due to atomic absorption in the target placed at the first setup, the photon flux at the excitation energies of the levels in the NRF target at the second setup will be attenuated. If it is assumed that there is no energy overlap between levels in the targets situated at the first and second setup, nuclear self absorption in the first target will not influence the photon flux impinging on the nuclei under investigation at the second setup. In this case, Eq. (3.9) should

Figure 3.14: Target placed at the second setup. The photon flux impinging on the second NRF target is also influenced by the first target which act as an absorber.

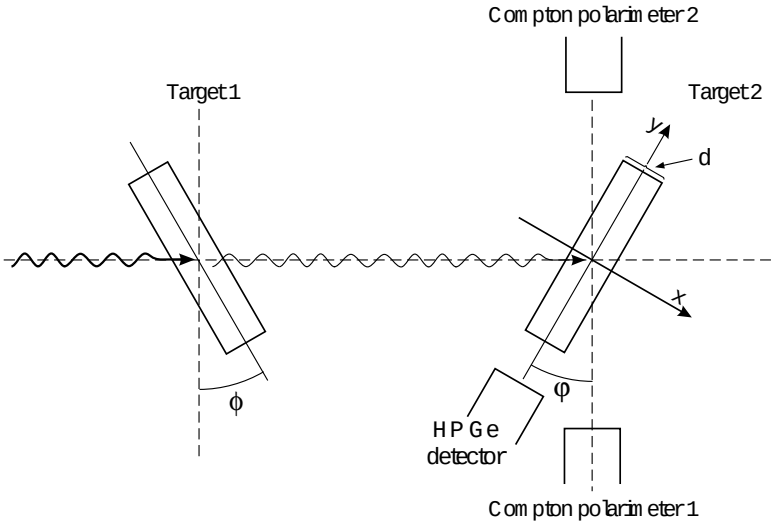

be modified and the area of a "target" peak is given by:

$$A_T(E,\theta,x)\ dE\ dx = N_\gamma(E)\cdot\epsilon(E,\theta)\cdot\frac{W_T(\theta)}{4\pi}\cdot\frac{N_T}{d}\cdot\exp\left[-\frac{\Sigma^{at}_{ab}}{\cos\phi}\right]\cdot\exp\left[-\Sigma^{at}\cdot v(\varphi)\cdot\frac{x}{d}\right]$$
$$\cdot\exp\left[-x\cdot\frac{N_T}{S\cdot d}\cdot\frac{\sigma_{D,T}(E)}{\cos\varphi}\right]\cdot Br\cdot\sigma_{D,T}(E)\ dE\ dx\ . \qquad (3.11)$$

The factor

$$\exp\left[-\frac{\Sigma^{at}_{ab}}{\cos\phi}\right]$$

describes the atomic absorption in the target at the first setup and ϕ is the angle between this target and an axis perpendicular to the beam axis (see Fig. 3.14). In this case, the total atomic absorption cross section in the first target equals:

$$\Sigma^{at}_{ab} = \frac{N_{Al}\sigma_{Al} + N_{T_1}\sigma_{T_1}}{S_{ab}}$$

with N_{Al} and N_{T_1} the total number of ^{27}Al and target atoms in the target of the first setup. It's obvious that doubly integrating Eq. (3.11) over the target thickness and over a single resonance after the expansion of the exponential terms will result in:

$$A_T(\theta) = A_0(\theta)\cdot\exp\left[-\frac{\Sigma^{at}_{ab}}{\cos\phi}\right]\cdot\left[\ 1\ -\frac{\Sigma^{at}}{2}\cdot v(\varphi)+\frac{(\Sigma^{at})^2}{6}\cdot v^2(\varphi)-\frac{N_{Sn}}{2\cdot S}\cdot\frac{I_{S,Sn}}{Br}\cdot\frac{1}{\sqrt{2\pi}\Delta\cos\varphi}\right.$$
$$+\ \Sigma^{at}\cdot v(\varphi)\cdot\frac{N_{Sn}}{3\cdot S}\cdot\frac{I_{S,Sn}}{Br}\cdot\frac{1}{\sqrt{2\pi}\Delta\cos\varphi}$$
$$\left.-\ (\Sigma^{at})^2\cdot v^2(\varphi)\cdot\frac{N_{Sn}}{8\cdot S}\cdot\frac{I_{S,Sn}}{Br}\cdot\frac{1}{\sqrt{2\pi}\Delta\cos\varphi}\right]\ . \qquad (3.12)$$

For the NRF experiments carried out at the first and second setup mixed targets containing ^{27}Al as calibration standard are used. As a consequence, the nuclear self absorption in the first target caused by the levels of ^{27}Al will diminish the photon flux which is needed to excite the ^{27}Al calibration levels in the second target. To take the nuclear self absorption in the first target into account, an additional exponential factor should be added in Eq. (3.11). The area of an Al peak obtained in photon scattering off the second target becomes:

$$A_{Al}(E,\theta,x)\ dE\ dx = N_\gamma(E)\cdot\epsilon(E,\theta)\cdot\frac{W_{Al}(\theta)}{4\pi}\cdot\frac{N_{Al}}{d}\cdot\exp\left[-\frac{\Sigma^{at}_{ab}}{\cos\phi}\right]\cdot\exp\left[-\frac{N^{ab}_{Al}\cdot\sigma_{D,Al}(E)}{S_{ab}\cdot\cos\phi}\right]$$
$$\cdot\exp\left[-\Sigma^{at}\cdot v(\varphi)\cdot\frac{x}{d}\right]\cdot\exp\left[-x\cdot\frac{N_{Al}}{S\cdot d}\cdot\frac{\sigma_{D,Al}(E)}{\cos\varphi}\right]\cdot Br\cdot\sigma_{D,Al}(E)\ dE\ dx\ .$$

After calculating the double integral over the target thickness and a single nuclear resonance, the following relationship between the measured peak areas $A_{Al}(\theta)$ and the complete scattering intensity $A_{Al,0}(\theta)$ is obtained:

$$\begin{aligned}
A_{Al}(\theta) \;=\; & A_{Al,0}(\theta)\cdot\exp\left[-\frac{\Sigma^{at}_{ab}}{\cos\phi}\right] \\
& \left[1-\frac{\Sigma^{at}\cdot v(\varphi)}{2}+\frac{(\Sigma^{at})^2\cdot v^2(\varphi)}{6}-\frac{N_{Al}}{2\cdot S\cdot\cos\varphi}\cdot\frac{I_{S,Al}}{Br}\cdot\frac{1}{\sqrt{2\pi}\Delta}\right. \\
& -\frac{N_{Al}\cdot(\Sigma^{at})^2\cdot v^2(\varphi)}{8\cdot S\cdot\cos\varphi}\cdot\frac{I_{S,Al}}{Br}\cdot\frac{1}{\sqrt{2\pi}\Delta}-\frac{N^{ab}_{Al}}{S_{ab}\cdot\cos\phi}\cdot\frac{I_{S,Al}}{Br}\cdot\frac{1}{\sqrt{2\pi}\Delta} \\
& +\frac{N^{ab}_{Al}\cdot\Sigma^{at}\cdot v(\varphi)}{2\cdot S_{ab}\cdot\cos\phi}\cdot\frac{I_{S,Al}}{Br}\cdot\frac{1}{\sqrt{2\pi}\Delta}-\frac{N^{ab}_{Al}\cdot(\Sigma^{at})^2\cdot v(\varphi)^2}{6\cdot S_{ab}\cdot\cos\phi}\cdot\frac{I_{S,Al}}{Br}\cdot\frac{1}{\sqrt{2\pi}\Delta} \\
& +\frac{N^{ab}_{Al}\cdot N_{Al}}{2\cdot S_{ab}\cdot S\cdot\cos\phi\cdot\cos\varphi}\cdot\left(\frac{I_{S,Al}}{Br}\right)^2\cdot\frac{1}{\sqrt{3}\pi\Delta^2} \\
& -\frac{N^{ab}_{Al}\cdot N_{Al}\cdot\Sigma^{at}\cdot v(\varphi)}{3\cdot S_{ab}\cdot S\cdot\cos\phi\cdot\cos\varphi}\cdot\left(\frac{I_{S,Al}}{Br}\right)^2\cdot\frac{1}{\sqrt{3}\pi\Delta^2} \\
& \left.+\frac{N^{ab}_{Al}\cdot N_{Al}\cdot(\Sigma^{at})^2\cdot v^2(\varphi)}{8\cdot S_{ab}\cdot S\cdot\cos\phi\cdot\cos\varphi}\cdot\left(\frac{I_{S,Al}}{Br}\right)^2\cdot\frac{1}{\sqrt{3}\pi\Delta^2}\right]\ . \qquad (3.13)
\end{aligned}$$

In this complex formula, the higher order terms tend to be very small and can be neglected.

At first, the measured peak areas of the ^{27}Al calibration standard can be corrected using Eq. (3.13). Subsequently, the total cross sections I_S can be determined iteratively from Eq. (3.11) and Eq. (3.8) as was explained in the preceding paragraph.

3.6.5.3 Determination of the target angles

An important quantity in the Eqs. (3.9), (3.11), and (3.13) to correct the measured γ intensities for atomic absorption and nuclear self absorption is the angle φ between the beam axis and the normal to the NRF target. This angle influences the average path length through the target a photon has to overcome to reach a detector placed at a scattering angle θ. It can be measured with good accuracy before or after a NRF measurement. The angle φ can also be deduced from a comparison of the observed intensities of the γ transitions in the ^{27}Al calibration standard at different scattering angles θ. As described in the beginning of section 3.6.5, the nuclear self

absorption plays only a role for the incoming photons traveling parallel to the beam axis through the target. Nuclear resonantly scattered photons can not undergo further nuclear resonant scattering. Hence, the nuclear self absorption is independent of the scattering angle θ. If only the influence of the atomic absorption on the peak areas is considered, the γ intensity equals:

$$A_{Al}(\theta, x)\ dx = N_\gamma(E) \cdot W_{Al}(\theta) \cdot \frac{N_{Al}}{d} \cdot \epsilon(E, \theta) \cdot I_S \cdot \int_0^d \exp\left[-\Sigma^{at} \cdot v(\varphi) \cdot \frac{x}{d}\right]\ dx$$

Integrating over the target thickness results in:

$$A_{Al}(\theta) = N_\gamma(E) \cdot W_{Al}(\theta) \cdot N_{Al} \cdot \epsilon(E, \theta) \cdot I_S \cdot \frac{1 - \exp\left[-\Sigma^{at} \cdot v(\varphi)\right]}{\frac{\Sigma^{at}}{d} \cdot v(\varphi)}$$

This relation can be used to compare how the atomic absorption in the target influences the γ intensity of a certain γ transition in the ^{27}Al calibration standard at different scattering angles:

$$\frac{A_{Al}(90°) \cdot W_{Al}(127°) \cdot \epsilon(E, 127°)}{A_{Al}(127°) \cdot W_{Al}(90°) \cdot \epsilon(E, 90°)} = \frac{1 - \exp\left[-\Sigma^{at} \cdot v_{90°}(\varphi)\right] \cdot v_{127°}(\varphi)}{1 - \exp\left[-\Sigma^{at} \cdot v_{127°}(\varphi)\right] \cdot v_{90°}(\varphi)}$$

The left side of this formula contains only quantities which are measured in the NRF experiment (the angular distributions are known from literature). The right side gives the expected ratio taking into account the angle φ. This enables the determination of the angle φ with a precision of 1°. This formula can be immediately applied for a NRF target placed at the second setup: the amount of atomic absorption in the target at the first setup is the same for all scattering angles and can be neglected.

Chapter 4

Experimental results

As described in the previous chapters, the NRF technique provides an outstanding tool for the investigation of low multipolarity (dipole and electric quadrupole) excitations in even-even as well as odd-mass nuclei. This work focuses on the nuclear structure of levels below an excitation energy of 4 MeV in nuclei in the Z = 50 region. The ^{118,120,122}Sn nuclei were chosen to investigate the concentration of the electric dipole strength below 4 MeV. Subsequently, NRF measurements were carried out on the adjacent odd-mass nuclei ^{117}Sn (N = 67) and ^{121,123}Sb (Z = 51) to study how the electric dipole strength observed in the even-even nuclei is fragmented and distributed in the odd-mass nuclei. The NRF facility installed at the 4.3 MV Dynamitron accelerator was the best opportunity to perform these studies. The use of the intense continuous γ beam makes irradiation times in angular distribution (γ, γ') measurements extremely short. Annoying problems like sudden "jumps" in the recorded spectra occurring in long-time measurements (due to instabilities of the data acquisition system), are avoided. In addition, the Stuttgart University disposes of excellent Compton polarimeters which allow to determine accurately the parity of the photo-excited levels.

In a first stage, the even-even nuclei ^{118,120,122}Sn were investigated. Angular distribution measurements were performed on ^{120}Sn and ^{122}Sn at the first setup. This setup consisted of three HP Ge detectors installed at the scattering angles of 90°, 127°, and 150° degree and with respective total efficiencies of 100%, 100%, and 22% (relative to a 3 x 3 in^2. NaI(Tl) detector). The NRF spectrum recorded with the HP Ge detector placed at the scattering angle of 150° and with the lowest efficiency, contained too low statistics to be used in the analysis. Compton polarimetry measurements were performed at the second setup on ^{118}Sn and ^{122}Sn. At this setup, two Compton polarimeters were situated. As already mentioned, the core signals of the Compton polarimeters carry the full energy information of the detected γ rays in the sectors. Combined with the information of an additional HP Ge detector, placed at 127°, angular distribution measurements are carried out at this setup simultaneously.

The NRF experiments on the odd-mass ^{117}Sn and ^{121,123}Sb nuclei have all been performed at the first setup, as it is impossible with the actual setups to determine the parities of the excited levels in an odd-mass nucleus. During the course of the experiments, new investments gradually improved the NRF facility installed at the first setup. For the NRF measurements on ^{117}Sn, the detector installed at 150° was replaced by an HP Ge detector with an efficiency of

Table 4.1: Overview of the characteristics of the NRF experiments performed on the even-even $^{118-122}Sn$ and the odd mass ^{117}Sn and $^{121,123}Sb$ nuclei.

First setup, angular distribution measurements					
	^{120}Sn	^{122}Sn	^{117}Sn	^{121}Sb	^{123}Sb
target weight (mg)	2500	2847	1649	2431	2376
isotopic enrichment (%)	97.2	95.8	92.1	99.5	99.0
chemical composition[b)]	met.	met.	met.	pow.	pow.
weight of ^{27}Al calibration standard (mg)	1187	1187	780	1179	1013
weight of ^{13}C calibration standard (mg)	-	-	-	-	100
end point energy (MeV)	4.1	4.1	4.1	4.1	3.8
detector effi. (%) (thickness lead absorber 90°(mm))	100(35)	100(35)	100(31)	100(33)	100(28)
detector effi. (%) (thickness lead absorber 127°(mm))	100(25)	100(25)	100(20)	100[a](19)	100[a](19)
detector effi. (%) (thickness lead absorber 150°(mm))	22(9)	22(9)	100(18)	100(23)	100(20)
total measuring time (days)	2	2	4.5	4.2	4.5
Second setup, Compton polarimeter measurements					
	^{118}Sn		^{122}Sn		
target weight (mg)	6484		4717		
isotopic enrichment (%)	98.5		95.8		
chemical composition[b)]	met.		met.		
weight of ^{27}Al calibration standard (mg)	2361		2179		
end point energy (MeV)	4.1		4.1		
for details of the Compton polarimeters: see Table 3.1					
detector effi. (%) (thickness lead absorber 127°(mm))	38(9)		38(9)		
total measuring time (days)	11		12		

[a] This detector was surrounded with a BGO anti- Compton shield.

[b)] met. = metallic and pow. = powder

100%. In the last NRF measurements on ^{121,123}Sb, the response function of the Ge detector at 127° was improved by an active BGO-anti-Compton shielding.

All the technical details, as target weight, chemical composition, detector efficiencies, ... are given in Table 4.1. In all these NRF measurements, mixed targets in which ^{27}Al disks (see Appendix D) are alternated with the NRF target under investigation have been used for calibration purposes. Due to technical problems with the Dynamitron accelerator during the ^{123}Sb NRF measurements, the end point energy was shifted down to 3.8 MeV. As a consequence, the 3956 keV level of the ^{27}Al calibration standard could not be excited. Therefore, an additional ^{13}C disk was placed at the backside of the target. The ^{13}C nucleus has two levels at 3089 and 3684 keV (below an excitation energy of 4 MeV) which can be used to monitor the photon flux. Details of it can be found in Appendix E.

In this Chapter an overview of the results of all the performed NRF experiments will be given. A detailed discussion of the results is postponed to Chapter 5.

4.1 Photon scattering off the even-even ^{116,118,120,122,124}Sn isotopes

The even-mass ^{116}Sn and ^{124}Sn nuclei have been investigated in previous NRF experiments with different end point energies up to the particle threshold at the Stuttgart [Gova94a] and Gent [Gova98, Gova96] NRF facilities. The results obtained on these nuclei below an excitation energy of 4 MeV are incorporated in this work in order to receive systematic results in a broad mass range. The high energy part (between 2.6 and 3.6 MeV) of the recorded (γ, γ') spectra of the ^{118,120,122}Sn isotopes is shown in Fig. 4.1 together with those obtained for ^{116}Sn and ^{124}Sn [Gova94a]. All these spectra are obtained at the NRF facility installed at the Stuttgart 4.3 MV Dynamitron accelerator. The use of large volume HP Ge detectors with an efficiency of 100% combined with the possible counting rates up to 5 kHz, allow to record high quality NRF spectra. In each of the spectra shown in Fig. 4.1, one strong dominating peak is observed at a photon energy varying between 3.2 – 3.5 MeV. The peak area of these γ transitions was determined with a statistical precision of less than 1.7%. Therefore, it was necessary to reckon with the influences of atomic absorption and nuclear self absorption in the target on the observed γ intensities, as described in section 3.6.5. At the first setup, the calculated total absorption (atomic absorption and nuclear self absorption) of the 3279 (^{120}Sn) and 3359 keV (^{122}Sn) γ transitions amounts to an average value of 19.2% at the scattering angle of 90° and 9.3% at 127°, the corrections in ^{120}Sn and ^{122}Sn being nearly the same. Note that the total cross sections I_S are determined relatively to the 2982 keV transition in ^{27}Al (see Eq. (3.8)), having a total absorption value of 16.9% at 90° and 6.8% at 127°. Hence, the total cross sections of these strong γ transitions in the ^{120,122}Sn nuclei were corrected with only 1.9% at 90° and 2.3% at 127°. In the case of ^{118}Sn investigated at the second setup, the total cross section of the 3270 keV level was corrected by 3.8% at 90° and 4.4% at 127°. Due to the different composition of the targets placed at the first setup, the total cross section of the 3359 keV level in ^{122}Sn had to be corrected by 1.3% at 90° and 2.1% at 127°. These absorption corrections have also been performed for the much weaker lines observed in the spectra, but they were of relatively lesser importance given the lower statistical precision of these weak lines. The angles of the targets were measured and verified using the method outlined in section 3.6.5.3. The angle φ of the first target was 10° (counter clockwise) as depicted in Fig. 3.13 and for the second NRF target it was 16° (clockwise !) as shown in Fig. 3.14.

The results of the angular distribution measurements performed at the first and second setup are depicted in Fig. 4.2. The dashed lines in each panel of this figure represent the expected ratios of the angular distribution functions $W(90°)/W(127°)$ for $0 - 1 - 0$ ($W(90°)/W(127°) = 0.75$) and $0 - 2 - 0$ ($W(90°)/W(127°) \approx 2.00$) spin sequences, corrected for the solid angles of the detectors, as well as the isotropic distribution (solid line). The solid diamonds correspond to the results for the γ transitions observed in the Sn nuclei, the open diamonds with the γ transitions in the ^{27}Al calibration standard. These angular distribution measurements show, with very high precision, that the strongest γ transition detected in each of the Sn nuclei stems from the excitation of a spin $J = 1$ state. Further on, also a few quadrupole excitations were found. The angular correlations of the γ transitions in the ^{27}Al calibration standard are nearly isotropic according with the half integer spin of the involved levels and the mixing ratios of the

Figure 4.1: High energy part (2600 - 3600 keV) of the $^{116,118,120,122,124}Sn$ NRF spectra. A dominating peak corresponding to the excitation of a 1^- level has been observed in each spectrum (marked by "1^-"). The accompanying single escape peak is labeled with "SE(1^-)". Prominent 2^+ states are marked with "2^+". The 2614 keV background line from the decay of ^{208}Pb fed by the natural ^{232}Th α-decay chain is labeled with "Bg". Lines stemming from the ^{27}Al calibration standard are indicated with "Al".

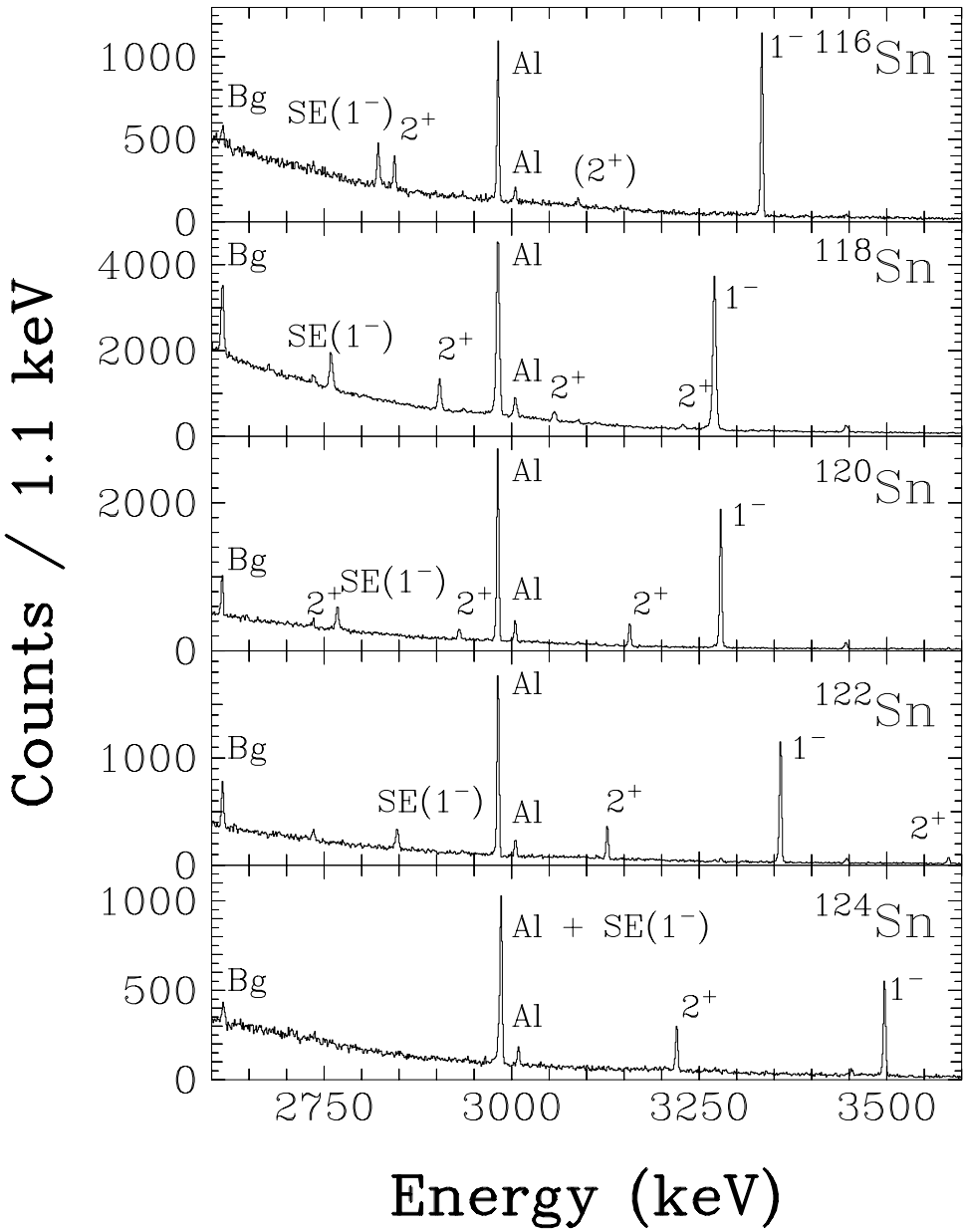

transitions.

Only in the case of the strongest dipole transitions, a parity could be assigned to the corresponding excited level. The results of the photon linear polarization measurements on ^{118}Sn and ^{122}Sn using Compton polarimeters are shown in Fig. 4.3. The dashed lines correspond to the expected azimuthal asymmetries ϵ considering the polarization sensitivity Q of the Compton polarimeter. A measured positive azimuthal asymmetry points to an $M1$ or $E2$ transition, whereas a negative azimuthal asymmetry gives evidence for an $E1$ transition. The measured negative azimuthal asymmetries for the 3270 and 3359 keV γ transitions in ^{118}Sn and ^{122}Sn, represented by the solid symbols in Fig. 4.3, are more than three standard deviations away from the opposite positive azimuthal asymmetry. Therefore, it can be concluded that they belong to the excitation of 1^- levels in the respective nuclei. In open diamonds, also the azimuthal asymmetries for the γ transitions in the ^{27}Al calibration standard are given. These nearly vanishing azimuthal asymmetries prove that the Compton polarimeter device has no intrinsic asymmetry between its different sectors. The negative parities for the corresponding $J = 1$ levels in ^{116}Sn and ^{124}Sn at 3334 and 3490 keV were deduced form the observed azimuthal asymmetries ϵ in NRF experiments with partially linearly polarized off-axis bremsstrahlung in the entrance channel at the 15 MeV linac in Gent [Gova94b]. After a correction for feeding from higher lying levels, a conclusive negative parity was obtained. For ^{120}Sn, the negative parity assignment to the 3278 keV level is based on the similar properties of the $J = 1$ levels in all the investigated even-even neighbouring Sn isotopes. Besides the strong dipole transitions, a few other dipole and quadrupole transitions are observed in each nucleus. These transitions were all too weak to allow any conclusion about the parity of the excited levels from the photon linear polarization measurements. Nevertheless, a positive parity can be deduced for the levels excited via quadrupole transitions from the knowledge that $M2$ excitations have scattering intensities below the experimental detection limits.

Most of the levels observed in these NRF experiments were already known from previous (n,n'γ)-studies [Govo91b]. The excitation energies of the strongest 1^- levels in the even-mass Sn isotopes were determined in this (n,n'γ)-work, but the enhanced ground state transitions from these levels correspond to too short lifetimes to be measured accurately with the Doppler Shift Attenuation Method (DSAM). In NRF such strong transitions have a sufficient large ground state transition width Γ_0 which can be determined precisely from the measured total cross sections I_S. All the photon scattering results for ^{116,118,120,122,124}Sn are summarized in Table 4.2. Energies are corrected for recoil and, if possible, a weighted average was taken of the results at the scattering angles of 90° and 127°. In general, the excitation energies are measured to a precision better than 1 keV. In columns 2 and 3, the spins deduced from the present experiments are compared with the results of the (n,n'γ)-experiment [Govo91b]. No contradiction is found. In ^{118}Sn a new level at 3982 keV and in ^{122}Sn a new level at 3871 keV were observed. In the last column the reduced excitation probabilities $B(E1)\uparrow$ and $B(E2)\uparrow$ are given according with the observed spin sequence, the parity of the excited level and the known branching ratios Γ_0/Γ. If the spin could not be determined in this work, it was adopted from the earlier (n,n'γ)-work [Govo91b]. Inelastic γ transitions were not observed in these NRF experiments, therefore the branching ratio Γ_0/Γ values are taken from the literature, mainly from recent (n,n'γ) investigations [Demi90a,

Figure 4.2: Angular distribution ratios $W(90°)/W(127°)$ measured at the first and second setup of the Stuttgart NRF facility. The four upper panels show data taken at the first setup with two HP Ge detectors. The two lower panels contain data from setup 2 taken with a Compton polarimeter and an HP Ge-detector. The dashed lines represent the theoretical angular distribution ratios for 0–1–0 (D) and 0–2–0 (Q) spin sequences and the solid line the isotropic distribution. The open symbols mark the intensity distributions of the transitions in the ^{27}Al calibration standard. The results for the transitions in the Sn nuclei are denoted with solid symbols.

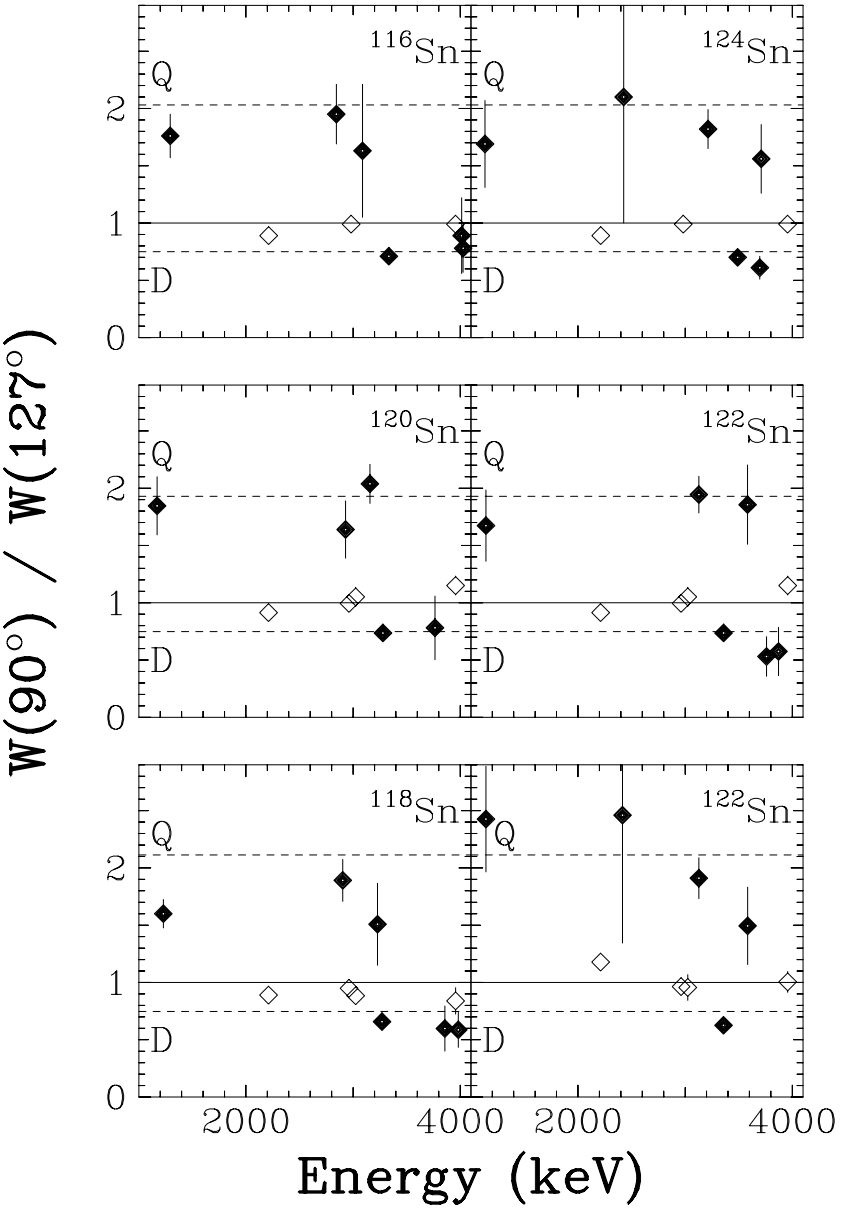

Figure 4.3: Azimuthal asymmetries ϵ measured by a Compton polarimeter. Solid symbols correspond to the $E1$ excitations in ^{118,122}Sn; open symbols correspond to the unpolarized transitions in ^{27}Al, which are used for the photon flux calibration. Taken from [Beli00]

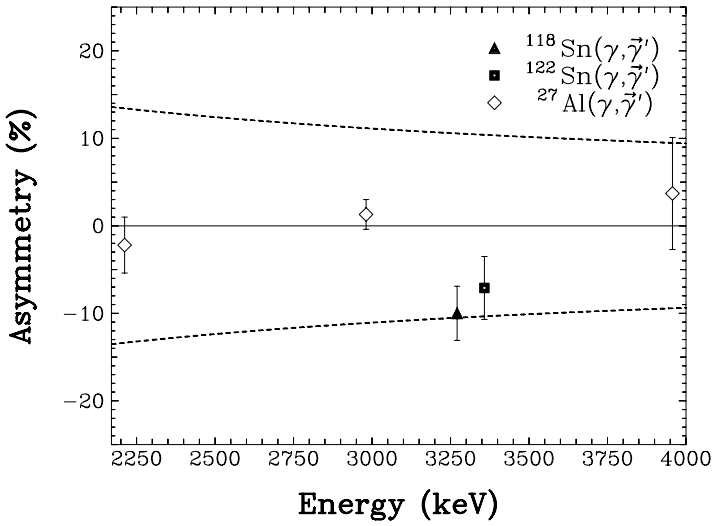

Mikh89, Demi92, Demi91, Demi90b]. In the case of ^{116}Sn, the adopted decay branching for the 2843.9 keV level in Nucl. Data Sheets [Blac94] is not in agreement with data from (n,γ)-work [Rama91], from ^{116}Sb (15.8 min) EC-decay studies [Gacs94] (although the data from both works were included in this issue of the Nucl. Data Sheets) and from (n,n'γ)-work [Demi90a]. The results from Ref. [Demi90a] are in very good agreement with the data from the (n,γ)-experiment with exception of the 4013 keV level. For this level the data from Ref. [Rama91] were taken.

In columns 7 and 8 of Table 4.2, the ground state decay widths Γ_0 deduced from our experiments are compared with the ones derived from lifetime τ measurements [Govo91b]. The ground state decay widths $\Gamma_{0,(\gamma,\gamma')}$ obtained in (γ,γ')-experiments may be smaller than the decay widths $\Gamma_{0,(n,n'\gamma)}$ found in the (n,n'γ)-measurements. This can be understood from the equations used in the analysis. In NRF, the scattering intensity is proportional to Γ_0^2/Γ whereas in (n,n'γ)-experiments the lifetime τ is measured:

$$\Gamma_{0,(\gamma,\gamma')} = \frac{\Gamma_0^2}{\Gamma}\cdot\frac{\Gamma}{\Gamma_0}$$
$$\Gamma_{0,(n,n'\gamma)} = \frac{\hbar}{\tau}\cdot\frac{\Gamma_0}{\Gamma}\,.$$

If the branching ratio Γ_0 / Γ is overestimated due to unobserved transitions to lower-lying excited states $\Gamma_{0,(\gamma,\gamma')}$ will be underestimated and $\Gamma_{0,(n,n'\gamma)}$ will be overestimated. For the strongest $E1$ transition in each of the Sn nuclei, the discrepancy between both values has another origin: strong transitions correspond to short lifetimes, which are difficult to be measured accurately with the Doppler Shift Attenuation Method applied in the (n,n'γ)-experiments.

Table 4.2: Properties of the levels observed in ^{116}Sn, ^{118}Sn, ^{120}Sn, ^{122}Sn and ^{124}Sn.

Energy (keV)	J^π (γ,γ')	J^π [a] $(n,n\gamma')$	I_S (eVb)	Γ_0^2/Γ (meV)	Γ_0/Γ [b]	$\Gamma_{0,(\gamma,\gamma')}$ (meV)	$\Gamma_{0,(n,n'\gamma)}$ (meV)	$B(E1\uparrow)$ $(10^{-3}\cdot e^2fm^2)$ (e^2fm^4)
				^{116}Sn				
1293.6 (3)	2_1^+	2_1^+	12.6 (12)	1.10 (10)	1	1.10 (10)	-	1883 (171)
2843.9 (3)	2^+	2^+	5.6 (6)	2.37 (26)	0.745 (19)	3.18 (36)	$4.05^{+0.71}_{-0.76}$	106 (12)
3088.7 (6)	(2^+)	2^+	2.2 (4)	1.11 (21)	0.654 (14)	1.70 (32)	$1.43^{+0.83}_{-0.76}$	37 (7)
3333.7 (3)	1^-	$1^{(+)}$	87.8 (87)	84.7 (84)	1	84.7 (84)	51^{+15}_{-12}	6.55 (65)
4012.9 (6)	1	1	6.1 (26)	8.5 (36)	0.714 (89)	11.9 (53)	16^{+11}_{-6}	0.53 (27)
4026.8 (5)	1	1	10.4 (40)	14.6 (56)	1	14.6 (56)	< 27	0.64 (25)
				^{118}Sn				
1229.6 (4)	2_1^+	2_1^+	11.8 (16)	0.93 (13)	1	0.93 (13)	-	2051 (286)
2903.8 (6)	2^+	2^+	5.8 (5)	2.54 (22)	0.730 (19)	3.47 (31)	$4.33^{+0.89}_{-0.90}$	105 (13)
3057.0 (5)	-	2^+	2.3 (3)	1.12 (13)	0.815 (14)	1.37 (16)	$3.35^{+0.65}_{-1.26}$	32 (4)
3228.2 (6)	(2^+)	2^+	1.5 (3)	0.79 (16)	1	0.79 (16)	$2.99^{+0.45}_{-1.84}$	14 (3)
3270.3 (5)	1^-	1	95.4 (71)	88.5 (65)	1	88.5 (65)	94^{+67}_{-54}	7.25 (54)
3856.9 (10)	1	$1,2^+$	2.3 (4)	2.98 (57)	0.543 (55)	5.5 (12)	-	0.27(6)
3982.2 (8)	1	-	4.5 (8)	6.2 (11)	-	6.2 (11)	-	0.28 (5)
				^{120}Sn				
1171.2 (6)	2_1^+	2_1^+	12.6 (15)	0.90 (11)	1	0.90 (11)	-	2521 (299)
2728.9 (11)	-	2^+	1.5 (6)	0.58 (23)	0.441 (25)	1.32 (52)	$0.83^{+0.38}_{-0.31}$	54 (21)
2930.2 (6)	2^+	2^+	3.9 (5)	1.76 (21)	0.649 (25)	2.71 (35)	$3.29^{+0.99}_{-1.04}$	78 (10)
3157.6 (5)	2^+	2^+	8.4 (8)	4.36 (39)	0.825 (16)	5.29 (49)	$7.5^{+1.8}_{-1.6}$	104 (10)
3278.8 (6)	$1^{(-)}$	1	100.2 (67)	93.4 (63)	1	93.5 (63)	39^{+16}_{-10}	7.60 (51)
3284.9 (8)	-	2^+	0.6 (2)	0.31 (11)	0.630 (25)	0.50 (17)	$1.7^{+1.5}_{-1.3}$	8 (3)
3582.5 (7)	-	2^+	0.8 (2)	0.56 (15)	0.611 (50)	0.91 (26)	$5.0^{+5.0}_{-2.7}$	10 (3)
3764.6 (15)	1	1	2.2 (4)	2.71 (51)	0.529 (42)	5.13 (96)	-	0.28 (5)
3835.6 (10)	-	2^+	1.1 (4)	0.86 (31)	0.489 (40)	1.77 (65)	$1.8^{+2.2}_{-1.5}$	13 (5)
4006.4 (9)	-	2^+	3.2 (8)	2.70 (77)	1	2.70 (77)	-	16 (5)
				^{122}Sn				
1140.8 (8)	2_1^+	2_1^+	10.7 (15)	0.73 (10)	1	0.73 (10)	-	2328 (333)
2415.5 (9)	-	2^+	1.7 (4)	0.50 (11)	0.706 (22)	0.71 (16)	$0.97^{+0.25}_{-0.23}$	54 (12)
3127.6 (7)	2^+	2^+	11.2 (10)	5.70 (52)	1	5.70 (52)	$10.6^{+2.3}_{-2.1}$	118 (11)
3358.5 (8)	1^-	1	96.7 (72)	94.6 (71)	1	94.6 (71)	73^{+59}_{-26}	7.16 (54)
3582.5 (8)	2^+	2^+	4.3 (6)	2.89 (38)	0.813 (23)	3.56 (48)	$13.4^{+7.2}_{-5.0}$	30 (4)
3751.5 (11)	-	2^+	1.6 (4)	1.16 (30)	1	1.16 (30)	$8.2^{+8.2}_{-4.6}$	10 (2)
3759.2 (12)	1	1	2.4 (5)	2.90 (62)	0.344 (34)	8.4 (18)	$5.7^{+17.0}_{-3.4}$	0.46 (10)
3819.7 (16)	-	2^+	1.0 (3)	0.76 (24)	0.475 (39)	1.60 (52)	$4.5^{+3.4}_{-2.5}$	12 (4)
3871.0 (9)	1	-	2.1 (5)	2.72 (64)	-	2.72 (64)	-	0.13 (3)
3929.9 (11)	-	$1,2^+$	1.9 (6)	1.52 (44)	0.812 (53)	1.88 (55)	-	0.089 (26) 12 (4)
				^{124}Sn				
1131.8 (4)	2_1^+	2_1^+	7.3 (10)	0.49 (7)	1	0.49 (7)	-	1629 (224)
2426.5 (5)	(2^+)	2^+	1.3 (3)	2.1 (11)	0.654 (45)	0.63 (16)	$0.85^{+0.32}_{-0.31}$	46 (12)
3214.8 (4)	2^+	2^+	16.5 (18)	8.87 (97)	0.852 (23)	10.4 (12)	$15.6^{+4.5}_{-3.1}$	188 (21)
3490.1 (3)	1^-	1	85.4 (93)	90.2 (98)	1	90.2 (98)	73^{+91}_{-29}	6.08 (66)
3697.4 (5)	1	1 (2^+)	9.5 (14)	11.3 (17)	0.855 (40)	13.2 (21)	$13.4^{+6.7}_{-4.2}$	0.75 (12)
3710.5 (5)	(2^+)	2^+	9.2 (14)	6.6 (10)	0.775 (40)	8.5 (14)	$11.9^{+11.3}_{-2.2}$	75 (12)

[a] See Ref. [Govo91b]

[b] See for ^{116}Sn Ref. [Demi90a], for ^{118}Sn Ref. [Mikh89], for ^{120}Sn Ref. [Demi92] for ^{122}Sn Ref. [Demi91] and for ^{124}Sn Ref. [Demi90b]

[c] See Ref. [Rama91]

In each of the even-mass Sn nuclei, the well known first collective 2_1^+ state was also observed in these NRF experiments. The corresponding reduced electric quadrupole excitation probability $B(E2)\uparrow$ have also been investigated in Coulomb excitation experiments [Spea89b, Jons81, Back81]. The agreement between the Coulomb excitation and the NRF results for ^{118}Sn and ^{124}Sn is excellent. For ^{116}Sn and ^{122}Sn the $B(E2)\uparrow$ values differ by 15% and for ^{120}Sn by 20%. However, these transitions are located in a region of the NRF spectrum where the background increases highly due to nonresonant scattering of the photons, resulting in the statistical uncertainties of 10 to 15% mentioned in Table 4.2. The $E2$ strength might also be overestimated due to feeding from higher lying excited levels. Thus for these last nuclei the agreement between the NRF and Coulomb excitation results can be considered as fair.

In conclusion, it should be remarked that the $E1$ strength below an excitation energy of 4 MeV is mainly concentrated in the first observed 1^- state. In Chapter 5 arguments will be given that these states can be interpreted as being the member of a coupled quadrupole-octupole two-phonon $[2_1^+ \otimes 3_1^-]$ quintuplet.

4.2 Photon scattering off ^{117}Sn

The NRF experiments performed on the odd-mass nuclei adjacent to the even-mass Sn nuclei are intended to investigate the fragmentation and distribution of the $E1$ strength found in the even-mass Sn nuclei. Part of the recorded ^{117}Sn (γ,γ') spectrum ($2.6 \leq E_\gamma \leq 3.6$ MeV) is shown in Fig. 4.4 together with the spectra of its even-even ^{116}Sn and ^{118}Sn neighbours. In the previous paragraph, it was shown that in the even-even ^{116,118}Sn isotopes the $E1$ strength in the energy region below 4 MeV is mostly concentrated in the first 1_1^- state, with an underlying two-phonon $[2_1^+ \otimes 3_1^-]$ character (see further Chapter 5). In the spectra of the even-even nuclei, the dominating peak at an energy of about 3.3 MeV corresponds to the de-excitation of this two-phonon 1^- state into the ground state. In comparison to the spectra of the even-even Sn nuclei, the ^{117}Sn spectrum contains a lot of γ transitions superimposed on the smooth background in the vicinity of the two-phonon 1^- states . The peaks due to the de-excitation of the two-phonon $[2_1^+ \otimes 3_1^-]_{1^-}$ states in the ^{116,118,120}Sn nuclei are also observed in the spectrum of ^{117}Sn due to the small admixtures of 0.86%, 5.81% and 0.76% in the target. In Fig. 4.4b only the peak for ^{118}Sn can be clearly distinguished due to the scale used.

All observed γ transitions in ^{117}Sn are listed in Table 4.3 with the corresponding level excitation energies, the measured total elastic scattering cross sections I_S, the extracted transition width ratios $g \cdot \frac{\Gamma_0^2}{\Gamma}$ (depending on the statistical spin factor g, see section 2.1) and deduced electric excitation probabilities $B(E1)\uparrow$. The total elastic scattering cross sections have been determined from a summed spectrum over the three scattering angles. In the NRF experiments on ^{117}Sn, the three HP Ge detectors at the scattering angles of 90°, 127°, and 150° have nearly the same efficiency (see Table 4.1) and in the summed spectra the angular dependence of the transition intensity on the possible spin cascade is averaged out. Both arguments justify that the total scattering cross sections I_S can unambiguously be extracted from the summed spectrum independently of the induced spin sequence. In the summed spectrum, the statistical accuracy is better than in the individual spectra which allows to observe some weaker lines. In total, more

Figure 4.4: Photon scattering spectrum of the odd-mass ^{117}Sn nucleus (summed spectrum) inserted between those of the even-even ^{116}Sn and ^{118}Sn nuclei (at a scattering angle of 127°), all taken with an end point energy of 4.1 MeV.

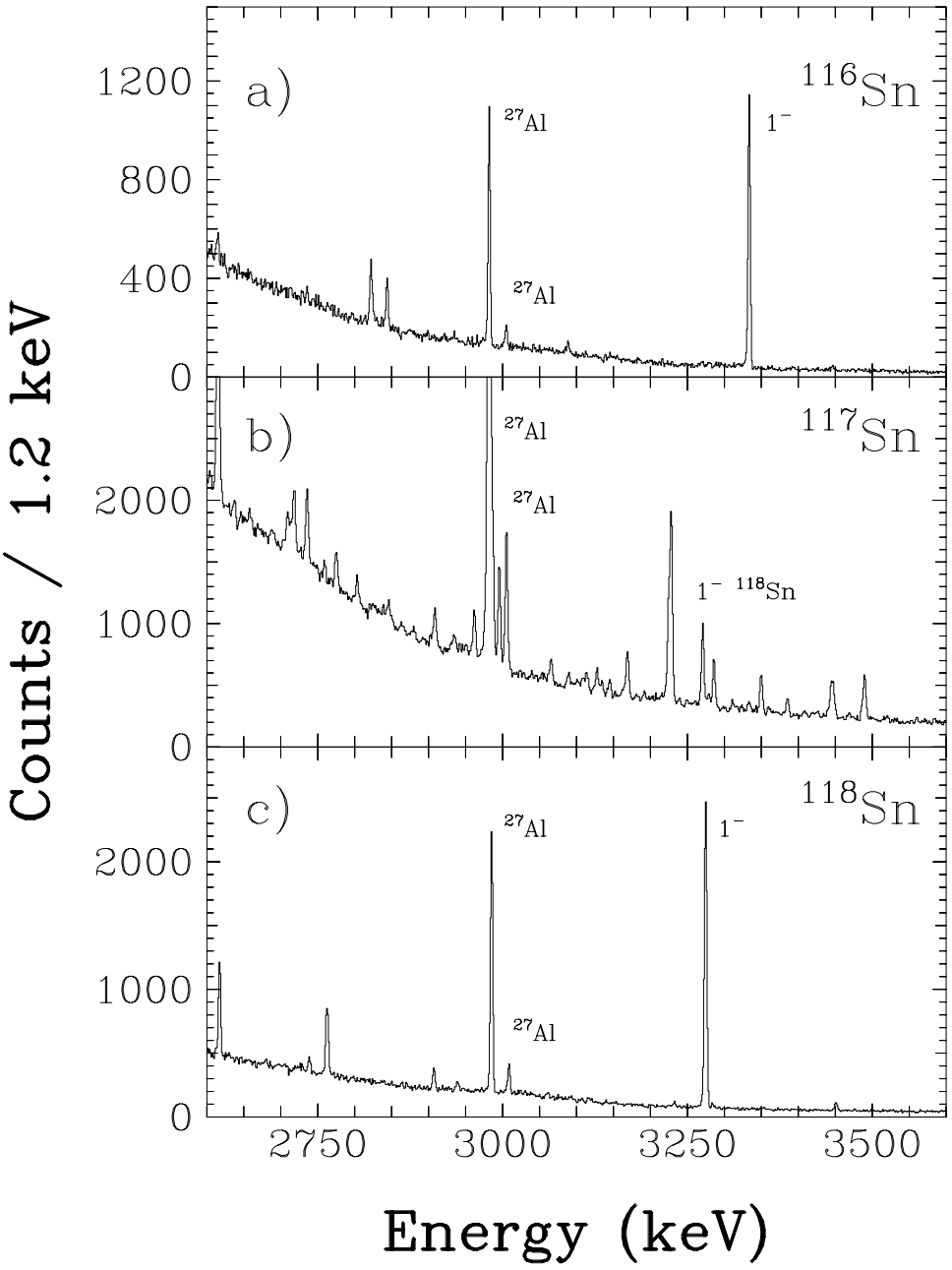

than 50 mainly hitherto unknown levels were found [Blac87]. As the spin of most excited levels is unknown (see further) and parities can not be assigned in the case of an odd-mass nucleus, it was assumed in the calculation of the $B(E1)\uparrow$ excitation strengths that all levels are excited via pure electric dipole transitions. This assumption is justified as in general $E1$ transitions have higher transition probabilities than $M1$ or $E2$ transitions. It should however be remarked that this assumption contains some risk as will become clear in Chapter 5.

In some cases, the observed angular distribution ratios provide an indication of the spin J of the photo-excited levels. These results are summarized in Table 4.4. In the first column the energies of these levels are given. In the next columns the observed angular distribution ratios $W(90°)/W(127°)$, $W(90°)/W(150°)$, and the suggested spin are presented. The experimentally observed angular distribution ratios $W(90°)/W(150°)$ versus $W(90°)/(127°)$ are represented in Fig. 4.5 by open points with error bars. For detailed aspects of this figure see section 2.2.2. Two groups of γ transitions can be clearly observed. For a first group of 5 levels, located around the solid triangle, a probable spin assignment of 3/2 can be given. A second group of 6 levels can be found around the solid square. Here an assignment of 1/2 can be given, however a spin of 3/2 for these levels can not be excluded. The assignment of $J = 1/2$ is preferred for these states because it is assumed that strong transitions should have an $E1$ character. These $E1$ transitions have an isotropic distribution only for excited states with $J = 1/2$. However a spin J of 3/2 cannot be excluded for these levels as transitions with a mixing ratio δ around -3.73 or 0.27 lead to an isotropic distribution too. All the spins given in Table 4.4 were assigned at least at a statistical significance level of 1σ. Under these conditions, no levels with a spin of 5/2 were found centered around the solid star.

Five of the observed γ transitions are probably due to inelastic de-excitations of a level to the well known first $3/2^+$ state in ^{117}Sn at 158.562(12) keV [Blac87]. They are summarized in Table 4.5. In this Table the level excitation energies E_x, the energies E_γ of the de-exciting γ transitions, the branching ratio Γ_1/Γ_0, the ground state transition widths $g \cdot \Gamma_0$ and reduced electric dipole excitation probabilities corrected for the observed inelastic decays, are given. All levels are included for which holds:

$$E_i - (E_x - E_{158}) < \Delta E \tag{4.1}$$

with:

$$\Delta E = \sqrt{(\Delta E_x)^2 + (\Delta E_i)^2 + (\Delta E_{158})^2} \tag{4.2}$$

and E_x, E_i, E_{158} and ΔE_x, ΔE_i, ΔE_{158} the excitation energies of the level, the energy of the inelastic γ transition and the first $3/2^+$ state and their respective uncertainties. The branching ratio Γ_1/Γ_0 of the decay strength to the first excited state compared to the transition strength to the ground state can immediately be determined from the measured scattering intensities A in the (γ,γ')-spectrum:

$$\frac{\Gamma_1}{\Gamma_0} = \frac{A(E_i) \cdot \epsilon(E_x)}{A(E_x) \cdot \epsilon(E_i)}$$

with the ϵ the detector efficiency. In this formula, the influence of the angular correlation functions is neglected because they are expected to be nearly isotropic. Using the above mentioned energy rule for detecting inelastic decays two other candidates were found. The γ ray with the

Table 4.3: Properties of the observed levels in ^{117}Sn.

Energy (keV)	I_S (eVb)	$g \cdot \frac{\Gamma_0^2}{\Gamma}$ (meV)	$B(E1)\uparrow$ [a] ($10^{-3}\ e^2fm^2$)	Energy (keV)	I_S (eVb)	$g \cdot \frac{\Gamma_0^2}{\Gamma}$ (meV)	$B(E1)\uparrow$ [a] ($10^{-3}\ e^2fm^2$)
1447.2 (4)	2.31 (40)	1.26 (22)	0.398 (68)	3224.6 (11)	5.71 (51)	15.45 (137)	0.440 (39)
1510.1 (3)	4.12 (48)	2.45 (29)	0.679 (80)	3228.2 (7)	12.80 (91)	34.71 (247)	0.986 (71)
2048.2 (3)	6.20 (49)	6.77 (54)	0.752 (60)	3286.0 (4)	3.57 (35)	10.05 (97)	0.284 (26)
2128.6 (4)	1.05 (22)	1.24 (25)	0.123 (25)	3349.9 (3)	3.25 (31)	9.50 (90)	0.242 (23)
2280.4 (6)	0.45 (16)	0.61 (22)	0.049 (18)	3360.1 (8)	0.55 (20)	1.60 (59)	0.040 (15)
2304.6 (5)	0.73 (18)	1.01 (25)	0.079 (20)	3385.4 (4)	1.39 (21)	4.15 (63)	0.102 (16)
2356.7[b] (8)	0.80 (25)	1.15 (36)	0.084 (27)	3408.5 (9)	0.52 (19)	1.57 (58)	0.038 (14)
2367.3 (2)	7.86 (55)	11.46 (80)	0.825 (58)	3425.8 (9)	0.60 (25)	1.84 (75)	0.044 (18)
2415.9 (3)	1.86 (23)	2.82 (35)	0.191 (24)	3468.8 (6)	0.47 (16)	1.47 (49)	0.034 (11)
2515.8 (5)	0.72 (17)	1.18 (28)	0.071 (17)	3489.6 (3)	5.46 (48)	17.31 (151)	0.389 (34)
2590.2 (5)	1.00 (23)	1.75 (40)	0.096 (22)	3520.4 (7)	0.53 (20)	1.70 (64)	0.037 (14)
2709.1 (5)	1.46 (22)	2.80 (42)	0.134 (20)	3560.5 (6)	0.54 (16)	1.79 (53)	0.038 (11)
2718.2 (4)	1.74 (43)	3.34 (82)	0.159 (39)	3719.8[c] (7)	3.16 (45)	11.38 (163)	0.211 (30)
2775.2 (4)	1.02 (19)	2.04 (37)	0.091 (17)	3749.4 (4)	2.08 (34)	7.62 (123)	0.138 (22)
2803.4[b] (5)	1.19 (20)	2.43 (42)	0.105 (18)	3761.4[b] (8)	0.90 (32)	3.32 (117)	0.060 (21)
2864.1 (11)	0.57 (21)	1.21 (45)	0.049 (18)	3773.3 (13)	0.91 (39)	3.37 (144)	0.060 (26)
2879.8 (9)	0.58 (20)	1.25 (42)	0.050 (17)	3788.3 (7)	1.57 (36)	5.87 (133)	0.103 (24)
2908.5 (4)	2.15 (28)	4.73 (62)	0.184 (24)	3871.3 (4)	5.05 (65)	19.71 (255)	0.325 (42)
2961.9 (4)	2.66 (28)	6.08 (63)	0.224 (23)	3883.2 (4)	3.58 (53)	14.06 (207)	0.229 (34)
2986.7 (3)	7.28 (85)	16.89 (197)	0.606 (71)	3900.2 (6)	1.09 (29)	4.33 (117)	0.070 (19)
2995.7 (3)	5.48 (41)	12.80 (96)	0.455 (34)	3920.1 (7)	1.45 (40)	5.79 (158)	0.092 (25)
3065.7[b] (5)	1.53 (22)	3.74 (55)	0.124 (18)	3930.4 (5)	1.12 (29)	4.51 (117)	0.071 (19)
3100.8 (7)	0.76 (15)	1.91 (38)	0.061 (12)	3949.8 (16)	3.21 (137)	13.03 (558)	0.202 (87)
3108.2 (7)	0.83 (17)	2.08 (43)	0.066 (14)	3980.9 (5)	3.47 (68)	14.31 (280)	0.217 (43)
3127.8[b] (4)	1.75 (21)	4.45 (53)	0.139 (17)	3994.0 (6)	1.73 (46)	7.17 (189)	0.108 (29)
3134.3 (6)	0.96 (17)	2.46 (43)	0.076 (13)	4013.6 (6)	2.54 (77)	10.65 (324)	0.157 (48)
3144.9 (5)	1.11 (18)	2.86 (45)	0.088 (14)	4027.8 (4)	6.56 (129)	27.70 (544)	0.405 (80)
3169.1 (4)	3.36 (32)	8.78 (83)	0.264 (25)	4043.6 (7)	3.94 (113)	16.78 (482)	0.242 (70)

[a] Assuming all observed transitions have an electric dipole character

[b] This γ transition might be due to an inelastic decay of a higher-lying level; see Table 4.5

[c] multiplet

Table 4.4: Suggested spin assignments for some levels in ^{117}Sn. For each level, the observed angular correlation ratio $W(90°)/W(127°)$ and $W(90°)/W(150°)$ are given. The last column contains the suggested spin.

Energy (keV)	$\frac{W(90°)}{W(127°)}$	$\frac{W(90°)}{W(150°)}$	J
2048.2	0.952 (86)	1.043 (95)	$(\frac{1}{2},\frac{3}{2})^{a)}$
2367.3	0.780 (53)	0.716 (47)	$\frac{3}{2}$
2986.7	0.983 (174)	0.902 (120)	$(\frac{1}{2},\frac{3}{2})^{a)}$
2995.7	0.882 (70)	0.773 (60)	$\frac{3}{2}$
3169.1	0.942 (106)	0.670 (77)	$\frac{3}{2}$
3224.6	0.984 (126)	0.939 (104)	$(\frac{1}{2},\frac{3}{2})^{a)}$
3228.2	0.825 (60)	0.842 (58)	$\frac{3}{2}$
3286.0	1.139 (130)	1.055 (135)	$(\frac{1}{2},\frac{3}{2})^{a)}$
3349.9	1.020 (134)	0.992 (139)	$(\frac{1}{2},\frac{3}{2})^{a)}$
3489.6	0.827 (89)	0.697 (75)	$\frac{3}{2}$
3871.3	0.899 (146)	0.969 (159)	$(\frac{1}{2},\frac{3}{2})^{a)}$

$^{a)}$ A spin of 1/2 is most likely, but a 3/2 spin cannot be excluded. See text for more details.

Figure 4.5: Observed angular distribution ratios $W(90°)/W(150°)$ versus $W(90°)/(127°)$ (open points with error bars). The square represents the unique location for 1/2 – 1/2 – 1/2 spin sequences. Pure $E1$, $M1$ or $E2$ transitions in a 1/2 – 3/2 – 1/2 spin sequence are marked with the triangle. $E1$ and mixed $M1/E2$ transitions ($\delta \neq 0$, $\pm\infty$) in this spin sequence are located on the solid line. The star corresponds to a pure $E2$ transition in a 1/2 – 5/2 – 1/2 spin sequence.

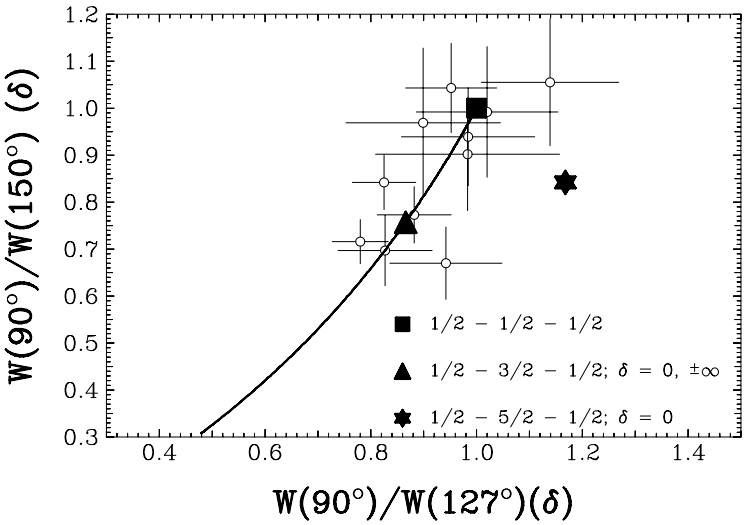

Table 4.5: Levels with probable inelastic transitions to the 158.562 keV ($3/2^+$) level in ^{117}Sn. Column two and three contain for each level the energy of the observed γ rays and the branching ratio Γ_1/Γ_0. The given ground state decay widths $g \cdot \Gamma_0$ and the $B(E1)\uparrow$ strengths are corrected for the possible inelastic transitions.

E_x (keV)	E_γ (keV)	Γ_1/Γ_0	$g \cdot \Gamma_0$ (meV)	$B(E1)\uparrow$ (10^{-3} e^2fm^2)
2515.8 (5)	2515.8 (5)	1.28 (44)	2.7 (8)	0.162 (49)
	2356.7 (8)			
2961.9 (4)	2961.9 (4)	0.51 (8)	9.2 (11)	0.338 (39)
	2803.4 (5)			
3224.6 (11)	3224.6 (11)	0.31 (4)	20.3 (6)	0.577 (17)
	3065.7 (5)			
3286.0 (4)	3286.0 (4)	0.55 (5)	16.3 (16)	0.439 (43)
	3127.8 (4)			
3920.1 (7)	3920.1 (7)	0.96 (38)	11.4 (38)	0.180 (60)
	3761.4 (8)			

energy of 3560.5 keV can be due to an inelastic transition of one line from the multiplet at 3719.8 keV to the first $3/2^+$ state. Also the γ rays with the energy of 2986.7 and 3144.9 keV fulfill the energy relation. However, if the 2986.7 keV γ ray is seen as completely inelastic, an unreasonable low branching ratio Γ_0/Γ of 12% for the 3144.9 keV level is obtained. Both cases are not considered in Table 4.5. Certainty about the observed probable inelastic γ transitions would require time coincidence or excitation function measurements which are beyond the scope of this work. With the above mentioned method, our experimental results show no further candidates for inelastic transitions to other excited levels.

4.3 Photon scattering off ^{121}Sb and ^{123}Sb

The recorded (γ,γ') spectra on ^{121}Sb and ^{123}Sb for excitation energies between 2.6 and 3.6 MeV are shown in Fig. 4.6, together with those for the even-even ^{120,122,124}Sn. As was the case in ^{117}Sn, it can be clearly seen from these spectra that the electromagnetic excitation strength in both nuclei is highly fragmented compared to the strength observed in the even-even ^{120,122,124}Sn neighbours. However, the number of peaks stemming from resonant photon scattering events on ^{121}Sb is larger than in the ^{123}Sb case. In total 164 γ transitions were observed in ^{121}Sb of which 114 transitions lay below the excitation energy of 3.5 MeV (energy of the highest level observed in ^{123}Sb). In ^{123}Sb, 83 γ transitions were detected. It should be remembered that the end point energy of the bremsstrahlung spectrum in the ^{123}Sb measurement was shifted down to 3.8 MeV. All the results from both NRF measurements are listed in Tables 4.6 and 4.7. They are obtained from an analysis of the summed spectra over the three scattering angles of 90°, 127°, and 150°. For each nucleus the energy of the observed γ transitions are given. In the next columns the measured total scattering cross sections I_S and the transition width ratios $g \cdot \Gamma_0^2/\Gamma$ are given (for a definition of the statistical spin factor g see Section 2.1). As neither spins nor parities can be determined in NRF experiments on odd-mass nuclei, it was assumed that all levels are populated via pure electric dipole transitions and the corresponding reduced electric dipole excitation probabilities $B(E1)\uparrow$ have been extracted (under this assumption).

As stated in Chapter 2, in NRF experiments on odd-mass nuclei with a ground state spin higher than 1/2 no spin information is accessible. The odd-mass nuclei ^{121}Sb and ^{123}Sb have ground state spins of 5/2 and 7/2 leading to isotropic angular distributions. However, if the half life $T_{1/2}$ of a level is known, the spin of the excited level can be deduced indirectly. The 1385 keV level in ^{121}Sb has a half life of 0.064 (6) ps [Tamu00] and the 1088 keV level in ^{123}Sb has a half life of 0.65 (5) ps [Ohya93]. The half life $T_{1/2}$ can be converted into the total transition width Γ of the level via the Heisenberg uncertainty relation (under the best circumstances):

$$\Gamma = \frac{\hbar \cdot \ln(2)}{T_{1/2}} \quad . \tag{4.3}$$

Both mentioned levels decay directly into the ground state [Tamu00, Ohya93] and thus in both cases the ground state transition widths Γ_0 are equal to the total decay width Γ. Finally, the statistical spin factor g can be deduced from the comparison of the measured transition width ratio $g \cdot \Gamma_0^2/\Gamma$ and the ground state transition width Γ_0. In the case of ^{121}Sb, the determined spin factor g equals 0.56 (7) and agrees almost within the error with the spin factor for a $5/2-3/2-5/2$ spin sequence of 0.66. So it is concluded that the 1385 keV level in ^{121}Sb should have a 3/2 spin. In the ^{123}Sb case the spin factor g amounts to 1.60 (24) and coincides with the value of 1.38 corresponding with the spin sequence $7/2-11/2-7/2$. In Ref. [Ohya93] the spins 9/2 and 11/2 are proposed for the 1088 keV level.

The results obtained in this NRF work can be compared with data obtained by Booth et al. [Boot73] who performed NRF measurements with different end point energies between 0 and 2.5 MeV at the 3 MeV electron Van de Graaff accelerator of the Massachusetts Institute of Technology (Boston). In these NRF measurements a natural Sb target was used. Natural Sb consists for 57.3% of ^{121}Sb and for 42.7% of ^{123}Sb. In total 43 levels were identified in $^{\text{nat}}$Sb. A

good agreement within the statistical accuracy exists for all levels which have been observed in this NRF work and in the work of Booth et al. .

As in the ^{117}Sn case, a study of inelastic transitions has been made. However, the situation met in the Sb nuclei is much more complicated. Again the energy condition:

$$E_i - (E_x - E_{\rm fin}) < \Delta E \tag{4.4}$$

with:

$$\Delta E = \sqrt{(\Delta E_x)^2 + (\Delta E_i)^2 + (\Delta E_{\rm fin})^2}$$

and with E_x, E_i, $E_{\rm fin}$ and ΔE_x, ΔE_i, $\Delta E_{\rm fin}$ the excitation energies of the level, the energy of the inelastic γ transition and the energy of the final state and their respective uncertainties was used. In the search for inelastic transitions all observed levels in these NRF experiments as well as the lowest levels known from literature data [Tamu00, Ohya93], have been included. In total 213 inelastic γ transitions were found in ^{121}Sb and 61 inelastic transitions in the case of ^{123}Sb. As only the energy relation (4.4) was imposed, a lot of levels appear as candidate for an inelastic transition in different spin cascades. The huge number of inelastic candidates is due to the large number of γ transitions which have been detected and to the uncertainty on the energies. In the NRF work by Booth et al. [Boot73], it was remarked that a lot of peaks in the NRF spectra show up with a satellite peak with a difference in energy equal to the energy of the first excited states in the ^{121}Sb and ^{123}Sb nuclei (it means that this satellite peak might stem from an inelastic transition). Therefore, in Table 4.8 the levels are given which possibly branch to the first excited states of 37.133 (8) and 160.33 (5) keV in ^{121}Sb and ^{123}Sb [Tamu00, Ohya93] respectively. The obtained branching ratios to the first excited state which were also found by Booth et al. are given for comparison. In ^{121}Sb, three γ transitions are found which stem either from a ground state transition of one level accompanied by a possible inelastic branch or from an inelastic transition of another level to the first excited state. These three cases are: $2399 \xrightarrow{2361} 37$ or $2436 \xrightarrow{2399} 37$ and, $2836 \xrightarrow{2798} 37$ or $2873 \xrightarrow{2836} 37$ and, $2912 \xrightarrow{2873} 37$ or $2947 \xrightarrow{2912} 37$. Also a mixture of these extreme cases might be possible. The first case has also been reported by Booth et al. [Boot73]. This illustrates again the complexity and difficulties encountered in the Sb nuclei to assign inelastic transitions. For a further discussion of the results obtained for the ^{121,123}Sb nuclei, it will be assumed that all observed γ transitions are ground state transitions. In Chapter 5, the total strength detected in a certain energy region will be compared with other nuclei. Inelastic transitions to the first excited states in nuclei do not change appreciably the value of such a summed strength.

Figure 4.6: Part of the recorded NRF spectra on the odd-mass nuclei ^{121}Sb and ^{123}Sb. A noticeable fragmentation of electromagnetic strength has been observed in both nuclei, compared to the even-even $^{120,122,124}Sn$ neighbours for which the same part of the NRF spectra is also shown in this figure.

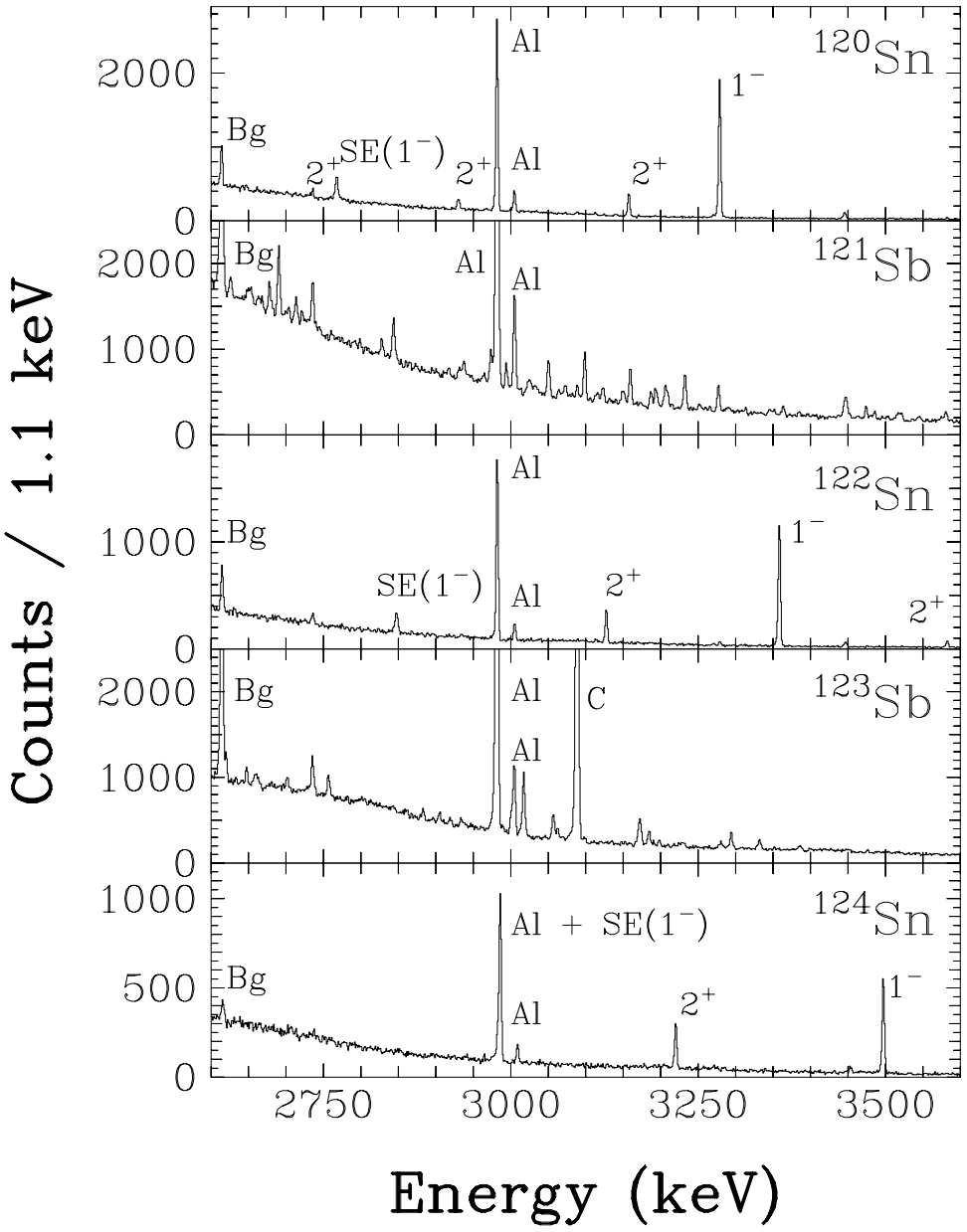

Table 4.6: Properties of the observed levels in ^{121}Sb.

Energy (keV)	I_S (eVb)	$g \cdot \frac{\Gamma_0^2}{\Gamma}$ (meV)	$B(E1)\uparrow$ $(10^{-3} \cdot e^2 fm^2)$	Energy (keV)	I_S (eVb)	$g \cdot \frac{\Gamma_0^2}{\Gamma}$ (meV)	$B(E1)\uparrow$ $(10^{-3} \cdot e^2 fm^2)$
1385.2 (3)	7.93 (64)	3.96 (32)	1.423 (115)	2690.4 (3)	4.14 (34)	7.79 (65)	0.382 (32)
1518.9 (3)	6.47 (55)	3.88 (33)	1.058 (90)	2698.8 (8)	0.53 (14)	1.00 (27)	0.048 (13)
1590.4 (4)	2.97 (43)	1.95 (28)	0.464 (67)	2703.8 (6)	0.90 (16)	1.72 (31)	0.083 (15)
1628.4 (3)	4.19 (45)	2.89 (31)	0.640 (68)	2713.5 (4)	1.73 (20)	3.32 (39)	0.159 (19)
1736.3 (2)	8.93 (62)	7.00 (48)	1.278 (88)	2721.4 (6)	0.57 (16)	1.11 (32)	0.052 (15)
1758.5 (4)	0.49 (16)	0.40 (13)	0.070 (23)	2723.0 (9)	0.66 (17)	1.28 (33)	0.060 (16)
1810.8 (5)	4.79 (42)	4.09 (36)	0.658 (57)	2725.8 (12)	0.48 (17)	0.92 (32)	0.044 (15)
1910.6 (3)	0.67 (21)	0.64 (20)	0.087 (27)	2740.4 (10)	0.41 (15)	0.81 (30)	0.037 (14)
1927.1 (5)	0.60 (20)	0.58 (19)	0.078 (25)	2745.0 (9)	0.47 (15)	0.92 (29)	0.043 (13)
1981.6 (4)	0.42 (18)	0.43 (18)	0.053 (23)	2761.2 (8)	0.43 (16)	0.85 (32)	0.039 (15)
1988.9 (8)	1.04 (31)	1.08 (32)	0.131 (38)	2775.1 (6)	0.28 (12)	0.55 (24)	0.025 (11)
2016.5 (9)	0.70 (26)	0.75 (28)	0.087 (32)	2783.7 (7)	0.26 (12)	0.53 (24)	0.024 (11)
2025.7 (7)	1.18 (30)	1.26 (32)	0.144 (37)	2791.9 (9)	0.69 (26)	1.39 (53)	0.061 (23)
2063.4 (5)	1.30 (25)	1.44 (28)	0.156 (30)	2798.8 (6)	0.70 (18)	1.44 (37)	0.063 (16)
2093.0 (7)	0.85 (28)	0.97 (32)	0.101 (33)	2806.2 (7)	0.33 (15)	0.68 (31)	0.029 (14)
2097.9 (5)	1.04 (27)	1.19 (31)	0.123 (32)	2810.0 (7)	0.36 (16)	0.75 (33)	0.032 (14)
2114.1 (4)	1.09 (22)	1.27 (25)	0.128 (26)	2828.2 (5)	1.49 (41)	3.11 (86)	0.131 (36)
2121.3 (7)	0.87 (25)	1.02 (29)	0.103 (29)	2835.6 (8)	0.60 (20)	1.26 (41)	0.053 (17)
2140.2 (7)	1.10 (27)	1.32 (32)	0.128 (31)	2843.6 (3)	3.56 (33)	7.49 (69)	0.311 (29)
2235.5 (3)	2.91 (30)	3.79 (39)	0.324 (33)	2860.1 (5)	0.25 (10)	0.53 (21)	0.022 (9)
2243.1 (7)	0.91 (24)	1.19 (31)	0.101 (26)	2865.2 (6)	0.37 (13)	0.79 (28)	0.032 (11)
2255.2 (6)	0.51 (19)	0.67 (25)	0.056 (21)	2873.4 (9)	0.37 (15)	0.80 (32)	0.032 (13)
2259.1 (3)	1.98 (25)	2.63 (33)	0.218 (27)	2895.2 (8)	0.28 (13)	0.61 (29)	0.024 (11)
2265.9 (4)	1.06 (21)	1.42 (28)	0.116 (23)	2911.6 (11)	0.26 (11)	0.58 (25)	0.022 (10)
2280.4 (6)	1.01 (24)	1.37 (32)	0.110 (26)	2917.3 (6)	0.63 (14)	1.40 (32)	0.054 (12)
2286.3 (5)	0.64 (18)	0.87 (24)	0.069 (19)	2931.5 (6)	0.88 (16)	1.96 (35)	0.074 (13)
2289.8 (4)	0.24 (10)	0.33 (14)	0.026 (11)	2937.4 (4)	1.52 (20)	3.40 (46)	0.128 (17)
2323.5 (4)	0.81 (17)	1.14 (24)	0.087 (18)	2947.3 (12)	0.31 (15)	0.69 (34)	0.026 (13)
2361.7 (3)	2.19 (25)	3.18 (36)	0.231 (26)	2964.0 (7)	0.65 (17)	1.48 (39)	0.054 (14)
2398.8 (3)	5.00 (38)	7.48 (57)	0.518 (40)	2973.6 (3)	2.99 (32)	6.87 (73)	0.250 (26)
2435.8 (3)	3.36 (32)	5.20 (49)	0.343 (32)	2994.1 (3)	1.74 (21)	4.05 (48)	0.144 (17)
2442.0 (3)	0.50 (14)	0.78 (22)	0.051 (15)	3024.6 (6)	1.54 (53)	3.66 (125)	0.126 (43)
2447.7 (4)	0.48 (14)	0.74 (22)	0.048 (14)	3033.1 (10)	1.58 (63)	3.77 (152)	0.129 (52)
2459.2 (6)	0.43 (16)	0.68 (25)	0.043 (16)	3050.4 (3)	3.33 (30)	8.06 (72)	0.271 (24)
2477.0 (4)	0.48 (13)	0.76 (21)	0.048 (13)	3064.1 (6)	0.65 (13)	1.60 (32)	0.053 (11)
2497.7 (3)	3.15 (31)	5.11 (51)	0.313 (31)	3068.9 (9)	0.39 (13)	0.96 (31)	0.032 (10)
2541.6 (6)	0.38 (12)	0.64 (21)	0.037 (12)	3072.9 (5)	1.16 (17)	2.85 (41)	0.094 (13)
2573.8 (7)	0.98 (23)	1.68 (39)	0.094 (22)	3078.2 (10)	0.30 (11)	0.74 (28)	0.024 (9)
2579.2 (14)	0.40 (20)	0.70 (34)	0.039 (19)	3082.7 (8)	0.40 (12)	1.00 (30)	0.032 (10)
2585.6 (8)	0.81 (21)	1.40 (37)	0.077 (20)	3098.7 (3)	4.19 (34)	10.48 (85)	0.336 (27)
2626.1 (5)	0.97 (18)	1.74 (33)	0.092 (17)	3116.0 (6)	0.75 (22)	1.90 (55)	0.060 (17)
2649.0 (7)	0.38 (15)	0.69 (27)	0.035 (14)	3122.9 (4)	1.60 (21)	4.05 (53)	0.127 (17)
2653.5 (6)	0.91 (17)	1.66 (31)	0.085 (16)	3132.0 (7)	0.34 (13)	0.87 (33)	0.027 (10)
2663.0 (7)	0.66 (15)	1.22 (28)	0.062 (14)	3148.8 (7)	1.00 (28)	2.57 (71)	0.079 (22)
2668.1 (7)	0.61 (15)	1.13 (28)	0.057 (14)	3151.7 (8)	0.80 (27)	2.08 (69)	0.063 (21)
2678.1 (4)	1.74 (20)	3.25 (38)	0.162 (19)	3159.5 (3)	3.69 (33)	9.57 (85)	0.290 (26)

continued on next page

Energy (keV)	I_S (eVb)	$g \cdot \frac{\Gamma_0^2}{\Gamma}$ (meV)	$B(E1)\uparrow$ $(10^{-3} \cdot e^2 fm^2)$	Energy (keV)	I_S (eVb)	$g \cdot \frac{\Gamma_0^2}{\Gamma}$ (meV)	$B(E1)\uparrow$ $(10^{-3} \cdot e^2 fm^2)$
3186.9 (4)	1.30 (21)	3.44 (56)	0.101 (17)	3672.6 (11)	0.60 (21)	2.11 (73)	0.041 (14)
3193.7 (4)	2.32 (29)	6.15 (77)	0.180 (23)	3677.3 (10)	0.72 (21)	2.53 (75)	0.049 (14)
3206.6 (4)	2.80 (41)	7.49 (110)	0.217 (32)	3693.7 (9)	0.62 (19)	2.20 (67)	0.042 (13)
3210.1 (5)	0.62 (27)	1.68 (74)	0.048 (21)	3706.3 (7)	0.52 (17)	1.86 (62)	0.035 (12)
3215.0 (7)	0.35 (13)	0.95 (36)	0.027 (10)	3712.1 (9)	0.53 (20)	1.89 (71)	0.035 (13)
3232.5 (3)	4.01 (34)	10.90 (93)	0.308 (26)	3719.2 (11)	0.42 (20)	1.52 (73)	0.028 (14)
3252.1 (7)	0.78 (18)	2.16 (50)	0.060 (14)	3731.7 (5)	0.70 (19)	2.54 (69)	0.047 (13)
3259.9 (7)	0.26 (12)	0.72 (33)	0.020 (9)	3748.9 (5)	0.73 (19)	2.66 (68)	0.048 (12)
3265.9 (5)	0.34 (11)	0.95 (31)	0.026 (9)	3755.6 (7)	0.40 (15)	1.48 (57)	0.027 (10)
3277.1 (3)	2.95 (27)	8.23 (76)	0.223 (21)	3759.4 (9)	0.30 (15)	1.10 (53)	0.020 (10)
3290.3 (9)	1.49 (29)	4.20 (82)	0.113 (22)	3771.8 (8)	0.50 (19)	1.84 (69)	0.033 (12)
3308.5 (11)	0.52 (24)	1.47 (69)	0.039 (18)	3775.1 (7)	0.68 (20)	2.50 (73)	0.044 (13)
3313.7 (5)	0.51 (17)	1.47 (50)	0.038 (13)	3781.3 (5)	0.80 (20)	2.98 (74)	0.053 (13)
3345.8 (8)	0.91 (24)	2.66 (70)	0.068 (18)	3787.3 (7)	0.54 (17)	2.02 (65)	0.035 (11)
3351.7 (7)	0.58 (20)	1.70 (58)	0.043 (15)	3792.6 (7)	0.53 (18)	1.97 (69)	0.035 (12)
3363.6 (4)	1.28 (20)	3.77 (58)	0.095 (15)	3800.4 (9)	0.44 (18)	1.66 (66)	0.029 (11)
3384.9 (6)	0.57 (16)	1.71 (47)	0.042 (11)	3804.3 (10)	0.43 (18)	1.63 (67)	0.028 (12)
3437.1 (8)	0.38 (18)	1.16 (57)	0.027 (13)	3812.9 (6)	0.46 (17)	1.74 (63)	0.030 (11)
3474.2 (4)	1.74 (28)	5.47 (89)	0.125 (20)	3838.1 (9)	0.41 (18)	1.59 (68)	0.027 (12)
3480.5 (9)	0.70 (33)	2.20 (103)	0.050 (23)	3844.6 (8)	0.45 (18)	1.73 (67)	0.029 (11)
3485.8 (5)	1.11 (28)	3.50 (88)	0.079 (20)	3849.1 (7)	0.54 (18)	2.06 (70)	0.035 (12)
3495.6 (8)	0.38 (14)	1.20 (44)	0.027 (10)	3854.2 (7)	0.54 (19)	2.07 (72)	0.035 (12)
3503.2 (6)	0.51 (16)	1.63 (50)	0.036 (11)	3858.1 (7)	0.53 (19)	2.04 (72)	0.034 (12)
3512.7 (11)	0.35 (16)	1.13 (52)	0.025 (11)	3863.8 (6)	0.72 (22)	2.81 (85)	0.046 (14)
3517.0 (6)	1.17 (21)	3.76 (68)	0.083 (15)	3867.0 (8)	0.55 (20)	2.15 (79)	0.036 (13)
3521.3 (5)	1.15 (21)	3.72 (68)	0.081 (15)	3870.1 (8)	0.53 (20)	2.07 (80)	0.034 (13)
3544.9 (7)	1.10 (24)	3.59 (77)	0.077 (17)	3894.0 (9)	0.58 (23)	2.27 (89)	0.037 (14)
3570.2 (13)	0.35 (16)	1.16 (53)	0.024 (11)	3899.6 (10)	0.54 (23)	2.12 (90)	0.034 (15)
3575.0 (7)	0.95 (20)	3.15 (66)	0.66 (14)	3905.2 (6)	1.23 (32)	4.89 (127)	0.078 (20)
3580.7 (4)	2.06 (27)	6.88 (89)	0.143 (19)	3909.4 (11)	0.56 (26)	2.23 (104)	0.036 (17)
3587.6 (10)	0.44 (15)	1.47 (51)	0.030 (11)	3916.0 (8)	0.73 (26)	2.91 (102)	0.046 (16)
3614.5 (6)	0.90 (20)	3.05 (69)	0.062 (14)	3923.4 (7)	0.90 (29)	3.61 (115)	0.057 (18)
3621.4 (11)	0.33 (15)	1.13 (51)	0.023 (10)	3929.1 (8)	0.96 (30)	3.87 (120)	0.061 (19)
3638.9 (8)	0.44 (16)	1.52 (54)	0.030 (11)	3933.3 (9)	0.77 (29)	3.11 (118)	0.049 (18)
3642.0 (7)	0.52 (17)	1.81 (58)	0.036 (11)	3940.9 (7)	0.88 (32)	3.57 (131)	0.056 (20)
3648.5 (8)	0.32 (14)	1.11 (47)	0.022 (9)	3972.7 (11)	1.69 (63)	6.94 (258)	0.106 (39)

Table 4.7: Properties of the observed levels in ^{123}Sb.

Energy (keV)	I_S (eVb)	$g \cdot \frac{\Gamma_0^2}{\Gamma}$ (meV)	$B(E1)\uparrow$ $(10^{-3} \cdot e^2fm^2)$	Energy (keV)	I_S (eVb)	$g \cdot \frac{\Gamma_0^2}{\Gamma}$ (meV)	$B(E1)\uparrow$ $(10^{-3} \cdot e^2fm^2)$
1030.6 (3)	10.91 (85)	3.02 (23)	2.632 (204)	2521.8 (3)	2.98 (26)	4.94 (43)	0.294 (25)
1089.0 (3)	3.61 (49)	1.12 (15)	0.825 (112)	2597.7 (4)	1.10 (15)	1.93 (27)	0.105 (15)
1353.4 (4)	1.48 (31)	0.70 (15)	0.271 (57)	2605.9 (8)	0.37 (12)	0.66 (21)	0.036 (12)
1424.8 (4)	0.73 (22)	0.39 (12)	0.128 (38)	2620.1 (4)	1.65 (19)	2.95 (33)	0.157 (18)
1509.0 (4)	1.74 (30)	1.03 (18)	0.287 (50)	2647.4 (4)	0.89 (15)	1.63 (28)	0.084 (14)
1513.4 (3)	3.16 (36)	1.89 (22)	0.520 (60)	2701.6 (5)	0.83 (16)	1.57 (31)	0.076 (15)
1764.3 (3)	2.51 (29)	2.04 (24)	0.354 (41)	2756.7 (4)	1.56 (20)	3.08 (40)	0.141 (18)
1777.7 (4)	1.96 (27)	1.61 (23)	0.274 (38)	2843.1 (10)	0.43 (17)	0.90 (35)	0.038 (15)
1896.4 (3)	2.03 (26)	1.90 (24)	0.266 (34)	2860.6 (9)	0.46 (17)	0.98 (35)	0.040 (14)
2011.6 (4)	0.60 (15)	0.63 (16)	0.074 (18)	2883.1 (5)	0.77 (15)	1.67 (33)	0.067 (13)
2036.4 (4)	0.66 (16)	0.72 (17)	0.081 (19)	2904.9 (5)	0.92 (17)	2.02 (37)	0.079 (15)
2047.6 (3)	3.22 (32)	3.51 (34)	0.390 (38)	2919.0 (6)	0.60 (15)	1.32 (34)	0.051 (13)
2059.0 (6)	1.17 (25)	1.29 (27)	0.141 (30)	2934.6 (7)	0.92 (20)	2.06 (44)	0.078 (17)
2112.9 (9)	0.32 (16)	0.37 (19)	0.037 (19)	2989.0 (6)	0.85 (23)	1.98 (52)	0.071 (19)
2118.3 (6)	0.58 (18)	0.68 (21)	0.068 (21)	3000.8 (5)	1.49 (42)	3.49 (99)	0.123 (35)
2137.9 (8)	0.81 (22)	0.96 (27)	0.094 (26)	3017.3 (3)	6.32 (46)	14.96 (109)	0.520 (38)
2170.0 (6)	0.33 (13)	0.40 (17)	0.037 (15)	3056.8 (3)	2.69 (27)	6.53 (66)	0.218 (22)
2230.3 (4)	1.54 (22)	1.99 (29)	0.171 (25)	3062.6 (4)	0.92 (17)	2.23 (41)	0.074 (14)
2235.0 (6)	0.56 (21)	0.72 (27)	0.062 (23)	3098.1 (7)	0.49 (15)	1.24 (36)	0.040 (12)
2238.6 (6)	0.42 (18)	0.55 (23)	0.047 (20)	3120.3 (8)	0.28 (12)	0.70 (30)	0.022 (9)
2252.0 (6)	0.35 (13)	0.46 (18)	0.038 (15)	3134.5 (8)	0.42 (14)	1.07 (36)	0.033 (11)
2262.2 (6)	0.74 (19)	0.99 (25)	0.082 (21)	3147.9 (5)	0.27 (10)	0.69 (25)	0.021 (8)
2270.0 (7)	0.61 (16)	0.82 (21)	0.067 (17)	3152.4 (6)	0.30 (11)	0.77 (27)	0.023 (8)
2273.8 (6)	1.39 (19)	1.87 (26)	0.152 (21)	3158.5 (10)	0.31 (14)	0.80 (36)	0.024 (11)
2278.7 (6)	0.85 (15)	1.14 (21)	0.092 (17)	3184.5 (4)	2.28 (26)	6.03 (68)	0.178 (14)
2283.3 (7)	0.70 (16)	0.95 (21)	0.076 (17)	3190.6 (3)	0.36 (9)	0.96 (24)	0.028 (7)
2287.3 (10)	0.43 (14)	0.59 (20)	0.047 (16)	3198.2 (5)	0.86 (17)	2.30 (45)	0.067 (13)
2292.1 (8)	0.50 (14)	0.68 (19)	0.054 (15)	3209.8 (8)	0.27 (12)	0.74 (32)	0.021 (9)
2296.6 (4)	1.59 (19)	2.19 (27)	0.173 (21)	3228.4 (9)	1.53 (30)	4.16 (82)	0.118 (23)
2300.8 (5)	0.99 (16)	1.36 (22)	0.107 (18)	3277.6 (10)	0.50 (22)	1.40 (61)	0.038 (17)
2306.4 (3)	1.99 (21)	2.75 (29)	0.214 (22)	3281.4 (8)	0.95 (24)	2.67 (68)	0.072 (18)
2322.3 (3)	3.60 (30)	5.05 (43)	0.385 (33)	3294.1 (3)	2.72 (28)	7.68 (78)	0.205 (21)
2329.5 (3)	2.80 (26)	3.95 (37)	0.298 (28)	3331.9 (5)	1.92 (28)	5.56 (80)	0.144 (21)
2371.3 (3)	3.67 (30)	5.37 (43)	0.384 (31)	3351.7 (6)	0.27 (11)	0.78 (32)	0.020 (8)
2423.2 (4)	1.70 (24)	2.59 (36)	0.174 (24)	3385.7 (7)	1.23 (24)	3.66 (72)	0.090 (18)
2429.3 (3)	1.45 (20)	2.23 (30)	0.148 (20)	3399.7 (9)	0.44 (14)	1.32 (43)	0.032 (11)
2447.2 (6)	1.00 (20)	1.55 (31)	0.101 (20)	3412.3 (10)	0.39 (14)	1.17 (44)	0.028 (11)
2455.4 (6)	0.97 (29)	1.52 (46)	0.098 (30)	3418.3 (10)	0.46 (16)	1.40 (49)	0.033 (12)
2459.1 (4)	2.01 (33)	3.17 (52)	0.204 (34)	3427.6 (9)	0.49 (16)	1.49 (48)	0.035 (11)
2487.0 (4)	1.51 (19)	2.43 (31)	0.151 (19)	3476.2 (6)	0.48 (17)	1.51 (52)	0.034 (12)
2507.3 (6)	0.50 (14)	0.81 (23)	0.049 (14)				

Table 4.8: *Possible inelastic transitions to the first excited states of 37.133 (8) and 160.33 (5) keV in ^{121}Sb and ^{123}Sb.*

E_x (keV)	E_γ (keV)	Γ_1/Γ_0	Γ_1/Γ_0 [a)]	$g \cdot \Gamma_0$ (meV)	$B(E1)\uparrow$ ($10^{-3} e^2 fm^2$)
		^{121}Sb			
2025.7 (7)	2025.7 (7)	0.92 (31)		2.41 (74)	0.277 (85)
	1988.9 (8)				
2063.4 (5)	2063.4 (5)	0.94 (26)		2.79 (66)	0.303 (71)
	2025.7 (7)				
2280.4 (6)	2280.4 (6)	0.93 (28)		2.64 (72)	0.213 (58)
	2243.1 (7)				
2323.5 (4)	2323.5 (4)	0.81 (24)		2.07 (51)	0.157 (39)
	2286.3 (5)				
2398.8 (3)	2398.8 (3)	0.45 (4)	0.54 (20)	10.88 (88)	0.753 (61)
	2361.7 (3)				
2435.8 (3)	2435.8 (3)	1.53 (10)	< 1.85	13.17 (134)	0.870 (89)
	2398.8 (3)				
2579.2 (14)	2579.2 (14)	0.98 (52)		1.38 (76)	0.077 (42)
	2541.6 (6)				
2663.0 (7)	2663.0 (7)	1.51 (38)		3.06 (84)	0.155 (43)
	2626.1 (5)				
2690.4 (3)	2690.4 (3)	0.23 (4)		9.56 (84)	0.469 (41)
	2653.5 (6)				
2740.4 (10)	2740.4 (10)	2.26 (82)		2.63 (118)	0.122 (55)
	2703.8 (6)				
2798.8 (6)	2798.8 (6)	0.63 (26)		2.34 (70)	0.102 (30)
	2761.2 (9)				
2828.2 (5)	2828.2 (5)	0.47 (20)		4.58 (142)	0.193 (60)
	2791.9 (9)				
2835.6 (8)	2835.6 (8)	1.21 (44)		2.78 (107)	0.116 (45)
	2798.8 (6)				
2843.6 (3)	2843.6 (3)	0.10 (4)		8.21 (82)	0.341 (34)
	2806.2 (7)				
2865.2 (6)	2865.2 (6)	4.18 (166)		4.09 (194)	0.166 (79)
	2828.2 (5)				
2873.4 (9)	2873.4 (9)	1.66 (77)		2.14 (105)	0.086 (42)
	2835.6 (8)				
2911.6 (11)	2911.6 (11)	1.47 (79)		1.43 (77)	0.056 (30)
	2873.4 (9)				
2931.5 (6)	2931.5 (6)	0.33 (15)		2.61 (55)	0.099 (21)
	2895.2 (9)				
2947.3 (12)	2947.3 (12)	0.89 (54)		1.31 (75)	0.049 (28)
	2911.6 (11)				
3105.9 (12)	3105.9 (12)	1.93 (106)		1.55 (96)	0.049 (31)
	3068.9 (9)				
3116.0 (6)	3116.0 (6)	0.42 (18)		2.69 (85)	0.085 (27)
	3078.2 (10)				

continued on next page

E_x (keV)	E_γ (keV)	Γ_1/Γ_0	Γ_1/Γ_0 [a)]	$g \cdot \Gamma_0$ (meV)	$B(E1)\uparrow$ ($10^{-3} e^2 f m^2$)
3252.1 (7)	3252.1 (7)	0.47 (18)		3.17 (83)	0.088 (23)
	3215.0 (7)				
3290.3 (9)	3290.3 (9)	0.55 (14)		6.50 (139)	0.174 (37)
	3252.1 (7)				
3302.7 (6)	3302.7 (6)	1.37 (76)		1.74 (104)	0.046 (27)
	3265.9 (5)				
3313.7 (5)	3313.7 (5)	5.98 (184)		10.23 (439)	0.269 (115)
	3277.1 (3)				
3345.8 (8)	3345.8 (8)	0.59 (29)		4.23 (134)	0.108 (34)
	3308.5 (12)				
3474.2 (4)	3474.2 (4)	0.23 (11)		6.72 (125)	0.153 (28)
	3437.1 (8)				
3517.0 (11)	3517.0 (11)	0.63 (29)		6.12 (154)	0.134 (34)
	3480.5 (9)				
3677.3 (10)	3677.3 (10)	0.66 (27)		4.19 (143)	0.080 (27)
	3638.9 (8)				
3731.7 (5)	3731.7 (5)	0.96 (34)		4.98 (161)	0.092 (30)
	3693.7 (9)				
3748.9 (5)	3748.9 (5)	0.79 (32)		4.75 (149)	0.086 (27)
	3712.1 (9)				
3755.6 (7)	3755.6 (7)	1.14 (64)		3.16 (154)	0.057 (28)
	3719.2 (11)				
3792.6 (8)	3792.6 (8)	0.68 (39)		3.31 (139)	0.058 (24)
	3755.6 (7)				
3812.9 (6)	3812.9 (6)	1.63 (68)		4.57 (204)	0.079 (35)
	3775.1 (7)				
3838.1 (9)	3838.1 (9)	1.19 (64)		3.48 (181)	0.059 (31)
	3800.4 (9)				
		^{123}Sb			
1513.4 (3)	1513.4 (3)	0.56 (11)	0.81 (39)	2.95 (39)	0.813 (109)
	1353.4 (4)				
2273.8 (5)	2273.8 (5)	0.27 (13)		2.36 (41)	0.192 (33)
	2112.9 (9)				
2278.7 (6)	2278.7 (6)	0.80 (24)		2.06 (47)	0.166 (38)
	2118.3 (6)				
2423.2 (4)	2423.2 (4)	0.51 (12)		3.91 (63)	0.262 (42)
	2262.2 (6)				
2447.2 (6)	2447.2 (6)	0.50 (17)		2.33 (53)	0.152 (35)
	2287.3 (10)				
2647.4 (4)	2647.4 (4)	1.96 (32)		4.82 (98)	0.248 (50)
	2487.0 (4)				
3281.4 (8)	3281.4 (8)	0.35 (16)		3.61 (102)	0.098 (28)
	3120.3 (8)				
3294.1 (3)	3294.1 (3)	0.19 (6)		9.12 (102)	0.244 (27)
	3134.5 (8)				

[a)] See Ref. [Boot73]

4.4 Sensitivity of the NRF facility

The reported results on ^{117}Sn and ^{121,123}Sb show a high concentration of very weak γ transitions corresponding to cross sections of less than 1 eVb. It might be questioned if these γ transitions are deduced from real peaks and not from "statistical fluctuations of the continuous background". To answer this criticism it is necessary to determine the experimental sensitivity of the used NRF setup.

The sensitivity limit can be extracted from the mathematical formalism of peak fitting. The peak area A is determined by the value of the fit function y_i^{Fit} and the background counting rate y_i^{bg} in the ith channel:

$$A = \sum_{i=1}^{N} \left(y_i^{Fit} - y_i^{bg} \right)$$

with a summation over all relevant channels. Due to the narrow width of the NRF peaks, the background counting rate y_i^{bg} can be treated as being constant and:

$$A = \sum_{i=1}^{N} y_i^{Fit} - N \cdot y_i^{bg} \ . \tag{4.5}$$

The error on the fitted peak area equals:

$$\Delta(A) = \sqrt{\sum_{i=1}^{N} y_i^{Fit} + N \cdot y_i^{bg}} \ .$$

Using Eq. (4.5), the term $\sum_{i=1}^{N} y_i^{Fit}$ can be replaced:

$$\Delta(A) = \sqrt{A + 2N \cdot y_i^{bg}} \ .$$

Due to the high background counting rate, the influence of the peak area in the statistical error can be neglected:

$$\Delta(A) = \sqrt{2N \cdot y_i^{bg}} \ . \tag{4.6}$$

This relation can be used to estimate the minimal area a peak should have in order to be observed in the spectrum. For instance, in the case of a statistical precision of 30%, the minimal peak area amounts to:

$$A = \frac{\Delta(A)}{30\%} \cdot 100\% \ .$$

The obtained minimal peak area depends on the background counting rate and the peak width.

The detection limits for the NRF experiments on ^{121}Sb are shown in Fig. 4.7. The blue line describes the minimal total cross section I_S a level should have in order to observe a peak area in the NRF spectrum according to a statistical precision of 50%. The red curve denotes the detection limit for the observation of a peak with 30% error. The extracted total cross sections I_S from the ^{121}Sb are plotted as well in Fig. 4.7. To avoid overloading of the figure, 22 γ transitions corresponding to a total cross section I_S of more than 2.0 eVb have been omitted. At low energies the detection limit increases due to the quickly increasing background towards lower energies. At the higher energy part, the detection limit increases because of the fast

Figure 4.7: Detection limits for the NRF experiments on ^{121}Sb. The blue line corresponds to the minimal total cross section I_S a level should have in order to be observed with an accuracy of 50% in the recorded NRF spectrum. The detection limit according with a statistical precision of 30% is denoted by the red line.

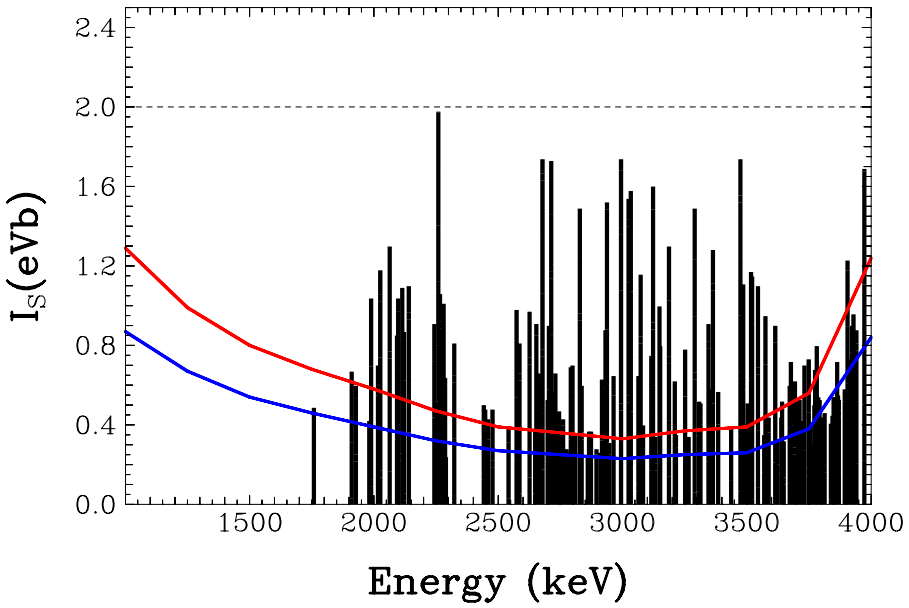

decreasing photon flux near the bremsstrahlung end point energy. It can be seen that most of the observed transitions lay above the two detection limits. A few have a total cross section lying in between. It can be concluded that the sensitivity of the present NRF facility in Stuttgart allows the observation of weak γ transitions with a total cross section I_S of the order 1 eVb in the odd-mass ^{121,123}Sb nuclei.

Chapter 5

Discussion

Since the last decades, much experimental and theoretical interest goes to the study of the coupling between two or more low-lying collective modes in spherical as well as deformed nuclei. Low-lying natural parity states in heavy nuclei have long been described in terms of phonons in collective [Bohr75], algebraic [Iach87], and microscopic models [Solo92]. The low-lying β and γ vibrations of deformed nuclei fall into this category as well as the lowest 2^+ and 3^- states of spherical nuclei. In this phonon picture, one naturally expects to observe multiphonon excitations built upon these states. However, if one attempts to construct multiphonon wave functions, the underlying single particle degrees of freedom become more and more important, leading to significant anharmonicities. It is therefore of great interest to study multiphonon excitations in order to learn about the interplay of collective and single particle degrees of freedom in complex multinucleon systems.

Within the scope of such multiphonon investigations, this Ph. D. work aims to search for mixed $[2_1^+ \otimes 3_1^-]$ two-phonon excitations in even- and odd-mass nuclei located at and close to the Z = 50 shell closure. Due to the high selectivity of the NRF method this study is limited to the two-phonon members which are accessible via $E1$ excitations. At first, these investigations will be focussed on the characteristics of the 1^- member of the $[2_1^+ \otimes 3_1^-]$ two-phonon quintuplet in the even-even ^{116,118,120,122,124}Sn isotopes. The Sn mass chain contains seven stable even-even isotopes (see Fig. 5.1) of which five ($A = 116, 118, \ldots, 124$) have reasonable natural abundances in order to get isotopically enriched targets of a few grams. The semimagic Sn nuclei form the longest chain of stable isotopes and therefore represent the most favourable and even unique case to study the mass dependence of the two-phonon $[2_1^+ \otimes 3_1^-]_{1^-}$ properties. Secondly, the question is addressed how the observed $B(E1)\uparrow$ strength of the $[2_1^+ \otimes 3_1^-]_{1^-}$ level will be fragmented and distributed when an unpaired particle (proton or neutron) couples to the $[2_1^+ \otimes 3_1^-]$ quintuplet in the adjacent odd-mass nuclei. In ^{117}Sn the case of the coupling of an unpaired mid shell neutron is met. In ^{121}Sb and ^{123}Sb, the unpaired proton is located just outside the closed Z = 50 proton shell. From core coupling models, it is expected that a particle just outside a closed shell acts more like a pure spectator than a particle halfway the shell. Although the NRF technique is ideally suited and very sensitive for the investigation of low multipolarity transitions in nuclei, the obtained experimental information will be often too sparse to allow a complete interpretation. Therefore, the (γ, γ') data will be compared to theoretical calculations

Figure 5.1: Excerpt of the table of isotopes: the Z = 50 semimagic nuclei. All depicted nuclei are stable. The nuclei surrounded by solid lines have been investigated in this work.

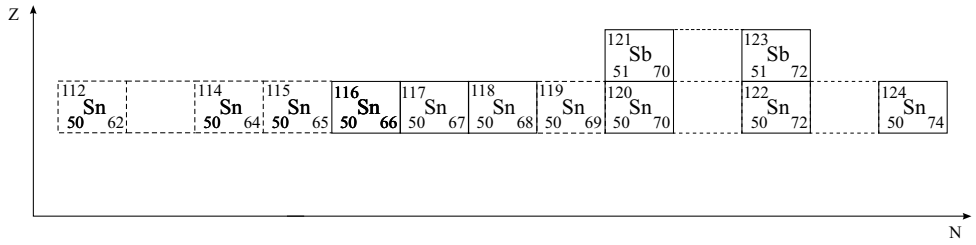

performed within the framework of the quasiparticle phonon model (QPM).

A similar systematic study has been performed on the N = 82 isotones: ^{136}Ba, ^{140}Ce, ^{142}Nd, and ^{144}Sm [Herz95b]. In all of these even-even spherical semimagic nuclei (see Fig. 5.2), two-phonon $[2^+_1 \otimes 3^-_1]_{1^-}$ states were observed. Subsequently, the fragmentation and distribution of the electromagnetic strength in the odd-mass nuclei ^{143}Nd [Zilg93, Herz95a], ^{139}La, and ^{141}Pr [Herz95c] was investigated. The latter nuclei represent a mirror-like situation compared to the odd-mass Sn nuclei. In ^{139}La and ^{141}Pr, the unpaired proton is situated between the 50 and 82 closed shells. The unpaired neutron in ^{143}Nd, is located just outside the closed major N = 82 shell. The results obtained in this work can immediately be compared to the results in these N = 82 isotones.

Figure 5.2: Extract of the table of isotopes: the N = 82 semimagic isotones.

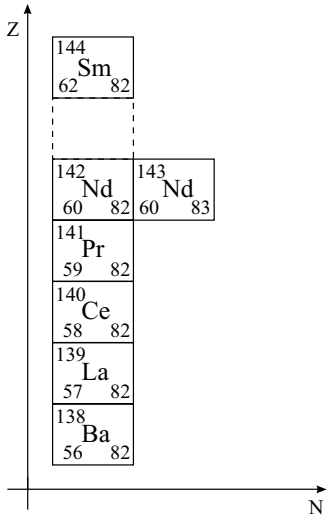

5.1 Two-phonon $[2^+_1 \otimes 3^-_1]_{1^-}$ states in the ^{116,118,120,122,124}Sn isotopes

The Sn isotopes have a spherical shape with low deformation parameters [Fult69, Lepr76]. In these nuclei, the giant dipole resonance (GDR) peaks as a single resonance at an energy of about 15.0 MeV and has a width of 4.5 MeV. The low energy level scheme of such spherical nuclei is characterised by strong collective quadrupole (2^+) and octupole (3^-) vibrational states (see Fig. 5.3). Higher lying levels exhibit properties which suggest large two- or multiphonon components in their wave functions. For instance, the properties of the two-phonon $[2^+_1 \otimes 2^+_1]$ triplet are well known in many closed and near closed shell nuclei [Bohr75] (see Fig. 5.3). Higher in excitation energy, the mixed quadrupole-octupole two-phonon $[2^+_1 \otimes 3^-_1]$ quintuplet consisting

Figure 5.3: Schematic view of the level scheme of an even-even vibrational nucleus. The low-lying level scheme is dominated by the strong quadrupole (2_1^+) and octupole (3_1^-) vibrational states. Higher in excitation energy, multiplets of states are found as a result of a coupling between the collective modes. The example of the $[2_1^+ \otimes 2_1^+]$ triplet and the $[2_1^+ \otimes 3_1^-]$ quintuplet are given.

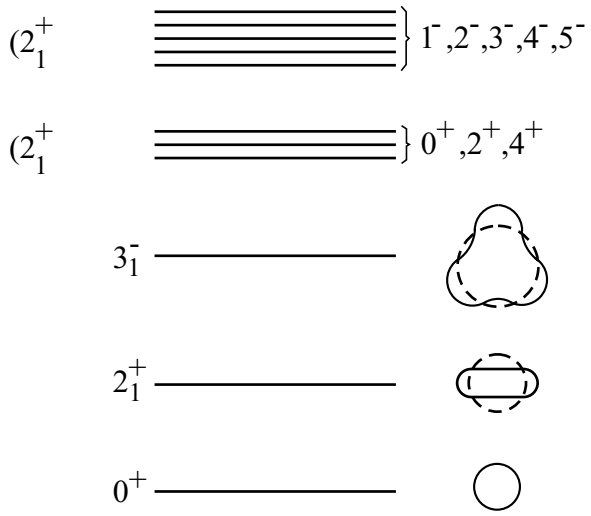

of the negative parity states $J^\pi = 1^-, 2^-, 3^-, 4^-$, and 5^- is expected to be found. The properties of this negative-parity quintuplet have already been calculated in different theoretical approaches [Lipa66, Radu70, Voge71].

Due to the high spin selectivity of the real photon probe, the NRF studies on the even-even Sn isotopes focus on the 1^- member of the two-phonon quintuplet. To interpret an observed 1^- level as being the member of a $[2_1^+ \otimes 3_1^-]$ two-phonon multiplet, four experimental signatures can be verified:

- excitation energy of the 1^- state
- decay strength of the $1^- \rightarrow 0^+_{g.s.}$ γ transition
- decay pattern of the 1^- state
- correlation between the $B(E1; 1_1^- \rightarrow 0^+_{g.s.})$ and $B(E1; 3_1^- \rightarrow 2_1^+)$ reduced $E1$ transition probabilities

5.1.1 Excitation energies and decay strength of the 1_1^- states in the even-mass Sn nuclei

In all the ^{116,118,120,122,124}Sn nuclei, one strong electric dipole transition was observed to a level around 3.3 MeV excitation energy (see Table 4.2). In Fig. 5.4a) the measured excitation energies

of these levels (black crosses) are compared to the summed energies $E_x(2_1^+) + E_x(3_1^-)$ (open crosses) of the first collective quadrupole and octupole states in the Sn nuclei. The open squares represent the energies of the first quadrupole phonons in the Sn nuclei which are known to be very stable in energy and excitation strength throughout the Sn chain. The excitation energies of the octupole phonons are indicated with open diamonds. The summed energies of the quadrupole and octupole phonon, represented by open crosses in Fig. 5.4a), would be found for a completely harmonic coupling of the phonons. The experimentally observed excitation energies (solid crosses) lay all a little lower than these summed energies but follow clearly the same tendency. The energy ratio $R_E = [E_x(1^-)]/[E_x(2_1^+) + E_x(3_1^-)]$ is about 92.6% and is very constant in the entire isotopic Sn mass chain with fluctuations of only 1%.

In Fig. 5.4b) the derived reduced electric dipole excitation probabilities are plotted. The $B(E1)\uparrow$ strengths are found to be remarkably constant ($\approx 7 \cdot 10^{-3} \cdot e^2fm^2$), showing only a flat maximum at ^{120}Sn. These strengths are larger than 1 mW.u. and are therefore among the strongest transitions in the $91 \leq A \leq 150$ mass region [Endt81].

The measured excitation energies $E_x(1_1^-)$, close to the summed energy $E_x(2_1^+) + E_x(3_1^-)$, and the enhanced $E1$ transition probability to each 1^- level, strongly favor the interpretation of these states as being the 1_1^- member of the two-phonon $[2_1^+ \otimes 3_1^-]$ quintuplet. The interpretation is facilitated by the fact that these states are the only reasonable candidates in the measured level scheme. The uniformity of their properties points to the excitation of collective modes in the Sn isotopes.

5.1.2 Decay pattern

The measured excitation energies $E_x(1_1^-)$ and the enhanced electric dipole transitions only provide a hint for an underlying two-phonon configuration of the observed 1_1^- states. In Fig. 5.5 is illustrated how a direct experimental proof for a two-phonon character of these states can be achieved by measuring their inelastic decay strengths to the quadrupole and octupole one-phonon states. In a two-phonon picture for the 1_1^- state, its $E2$ decay strength to the 3_1^- octupole one-phonon should be equal to the decay strength of the 2_1^+ quadrupole one-phonon into the ground state (both transitions are indicated by blue arrows in Fig. 5.5). This proves that in both transitions the same 2_1^+ quadrupole one-phonon has been exchanged. The same relation should hold for the $E3$ transitions from the 1_1^- state to the 2_1^+ quadrupole one-phonon and from the 3^- octupole one-phonon to the ground state, due to an exchange of the 3_1^- octupole one-phonon in both cases (indicated by green arrows in Fig. 5.5). From such an experimental study, it can really be concluded that the quadrupole and octupole vibrational phonons must be the building blocks of the 1_1^- state. In practice, the observation of the $E3$ component in the $1_1^- \rightarrow 2_1^+$ transition represents an experimental challenge as the $E1$ component will be dominating.

Unfortunately, the sensitivity of the present NRF facilities is too low to detect such weak inelastic transitions. The corresponding inelastic photons are expected in an energy region of the spectra ($[2_1^+ \otimes 3_1^-]_{1^-} \rightarrow 3_1^- \cong 1$ MeV and $[2_1^+ \otimes 3_1^-]_{1^-} \rightarrow 2_1^+ \cong 2$ MeV) where the continuous background already drastically increases due to nonresonant scattering events in the NRF target. From the obtained (γ, γ') data, only upper limits can be deduced for the possible

Figure 5.4: (a) Energies of the 2_1^+ (open squares), 3_1^- (open diamonds) one-phonon states, and the 1^- (solid crosses) two-phonon states in $^{116,118,120,122,124}Sn$ compared to the sum energies $E_x(2_1^+) + E_x(3_1^-)$ (open crosses). (b) Experimental $B(E1)\uparrow$ values for the $E1$ two-phonon excitations.

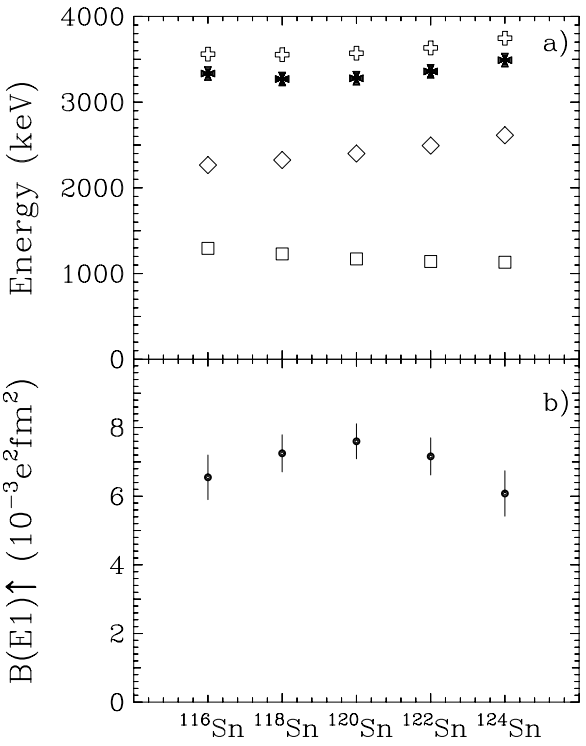

inelastic branching ratios. The upper limit values for the inelastic decay branching ratio of the $[2_1^+ \otimes 3_1^-]_{1^-} \rightarrow 2_1^+$ transition in comparison with QPM calculations for each of the investigated Sn nuclei are given in Table 5.1. The upper limits are deduced from the spectra recorded at a scattering angle of 127°, where the peak-to-background ratio is better. The minimal area A_{inel} needed to observe the inelastic decay transition in the spectrum, was estimated to be at least two standard background error deviations (see Eq. 4.6 in section 4.4). The upper limit for the inelastic decay branching ratio $\Gamma_{1_1^- \rightarrow 2_1^+}/\Gamma_0$ can immediately be estimated from the known detection efficiencies ϵ and the angular distribution functions (according with the involved spin sequence):

$$\frac{\Gamma_{1_1^- \rightarrow 2_1^+}}{\Gamma_0} = \frac{A_{inel} \cdot W_{0-1-0}(127°) \cdot \epsilon(E_{el}, 127°)}{A_{el} \cdot W_{0-1-2}(127°) \cdot \epsilon(E_{inel}, 127°)} \ .$$

The corresponding upper limit for the decay branching ratio R_{exp} expressed in terms of the reduced de-excitation probabilities is given by the relation:

$$R_{exp} = \frac{B(E1; 1_1^- \rightarrow 2_1^+)}{B(E1; 1_1^- \rightarrow 0^+)} = \frac{\Gamma_{2_1^+} \cdot E_{el}^3}{\Gamma_0 \cdot E_{inel}^3} \ . \qquad (5.1)$$

Figure 5.5: Schematic presentation of the decay pattern of $[2^+_1 \otimes 3^-_1]_{1^-}$ two-phonon states. The coloured arrows indicate which transition strengths should be equal in a two-phonon picture. For details see text.

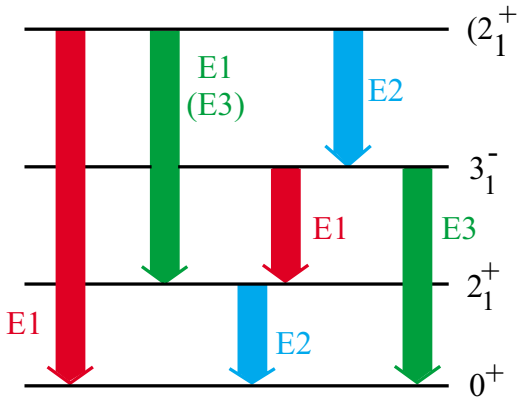

The lower experimental upper limits in Table 5.1 for the decay branchings in ^{118,120,122}Sn compared to the earlier results in ^{116,124}Sn [Gova96] are due to the higher statistical accuracy in the recent NRF measurements. The much higher background in the region of the possible $[2^+_1 \otimes 3^-_1]_{1^-} \rightarrow 3^-_1$ transition inhibits extracting a reasonable upper limit in this case.

Table 5.1: Experimental upper limits for the decay branchings of the 1^- two-phonon states to the 2^+_1 one-phonon levels compared with QPM predictions.

Isotope	E_x (1^-)	$\Gamma_{1^-_1 \rightarrow 2^+_1}/\Gamma_0$ (Exp.)	Γ_0/Γ (Exp.)	R_{exp} [a]	R_{QPM} [a]
^{116}Sn [b]	3334	≤ 0.030	≥ 0.971	≤ 0.131	0.010
^{118}Sn	3270	≤ 0.021	≥ 0.980	≤ 0.086	0.013
^{120}Sn	3278	≤ 0.017	≥ 0.983	≤ 0.064	0.035
^{122}Sn	3358	≤ 0.019	≥ 0.982	≤ 0.066	0.036
^{124}Sn [b]	3490	≤ 0.027	≥ 0.974	≤ 0.088	0.019

[a] For the definition of R see Eq. (5.1)

[b] See Ref. [Gova96]

In inelastic neutron scattering $(n, n'\gamma)$ experiments on ^{142}Nd [Belg95] it was attempted to observe inelastic transitions from the two-phonon $[2^+_1 \otimes 3^-_1]_{1^-}$ state [Metz78, Pitz90] to the one-phonon states. Inelastic neutron scattering populates levels nonselectively and hence, the decay properties of the 2^+_1 and 3^-_1 states can be determined simultaneously. Moreover, the γ ray background at the energies of the inelastic decay transitions is more than an order of magnitude lower compared to NRF spectra, resulting in a better peak-to-background ratio. In these inelastic neutron scattering experiments a decay transition from the 1^- two-phonon

candidate in ^{142}Nd to the 2_1^+ quadrupole phonon could be detected. Unfortunately, the inelastic transition from the 1^- level to the 3^- level overlapped with another γ transition and could not be extracted unambiguously.

Inelastic proton scattering $(p,p'\gamma)$ experiments represent an even better tool to investigate weak inelastic branchings in nuclei. This technique has been applied successfully on the ^{142}Nd and ^{144}Sm isotones [Wilh96, Wilh98]. In these experiments proton beam energies were adjusted to excite the $(\nu 3p_{3/2})$ isobaric analogue resonance, which allows to excite selectively negative parity states with a spin of 0 to 4. By selecting proton energy losses corresponding to an excitation energy in the vicinity of the two-phonon 1^- states in ^{142}Nd and ^{144}Sm, very clean γ ray spectra are obtained with low background. In these experiments, both inelastic γ transitions of $1^- \rightarrow 2^+$ and $1^- \rightarrow 3^-$ were observed. Comparing the coincidence counting rates of the detected "inelastic" γ rays with the coincidence counting rate of the 1^- state, proved that these transitions really accord with the excitation of the 1^- level. It was found that the decay strength of the investigated 1^- states to the octupole phonon equals within the statistical error the decay strength of the quadrupole phonon into the ground state. Hence, the most direct proof for the underlying two-phonon character of the 1^- level was established. Also the decay strength of the 1^- states to the quadrupole phonon was measured, but in this case the important $E3$ transition is masked by the much faster $E1$ component. This is a so-called "octupole $E1$ transition": an $E1$ transition accompanying the destruction of an octupole phonon.

It is interesting to compare the upper limits for the decay branching ratio $\Gamma_{1_1^- \rightarrow 2_1^+}/\Gamma_0$ obtained in this work with the $(p,p'\gamma)$ results on ^{142}Nd and ^{144}Sm [Wilh96, Wilh98]. The decay branching ratios $\Gamma_{1_1^- \rightarrow 2_1^+}/\Gamma_0$ deduced from the measured relative intensities I_γ amount to 0.037 for ^{142}Nd and 0.019 in the case of ^{144}Sm. The lowest upper limits in the ^{118,120,122}Sn isotopes, extracted from the detected (γ,γ') background are all lower than the measured branching ratio in ^{142}Nd and are equal to the ^{144}Sm case. Recently, an upper limit of the decay branching ratio $\Gamma_{1_1^- \rightarrow 2_1^+}/\Gamma_0$ was determined for the two-phonon state in ^{138}Ba and amounts to 0.038 [Herz99]. Therefore, it can be concluded that the real inelastic transitions in the Sn isotopes should maybe even weaker.

5.1.3 Correlation between the $B(E1; 1_1^- \rightarrow 0_{g.s.}^+)$ and $B(E1; 3_1^- \rightarrow 2_1^+)$ strengths

Up till now, in many heavy vibrational nuclei the $[2_1^+ \otimes 3_1^-]$ two-phonon character of the first observed 1^- state is concluded from the following observations:

- the excitation energies and the $B(E1)\uparrow$ transition strengths show a smooth mass dependence;
- the excitation energy equals within 10% the sum energy of the 2_1^+ and 3_1^- phonons;
- the $B(E1; 1^- \rightarrow 0_{g.s}^+)$ transition strength is enhanced.

Detailed information on the decay pattern of the 1_1^- state is still sparse. However, recently an additional independent signature for the two-phonon character of the 1_1^- state could be identified.

Table 5.2: Measured $E1$ transition strengths between low-lying states in vibrational nuclei. Displayed are the excitation energies of the two-phonon 1^- state and the 3^-_1 octupole phonon state and the corresponding $E1$ transition strengths to the ground state and to the 2^+_1 quadrupole phonon state. This table is taken from Ref. [Piet99a].

Nuclide	$E(1^-)$ (keV)	$B(E1;1^- \to 0^+_{g.s})$ $(10^{-3} \cdot e^2fm^2)$	Ref.	$E(3^-)$ (keV)	$B(E1;3^-_1 \to 2^+_1)$ $(10^{-3} \cdot e^2fm^2)$	Ref.
^{144}Sm	3225	6.5 (9)	[Wilh96]	1810	5.0 (7)	[Barf89]
^{144}Nd	2185	3.2 (2)	[Ecke97]	1511	1.8 (2)	[Robi94]
^{142}Nd	3425	5.8 (12)	[Wilh98, Pitz90]	2084	7.5 (35)	[Belg95]
^{140}Ce	3643	5.6 (3)	[Herz95b]	2464	6.6	[Chan91]
^{124}Sn	3490	2.0 (2)	[Gova94b]	2614	2.0 (2)	[Govo91b]
^{122}Sn	3359	2.4 (1)	this work	2493	2.2 (2)	[Govo91b]
^{120}Sn	3279	2.5 (1)	this work	2401	2.0 (2)	[Govo91b]
^{118}Sn	3271	2.4 (1)	this work	2325	2.3 (4)	[Govo91b]
^{116}Sn	3334	2.2 (2)	[Gova94b]	2266	1.7 (6)	[Govo91b]
^{106}Pd	2485	0.42 (2)	[Mats97]	2084	0.20 (9)	[Fren94]
^{88}Sr	4744	0.9 (2)	[Metz75]	2734	0.764 (4)	[Müll88]
^{52}Cr	5544	0.7 (1)	[Ende98]	4563	0.36 (6)	[Jund94]

In a completely harmonic coupling picture of the constituent phonons, the $1^-_1 \to 0^+_{g.s.}$ and the $3^-_1 \to 2^+_1$ γ transitions have a common nature: two phonons are involved simultaneously (indicated by red arrows in Fig. 5.5). For the $1^-_1 \to 0^+_{g.s.}$ decay, the quadrupole and octupole phonons are annihilated. In the $3^-_1 \to 2^+_1$ γ transition, the octupole phonon is annihilated while the quadrupole phonon is created. An empirical correlation between both two-phonon $E1$ transitions was observed recently by Pietralla [Piet99a]. In Table 5.2, the even-even vibrational nuclei are cited for which the $E1$ strength of the $1^-_1 \to 0^+_{g.s.}$ and the $3^-_1 \to 2^+_1$ transitions are known. Although these $E1$ transition strengths can differ by more than one order of magnitude for different nuclei, the ratio of the $B(E1;1^- \to 0^+_{g.s.})$ value to the $B(E1;3^-_1 \to 2^+_1)$ value remains constant within a factor of two, as illustrated in Fig. 5.6. For most even-even vibrational nuclei holds:

$$R = \frac{B(E1;1^-_1 \to 0^+_{g.s.})}{B(E1;3^-_1 \to 2^+_1)} \cong 1 \ . \tag{5.2}$$

From the observed approximate constancy of the ratio R in such a wide mass range, a common nature for the $1^-_1 \to 0^+_{g.s.}$ and the $3^-_1 \to 2^+_1$ transitions can be concluded as stated above. This correlation of $E1$ strengths can be considered as an additional support for the quadrupole-octupole coupled character of the 1^- states. The investigated Sn nuclei in this work, fit perfectly into this systematics (see red points in Fig. 5.6).

The involved $E1$ transitions were discussed quantitatively in terms of the bosonic phonon model. In this model, the phonons are treated as bosons and fulfill the boson commutation rela-

Figure 5.6: Ratio of measured low-lying $E1$ transition strengths in vibrators. For each nucleus included in Table 5.2 the $B(E1; 3_1^- \rightarrow 2_1^+)$ value is plotted versus the $B(E1; 1^- \rightarrow 0_{g.s.}^+)$ value. The red points represent the results for the ^{116,118,120,122,124}Sn studied in this work. This figure is taken from [Piet99a].

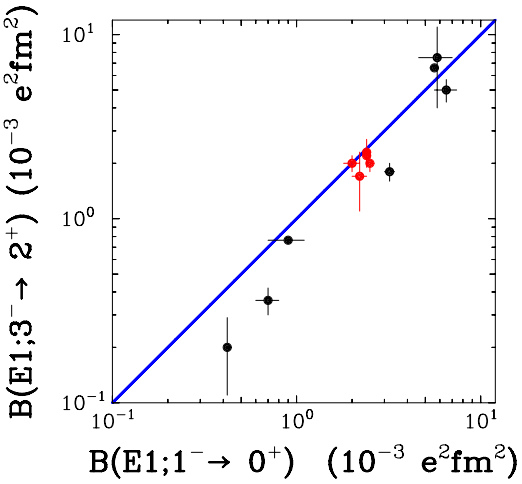

tions. Using a bosonic formulation of the quadrupole-octupole coupled $E1$ transition operator, a parameter free prediction of the ratio R was obtained:

$$R = \frac{B(E1; 1_1^- \rightarrow 0_{g.s.}^+)}{B(E1; 3_1^- \rightarrow 2_1^+)} = \frac{7}{3} \, .$$

This prediction agrees within a factor of two with the experimental deduced ratio in Eq. (5.2).

However, it was demonstrated by Ponomarev [Pono99c], that any nuclear model based on a quasiparticle random phase approximation (QRPA), taking into account the internal fermion structure of the phonons, would result for the ratio R in:

$$0 < R < \frac{7}{3} \, .$$

In this paper, it is proved that the value $R = 7/3$ corresponds to extremely collective vibrations. Therefore this value can be regarded as an unreachable upper limit. The other extreme limit is $R = 0$, corresponding to noncollective vibrations. Calculations in a first order approximation resulted in $R \cong 0.9$, close to the empirical value in Eq. (5.2).

5.1.4 Comparison with QPM calculations

The only unambiguous identification of the 1_1^- states observed in the even-mass Sn nuclei as a member of the two-phonon $[2_1^+ \otimes 3_1^-]$ quintuplet would be a direct measurement of its $E2$ and $E3$ decay transitions into the 3_1^- and 2_1^+ one-phonon states. As stated in Section 5.1.2, because of background and transition intensity considerations, this is not possible in the present NRF experiments. A theoretical approach describing in a reasonable way the experimental data

(excitation energy and decay properties) may provide with some confidence the structure of the 1^-_1 states. In fact, the direct decay of the two-phonon state into the ground state is a "forbidden" transition [Pono98a] and, thus, rather sensitive to the details of the calculations. The model to be used should prove its ability to describe multiphonon configurations. Also as shown by Heyde and De Coster [Gova94b, Heyd97] one-particle-one-hole ($1p$-$1h$) admixtures at the low-energy tail of the giant dipole resonance, into the low-lying two-phonon 1^- states appreciably change their decay properties to the ground state, indicating that the GDR phonons should be included in the model space. One of the models satisfying these demands is the quasiparticle phonon model (QPM). It has been already used to interpret the observed enhanced $E1$ strengths in the N = 82 isotones [Pono98a, Grin94].

A detailed description of the QPM formalism is out of the scope of this Ph. D. work. Technical details of the application of the QPM to the description of the properties of low-lying states in spherical nuclei can be found in [Solo92]. In this section, the main features of the QPM will be briefly discussed and some of the specific aspects of the present calculations for the tin isotopes will be given.

In QPM calculations excited states in even-even nuclei with angular momentum J and with projection M are described by a wave function including different one-, two- and three-phonon configurations:

$$\Psi^{\nu}_{JM} = \Bigg\{ \sum_{\alpha} S^{\nu}_{\alpha}(J) Q^{+}_{\alpha} \;+\; \sum_{\alpha\beta} \frac{D^{\nu}_{\alpha\beta}(J) \;\; [Q^{+}_{\alpha} \otimes Q^{+}_{\beta}]_{JM}}{\sqrt{1+\delta_{\alpha,\beta}}} + \sum_{\substack{\alpha\beta\gamma \\ I}} \frac{T^{\nu}_{\alpha\beta\gamma}(J) \;\; [[Q^{+}_{\alpha} \otimes Q^{+}_{\beta}]_{I} \otimes Q^{+}_{\gamma}]_{JM}}{\sqrt{1+\delta_{\alpha,\beta}+\delta_{\alpha,\gamma}+\delta_{\beta,\gamma}+2\delta_{\alpha,\beta,\gamma}}} \Bigg\} \, |\rangle_{ph} \; . \tag{5.3}$$

In this expression $|\rangle_{ph}$ is the wave function of the 0^+ ground state, the phonon vacuum. The Greek characters α, β and γ represent the phonon's indexes (λ, μ, i) with λ the multipolarity, μ its projection and $i = 1,\ 2,\ 3,\ \ldots$ labeling whether the phonon with quantum numbers λ^{π} has the lowest, next to lowest, etc. excitation energy. Multiphonon configurations are constructed by folding the phonon operators. The phonons, $Q^{+}_{\lambda\mu i}$, (treated as quasi-bosons) are composed of many two-quasiparticle components of a definite spin and parity λ^{π}:

$$Q^{+}_{\lambda\mu i} = \frac{1}{2} \sum_{\tau}^{n,p} \sum_{\substack{jj' \\ mm'}} \Big\{ \psi^{\lambda i}_{jj'} \; C^{\lambda\mu}_{jm \;\; j'm'} \; \alpha^{+}_{jm} \alpha^{+}_{j'm'} - (-1)^{\lambda-\mu} \varphi^{\lambda i}_{jj'} \; C^{\lambda-\mu}_{j'm' \;\; jm} \; \alpha_{j'm'} \alpha_{jm} \Big\} \; , \tag{5.4}$$

where α^{+}_{jm} (α_{jm}) is a creation (annihilation) operator of a quasi-particle on a level of an average field with quantum numbers $j \equiv |n,\ l,\ j\rangle$ and projection m. The factors ψ and φ are forward and backward amplitudes. The energy spectrum of the one-phonon excitations and their internal fermion structure is obtained by solving the quasiparticle–RPA equations. The spectrum of excited states described by the wave function in Eq. (5.3) is obtained by a diagonalization of the model Hamiltonian in the space of these states. The diagonalization also yields the contribution of one- and multiphonon configurations, with respective coefficients $S^{\nu}(J)$, $D^{\nu}(J)$, and $T^{\nu}(J)$, to the structure of each $\nu = 1,\ 2,\ 3,\ \ldots$ excited state with quantum numbers J^{π}.

The situation with low-lying 1^- states in spherical nuclei is rather different as compared to 2^+ or 3^- states (quadrupole or octupole vibrations). This is due to the fact that the first one-phonon 1^- configurations have excitation energies larger than the two- and even the three-phonon ones. Thus, although many one- and multiphonon configurations at low energies have been included in the QPM calculations, the most important ones for the description of the properties of the 1_1^- state are the two-phonon configuration $[2_1^+ \otimes 3_1^-]_{1^-}$, which has the lowest excitation energy and the one-phonon 1^- configurations at higher energies belonging to the giant dipole resonance (GDR). The traces of the last are hardly seen in the wave function of the $[2_1^+ \otimes 3_1^-]_{1^-}$ state [Pono98a] and they do not affect its excitation energy. They are only important to achieve a correct $B(E1)$ transition probability for this state. This is because the reduced matrix element of their electromagnetic excitation $\langle 1^-_{\rm GDR}||\mathcal{M}(\rm E1)||0^+_{\rm g.s.}\rangle$ is about two orders of magnitude larger as compared to the matrix element of the direct excitation of the two-phonon configuration $\langle [2_1^+ \otimes 3_1^-]_{1^-}||\mathcal{M}(\rm E1)||0^+_{\rm g.s.}\rangle$ from the ground state. Thus, even a contribution of less than 1% of the GDR phonons in the wave function of the 1_1^- state changes essentially the $B(E1)$ strength for this state. The inclusion of the high-lying GDR phonons [Gova94b] is a microscopic treatment of the phenomenologic core polarization effects for low-energy $E1$ transitions as suggested in [Bohr75].

The direct excitation of multiphonon configurations from the ground state by means of an one-body operator from the external electromagnetic field takes place due to ground state correlations in microscopic RPA theories [Voro84], resulting in a nonvanishing value of the matrix element $\langle [2_1^+ \otimes 3_1^-]_{1^-}||\mathcal{M}(\rm E1)||0^+_{\rm g.s.}\rangle$. However, there are two main reasons why the reduced matrix element $\langle [2_1^+ \otimes 3_1^-]_{1^-}||\mathcal{M}(\rm E1)||0^+_{\rm g.s.}\rangle$ is much weaker as compared to the reduced matrix element $\langle 1^-_{\rm GDR}||\mathcal{M}(\rm E1)||0^+_{\rm g.s.}\rangle$. First, the interference between different elements contributing in the $\langle [2_1^+ \otimes 3_1^-]_{1^-}||\mathcal{M}(\rm E1)||0^+_{\rm g.s.}\rangle$ transition matrix has a destructive nature while the excitation of the GDR corresponds to an exchange of collective phonons. Secondly, the direct excitation from the ground state of the two-phonon state $[2_1^+ \otimes 3_1^-]_{1^-}$ which is of isoscalar nature, occurs by a practically isovector $E1$ operator. Thus, additional destructive interference between proton and neutron parts takes place. When the main isoscalar two-phonon component $[2_1^+ \otimes 3_1^-]_{1^-}$ is coupled to these small admixtures of the isovector GDR phonons in the wave function of the 1_1^- state, destructive interference again takes place producing the core polarization effect as mentioned above. As a consequence, the $E1$ excitations to the two-phonon 1^- states of a few mW. u. are very weak if compared to the GDR photo-excitation which is of the order of 10 W. u. , however they are strong in comparison with other low-energy $E1$ transitions.

Taking into account these several destructive interference effects in describing the $B(E1)$ transition probabilities for the excitation of the 1_1^- state, it is clear that the results of the calculations are rather sensitive to their details. First of all, it is important how relevant a theoretical description of the collective properties of the 2_1^+ and 3_1^- phonons expressed by the ψ and φ amplitudes in Eq. (5.4) is for the excitation of the main two-phonon configuration of this state. For that reason, parameters of the residual interaction in the model Hamiltonian have been adjusted to reproduce the $B(E2, 0^+_{g.s.} \rightarrow 2_1^+)$ and $B(E3, 0^+_{g.s.} \rightarrow 3_1^-)$ reduced transition probabilities, known from experiment, for each of the specific nuclei using the wave function in Eq. (5.4). On the other hand, taking into account a smooth A dependence for the properties of

an average field, the same single particle spectrum for all the tin isotopes under consideration was used. The strength of the monopole pairing for neutrons has been adjusted for each nucleus to reproduce the pairing energies.

The excitation energy of the first 1^- state in respect to the sum of the energies of the first 2^+ and 3^- collective phonons is determined by two main physical effects. First of all, an anharmonicity feature of the two-phonon configuration $[2^+_1 \otimes 3^-_1]_{1^-}$ itself, which occurs due to the internal fermion structure of the phonons, results in a shift of 200–300 keV for this configuration to higher excitation energies (an interaction with other two-phonon configurations, which may also affect the position of it, is rather weak in these semimagic nuclei). The interaction of this $[2^+_1 \otimes 3^-_1]_{1^-}$ configuration with the three-phonon ones, on the other hand, results in an effect with opposite sign. That is why the inclusion of the three-phonon configuration in the wave function of the excited states in Eq. (5.4) is important for a correct description of the energy of the 1^-_1 state.

Table 5.3: Properties of the low-lying 2^+, 3^-, and 1^- levels in the even-even stable Sn isotopes. Excitation energies E_x and reduced transition probabilities $B(E\lambda)$ are compared with the results of the QPM calculations, given in brackets [ ].

	^{116}Sn	^{118}Sn	^{120}Sn	^{122}Sn	^{124}Sn
$E_x(2^+)$ (MeV)	1.294	1.230	1.171	1.141	1.132
	[1.31]	[1.23]	[1.14]	[1.13]	[1.11]
$B(E2, 0^+ \to 2^+)^{a)}$ (10^4 e^2fm^4)	0.195 (10)	0.217 (5)	0.200 (3)	0.194 (11)	0.166 (4)
	[0.20]	[0.20]	[0.20]	[0.18]	[0.17]
$E_x(3^-)$ (MeV)	2.266	2.325	2.401	2.493	2.614
	[2.25]	[2.35]	[2.42]	[2.49]	[2.65]
$B(E3, 0^+ \to 3^-)^{b)}$ (10^6 e^2fm^6)	0.127 (17)	0.115 (10)	0.115 (15)	0.092 (10)	0.073 (10)
	[0.12]	[0.12]	[0.12]	[0.089]	[0.074]
$B(E1, 3^- \to 2^+)^{a)}$ (10^{-3} e^2fm^2)	$1.67^{+0.41}_{-0.75}$	$2.28^{+0.34}_{-0.43}$	2.02 (17)	2.24 (14)	2.02 (16)
	[2.0]	[2.0]	[1.8]	[1.2]	[0.95]
$E_x(1^-)$ (MeV)	3.334	3.271	3.279	3.359	3.490
	[3.35]	[3.29]	[3.32]	[3.42]	[3.57]
$R_E = [E_x(1^-)]/[E_x(2^+) + E_x(3^-)]$	0.937	0.920	0.918	0.924	0.932
$B(E1, 0^+ \to 1^-)$ ($10^{-3}e^2fm^2$)	6.55 (65)$^{c)}$	7.20 (54)	7.60 (51)	7.16 (54)	6.08 (66)$^{c)}$
	[8.2]	[8.6]	[7.2]	[4.9]	[3.5]

$^{a)}$ From Ref. [Govo91b]
$^{b)}$ From Ref. [Spea89a]
$^{c)}$ From Ref. [Gova94b]

The QPM predictions for the 1^- two-phonon level are compared with the observed properties in the NRF measurements in the last lines of Table 5.3. The energies are in very good agreement and express the low anharmonicity. The theoretical $B(E1)\uparrow$ strength decreases with increasing neutron number of the Sn nuclei. This is not supported by the experimental data, where the $B(E1)\uparrow$ reduced excitation probabilities are found almost mass independent. The strength of the

residual interaction has been fitted to reproduce the experimental values of the $B(E2,\ 0^+_{g.s.} \rightarrow 2^+_1)$ and $B(E3,\ 0^+_{g.s.} \rightarrow 3^-_1)$ strengths. Thus, the decreasing tendency in the $E1$ transition rates for ^{122}Sn and ^{124}Sn may be traced back to the decreasing tendency in the $B(E2)$ and $B(E3)$ values as reported in Refs. [Govo91b, Spea89a]. If in disagreement with Refs. [Govo91b, Spea89a] the $B(E2)$ and $B(E3)$ values for ^{122}Sn and ^{124}Sn would remain constant, like for the other Sn isotopes, the theory would also predict a constant behaviour of the $B(E1,\ 3^-_1 \rightarrow 2^+_1)$ and $B(E1,\ 0^+_{g.s.} \rightarrow (2^+_1 \otimes 3^-_1)_{1^-})$ transition rates for all isotopes under consideration. The predicted energy of the 1^-_1 state would be even closer to its experimental value for the two heaviest isotopes because an increase of the collectivity of the 2^+_1 and 3^-_1 phonons is followed by a decrease of their energies.

5.1.5 Observation of two-phonon $[2_1^+ \otimes 3_1^-]_{1^-}$ states in other nuclei

Candidates for two-phonon $[2_1^+ \otimes 3_1^-]_{1^-}$ states were firstly proposed by Metzger from his pioneering (γ,γ') experiments on ^{142}Nd [Metz78] and ^{144}Sm [Metz76] in the seventies. The spectroscopic information on these 1^- states in the N = 82 isotones was gradually improved in later NRF experiments on ^{138}Ba [Herz95b], ^{140}Ce [Herz95b] and ^{142}Nd [Pitz90]. A survey on the systematics of the first 1^- states in the N = 82 isotones is given in Ref. [Herz95b]. The two-phonon $[2_1^+ \otimes 3_1^-]$ character of these states was concluded from their excitation energies close to the completely harmonic coupling limit $E_x(2^+_1) + E_x(3^-_1)$ and from the observed enhanced reduced electric dipole excitation probabilities. The results are summarized in Table 5.4. In comparison with the Sn isotopes, the excitation energies and the $B(E1)\uparrow$ strengths of the 1^-_1 states in the N = 82 isotones show much more variation. This is due to the higher variation in the excitation energies (mainly of the 2^+_1 one-phonon states) and strengths of the constituent phonons.

The results of a systematic study on two-phonon $[2_1^+ \otimes 3_1^-]_{1^-}$ states in the ^{110,112,114,116}Cd (Z = 48) isotopes will become available soon [Kohs00]. The Cd isotopes represent a chain of classical vibrator nuclei and hence, should exhibit multiphonon states. All the stable even-even Cd isotopes have been investigated in (γ,γ') experiments at the NRF facility in Stuttgart. Photon linear polarization measurements have been carried out on all the even-even Cd isotopes making use of the available Compton polarimeters in order to determine the parities of the strongest excited levels. The knowledge of the parities plays a crucial role in the establishment of two- and multiphonon states. From the measured experimental signatures, two-phonon $[2_1^+ \otimes 3_1^-]_{1^-}$ candidates in the even-even Cd isotopes are proposed. Moreover, energy and strength considerations indicate that also the 1^- members of the two-phonon $[2_2^+ \otimes 3_1^-]$ quintuplet and the three-phonon $[2_1^+ \otimes 2_1^+ \otimes 3_1^-]$ septuplet might have been observed [Kohs00]. Part of this work has already been published in Refs. [Geig94, Lehm00] in which candidates for two-phonon $[2_1^+ \otimes 3_1^-]_{1^-}$ states are given (see Table 5.4).

Similar to the Cd isotopes, candidates for two-phonon $[2_1^+ \otimes 3_1^-]_{1^-}$ states are found in the even-even Te (Z = 52) isotopes. The ^{124}Te isotope has been investigated in (n,γ) and (γ,γ') studies [Geor95a, Geor95b]. A strongly populated 1^- state was observed which exhibits clearly two-phonon properties. Higher in excitation energy, another 1^- state was found which significantly decays to the second 2^+ state. This 2^+_2 level has a dominant two-phonon $[2_1^+ \otimes 2_1^+]$ configuration

Table 5.4: *Possible two-phonon $[2_1^+ \otimes 3_1^-]_{1^-}$ states observed in different nuclei. The second part of this table contains 1^- states which are interpreted as candidates for a novel two-phonon excitation in deformed rare earth nuclei.*

Isotope	Energy (keV)	R_E (%)	$B(E1)\uparrow$ $(10^{-3} \cdot e^2fm^2)$	$B(E1)\uparrow$ (mW.u.)	Ref.
N = 82 region					
$^{138}_{56}Ba_{82}$	4026	93.3	12.9 (27)	2.5 (5)	[Herz95b]
$^{140}_{58}Ce_{82}$	3643	89.7	16.8 (12)	3.2 (2)	[Herz95b]
$^{142}_{60}Nd_{82}$	3425	93.6	16.2 (24)	3.1 (5)	[Pitz90]
$^{144}_{60}Nd_{84}$	2185	99.0	9.51 (63)	1.8 (1)	[Ecke97]
$^{144}_{62}Sm_{82}$	3225	92.9	18.9 (27)	3.6 (5)	[Metz76]
Z = 50 region					
$^{106}_{46}Pd_{60}$	2485	95.7	1.26 (34)	0.29 (8)	[Mats97]
$^{108}_{46}Pd_{62}$	2286	92.1	1.33 (31)	0.30 (7)	[Mats97]
$^{112}_{48}Cd_{64}$	2506	95.5	1.65 (8)	0.37 (2)	[Lehm00]
$^{114}_{48}Cd_{66}$	2456	97.6	1.92 (18)	0.42 (12)	[Geig94]
$^{116}_{50}Sn_{66}$	3334	93.7	6.55 (65)	1.43 (14)	[Gova94b]
$^{118}_{50}Sn_{68}$	3271	92.0	7.20 (54)	1.55 (12)	this work
$^{120}_{50}Sn_{70}$	3279	91.8	7.60 (51)	1.61 (11)	this work
$^{122}_{50}Sn_{72}$	3359	92.4	7.16 (54)	1.50 (11)	this work
$^{124}_{50}Sn_{74}$	3490	93.2	6.08 (66)	1.27 (14)	[Gova94b]
$^{122}_{50}Te_{70}$	2592	93.8	$3.03^{+0.63}_{-0.27}$	$0.64^{+0.13}_{-0.06}$	[Schw97]
$^{124}_{52}Te_{72}$	2747	94.9	2.26	0.47	[Geor95a, Geor95b]
$^{126}_{52}Te_{74}$	2974	97.4	1.86 (24)	0.38 (5)	[Schw97]
$^{130}_{52}Te_{76}$	3567	106.0	$0.69^{+39}_{-0.12}$	$0.14^{+0.08}_{-0.02}$	[Schw97]
N = 50 region					
$^{88}_{38}Sr_{50}$	4743	103.8	2.55 (54)	0.67 (14)	[Metz75]
Z = 28 region					
$^{58}_{28}Ni_{30}$	6027	101.6	5.8 (2)	2.00 (7)	[Bauw00]
N = 28 region					
$^{52}_{24}Cr_{28}$	5544	92.4	2.1 (4)	0.78 (15)	[Ende98]
Z = 20 region					
$^{40}_{20}Ca_{20}$	6950	0.91	4.5 (7)	1.99 (31)	[Hart00]
$^{48}_{20}Ca_{28}$	7298	0.88	18.6 (18)	7.28 (70)	[Hart00]
Deformed nuclei					
$^{150}_{60}Nd_{90}$	2414	102.9	3.0 (4)	0.55 (7)	[Pitz90]
$^{156}_{64}Gd_{92}$	2539	103.3	2.7 (7)	0.48 (12)	[Pitz89]
$^{158}_{64}Gd_{94}$	2447	106.1	1.8 (4)	0.32 (7)	[Pitz89]
$^{162}_{66}Dy_{96}$	2520	99.8	5.0 (4)	0.87 (7)	[Fried92]
$^{164}_{66}Dy_{98}$	2670	103.9	4.1 (7)	0.71 (12)	[Knei93]
$^{168}_{68}Er_{100}$	2137	98.0	1.34 (25)	0.23 (4)	[Mase96a]
$^{172}_{70}Yb_{102}$	2617	99.8	3.6 (10)	0.60 (17)	[Zilg90b]

according with quasiparticle phonon model calculations. Therefore, an underlying three-phonon $[2_1^+ \otimes 2_1^+ \otimes 3_1^-]$ configuration is adopted for the 1^- state. The proposed three-phonon $[2_1^+ \otimes 2_1^+ \otimes 3_1^-]_{1^-}$ state is situated 600 keV lower than the expected summed energy $2 \cdot E_x(2_1^+) + E_x(3_1^-)$. Therefore, the anharmonicity effects in this state are estimated to be much larger than in the two-phonon $[2_1^+ \otimes 3_1^-]_{1^-}$ states. In the (n,γ) experiments a 2^- state was populated in ^{124}Te which is believed to belong also to the three-phonon $[2_1^+ \otimes 2_1^+ \otimes 3_1^-]$ septuplet. Since the de-excitation of this level requires an $M2$ transition to the ground state, it was found to decay almost exclusively to the $[2_1^+ \otimes 3_1^-]_{1^-}$ state. From a comparison between quasiparticle phonon model calculations and the observed experimental level scheme in the ^{122,126,130}Te isotopes in (γ,γ') measurements, two-phonon $[2_1^+ \otimes 3_1^-]$ candidates were proposed [Schw97] (see Table 5.4).

The results on the Cd and Te isotopes illustrate that the strength of the two-phonon $[2_1^+ \otimes 3_1^-]_{1^-}$ states diminishes quickly when moving away from the closed Z = 50 proton shell. In the ^{106,108}Pd isotopes [Mats97], which build a transition path from spherical vibrators to deformed γ soft nuclei, 1^- states have been found which can be regarded as being the member of the two-phonon $[2_1^+ \otimes 3_1^-]$ quintuplet and having an $E1$ excitation strength similar to the Cd isotopes. The same effect of a reduction of the enhanced electric dipole strength towards the open shell, was observed in NRF studies on ^{144}Nd [Ecke97] with two neutrons outside the major N = 82 shell (see Table 5.4).

The available experimental information on two-phonon $[2_1^+ \otimes 3_1^-]_{1^-}$ states strongly reduces to lighter nuclei. The decreasing collectivity of the constituent phonons in these nuclei and the expectation of the two-phonon 1^- states in a region where also 1^- one-phonon levels occur, hamper the determination of the underlying configuration. As a consequence, about three good candidates for 1^- states with an underlying two-phonon configuration were found in ^{92}Mo by our NRF group. On the other hand, NRF experiments on ^{88}Sr revealed unexpectedly a possible positive parity for the 4742 keV level [Kaub00], a long standing two-phonon candidate proposed by Metzger [Metz75]. However, a more accurate parity assignment is required as the strength of the 4742 keV level fits perfectly into the systematics presented in paragraph 5.1.3. In ^{58}Ni one $[2_1^+ \otimes 3_1^-]_{1^-}$ candidate was recently proposed [Bauw00]. The semimagic nucleus ^{52}Cr [Ende98] and the doubly magic ^{40}Ca and ^{48}Ca [Hart00] nuclei represent the lightest nuclei in which a 1^- state was found with a propable two-phonon configuration. The strong $E1$ strength in ^{48}Ca is due to the admixture of fragments of the $E1$ pigmy resonance which are close in energy.

Interesting features of the first excited 1^- states were encountered in systematic investigations of the ^{144,148,150,152,154}Sm and ^{142,144,146,148,150}Nd isotonic chains. The excitation energy of the observed 1_1^- levels follow strongly the decreasing trend of the summed energies $E(2_1^+) + E(3_1^-)$ with increasing neutron number. This is mainly due to the energy of the first quadrupole phonon which drops quickly as the neutron number increases corresponding to a reduction in rigidity of the nucleus. The reduced dipole excitation probabilities firstly decrease till ^{146}Nd and ^{148}Sm, having both a neutron number of 86, and then rise again further away from the closed N = 82 shell to a value of about 4 mW.u. (which is about the same as in the spherical nuclei), indicating the changes in the underlying structure with increasing deformation of the nucleus. Additional credence for this double humped structure of the $B(E1)\uparrow$ strength as function of the neutron number has been given in a survey article on the lowest observed 1_1^- states in the A $\simeq$ 130 – 200

mass region [Fran98]. For the spherical nuclei in the vicinity of the neutron closed shell, the 1^- states stem from a coupling of the collective vibrational quadrupole and octupole phonons as stated above. In the deformed nuclei, these 1^- states are the head of a $K = 0$ rotational band built upon the coupling of the octupole vibration to the static quadrupole deformed core. Higher in excitation energy in the deformed rare earth nuclei, 1^- states have been detected which can be interpreted as candidates for a novel two-phonon excitation [Knei93]. The 1^- levels are expected to arise from a coupling of the $(J = 3^-, K = 1)$ octupole vibration and the $(J = 2^+, K = 2)$ γ vibration. These 1^- states were predicted by Donner and Greiner in their collective model [Donn66]. The two-phonon $[2^+_\gamma \otimes 3^-_{K=1}]_{1^-}$ states can be excited due to the coupling of the giant dipole resonance to the octupole vibration. For the excitation energies, the following relation was deduced [Knei93]:

$$E^{K=1}_{2\mathrm{ph}} = E^{K=1}_{\mathrm{oct}} + E^{K=2}_{\gamma}(2^+)$$

In Table 5.4 candidates for this type of two-phonon excitations in deformed rare earth nuclei from energy considerations are listed. In addition, these 1^- levels exhibit an uncommon decay pattern compared to the Alaga rules [Alag55], which may provide a hint for a possible K-mixing [Zilg90a]. As can be seen in Table 5.4, the energy rule is fulfilled for all proposed levels.

The experimental information about the other members of the two-phonon $[2^+_1 \otimes 3^-_1]$ quintuplet is still very sparse. Using the gamma-ray induced Doppler broadening (GRID) technique, the lifetimes of the 3^-_1, 5^-_1, and 1^-_1 states in ^{144}Nd [Robi94] could be extracted. The $E2$ decay rates in the $1^-_1 \rightarrow 3^-_1$ and $5^-_1 \rightarrow 3^-_1$ transitions are close to the $E2$ decay strength of the quadrupole phonon, in spite of the large errors. The $E3$ decay strength of $5^-_1 \rightarrow 2^+_1$ transition is similar to the $E3$ decay strength of the octupole phonon. The consistency of the measured decay strengths with the expected decay pattern of quadrupole octupole coupled states, favour an underlying two-phonon configuration.

In multiphonon excitation investigations, it is also of interest to observe two-phonon states belonging to the $[3^-_1 \otimes 3^-_1]$ quartet $(J^\pi = 0^+, 2^+, 4^+, 6^+)$. However, these studies are hampered by the lower excitation cross sections for these states. The most outstanding nuclei to search for such coupled octupole-octupole surface vibrations are the ^{146}Gd and ^{208}Pb nuclei. Both nuclei are soft to octupole deformation and as a consequence the first excited state is the 3^- collective octupole vibration. Therefore, in these nuclei the two-phonon $[3^-_1 \otimes 3^-_1]$ members are expected to be the lowest multiphonon states. The search for two-phonon $[3^-_1 \otimes 3^-_1]$ excitations in the doubly magic nucleus ^{208}Pb (Z = 82, N = 126) has a long history. The first breakthrough was achieved in $(n, n'\gamma)$ measurements which demonstrated an underlying two-phonon $[3^-_1 \otimes 3^-_1]$ character of a known 0^+ state in ^{208}Pb [Yeh96]. In these experiments, a cascade of two $E3$ transitions was observed which is a characteristic feature of two-phonon octupole excitations. It was the first time that an $E3 - E3$ cascade was detected in a nucleus outside the N = 82 region as well as the first $E3 - E3$ cascade leading directly to the ground state of an even-even nucleus. In a further analysis of these $(n, n'\gamma)$ measurements, levels with a spin assignment of 4^+ and $(2^+, 4^+)$ were proposed as members of the octupole-octupole quartet [Yeh98]. The arguments are based on excitation energy considerations and the observed fast "octupole $E1$ transitions" to the 3^- octupole phonon, which are comparable to "octupole $E1$ decays" of octupole-coupled states in

the neighbouring odd-mass nuclei. A theoretical analysis performed within the quasiparticle phonon model revealed interesting results on the fragmentation of the two-octupole phonon quartet in ^{208}Pb [Pono99b]. While the 0^+ and 4^+ members remain practically pure, the 2^+ member is fragmented over three states of which one level carries the main fraction. This picture changes completely for the 6^+ member which was found to be highly fragmented. The observed theoretical fragmentation might be an explanation for the failure to detect the $[3^-_1 \otimes 3^-_1]_{6^-}$ level in heavy ion Coulomb excitation experiments. This result is supported by data obtained in Coulomb excitation experiments [Vett98]. In these experiments, the lowest lying 6^+ state was found to be populated with a $B(E3)\uparrow$ strength which accounts for 20% of the harmonic value. No other traces of the 6^+ member were found at higher energies with a detection limit of 15% at 5.2 MeV and 100% at 6.0 MeV. The QPM studies [Pono99b] also put the method of detecting "fast octupole $E1$ transitions" as a signature of two-octupole phonon members, used in the $(n, n'\gamma)$ investigations [Yeh98], into question. Since QPM calculations for pure one- and two-phonon configurations revealed comparable $E1$ transition strengths between one-phonon states, the use of this method is highly questionable.

Nonetheless the ^{146}Gd nucleus reveals many of the features of a closed shell doubly magic nucleus, experimental information about the position of the two-octupole phonon quartet is still lacking. Candidates for the 4^+ and 6^+ members emerged from in-beam γ ray and conversion electron spectroscopy following the ^{144}Sm$(\alpha, 2n)$ reaction at 25.7 MeV [Yate86]. Additional conversion electron measurements following the ^{144}Sm$(\alpha, 2n)$ and ^{144}Sm(^{3}He,n) reactions revealed some candidates for the 0^+ member [Yate87]. However, it should be stressed that the nature of these states could not be unambiguously determined in these experiments.

More complex configurations of stretched octupole $[\nu^2 \otimes 3^-_1 \otimes 3^-_1]$ two-phonon states have been found in the ^{144}Nd [Barg95], ^{144}Sm [Gate90, Gate93], ^{146}Sm [Barg95], and ^{148}Gd [Luna84, Piip90, Piip93] nuclei.

At the end of this section, it should be stressed that the given two-phonon 1^- states in Table 5.4 are compiled from a lot of NRF work carried out in this region. As remarked in the previous sections, NRF experiments on their own can never provide a complete certainty about their two-phonon character. In some cases, even the parity of the $J = 1$ states was not established. However, the consistent systematics of the obtained results, from excitation energy considerations and enhanced electric dipole transition strengths, in such a broad mass range and the good agreement with theoretical calculations provide confidence for a possible two-phonon structure.

5.2 One-phonon 2^+ states in the ^{116,118,120,122,124}Sn isotopes

Besides the 1^- two-phonon states and in addition to the well known collective 2^+_1 quadrupole one-phonon states (see e.g. the results of Coulomb excitation experiments [Spea89b, Jons81, Back81]) several other 2^+ states of lower collectivity were observed in the Sn isotopes below an excitation energy of 4 MeV (see Table 4.2). Since in the NRF experiments on the even-mass Sn isotopes the scattering intensities for electric quadrupole transitions are about one order of magnitude weaker than the electric dipole ones, the NRF method allows to study collective and weakly collective

2^+ states with a one-phonon nature. This was demonstrated recently by the investigation of the mixed symmetry one-phonon 2^+_{ms} state in ^{136}Ba [Piet98b] and ^{94}Mo [Piet99b]. The observation of two-phonon 2^+ states in NRF experiments is not expected, because the corresponding scattering intensities are lying below the sensitivity of the setup.

In Table 5.5 and the bottom part of Fig. 5.7, the observed reduced quadrupole excitation probabilities $B(E2)\uparrow$ between 2 and 4 MeV in the different Sn isotopes are presented, taking into account the known branching ratios (see Section 4.1). This energy interval was chosen to eliminate the influence of the dominating 2^+_1 state. The total $E2$ strength in this energy region is about an order of magnitude weaker than for the 2^+_1 state and is nearly constant throughout the Sn isotopic chain.

Table 5.5: *Total B(E2)↑ strengths in the Sn isotopes between 2 and 4 MeV. The experimental data are compared with the results of QPM calculations.*

Isotope	$\sum_{2<E<4MeV} B(E2)\uparrow$ (e^2fm^4) (γ, γ')	$\sum_{2<E<4MeV} B(E2)\uparrow$ (e^2fm^4) QPM
^{116}Sn[a)]	143 (19)	203
^{118}Sn	151 (20)	226
^{120}Sn	283 (57)	240
^{122}Sn	236 (37)	237
^{124}Sn[a)]	309 (45)	217

[a)] See Ref. [Gova94b]

According with the spherical vibrator model, the first 2^+_1 state is highly collective with a large $B(E2)\uparrow$ strength of about 2000 e^2fm^4. The QPM wavefunction in Eq. (5.3) of this state consists for 96–99% of the first quadrupole RPA phonon. Its transition charge density is characterized by a surface peak typical for collective low-lying states and is in a good agreement with the experimental one [Wise92]. The QPM predicts for each Sn isotope another, however less collective, one-phonon 2^+ state with an energy between 3.0 and 3.2 MeV and a $B(E2)\uparrow$ strength of about 120–150 e^2fm^4. The other 2^+ phonons with an energy less than 5 MeV are noncollective (i.e. are practically pure two-quasiparticle configurations). Thus, their properties mainly depend on the average field used in the calculation and not on the strength of the residual interaction.

The QPM calculated $B(E2)$ strength distribution over the low-lying 2^+ excited states is determined by the one-phonon components of the wave function Eq. (5.3). It is compared to the experimental results in Table 5.5 and Fig. 5.7. The contribution of the two-phonon components to the reduced transition probability for direct excitation of the 2^+ states from the ground state does not exceed a few percent of the total $E2$ one-phonon strength for the energy interval between 2 and 4 MeV. Nevertheless, two-phonon configurations cannot be neglected in the description of the characteristics of the low-lying 2^+ states since their role is essential to achieve the correct

Figure 5.7: Comparison between the QPM calculated (top) and experimentally observed (bottom) $B(E2)\uparrow$ strengths for 2^+ states between 2 and 4 MeV in the even-mass Sn isotopes.

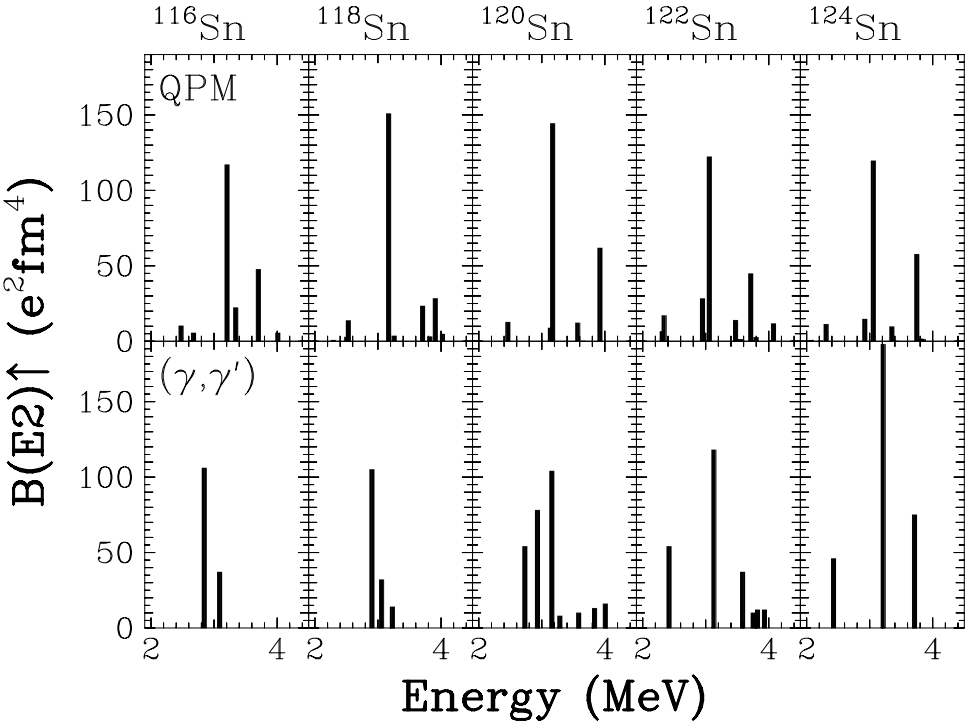

$E2$-strength fragmentation. A small admixture of one-phonon components stemming from the isoscalar giant quadrupole resonance does not change appreciably the total $E2$ strength in this energy region. The general agreement of the QPM predictions with experimental findings in both the $E2$ strength fragmentation and the total amount of strength is rather good.

5.3 Particle two-phonon states in ^{117}Sn, and ^{121,123}Sb

As a natural extension of the systematic investigations on the even-even spherical vibrational Sn nuclei, the question arises how the observed enhanced electric dipole excitation strength of the two-phonon $[2^+_1 \otimes 3^-_1]_{1^-}$ states fragments over several levels of a coupled particle two-phonon multiplet in the odd-mass adjacent nuclei. In such a study, the experimental technique and the theoretical model should meet some requirements. In the first place, the experimental probe should be very selective in the excitation of levels because of the high level density in odd-mass nuclei. The number of the involved levels in the odd-mass nucleus increases drastically compared to the even-even neighbouring nucleus: in the odd-mass nucleus levels with a spin equal $J_0 - 1$, J_0, and $J_0 + 1$ can be populated via dipole excitations from the ground state with spin J_0.

Quadrupole transitions will excite levels with a spin between J_0-2 and J_0+2. The real photon probe is such a selective experimental tool. Using an intensive bremsstrahlung source only dipole and to a much lesser extent also electric quadrupole excitations will be induced. Secondly, the theoretical model should be able to distinguish between the degrees of freedom of the collective phonons and the additional particle degrees of freedom which open extra possible excitation channels and which have no counterparts in the even-even nuclei.

Electric dipole excitations to a particle $[2_1^+ \otimes 3_1^-]$ two-phonon multiplet were for the first time identified in ^{143}Nd [Zilg93, Herz95a]. In the energy region between 2.8 and 3.8 MeV, 13 levels were observed for which an underlying particle two-phonon $f_{7/2} \otimes [2_1^+ \otimes 3_1^-]$ structure was suggested. The observed fragmentation and $B(E1)\uparrow$ strength distribution could be reproduced in a phenomenological simple core coupling model based on quadrupole-quadrupole coupling [Herz95a]. Moreover, the summed experimental $B(E1)\uparrow$ strength between 2.8 and 3.8 MeV agrees within the statistical error with the known $B(E1)\uparrow$ strength of the two-phonon $[2_1^+ \otimes 3_1^-]_{1^-}$ state in the neighbouring even-mass ^{142}Nd nucleus. It was concluded that the unpaired neutron in its $f_{7/2}$ orbital, outside the closed major N = 82 shell, couples extremely weakly to the two-phonon $[2_1^+ \otimes 3_1^-]$ quintuplet and plays the role of a pure spectator. Later on, similar NRF experiments performed on ^{139}La and ^{141}Pr [Herz95c, Herz95d] revealed also a large fragmentation of the electric dipole strength, but in both cases about 40% of the two-phonon $B(E1)\uparrow$ strength in the neighbouring even-mass ^{138}Ba, ^{140}Ce and ^{142}Nd [Herz95b] nuclei was observed. In ^{139}La and ^{141}Pr the odd proton in the partly filled shell couples more strongly to the two-phonon quintuplet. The phenomenological simple core coupling model, which was very successful in the ^{143}Nd case, failed to explain the high fragmentation and distribution of the $E1$ strength in ^{139}La and ^{141}Pr and the situation in these odd-mass nuclei was not well understood. Therefore it was interesting to repeat this kind of investigations in the Z = 50 region where the odd-mass nuclei ^{117}Sn and ^{121,123}Sb were chosen to search for the fragments of a particle two-phonon multiplet.

5.3.1 Particle two-phonon states in ^{117}Sn

The odd-mass ^{117}Sn nucleus was chosen to investigate the fragmentation of the two-phonon $B(E1)\uparrow$ strength from its even-mass ^{116}Sn and ^{118}Sn neighbours. In ^{117}Sn, the unpaired neutron is situated halfway between the major N = 50 and 82 shells. As an interesting property, the ground state spin J_0^π of $1/2^+$ limits the possible dipole excitations to levels with a spin $J = 1/2$ or $3/2$ and electric quadrupole excitations can only occur to states with a spin and parity J^π of $3/2^+$ and $5/2^+$.

According with the phenomenological core coupling model [Zilg93, Herz95a], the level scheme for ^{117}Sn can be obtained from the coupling of the unpaired $3s_{1/2}$ neutron to the ^{116}Sn core. This is schematically shown in Fig. 5.8. Each level in ^{116}Sn (except for $J = 0$ levels) gives rise to two new levels due to the spin 1/2 of the unpaired neutron. The low-lying level scheme of ^{116}Sn is dominated by the strong quadrupole (2^+) and octupole (3^-) vibrational states, typical for a spherical semimagic nucleus. The coupling of the $3s_{1/2}$ neutron to the first 2^+ state in ^{116}Sn results in two new levels $[3s_{1/2} \otimes 2_1^+]_{3/2^+}$ and $[3s_{1/2} \otimes 2_1^+]_{5/2^+}$ which can be excited in NRF via $M1$ and $E2$ transitions (solid lines in Fig. 5.8). The similar doublet consisting of

the $[3s_{1/2} \otimes 3^-_1]_{5/2^-}$ and $[3s_{1/2} \otimes 3^-_1]_{7/2^-}$ states requires $M2$ and $E3$ excitations which are not observable in NRF (dashed lines in Fig. 5.8). The aim of the NRF experiment on ^{117}Sn was to search for levels belonging to the $3s_{1/2} \otimes [2^+_1 \otimes 3^-_1]$ multiplet which can be populated via electric dipole transitions. When the quadrupole-octupole coupled two-phonon quintuplet is built on top of the $1/2^+$ ground state, a multiplet of 10 negative parity states is obtained of which 3 levels can be excited via $E1$ transitions (solid lines in Fig. 5.8). In this simple model, these three transitions carry the complete $B(E1)\uparrow$ strength of the two-phonon $[2^+_1 \otimes 3^-_1]_{1^-}$ level in ^{116}Sn. In Fig. 5.9b the obtained total scattering cross sections I_S for the photo-excited levels in ^{117}Sn (with exclusion of the lines which are probable due to inelastic scattering given in Table 4.5) and in its even-even neighbours ^{116}Sn (Fig. 5.9a) and ^{118}Sn (Fig. 5.9d) are plotted. The total scattering cross section for the excitation of the two-phonon $[2^+_1 \otimes 3^-_1]$ states in ^{116}Sn and ^{118}Sn has been reduced by a factor of 3. A strong fragmentation of the electromagnetic strength has been observed in ^{117}Sn compared to its even-even neighbours. It is already clear from the observed fragmentation of the strength that a phenomenological core coupling model, which was successful in describing the observed strength in ^{143}Nd [Zilg93, Herz95a], will be insufficient in the ^{117}Sn case.

From an experimental point of view, a first tool which can be used to catch a glimpse of the possible fragments of the $3s_{1/2} \otimes [2^+_1 \otimes 3^-_1]$ particle two-phonon multiplet, exists in the assumption that all the observed transitions in ^{117}Sn have a pure $E1$ character. By comparing the summed reduced dipole excitation strength in an arbitrary energy region around the two-phonon level of the even-even adjacent nuclei, one can get a hint for the underlying configuration. In Fig. 5.9b a resonance-like structure is observed between 2.7 and 3.6 MeV. The total summed $B(E1)\uparrow$ strength in this region amounts to 5.59 (64) $10^{-3} \cdot e^2fm^2$ or 85 (13) – 77 (14)% of the two-phonon $B(E1)\uparrow$ strength in the neighbouring nuclei ^{116}Sn and ^{118}Sn. This value is considerably higher than in the case of ^{139}La and ^{141}Pr where about 40% was observed. However, due to the rough assumptions made (all transitions having a pure $E1$ character), it is impossible to come to a definite conclusion.

The only direct experimental proof whether a level belongs to a particle two-phonon multiplet can be achieved by measuring the $E2$ decays as it was done in the N = 82 even-even nuclei to prove the two-phonon nature of the 1^-_1 state (see section 5.1.2). For instance, a good case would be the measurement of the $E2$ strength of the transition $3s_{1/2} \otimes [2^+_1 \otimes 3^-_1]_{1/2^-} \rightarrow [3s_{1/2} \otimes 3^-_1]_{5/2^-}$. However, the absolute values of the electromagnetic excitation strength are that low in odd-mass nuclei for each specific state that such an observation is not expected in the nearest future.

Due to a lack of spin and parity information of the photo-excited levels in ^{117}Sn in our NRF experiment and due to a lack of experimental data from other investigations [Blac87], it is needed to turn to a more elaborated theoretical interpretation to get more insight.

5.3.1.1 QPM formalism for odd-mass nuclei

As was shown in section 5.1.4 the quasiparticle phonon model (QPM) was already successful in describing the position and the $E1$ excitation probability of the lowest 1^-_1 states in the even-even $^{116-124}$Sn isotopes. This state has a two-phonon character with a contribution of the $[2^+_1 \otimes 3^-_1]_{1^-}$

Figure 5.8: Schematic level scheme for the odd-mass ^{117}Sn nucleus and the even-even core nucleus ^{116}Sn. The level scheme for ^{117}Sn can be obtained in a phenomenological simple core coupling model by coupling the $3s_{1/2}$ neutron to the even-even ^{116}Sn neighbour. The solid lines represent states which can be excited in NRF via $E1$, $M1$, and $E2$ transitions. The dashed lines correspond to states which will be not populated.

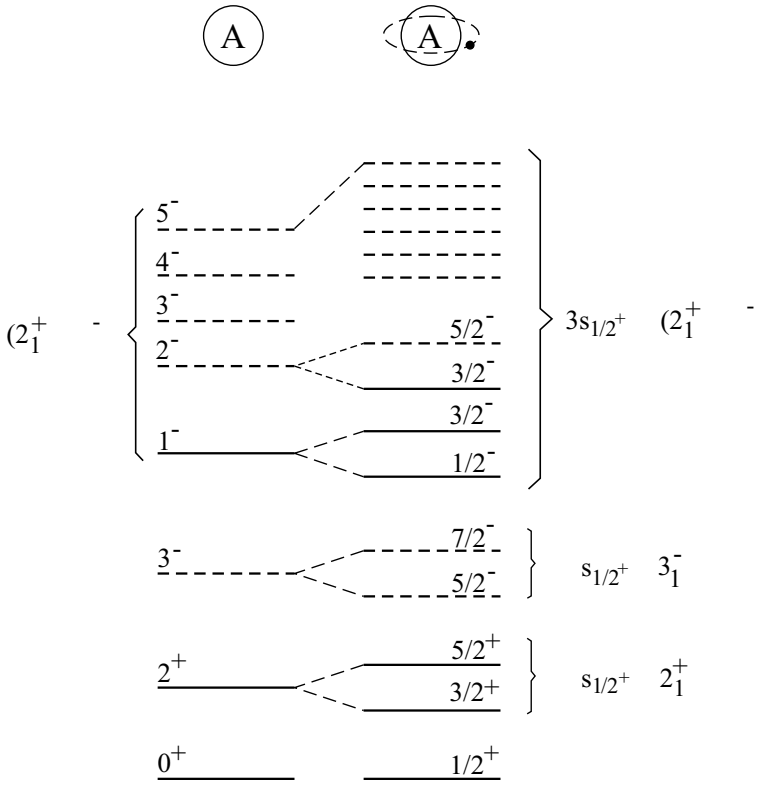

configuration of 96-99%. For odd-mass nuclei, this model was used to describe the fragmentation of deep-lying hole and high-lying particle states [Vdov85, Gale88] and the photo-production of isomers [Pono90, Hube93, Carr93]. It has already been applied to calculate the absolute amount of strength in ^{115}In [Cose95]. For the first time, it was extended to describe and understand the high fragmentation of the electromagnetic strength and the distribution of the $B(E1)\uparrow$, $B(M1)\uparrow$, and $B(E2)\uparrow$ strength in the energy region below 4 MeV.

General ideas about the QPM and its formalism to describe the excited states in odd-mass spherical nuclei with a wave function which includes up to "quasiparticle $\otimes$ two-phonon" configurations are presented in review articles [Vdov85, Gale88]. For this work, the QPM was extended by including "quasiparticle $\otimes$ three-phonon" configurations as well [Pono99d, Brys99]. A Woods-Saxon potential is used in the QPM as an average field for protons and neutrons. Phonons of different multipolarities and parities are obtained by solving the RPA equations with a separable form of the residual interaction including a Bohr-Mottelson form factor. The

Figure 5.9: Total integrated photon scattering cross sections I_S observed in ^{117}Sn b) centered between those observed in its even-even neighbours ^{116}Sn a) and ^{118}Sn d). The integrated elastic photon scattering cross sections calculated within the QPM are included in panel c) for comparison. The lines marked by a triangle correspond to levels with a 3/2 spin. The squares in b) represent levels with a (1/2, 3/2) spin, while in c) they correspond to 1/2 spins only.

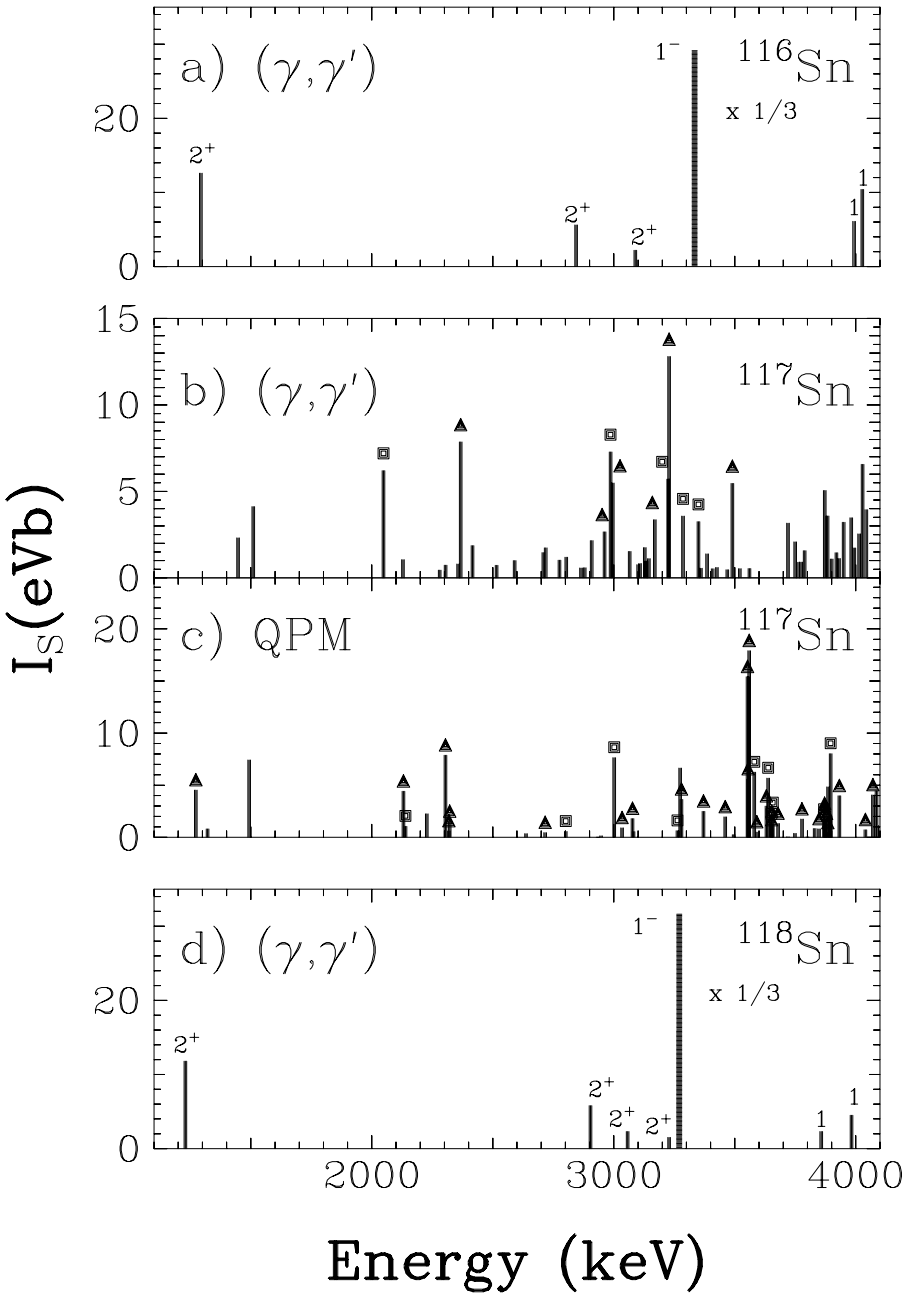

single-particle spectrum and phonon basis are fixed from calculations in the neighbouring even-even nuclear core, i.e. in ^{116}Sn if the ^{117}Sn nucleus is considered.

In the present calculations the wave functions of the ground state and the excited states are mixtures of different "quasiparticle $\otimes$ N-phonon" ($[qp \otimes Nph]$) configurations, where $N = 0$, 1, 2, 3:

$$\Psi^{\nu}(JM) = \Bigg\{ C^{\nu}(J)\alpha^{+}_{JM} + \sum_{j\beta_1} S^{\nu}_{j\beta_1}(J)[\alpha^{+}_{j} Q^{+}_{\beta_1}]_{JM} + \sum_{j\beta_1\beta_2} \frac{D^{\nu}_{j\beta_1\beta_2}(J)[\alpha^{+}_{j} Q^{+}_{\beta_1} Q^{+}_{\beta_2}]_{JM}}{\sqrt{1+\delta_{\beta_1\beta_2}}} + \sum_{j\beta_1\beta_2\beta_3} \frac{T^{\nu}_{j\beta_1\beta_2\beta_3}(J)[\alpha^{+}_{j} Q^{+}_{\beta_1} Q^{+}_{\beta_2} Q^{+}_{\beta_3}]_{JM}}{\sqrt{1+\delta_{\beta_1\beta_2}+\delta_{\beta_1\beta_3}+\delta_{\beta_2\beta_3}+2\delta_{\beta_1\beta_2\beta_3}}} \Bigg\} |\rangle_{g.s.} \qquad (5.5)$$

where the coefficients C, S, D, and T describe the contribution of each configuration to the norm of the wave function. The following notations α^{+} and Q^{+} are used for the coupling between the creation operators of quasiparticles and phonons [Brys99]:

$$[\alpha^{+}_{j} Q^{+}_{\lambda i}]_{JM} = \sum_{m\mu} C^{JM}_{jm\lambda\mu} \alpha^{+}_{jm} Q^{+}_{\lambda\mu i} \ ,$$

$$[\alpha^{+}_{j} Q^{+}_{\beta_1} Q^{+}_{\beta_2} Q^{+}_{\beta_3}]_{JM} = \sum_{\lambda_1\lambda_2} [\alpha^{+}_{j} [Q^{+}_{\beta_1} [Q^{+}_{\beta_2} Q^{+}_{\beta_3}]_{\lambda_1}]_{\lambda_2}]_{JM} \ ,$$

$$[Q^{+}_{\lambda_1 i_1} Q^{+}_{\lambda_2 i_2}]_{\lambda\mu} = \sum_{\mu_1\mu_2} C^{\lambda\mu}_{\lambda_1\mu_1\lambda_2\mu_2} Q^{+}_{\lambda_1\mu_1 i_1} Q^{+}_{\lambda_2\mu_2 i_2}$$

where C are Clebsh-Gordon coefficients. Quasiparticles are characterized by their shell quantum numbers $jm \equiv |nljm\rangle$ with a semi-integer value of the total angular momenta j. Phonons with quantum numbers $\beta \equiv |\lambda\mu i\rangle$ are linear superpositions of two-quasiparticle configurations [Brys99]:

$$Q^{+}_{\lambda\mu i} = \frac{1}{2} \sum_{\tau}^{n,p} \sum_{jj'} \left\{ \psi^{\lambda i}_{jj'} [\alpha^{+}_{j} \alpha^{+}_{j'}]_{\lambda\mu} - (-1)^{\lambda-\mu} \varphi^{\lambda i}_{jj'} [\alpha_{j'} \alpha_{j}]_{\lambda-\mu} \right\} \ . \qquad (5.6)$$

The spectrum of phonon excitations is obtained by solving the RPA equations for each multipolarity λ which is an integer value. The RPA equations also yield the forward (backward) $\psi^{\lambda i}_{jj'}$ ($\varphi^{\lambda i}_{jj'}$) amplitudes. The phonon's index i is used to distinguish between phonon excitations with the same multipolarity but with a difference in energy and structure. The RPA equations yield both, collective (e.g. 2^{+}_{1} and 3^{-}_{1}), and weakly collective phonons. The latter correspond to phonons for which some specific two-quasiparticle configuration is dominant in Eq. (5.6) while for other configurations $\psi^{\lambda i}_{jj'}, \varphi^{\lambda i}_{jj'} \approx 0$.

When the second, third, etc. terms in the wave function of Eq. (5.5) are considered, phonon excitations of the core couple to a quasiparticle at any level of the average field, not only at the ones with the quantum numbers J^{π} as for a pure quasiparticle configuration. It is only necessary that all configurations in Eq. (5.5) have the same total spin and parity. To achieve a correct position of the $[qp \otimes 2ph]$ configurations, which are of special interest in these studies, $[qp \otimes 3ph]$ configurations are important. The excitation energies and the contribution of the different components from the configuration space to the structure of each excited state (i.e. coefficients C, S, D, and T in Eq. (5.5)) are obtained by a diagonalization of the model Hamiltonian on a set

of employed wave functions. The coupling matrix elements between the different configurations in the wave functions of Eq. (5.5) in odd-mass nuclei are calculated on a microscopic footing, making use of the internal fermion structure of the phonons and the model Hamiltonian.

From the interaction matrix elements used in the QPM it is already clear that an unpaired quasiparticle does not behave as a spectator but modifies the interaction between the complex configurations compared to an even-mass nucleus. This takes place because the phonons possess an internal fermion structure and the interaction matrix elements depend on the interaction between the unpaired quasiparticle and the two-quasiparticle configurations composing the phonon operator.

It should be pointed out that in the present approach interaction matrix elements are calculated in first order perturbation theory. This means that any $[qp \otimes Nph]$ configuration interacts with the $[qp \otimes (N \pm 1)ph])$ ones, but its coupling to $[qp \otimes (N \pm 2)ph]$ configurations is not included in this theoretical treatment. The omitted couplings have nonvanishing interaction matrix elements only in second order perturbation theory. They are much smaller than the ones taken into account and they are excluded from consideration for technical reasons. The interaction with other $[qp \otimes Nph]$ configurations is reckoned with while treating the Pauli principle corrections. In a calculation of the self-energy of the complex configurations, a model Hamiltonian is applied written in terms of quasiparticle operators and exact commutation relations between quasiparticle and phonon operators. In this case, a "Pauli shift correction" is obtained for the energy of a complex configuration from the sum of the energies of its constituents. Also, when considering complex configurations their internal fermion structure is analyzed and the ones which violate the Pauli principle are excluded from the configuration space. Pauli principle corrections have been treated in a diagonal approximation (see, Ref. [Vdov85] for details).

In the actual calculations, the phonon basis includes the phonons with multipolarity and parity $\lambda^\pi = 1^\pm,\ 2^+,\ 3^-$ and 4^+. Several low-energy phonons of each multipolarity are included in the model space. The most important ones are the first collective $2^+,\ 3^-$ and 4^+ phonons and the ones which form the giant dipole resonance (GDR). Noncollective low-lying phonons of an unnatural parity and natural parity phonons of higher multipolarities are of a marginal importance. To make realistic calculations possible one has to truncate the configuration space. This has been done on the basis of excitation energy arguments. All $[qp \otimes 1ph]$ and $[qp \otimes 2ph]$ with $E_x \leq 6$ MeV, and $[qp \otimes 3ph]$ with $E_x \leq 8$ MeV configurations are included in the model space. The only exceptions are $[J_{g.s.} \otimes 1^-]$ configurations which have not been truncated at all to treat a core polarization effect due to the coupling of low-energy dipole transitions to the GDR on a microscopic level. Thus, for electric dipole transitions there are no renormalized effective charges and the values $e^{\rm eff}(p) = (N/A)\,e$ and $e^{\rm eff}(n) = -(Z/A)\,e$ were used to separate the center of mass motion. For $M1$ transitions $g_s^{\rm eff} = 0.64 g_s^{\rm free}$ is used as recommended in Ref. [Cose99]. By doing this all the important configurations for the description of low-lying states up to 4 MeV are included in the model space. The dimension of this space depends on the total spin of the excited states, and it varies between 500 and 700 configurations. This is the first time that QPM calculations were performed on an odd-mass nucleus taken into account the complete configuration space.

5.3.1.2 Comparison with (γ,γ') data and QPM calculations on ^{117}Sn

Since only $E1$, $M1$, and $E2$ transitions can be observed in NRF experiments, the discussion of the properties of the excited states in ^{117}Sn will be restricted to states with $J^\pi = 1/2^\pm$, $3/2^\pm$ and $5/2^+$. As the parities of the decaying levels are unknown and the spin could be assigned for only a few levels (see section 4.2), the best quantity for the comparison between the theoretical predictions and the experimental results are the total integrated cross sections I_s. The theoretical reduced excitation probabilities $B(\pi L)\uparrow$ can be transformed into I_S values via the following relation (combining Eqs. (2.7) and (2.8)):

$$I_S = \frac{8\pi^3(L+1)}{L[(2L+1)!!]^2}\left(\frac{E_x}{\hbar c}\right)^{2L-1} \cdot B(\pi L)\uparrow \cdot \frac{\Gamma_0}{\Gamma}\ , \tag{5.7}$$

where E_x is the excitation energy, L the multipolarity of the transition and Γ_0 denotes the partial ground state decay width. The obtained I_S values for the elastic transitions are plotted in Fig. 5.9c and compared with the results of the (γ,γ') experiments given in Fig. 5.9b. The inelastic decays are accounted for in the total decay widths Γ. Supporting the experimental findings, the QPM calculations also produce a strong fragmentation of the electromagnetic strength. The strongest transitions have an $E1$ character, but also $M1$ and $E2$ excitations yield comparable cross sections. The total cross section I_S is disentangled into its $E1$, $M1$, and $E2$ components in Fig. 5.10b and compared to the calculated I_S values of the core nucleus, ^{116}Sn (Fig. 5.10a). The calculated sum of the total cross sections of the plotted $E1$, $M1$, and $E2$ transitions in Fig 5.10b equals 73, 37 and 42 eVb. The summed experimental elastic cross section, of the levels shown in Fig. 5.9b, equals 133 (21) eVb and agrees within 15% with the theoretically predicted value of 152 eVb. It can be concluded that the contribution of $M1$ and $E2$ transitions can not be neglected before coming to a final conclusion. Assuming that all observed transitions have an $E1$ character as was done in section 5.3.1, oversimplifies the real situation.

Although the experimentally observed levels do not match in detail with the calculated level scheme one by one, some interesting general conclusions can be drawn. The most essential differences in the electromagnetic strength distribution over low-lying states in the even-even ^{116,118}Sn nuclei and the odd-mass ^{117}Sn nucleus take place for the electric dipole transitions. The reason becomes clear by considering which states can be excited from the ground state by $E1$ transitions. In the even-even core there is only one 1^- configuration with an excitation energy below 4 MeV (blue line in Fig. 5.10a). It has a $[2^+_1 \otimes 3^-_1]_{1^-}$ two-phonon nature. This is a general feature in heavy semimagic even-even nuclei [Pono98a]. All other 1^- configurations have excitation energies more than 1 MeV higher. Therefore, the 1^-_1 state has an almost pure two-phonon character in semimagic nuclei. In contrast, there are many $[qp \otimes 1ph]$ and $[qp \otimes 2ph]$ configurations with the same spin and parity close to the two corresponding configurations $[3s_{1/2} \otimes [2^+_1 \otimes 3^-_1]_{1^-}]_{1/2^-,3/2^-}$ in ^{117}Sn. Interactions lead to a strong fragmentation of these two main configurations. The resulting states are carrying a fraction of the $E1$ excitation strength from the ground state.

The predicted properties of some states with spin and parity $J^\pi = 1/2^-$ and $3/2^-$ which can be excited from the $1/2^+$ ground state in ^{117}Sn by an electric dipole transition are presented in

Figure 5.10: Comparison between theoretically predicted electromagnetic strength distributions in ^{116}Sn and ^{117}Sn. The blue lines in the panels a) and b) represent $E1$ excitations, while the green and red lines correspond to $M1$ and $E2$ excitations.

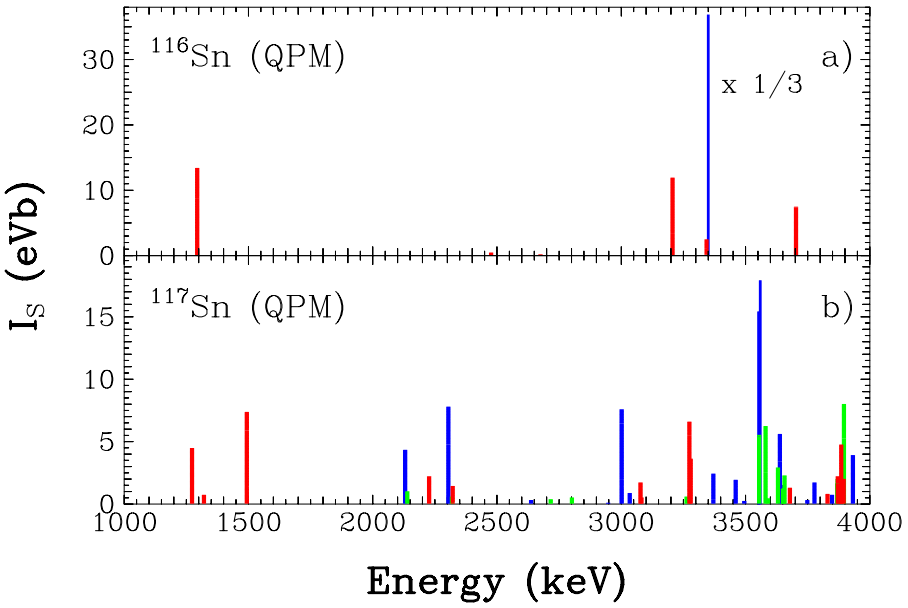

Table 5.6. A large part of the $[3s_{1/2} \otimes [2^+_1 \otimes 3^-_1]_{1^-}]_{1/2^-,3/2^-}$ configurations is concentrated in the $3/2^-$ states with an excitation energy of 3.04, 3.55 and 3.56 MeV and in the $1/2^-$ states at 3.00 and 3.63 MeV (see, fifth column of this table). The transitions to these states are indicated with blue lines in Fig. 5.10b (as well as four other states with a smaller contribution of these configurations). The $E1$ strength distribution among low-lying levels is even more complex because $3/2^-$ states at 2.13, 2.33 and 3.93 MeV have a noticeable contribution from the $3p_{3/2}$ one-quasiparticle configuration (indicated in the forth column of Table 5.6) with a large reduced excitation matrix element $\langle 3p_{3/2}||E1||3s_{1/2}\rangle$ for which there is no analogue in the even-even core ^{116}Sn. Also the coupling to $[3s_{1/2} \otimes 1^-_{\rm GDR}]$, which treats the core polarization effect, is somewhat different than in the core nucleus, because the blocking effect plays an important role in the interaction with other configurations (see, also Ref. [Cose95], where only the last type of transitions has been accounted for). The theoretically calculated total $B(E1)\uparrow$ strength in the energy region from 2.0 to 4.0 MeV is $7.2 \cdot 10^{-3}$ e^{2}fm^2. It agrees well with the calculated $B(E1, 0^+_{g.s.} \rightarrow [2^+ \otimes 3^-]_{1^-}) = 8.2 \cdot 10^{-3}$ e^{2}fm^2 in the neighbouring ^{116}Sn nucleus.

The calculations indicate that among the negative parity states in ^{117}Sn which are relatively strongly excited from the ground state, a few are characterized by a visible $E1$ decay into the low-lying $3/2^+_1$ state. These are $3/2^-$ states at 2.33, 3.65, and 3.93 MeV and a $1/2^-$ state at 3.63 MeV. The state at 2.33 MeV decays into the $3/2^+_1$ state due to single-particle transition with a large reduced excitation matrix element $\langle 2d_{3/2}||E1||3p_{3/2}\rangle$. The states at higher energies

decay into the $3/2^+_1$ state because of an admixture of $[3p_{1/2} \otimes [2^+_1 \otimes 3^-_1]_{1^-}]_{1/2^-,3/2^-}$ configurations in their wave functions.

Positive parity states in ^{117}Sn are de-exciting to the $1/2^+$ ground state by $M1$ or $E2$ or mixed $M1/E2$ transitions. The predicted properties of the $1/2^+$, $3/2^+$ and $5/2^+$ states in ^{117}Sn are presented in Table 5.7. The $B(E2)\uparrow$ strength distribution is dominated by the excitation of the $3/2^+$ state at 1.27 MeV and the $5/2^+$ state at 1.49 MeV (red lines in Fig. 5.10b)). The wave functions of these states carry 85% and 60% of the $[3s_{1/2} \otimes 2^+_1]$ configuration, respectively. These two states correspond with a high probability to the experimentally observed levels at 1447 and 1510 keV. A smaller fraction of the above mentioned configuration can be found in the $3/2^+$ state at 2.32 MeV (5%) and the $5/2^+$ state at 2.23 MeV (6%). The rather fragmented $E2$ strength at higher energies (red lines in Fig. 5.10b) is mainly due to $[3s_{1/2} \otimes 2^+_{4,5}]$ configurations which are much less collective than the first one. Fragmented $E2$ strength between 2.0 and 4.0 MeV originating from the excitation of the $2^+_{4,5}$ phonons has also been observed in NRF experiments on the even-mass ^{116}Sn nucleus (see section 5.2). It could be well reproduced by theoretical calculations (see red lines in Fig. 5.10a). In the odd-mass ^{117}Sn nucleus the corresponding strength is even more fragmented because of the higher density of the configurations. Nevertheless, these $E2$ excitations at high energies contribute appreciably to the reaction cross section, because the $E2$ photon scattering cross section is a cubic function of the excitation energy (see, Eq. (5.7)).

The $B(M1)\uparrow$ strength in the calculations is concentrated mainly above 3.5 MeV, indicated with green lines in Fig. 5.10d. The wave functions of the $1/2^+$ and $3/2^+$ states at these energies are very complex. The main configurations, responsible for the $M1$ strength, are the $[2d_{5/2,3/2} \otimes 2^+_i]$ ones which are excited because of the internal fermion structure of the phonons (similar to the $E1$ $0^+_{g.s.} \rightarrow [2^+_1 \otimes 3^-_1]_{1^-}$ excitations). They have no analogous transitions in even-even nuclei. The configuration $[3s_{1/2} \otimes 1^+_1]$ has an excitation energy of about 4.2 MeV but its contribution to the structure of states below 4 MeV is rather weak. Most of the states with the largest $B(M1)\uparrow$ values have $J^\pi = 1/2^+$ (see, Table 5.7).

Table 5.6: *Theoretical excitation energies (E_x) and $B(E1)\downarrow$ reduced transition probabilities for the decay of negative parity states in ^{117}Sn into the $1/2^+_1$ ground state and the low-lying $3/2^+_1$ state . Only the states with $B(E1, J^\pi \rightarrow 1/2^+_1) > 10^{-5}$ e^2fm^2 are presented. In the last two columns the contribution of the quasiparticle ($\alpha^+_{J^\pi}$) and the $[3s_{1/2} \otimes [2^+_1 \otimes 3^-_1]_{1^-}]_{J^\pi}$ configurations to the wave functions of the states (see Eq. (5.5)) is provided if it is larger than 0.1%.*

E_x	$B(E1)\downarrow$ (10^{-3} e^2fm^2)		$\alpha^+_{J^\pi}$	$[\frac{1}{2}^+ \otimes [2^+_1 \otimes 3^-_1]_{1^-}]$
(MeV)	$J^\pi \rightarrow 1/2^+_1$	$J^\pi \rightarrow 3/2^+_1$		
		$J^\pi = 3/2^-$		
2.13	0.329	0.092	1.0%	
2.33	0.560	0.180	1.8%	
2.64	0.030	0.024		
3.04	0.058	0.032		10.7%
3.37	0.121	0.039	0.4%	
3.46	0.072	0.002	0.2%	
3.49	0.011	0.002		
3.55	0.551	0.012		47.8%
3.56	0.660	0.038	0.1%	32.0%
3.65	0.160	0.336	0.5%	0.1%
3.75	0.015	0.003		
3.78	0.081	0.033	0.3%	
3.85	0.042	0.025		2.8%
3.93	0.235	0.205	0.9%	
4.21	0.087	0.047	0.3%	
4.32	0.133	0.074	0.5%	
		$J^\pi = 1/2^-$		
2.95	0.022	0.023		0.8%
3.00	0.698	0.072	0.1%	21.9%
3.63	0.560	0.250		62.9%
3.72	0.070	1.790		4.0%
4.45	0.020	0.005		

Table 5.7: *Theoretical excitation energies (E_x) and $B(M1)\downarrow$ and $B(E2)\downarrow$ reduced transition probabilities for the decay of positive parity states in ^{117}Sn into the $1/2_1^+$ ground state and the low-lying $3/2_1^+$ states. Only the states with $B(M1, J^\pi \rightarrow 1/2_1^+) > 10^{-2}$ μ_N^2 or $B(E2, J^\pi \rightarrow 1/2_1^+) > 1$ e^2fm^4 are presented.*

E_x	$B(M1)\downarrow$ (μ_N^2)		$B(E2)\downarrow$ (e^2fm^4)	
MeV	$J^\pi \rightarrow 1/2_1^+$	$J^\pi \rightarrow 3/2_1^+$	$J^\pi \rightarrow 1/2_1^+$	$J^\pi \rightarrow 3/2_1^+$
		$J^\pi = 1/2^+$		
2.14	0.011	0.001		
3.58	0.039	0.006		
3.66	0.010	0.014		
3.87	0.012	0.002		
3.89	0.035	0.012		
4.02	0.045	0.031		
4.10	0.200			
4.25	0.027			
		$J^\pi = 3/2^+$		
1.27			353.	1.
1.39			1.	353.
1.78		0.005	2.	7.
2.32	0.003		20.	12.
2.47			2.	10.
3.07			10.	
3.28			16.	
3.56	0.018	0.009		1.
3.63	0.010	0.040		
3.66	0.001	0.004	5.	
3.87		0.001	8.	2.
3.88	0.002		4.	1.
4.05	0.002		10.	
4.17			1.	
4.42	0.011	0.004		
		$J^\pi = 5/2^+$		
1.01			82.	11.
1.32			37.	309.
1.49			239.	25.
2.22			1.	4.
2.23			22.	1.
3.07			2.	1.
3.27			20.	
3.79			2.	
3.87			4.	
3.89			8.	
4.06			9.	
4.17			1.	

5.3.2 Particle two-phonon states in the odd-mass ^{121,123}Sb nuclei

In the odd-mass ^{121,123}Sb nuclei, the unpaired proton is located just outside the closed major Z = 50 shell. In such a case, core coupling models expect a relatively low fragmentation of the electromagnetic strength compared to the situation where an unpaired particle is situated in the middle of two shells. The coupling of the unpaired proton in the 5/2 ground state in ^{121}Sb to the two-phonon $[2_1^+ \otimes 3_1^-]$ quintuplet of the even-even ^{120}Sn core leads to a multiplet of 26 levels. For the obtained $2d_{5/2} \otimes [2_1^+ \otimes 3_1^-]$ multiplet, 14 levels can be excited via $E1$ transitions which are expected to carry the complete two-phonon $E1$ transition strength observed in ^{120}Sn. In ^{123}Sb, the two-phonon $[2_1^+ \otimes 3_1^-]$ quintuplet built on top of the 7/2 ground state, results in a $2d_{7/2} \otimes [2_1^+ \otimes 3_1^-]$ multiplet consisting of 31 states. The electromagnetic two-phonon $E1$ strength of the even-even ^{122}Sn core is expected to fragment over 15 levels.

In Fig. 5.11b) and d), the measured total scattering cross sections I_S in ^{121}Sb and ^{123}Sb are plotted, sandwiched between those observed in the even-even ^{120,122,124}Sn cores (Fig. 5.11a), c), and e)). Unexpectedly, a very high fragmentation of the electromagnetic strength has been detected below an excitation energy of 4 MeV in both Sb nuclei. Nevertheless, the total summed reduced electric dipole excitation strength $B(E1)\uparrow$ in the arbitrary energy region between 2.7 and 3.6 MeV around the two-phonon 1^- states in the even-even adjacent Sn nuclei, amounts to 6.38 (128) $10^{-3} \cdot e^2fm^2$ in ^{121}Sb. This value represents 84 (23) – 89 (25)% of the two-phonon $B(E1)\uparrow$ strength in the even-even ^{120}Sn and ^{122}Sn neighbours and is similar to the result obtained for ^{117}Sn. On the contrary, in ^{123}Sb the total summed $B(E1)\uparrow$ strength in the same energy region only amounts to 2.88 (54) $10^{-3} \cdot e^2fm^2$ or 40 (11) – 47 (14)% of its even-even ^{122}Sn and ^{124}Sn neighbours. This lower value might be due to the higher ground state spin of 7/2 in ^{123}Sb resulting in a higher fragmentation of the electromagnetic strength compared to ^{121}Sb. Part of the electromagnetic strength in ^{123}Sb can be missed if the strength of the individual fragments falls below the detection limits of the present NRF facility. In addition, due to the lower endpoint energy of 3.8 MeV in the ^{123}Sb NRF experiment, the highest observed level had an excitation energy of 3476 keV and hence, part of the electromagnetic strength between 3.5 and 3.6 MeV is missed. Remind that due to the lacking spin and parity information in these odd-mass Sb nuclei, it was assumed that all γ transitions have a pure $E1$ character.

Figure 5.11: Measured total scattering cross section I_S in ^{121}Sb and ^{123}Sb compared to those observed in the even-even adjacent Sn nuclei. A large fragmentation of the electromagnetic strength was observed.

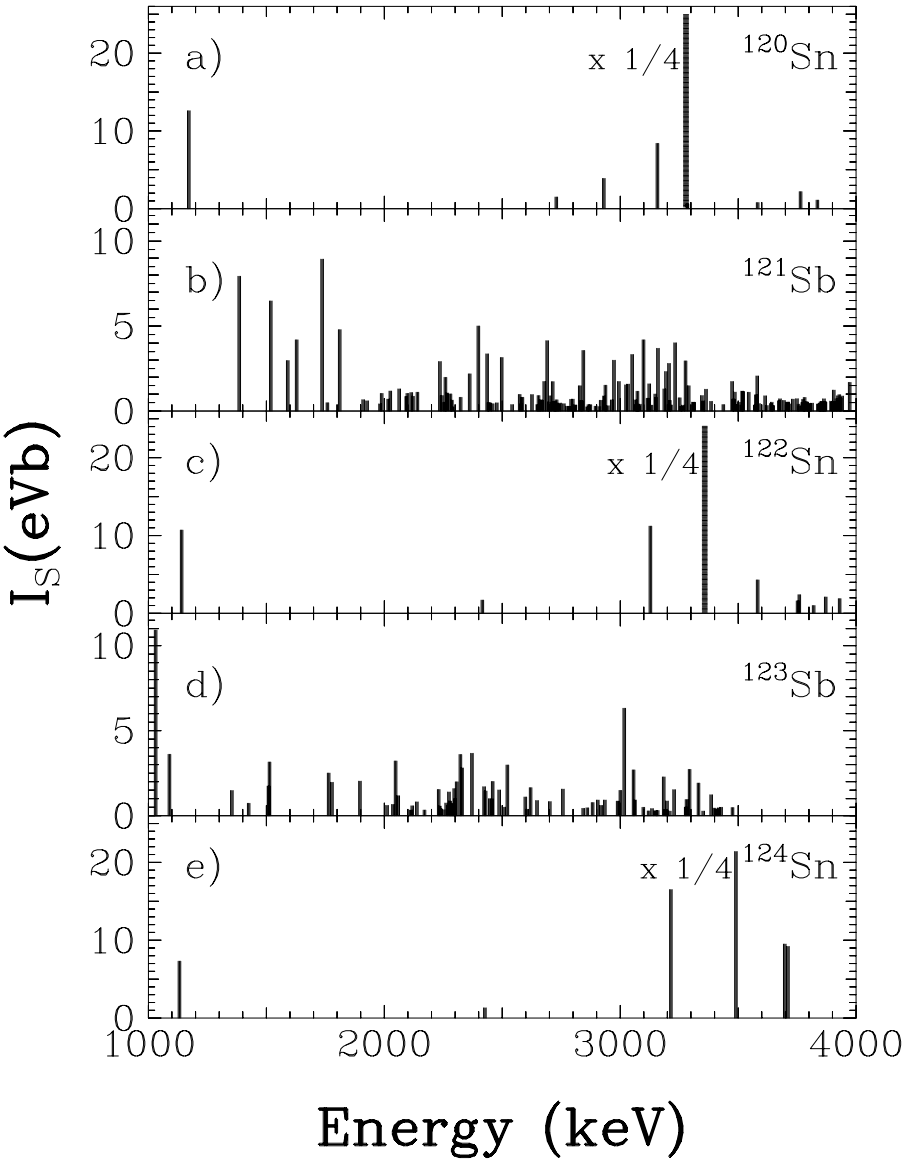

5.3.3 Comparison between the odd-mass nuclei in the Z = 50 and N = 82 regions

The experimental results obtained in the even-even and odd-mass isotopes in the Sn region are summarized in Table 5.8. In the case of the even-even Sn nuclei, the excitation energy $E(1^-)$ and the reduced dipole excitation probability $B(E1)\uparrow$ of the two-phonon $[2^+_1 \otimes 3^-_1]_{1^-}$ levels are given. For the odd-mass nuclei, the summed reduced electric dipole excitation probability in the arbitrary energy region between 2.7 and 3.6 MeV is presented (assuming a pure $E1$ character for all observed transitions) and a weighted average of the excitation energy has been calculated:

$$\langle E \rangle = \frac{\sum_{2.7}^{3.6} E_x \cdot B(E1)\uparrow}{\sum_{2.7}^{3.6} B(E1)\uparrow}$$

Real photon scattering results on ^{115}In [Cose91] have been included in Table 5.8 as well. The weighted average of the excitation energy in the odd-mass nuclei is found close to the excitation energy of the two-phonon 1^- states. It can be concluded that the detected electromagnetic strength is centered around the two-phonon $[2^+_1 \otimes 3^-_1]_{1^-}$ levels in the even-even neighbours. In all the odd-mass nuclei, a comparable percentage of the two-phonon $B(E1)\uparrow$ strength is found back. However, the systematics is broken in ^{123}Sb were only 44% has been resolved of the expected $B(E1)\uparrow$ strength. Possible explanations have been mentioned in the previous paragraph.

A similar study of the fragmentation and distribution of the low-lying electromagnetic strength was performed in even-even and odd-mass nuclei in the N = 82 region. The obtained results have also been included in Table 5.8. In order to make a comparison with the results in the N = 82 isotones, it is necessary to distinguish between two cases: in ^{117}Sn, ^{139}La, and ^{141}Pr the unpaired particle is situated between two major shells while in ^{121,123}Sb and ^{143}Nd the unpaired nucleon is located just outside a closed major shell.

In the odd-mass ^{139}La and ^{141}Pr nuclei, a low percentage of about 44% of the neighbouring two-phonon $B(E1)\uparrow$ strength has been found back, while the resolved summed $B(E1)\uparrow$ strength in ^{117}Sn is about twice larger. However, it should be noted that the detection limits in the NRF experiments on ^{139}La and ^{141}Pr were one order of magnitude higher than those in the experiments on ^{117}Sn. The weakest observed lines in ^{139}La and ^{141}Pr correspond to a total cross section I_S of 2.0 eVb while in ^{117}Sn γ transitions according with a total cross section of 0.3 eVb could be detected. In the ^{139}La and ^{141}Pr nuclei, respectively 17 and 10 γ transitions were found between 2.7 and 4 MeV which are believed to belong to the excitation of particle two-phonon states. In ^{117}Sn 29 γ transitions were found between 2.7 and 3.6 MeV. QPM calculations proved that most of the extracted levels in this energy region have a significant particle two-phonon contribution into their wave function. If the sensitivity limit in the NRF measurements on ^{117}Sn is reduced to the same value as for the ^{139}La and ^{141}Pr nuclei, only 10 γ transitions (between 2.7 and 3.6 MeV) could have been detected. In this case, the summed observed reduced electric dipole excitation probability would amount to only 4.07 (37) $10^{-3} \cdot e^2fm^2$ or 59 (11)% of the two-phonon $B(E1)\uparrow$ strength in the even-even adjacent nuclei. The lower values encountered in ^{139}La and ^{141}Pr might be due to the higher ground state spins of 7/2 and 5/2. The similar fragmentation and distribution of the electromagnetic strength in the odd-mass nuclei ^{117}Sn,

Table 5.8: Summary of the observed $E1$ strength in even-even and odd-mass nuclei in the $Z = 50$ and $N = 82$ regions. The fourth column contains the average percentage of the neighbouring two-phonon $B(E1)\uparrow$ strength which has been resolved in the odd-mass nuclei.

Isotope	Energy (keV)	$(10^{-3} \cdot e^2 fm^2)$		Ref.
Z = 50 region				
$^{115}_{49}In_{66}$	$\langle E \rangle = 3072$	$\sum_{2.7}^{3.6} B(E1)\uparrow = 5.37\ (83)$	82 (21)%	[Cose91]
$^{116}_{50}Sn_{66}$	$E(1_1^-) = 3334$	$B(E1)\uparrow = 6.55\ (65)$		[Gova94b]
$^{117}_{50}Sn_{67}$	$\langle E \rangle = 3191$	$\sum_{2.7}^{3.6} B(E1)\uparrow = 5.59\ (64)$	76 (14)%	this work
$^{118}_{50}Sn_{68}$	$E(1_1^-) = 3270$	$B(E1)\uparrow = 7.25\ (54)$		this work
$^{120}_{50}Sn_{70}$	$E(1_1^-) = 3279$	$B(E1)\uparrow = 7.60\ (51)$		this work
$^{121}_{51}Sb_{70}$	$\langle E \rangle = 3114$	$\sum_{2.7}^{3.6} B(E1)\uparrow = 6.38\ (128)$	87 (24)%	this work
$^{122}_{50}Sn_{72}$	$E(1_1^-) = 3359$	$B(E1)\uparrow = 7.16\ (54)$		this work
$^{123}_{51}Sb_{72}$	$\langle E \rangle = 3100$	$\sum_{2.7}^{3.6} B(E1)\uparrow = 2.88\ (54)$	44 (12)%	this work
$^{124}_{50}Sn_{74}$	$E(1_1^-) = 3490$	$B(E1)\uparrow = 6.08\ (66)$		[Gova94b]
N = 82 region				
$^{138}_{56}Ba_{82}$	$E(1_1^-) = 4026$	$B(E1)\uparrow = 12.9\ (27)$		[Herz95b]
$^{139}_{57}La_{82}$	$\langle E \rangle = 3407$	$\sum_{2.7}^{4} B(E1)\uparrow = 6.6\ (7)$	45 (11)%	[Herz95d]
$^{140}_{58}Ce_{82}$	$E(1_1^-) = 3643$	$B(E1)\uparrow = 16.8\ (9)$		[Herz95b]
$^{141}_{59}Pr_{82}$	$\langle E \rangle = 3294$	$\sum_{2.7}^{4} B(E1)\uparrow = 7.1\ (19)$	43 (16)%	[Herz95d]
$^{142}_{60}Nd_{82}$	$E(1_1^-) = 3425$	$B(E1)\uparrow = 16.2\ (24)$		[Pitz90]
$^{143}_{60}Nd_{83}$	$\langle E \rangle = 3168$	$\sum_{2.9}^{4} B(E1)\uparrow = 13.6\ (18)$	78 (22)%	[Herz95d]
$^{144}_{62}Sm_{82}$	$E(1_1^-) = 3225$	$B(E1)\uparrow = 18.9\ (27)$		[Metz76]

^{139}La and ^{141}Pr combined with the results from QPM calculations for ^{117}Sn, allow to assume that indeed an important part of the particle two-phonon $E1$ strength has been resolved in the NRF experiments on ^{139}La and ^{141}Pr.

To date, the best results in the search for particle two-phonon states accessible via $E1$ transitions from the ground state, were met in ^{143}Nd [Zilg93, Herz95a] where the unpaired neutron is located just outside the closed N = 82 shell. In the energy region between 2.9 and 4.0 MeV, 13 γ transitions have been detected. If it is assumed that all these transitions have a pure $E1$ character, the total summed $B(E1)\uparrow$ strength in this energy region equals within the statistical error the neighbouring two-phonon $E1$ strength in ^{142}Nd. Considering the ground state spin of 7/2, 15 levels belonging to the $f_{7/2} \otimes [2_1^+ \otimes 3_1^-]$ multiplet can be reached via $E1$ transitions. Six of the observed levels have a total scattering cross section which is higher than 10 eVb with a maximum of 35.6 eVb [Herz95d]. The fragmentation and distribution of the electromagnetic strength could be well reproduced in a simple core coupling model based on quadrupole-quadrupole coupling. As also in ^{121}Sb and ^{123}Sb, the unpaired proton is situated just outside the closed Z = 50 major shell, a similar picture for the fragmentation and strength

distribution was expected to be observed. Surprisingly, an enormous fragmentation and a flat distribution in the electromagnetic strength was found. In the energy region between 2.7 and 3.6 MeV, the maximum total scattering cross section was 4.19 eVb in ^{121}Sb and 6.32 eVb ^{123}Sb. If the same detection limits of the NRF measurement on ^{143}Nd are applied for ^{121}Sb, the $B(E1)\uparrow$ strength shrinks to 2.53 (25) $10^{-3} \cdot e^2fm^2$ or 34.3 (58)% of the neigbhouring Sn nuclei. In the case of ^{123}Sb the corresponding values are: 1.12 (10) $10^{-3} \cdot e^2fm^2$ and 17.0 (31)% It should be concluded that the situation met in the odd-mass Sb nuclei is completely different compared to the ^{143}Nd nucleus. Nevertheless, the summed $B(E1)\uparrow$ strength in ^{121}Sb in the actual NRF experiment is similar to the one measured in ^{143}Nd. This feature puts the use of the summed $E1$ strength as a signature of particle two-phonon states into question. It is clear that the condition of equal $E1$ strength for the two-phonon and particle two-phonon states is *needed* but certainly *not sufficient*.

Experimental information on particle two-phonon states is still very sparse. As shown in section 5.1.5, the $E1$ strength of $[2_1^+ \otimes 3_1^-]_{1^-}$ two-phonon states diminishes quickly in non semimagic nuclei. Therefore, the chance to detect particle$\otimes[2_1^+ \otimes 3_1^-]$ two-phonon states in their adjacent odd-mass nuclei in the near future is low. Some intermediate cases have been observed in the open shell nuclei ^{113}Cd [Geig94] and ^{133}Cs [Bess97], where a reasonable amount of strength compared to the even-even neighbours ^{114}Cd and ^{134}Ba was resolved. Note that up till now, no direct proof has been delivered for particle$\otimes[2_1^+ \otimes 3_1^-]$ two-phonon states by measuring the characteristic $E2$ and $E3$ decay strengths. However, in ^{147}Gd a two-phonon octupole state $[\nu f_{7/2} \otimes [3_1^- \otimes 3_1^-]]_{19/2^-}$ was found [Klei82]. The underlying two-phonon octupole configuration was deduced from the measured excitation energy (twice the octupole one-phonon energy) and from the measured two stretched $E3$ transition rates in the $[\nu f_{7/2} \otimes [3_1^- \otimes 3_1^-]]_{19/2^-} \rightarrow \nu f_{7/2}$ decay. To date, this is a very unique case.

Chapter 6

Conclusions

This work aimed to search for two-phonon excitations in even-even as well as odd-mass nuclei in the Z = 50 region. The nuclear resonance fluorescence technique was applied to determine model independently the excitation energies, spins, parities, transition width ratios and reduced excitation probabilities model independently for levels accessible via $E1$, $M1$, and $E2$ transitions and with an excitation energy below 4 MeV.

At first, the spherical semimagic ^{116,118,120,122,124}Sn nuclei were investigated systematically. The NRF experiments revealed that the low-lying level scheme is dominated in each of the Sn nuclei by an enhanced electric dipole transition of about $7.0 \cdot 10^{-3} e^2 fm^2$ (or 1.3 mW.u.) to a 1^- level with an excitation energy close to the harmonic coupling limit of $E(2_1^+) + E(3_1^-)$. Model independent parity assignments were obtained in linear polarization measurements using two Compton polarimeters (^{118}Sn and ^{122}Sn) or using off-axis linearly polarized 12 MeV bremsstrahlung in the entrance channel (^{116}Sn and ^{124}Sn [Gova94b]). The $B(E1)\uparrow$ excitation strengths were found to be nearly constant through the entire investigated Sn mass chain. The observed levels are interpreted as being the 1^- member of the two-phonon $[2_1^+ \otimes 3_1^-]$ quintuplet. The deduced upper limits for the inelastic decay branching $\Gamma_{1^- \to 2^+}/\Gamma_0$ of the two-phonon 1^- states to the 2_1^+ one-phonon state were found to be similar to the branchings measured in $(p, p'\gamma)$ experiments on ^{142}Nd and ^{144}Sm [Wilh96, Wilh98]. Finally, the measured $B(E1; 1_1^- \to 0_{g.s.}^+)$ strengths fit perfectly in the correlation between the $B(E1; 1_1^- \to 0_{g.s.}^+)$ and $B(E1; 3_1^- \to 2_1^+)$ strengths presented in [Piet99a]. Further credence to the two-phonon interpretation of the observed 1^- levels was added by the results of theoretical calculations performed within the QPM by Dr. Ponomarev. A detailed microscopic study revealed a practically pure two-phonon $[2_1^+ \otimes 3_1^-]$ configuration for the wave function of the 1^- states. The observed enhanced electric dipole strength of the "forbidden" $E1$ transitions could be reasonably well reproduced from a consideration of the internal fermion structure of the phonons and taking into account a delicate destructive interference with the 1^- GDR one-phonons.

Besides the 1^- two-phonon states and in addition to the well known collective 2_1^+ state, several other 2^+ states of lower collectivity were determined in the ^{116,118,120,122,124}Sn nuclei below an excitation energy of 4 MeV. The $B(E2)\uparrow$ strength distribution is rather similar along the chain of the Sn isotopes. A QPM analysis of 2^+ states shows that one-phonon configurations in their wave functions are responsible for the total $B(E2)\uparrow$ strength while the admixture of more

complex configurations lead to a fragmentation of the strength.

Secondly, the question was addressed how the observed enhanced electric dipole excitation probability in the even-even Sn nuclei is fragmented and distributed over several levels in the adjacent odd-mass ^{117}Sn and ^{121,123}Sb nuclei. In general, the information on particle$\otimes[2^+_1 \otimes 3^-_1]$ excitations in odd-mass spherical nuclei is still sparse. The NRF experiments performed on ^{117}Sn revealed a large fragmentation of the electromagnetic strength below 4 MeV. In ^{117}Sn, the unpaired neutron is located halfway between the major Z = 50 and N = 82 major shells, in a $3s_{1/2}$ orbital. The search for the fragments of the $3s_{1/2} \otimes [2^+_1 \otimes 3^-_1]$ multiplet carrying the $B(E1)\uparrow$ strength of the neighbouring ^{116}Sn and ^{118}Sn nuclei is complicated by the lack of spin and parity information for the odd-mass ^{117}Sn nucleus. In the energy region between 2.7 and 3.6 MeV, centered around the energy of the $[2^+_1 \otimes 3^-_1]_{1^-}$ states in the ^{116}Sn and ^{118}Sn nuclei, a resonance-like structure was detected. The total $B(E1)\uparrow$ strength amounts to 5.59 (64) $10^{-3} \cdot e^2fm^2$ under the assumption that all transitions have a pure $E1$ character. This value represents 85 (13) – 77 (14)% of the two-phonon $B(E1)\uparrow$ strength in the neighbouring ^{116}Sn and ^{118}Sn nuclei. QPM calculations carried out by Dr. Ponomarev for the first time in a complete configuration space for an odd mass nucleus can explain this fragmentation of the excitation strength and shed light on how the $B(E1)\uparrow$, $B(M1)\uparrow$, and $B(E2)\uparrow$ strength is distributed over the considered energy region. As an important outcome of these calculations, the QPM predicts five levels between 3.0 and 3.6 MeV which contain in their wave function a dominant $[3s_{1/2} \otimes [2^+_1 \otimes 3^-_1]_{1^-}]_{1/2^-,3/2^-}$ structure.

In the odd-mass ^{121,123}Sb nuclei, the unpaired protons are located in the $2d_{5/2}$ and $2d_{7/2}$ orbitals just outside the closed Z = 50 shell. The NRF measurements on ^{121,123}Sb nuclei demonstrated an unexpected high fragmentation of the electromagnetic strength. Nevertheless, the summed $B(E1)\uparrow$ strength in ^{121}Sb in the arbitrary excitation energy region between 2.7 and 3.6 MeV equals 6.38 (128) $10^{-3} \cdot e^2fm^2$ or 84 (23) – 89 (25)% of the neighbouring two-phonon $B(E1)\uparrow$ strength in the even-even ^{120}Sn and ^{122}Sn nuclei. On the other hand, in ^{123}Sb the summed $B(E1)\uparrow$ strength in the same energy region only amounts to 2.88 (54) $10^{-3} \cdot e^2fm^2$ or 40 (11) – 47 (14)% of the neighbouring two-phonon $B(E1)\uparrow$ strength in the ^{122}Sn and ^{124}Sn nuclei. Part of the strength in ^{123}Sb can be missed due to the higher half integer ground state spin and the lower end point energy used in the NRF experiments. For these odd-mass Sb nuclei, it was expected to find the electric dipole excitation strength concentrated in only a few levels as was the case in ^{143}Nd [Zilg93, Herz95a]. Therefore, it can be concluded that the condition of equal $B(E1)\uparrow$ strengths is not an absolute measure whether particle two-phonon states were observed or not. This strength condition is *needed*, but certainly not *sufficient*.

Appendix A

F-coefficients

The F-coefficients are defined as [Hage68]:

$$F_\nu(LL'J_1J_2) = (-1)^{J_1+J_2+1}\cdot\sqrt{(2L+1)(2L'+1)(2\nu+1)(2J_2+1)}\cdot\begin{pmatrix} L & L' & \nu \\ 1 & -1 & 0 \end{pmatrix}\cdot\begin{Bmatrix} J_2 & J_2 & \nu \\ L & L' & J_1 \end{Bmatrix}$$

These F-coefficients can be calculated using modern mathematical computer packages (e.g. Maple) or are tabulated in reference works [Sieg65, Waps87]. The F-coefficients important for this work are:

even-even nuclei:

$F_2(1\ 1\ 0\ 1) = \frac{\sqrt{2}}{2}$

$F_2(2\ 2\ 0\ 2) = -\frac{\sqrt{70}}{14}$ $\qquad$ $F_4(2\ 2\ 0\ 2) = \sqrt{\frac{8}{7}}$

odd mass nuclei with a ground state spin of 1/2:

$F_2(1\ 1\ \frac{1}{2}\ \frac{3}{2}) = \frac{1}{2}$

$F_2(1\ 2\ \frac{1}{2}\ \frac{3}{2}) = -\frac{\sqrt{3}}{2}$

$F_2(2\ 2\ \frac{1}{2}\ \frac{3}{2}) = -\frac{1}{2}$

$F_2(2\ 2\ \frac{1}{2}\ \frac{5}{2}) = -\sqrt{\frac{2}{7}}$ $\qquad$ $F_4(2\ 2\ \frac{1}{2}\ \frac{5}{2}) = -2\sqrt{\frac{2}{21}}$

$F_2(2\ 3\ \frac{1}{2}\ \frac{5}{2}) = -\sqrt{\frac{1}{7}}$ $\qquad$ $F_4(2\ 3\ \frac{1}{2}\ \frac{5}{2}) = \frac{5}{\sqrt{21}}$

$F_2(3\ 3\ \frac{1}{2}\ \frac{5}{2}) = -\frac{3}{\sqrt{14}}$ $\qquad$ $F_2(3\ 3\ \frac{1}{2}\ \frac{5}{2}) = \frac{1}{\sqrt{42}}$

odd mass nuclei with a ground state spin of 5/2:

$F_2(1\ 1\ \frac{5}{2}\ \frac{3}{2}) = \frac{1}{10}$

$F_2(1\ 2\ \frac{5}{2}\ \frac{3}{2}) = \frac{\sqrt{35}}{10}$

$F_2(2\ 2\ \frac{5}{2}\ \frac{3}{2}) = \frac{5}{14}$

$F_2(1\ 1\ \frac{5}{2}\ \frac{5}{2}) = -\frac{4\sqrt{14}}{35}$

$F_2(1\ 2\ \frac{5}{2}\ \frac{5}{2}) = -\frac{3}{\sqrt{35}}$

$F_2(2\ 2\ \frac{5}{2}\ \frac{5}{2}) = \frac{5\sqrt{14}}{98}$

$F_2(1\ 1\ \frac{5}{2}\ \frac{7}{2}) = \frac{\sqrt{21}}{14}$
$F_2(1\ 2\ \frac{5}{2}\ \frac{7}{2}) = -\frac{5\sqrt{7}}{14}$
$F_2(2\ 2\ \frac{5}{2}\ \frac{7}{2}) = -\frac{5}{14\sqrt{21}}$
$F_2(2\ 2\ \frac{5}{2}\ \frac{1}{2}) = 0$ $\quad F_4(2\ 2\ \frac{5}{2}\ \frac{1}{2}) = 0$
$F_2(2\ 3\ \frac{5}{2}\ \frac{1}{2}) = 0$ $\quad F_4(2\ 3\ \frac{5}{2}\ \frac{1}{2}) = 0$
$F_2(3\ 3\ \frac{5}{2}\ \frac{1}{2}) = 0$ $\quad F_4(3\ 3\ \frac{5}{2}\ \frac{1}{2}) = 0$
$F_2(2\ 2\ \frac{5}{2}\ \frac{9}{2}) = -\frac{\sqrt{155}}{21\sqrt{2}}$ $\quad F_4(2\ 2\ \frac{5}{2}\ \frac{9}{2}) = -\frac{\sqrt{286}}{63}$
$F_2(2\ 3\ \frac{5}{2}\ \frac{9}{2}) = -\frac{5\sqrt{21}}{42}$ $\quad F_4(2\ 3\ \frac{5}{2}\ \frac{9}{2}) = \frac{5\sqrt{455}}{126}$
$F_2(3\ 3\ \frac{5}{2}\ \frac{9}{2}) = -\frac{\sqrt{330}}{44}$ $\quad F_4(3\ 3\ \frac{5}{2}\ \frac{9}{2}) = -\frac{17\sqrt{13}}{198\sqrt{22}}$

odd mass nuclei with a ground state spin of 7/2:

$F_2(1\ 1\ \frac{7}{2}\ \frac{5}{2}) = \frac{1}{2\sqrt{14}}$
$F_2(1\ 2\ \frac{7}{2}\ \frac{5}{2}) = \frac{3\sqrt{3}}{\sqrt{14}}$
$F_2(2\ 2\ \frac{7}{2}\ \frac{5}{2}) = \frac{17}{14\sqrt{14}}$
$F_2(1\ 1\ \frac{7}{2}\ \frac{7}{2}) = -\frac{2}{\sqrt{21}}$
$F_2(1\ 2\ \frac{7}{2}\ \frac{7}{2}) = -\frac{1}{\sqrt{7}}$
$F_2(2\ 2\ \frac{7}{2}\ \frac{7}{2}) = \frac{8}{7\sqrt{21}}$
$F_2(1\ 1\ \frac{7}{2}\ \frac{9}{2}) = \frac{\sqrt{11}}{2\sqrt{30}}$
$F_2(1\ 2\ \frac{7}{2}\ \frac{9}{2}) = -\frac{\sqrt{7}}{2\sqrt{2}}$
$F_2(2\ 2\ \frac{7}{2}\ \frac{9}{2}) = -\frac{\sqrt{10}}{28\sqrt{33}}$
$F_2(2\ 2\ \frac{7}{2}\ \frac{3}{2}) = -\frac{1}{7}$ $\quad F_4(2\ 2\ \frac{7}{2}\ \frac{3}{2}) = 0$
$F_2(2\ 3\ \frac{7}{2}\ \frac{3}{2}) = \frac{\sqrt{3}}{\sqrt{2}\sqrt{7}}$ $\quad F_4(2\ 3\ \frac{7}{2}\ \frac{3}{2}) = 0$
$F_2(3\ 3\ \frac{7}{2}\ \frac{3}{2}) = \frac{1}{2}$ $\quad F_4(3\ 3\ \frac{7}{2}\ \frac{3}{2}) = 0$
$F_2(2\ 2\ \frac{7}{2}\ \frac{11}{2}) = -\frac{\sqrt{13}}{\sqrt{7}\sqrt{11}}$ $\quad F_4(2\ 2\ \frac{7}{2}\ \frac{11}{2}) = -\frac{2\sqrt{14}\sqrt{143}}{231\sqrt{3}}$
$F_2(2\ 3\ \frac{7}{2}\ \frac{11}{2}) = -\frac{\sqrt{7}}{\sqrt{2}\sqrt{11}}$ $\quad F_4(2\ 3\ \frac{7}{2}\ \frac{11}{2}) = \frac{5\sqrt{7}}{3\sqrt{3}\sqrt{11}}$
$F_2(3\ 3\ \frac{7}{2}\ \frac{11}{2}) = -\frac{3\sqrt{7}}{2\sqrt{143}}$ $\quad F_4(3\ 3\ \frac{7}{2}\ \frac{11}{2}) = -\frac{31\sqrt{154}}{726\sqrt{3}\sqrt{13}}$

Appendix B

Angular correlation functions

In this appendix, the appropriate angular distribution functions of resonantly scattered photons are given for ground state transitions in even-even and odd-mass nuclei.

even-even nuclei:

$0 \rightarrow 1 \rightarrow 0$

$$W(\theta) = \frac{3}{4}(1 + \cos^2\theta)$$

$0 \rightarrow 2 \rightarrow 0$

$$W(\theta) = \frac{5}{4}(1 - 3\cos^2\theta + 4\cos^4\theta)$$

odd-mass nuclei with a ground state spin of 1/2:

$\frac{1}{2} \rightarrow \frac{1}{2} \rightarrow \frac{1}{2}$

$$W(\theta) = 1$$

$\frac{1}{2} \rightarrow \frac{3}{2} \rightarrow \frac{1}{2}$, $L_1 = L_2 = 1$ (dipole transitions)

$$W(\theta) = 1 + \left(\frac{1}{1+\delta^2}\right)^2 \left(\frac{1}{4} - \sqrt{3}\delta + \frac{5}{2}\delta^2 + \sqrt{3}\delta^3 + \frac{1}{4}\delta^4\right) \times \frac{1}{2}(3\cos^2\theta - 1)$$

$\frac{1}{2} \rightarrow \frac{5}{2} \rightarrow \frac{1}{2}$, $L_1 = L_2 = 2$ (quadrupole transitions)

$$\begin{aligned} W(\theta) = 1 \quad &+ \quad \left(\frac{1}{1+\delta^2}\right)^2 \left(2 + 4\sqrt{2}\delta + 10\delta^2 + \frac{12}{\sqrt{2}}\delta^3 + \frac{9}{2}\delta^4\right) \times \frac{1}{14}(3\cos^2\theta - 1) \\ &+ \quad \left(\frac{1}{1+\delta^2}\right)^2 \left(8 - 40\sqrt{2}\delta + 96\delta^2 + \frac{20}{\sqrt{2}}\delta^3 + \frac{\delta^4}{2}\right) \times \frac{1}{168}(35\cos^4\theta - 30\cos^2\theta + 3) \end{aligned}$$

odd-mass nuclei with a ground state spin of 5/2:

$\frac{5}{2} \rightarrow \frac{3}{2} \rightarrow \frac{5}{2}$, $L_1 = L_2 = 1$ (dipole transitions)

$$W(\theta) = 1 + \left(\frac{1}{1+\delta^2}\right)^2 \left(\frac{1}{50} + \frac{\sqrt{7}}{5\sqrt{5}}\delta + \frac{201}{70}\delta^2 + \frac{\sqrt{5}}{\sqrt{7}}\delta^3 + \frac{25}{98}\delta^4\right) \times \frac{1}{4}(3\cos^2\theta - 1)$$

$\frac{5}{2} \rightarrow \frac{5}{2} \rightarrow \frac{5}{2}$, $L_1 = L_2 = 1$ (dipole transitions)

$$W(\theta) = 1 + \left(\frac{1}{1+\delta^2}\right)^2 \left(\frac{32}{175} + \frac{24\sqrt{2}}{35\sqrt{5}}\delta + \frac{232}{245}\delta^2 - \frac{3\sqrt{10}}{49}\delta^3 + \frac{25}{686}\delta^4\right) \times \frac{1}{2}(3\cos^2\theta - 1)$$

$\frac{5}{2} \to \frac{7}{2} \to \frac{5}{2}$, $L_1 = L_2 = 1$ (dipole transitions)

$$W(\theta) = 1 + \left(\frac{1}{1+\delta^2}\right)^2 \left(\frac{3}{2} - 5\sqrt{3}\delta + \frac{695}{14}\delta^2 + \frac{25}{7\sqrt{3}}\delta^3 + \frac{25}{588}\delta^4\right) \times \frac{1}{28}(3\cos^2\theta - 1)$$

$\frac{5}{2} \to \frac{1}{2} \to \frac{5}{2}$, $L_1 = L_2 = 2$ (quadrupole transitions)

$$W(\theta) = 1$$

$\frac{5}{2} \to \frac{9}{2} \to \frac{5}{2}$, $L_1 = L_2 = 2$ (quadrupole transitions), $\delta = 0$

$$W(\theta) = 1 + \frac{55}{588}(3\cos^2\theta - 1) + \frac{31}{5292}(35\cos^4\theta - 30\cos^2\theta + 3)$$

odd-mass nuclei with a ground state spin of 7/2:

$\frac{7}{2} \to \frac{5}{2} \to \frac{7}{2}$, $L_1 = L_2 = 1$ (dipole transitions)

$$W(\theta) = 1 + \left(\frac{1}{1+\delta^2}\right)^2 \left(\frac{1}{8} + 3\sqrt{3}\delta + \frac{1529}{28}\delta^2 + \frac{51\sqrt{3}}{7}\delta^3 + \frac{289}{392}\delta^4\right) \times \frac{1}{14}(3\cos^2\theta - 1)$$

$\frac{7}{2} \to \frac{7}{2} \to \frac{7}{2}$, $L_1 = L_2 = 1$ (dipole transitions)

$$W(\theta) = 1 + \left(\frac{1}{1+\delta^2}\right)^2 \left(\frac{4}{3} + \frac{8}{\sqrt{3}}\delta + \frac{52}{21}\delta^2 - \frac{32}{7\sqrt{3}}\delta^3 + \frac{64}{147}\delta^4\right) \times \frac{1}{14}(3\cos^2\theta - 1)$$

$\frac{7}{2} \to \frac{9}{2} \to \frac{7}{2}$, $L_1 = L_2 = 1$ (dipole transitions)

$$W(\theta) = 1 + \left(\frac{1}{1+\delta^2}\right)^2 \left(\frac{11}{60} - \frac{\sqrt{77}}{\sqrt{15}}\delta + \frac{293}{42}\delta^2 + \frac{\sqrt{35}}{7\sqrt{33}}\delta^3 + \frac{5}{6468}\delta^4\right) \times \frac{1}{4}(3\cos^2\theta - 1)$$

$\frac{7}{2} \to \frac{3}{2} \to \frac{5}{2}$, $L_1 = L_2 = 2$ (quadrupole transitions)

$$W(\theta) = 1 + \left(\frac{1}{1+\delta^2}\right)^2 \left(\frac{1}{49} - \frac{4\sqrt{3}}{7\sqrt{2}\sqrt{7}}\delta + \frac{5}{7}\delta^2 + \frac{\sqrt{6}}{\sqrt{7}}\delta^3 + \frac{1}{4}\delta^4\right) \times \frac{1}{2}(3\cos^2\theta - 1)$$

$\frac{7}{2} \to \frac{11}{2} \to \frac{7}{2}$, $L_1 = L_2 = 2$ (quadrupole transitions)

$$\begin{aligned} W(\theta) = 1 \quad &+ \quad \left(\frac{1}{1+\delta^2}\right)^2 \left(\frac{13}{7} + 2\sqrt{26}\delta + 17\delta^2 + \frac{21\sqrt{2}}{\sqrt{13}}\delta^3 + \frac{63}{52}\delta^4\right) \times \frac{1}{22}(3\cos^2\theta - 1) \\ &+ \quad \left(\frac{1}{1+\delta^2}\right)^2 \left(\frac{8008}{4851} + \frac{40\sqrt{2}\sqrt{13}}{9}\delta + \frac{54768}{693}\delta^2 - \frac{620\sqrt{7}}{99\sqrt{13}} + \frac{6727}{28314}\delta^4\right) \\ &\times \quad \frac{1}{264}(35\cos^4\theta - 30\cos^2\theta + 3) \end{aligned}$$

Appendix C

^{56}Co calibration standard

^{56}Co is an instable nucleus, β^+-decaying to ^{56}Fe with a half live of 77.3 days. In this process several levels of ^{56}Fe are populated which de-excite via γ transitions to the ground state of ^{56}Fe. In the next table, the energies of the emitted γ's are given as well as their relative γ intensities.

Energy E_γ (keV)	Relative intensity I_γ (%)
846.764 (6)	99.958 (5)
1037.844 (4)	14.03 (20)
1175.099 (8)	2.28 (3)
1238.287 (6)	67.0 (7)
1360.206 (6)	4.29 (4)
1771.350 (15)	15.51 (14)
1810.722 (17)	0.65 (1)
1963.714 (12)	0.713 (11)
2015.179 (11)	3.03 (5)
2034.759 (11)	7.78 (12)
2113.107 (12)	0.376 (7)
2212.921 (10)	0.388 (15)
2598.460 (10)	16.9 (3)
3009.596 (17)	1.06 (3)
3201.954 (14)	3.18 (10)
3253.417 (14)	7.79 (25)
3272.998 (14)	1.85 (6)
3451.154 (13)	0.93 (3)
3548.180 (120)	0.19 (1)

Taken from [Seel81, Lore87].

Appendix D

^{27}Al calibration standard

The odd-mass nucleus ^{27}Al is commonly used in NRF experiments as calibration standard to monitor the photon flux. Total scattering cross sections I_S of the excited levels in the NRF target are determined relatively to the 2982 keV transition. The next table contains the decay properties of the levels in ^{27}Al below an excitation energy of 4.4 MeV [Endt90].

			Br (%), $[E_\gamma]$			
E_x	J_i^π	τ	$\rightarrow 5/2^+$	$\rightarrow 1/2^+$	$\rightarrow 3/2^+$	other
(keV)			0 keV	844 keV	1014 keV	
0	$5/2^+$	stable				
843.76 (3)	$1/2^+$	50 (2) ps				
1014.45 (3)	$3/2^+$	2.12 (8) ps	97.10 (10)	2.90 (10)		
				[171]		
2211.1 (6)	$7/2^+$	39.1 (10) fs	100	< 0.2	< 0.1	
				[1367]	[1197]	
2734.9 (7)	$5/2^+$	13 (4) fs	22.1 (10)	1.80 (14)	75.7 (11)	0.40 (14)
				[1891]	[1720]	[< 1000]
2981.3 (7)	$3/2^+$	5.7 (3) fs	97.4 (5)	1.0 (3)	1.6 (4)	< 0.2
				[2138]	[1967]	[< 1000]
3004.2 (8)	$9/2^+$	88 (4) fs	88.6 (11)	< 2	< 0.5	< 12
				[2160]	[1990]	[< 1000]
3680.4 (9)	$1/2^+$	< 25 fs	1.9 (3)	59.8 (15)	38.3 (15)	< 0.8
				[2837]	[2666]	[< 1470]
3956.8 (4)	$3/2^+$	3.5 (4) fs	84.4 (17)	5.0 (18)	4.8 (16)	5.8, < 2.9
				[3113]	[2942]	[< 1230, < 1750]
4054.6 (6)	$1/2^-$	< 20 fs	< 1.0	86.4 (12)	13.6 (12)	< 2.5
				[3211]	[3040]	[< 1850]
Other levels: $E_x > 4.4$ MeV						

This table is taken from [Endt90].

The absolute lifetimes τ and the level widths Γ have been determined precisely in a nuclear self absorption experiment on ^{27}Al [Piet95a]. These results are summarized in the next table and the deduced total scattering cross sections I_S for the levels in ^{27}Al are given as well.

E_x [a)]	τ [b)] (fs)	Γ_0/Γ [a)] (%)	Γ [b)] (meV)	Γ_0 (meV)	I_S (eVb)
2211.1 (6)	38.1 (10)	100	17.19 (31)	17.19 (31)	18.0 (3)
2734.9 (7)	14 (6)	22.1 (10)	51 (7)	11.3 (21)	1.3 (2)
2982.0 (1)	5.63 (13)	97.4 (5)	116.7 (25)	113.7 (30)	31.9 (8)
3004.2 (8)	93 (39)	88.6 (11)	7.74 (46)	6.86 (49)	4.3 (3)
3956.8 (4)	3.94 (40)	85.3 (15)	177 (11)	151 (12)	21.1 (17)

[a)] Taken from [Endt90].

[b)] Taken from [Piet95a].

Appendix E

^{13}C calibration standard

The odd-mass nucleus ^{13}C has two levels below an excitation energy of 4 MeV which can be used for photon flux calibration purposes. Their level widths has been determined in nuclear self absorption measurements [More93]. The next table contains the lifetime τ, the level widths and deduced total scattering cross sections I_S.

E_x [a)]	J^π [a)]	τ [b)] (fs)	Γ [b)] (meV)	Γ_0/Γ [a)] (%)	Γ_0 (meV)	I_S (eVb)
3089.443 (20)	$1/2^+$	1.23 (9)	537 (42)	100	537 (42)	216 (17)
3684.507 (19)	$3/2^-$	1.63 (12)	403 (30)	99 (4)	399 (46)	224 (26)

[a)] Taken from [Fire96].

[b)] Taken from [More93].

References

[Alag55] G. Alaga, K. Alder, A. Bohr, and B. R. Mottelson. *Intensity rules for beta and gamma transitions to nuclear rotational states* Dan. Mat. Fys. Medd. 29 No. 9, 1 (1955).

[Albe88] S. Albers, A. Clauberg, A. Dewald, C. Wesselborg, A. Zilges, Verhandl. DPG (VI) 23 (1981) 227.

[Back81] A. Bäcklin and N. G. Jonsson. 0^+ *states and E0 and E2 transition rates in even Sn nuclei* Nucl. Phys. A351, 490 (1981).

[Barf89] A. F. Barfield, P. von Brentano, A. Dewald, K. O. Zell, N. V. Zamfir, D. Bucurescu, M. Ivascu, and O. Scholten. *Evidence for the two-body nature of the $E1$ transition operator in the sdf-interacting boson model* Z. Phys. A332, 29 (1989).

[Barg95] L. Bargioni, P. G. Bizetti, A. M. Bizetti-Sona, D. Bazzacco, S. Lunardi, P. Pavan, C. Rossi-Alvarez, G. de Angelis, G. Maron, and J. Rico. *Double-octupole excitations in the $N = 84$ nuclei ^{144}Nd and ^{146}Sm* Phys. Rev. C51, R1057 (1995).

[Bass79] R. Bass, J. Idzko, H. Pelz, K. Stelzer, Th. Weber, and R. Weniger. *Symmetrical four-crystal compton polarimeter for gamma rays: design and application* Nucl. Instr. Meth. 163, 377 (1979).

[Baus93] I. Bauske, J. M. Arais, P. von Brentano, A. Frank, H. Friedrichs, R. D. Heil, R.-D. Herzberg, F. Hoyler, P. Van Isacker, U. Kneissl, J. Margraf, H. H. Pitz, C. Wesselborg, and A. Zilges. *First observation of scissors mode states in an odd-mass nucleus* Phys. Rev. Lett. 71, 975 (1993).

[Bauw00] F. Bauwens, J. Bryssinck, D. De Frenne, K. Govaert, L. Govor, M. Hagemann, J. Heyse, E. Jacobs, W. Mondelaers, and V. Yu. Ponomarev. *Dipole transitions to bound states in ^{56}Fe and ^{58}Ni* Phys. Rev. C62, 024302 (2000).

[Belg95] T. Belgya, R. A. Gatenby, E. M. Baum, E. L. Johnson, D. P. DiPrete, S. W. Yates, B. Fazekas, and G. Molnár. *Two-phonon character of the lowest $J^\pi = 1^-$ state of ^{142}Nd* Phys. Rev. C52, R2314 (1995).

[Beli97] D. Belic. *Erprobung und Eichung eines sektorierten Ge-Compton-Polarimeters* Diploma Thesis, Institut für Strahlenphysik der Universität Stuttgart (1997).

[Beli00] D. Belic. PhD thesis, Institut für Strahlenphysik der Universität Stuttgart, in preparation.

[Berg81] U. E. P. Berg, D. Rück, K. Ackermann, K. Bangert, C. Bläsing, K. Kobras, W. Naatz, R. K. M. Schneider, R. Stock, and K. Wienhard. *Parities of dipole ground state transitions in* ^{52}Cr Phys. Lett. B103, 301 (1981).

[Berg87] U. E. P. Berg and U. Kneissl. *Recent progress on nuclear magnetic dipole excitations* Ann. Rev. Nucl. Part. Sci. 37, 33 (1987).

[Bess97] J. Besserer, O. Beck, P. von Brentano, T. Eckert, R.-D. Herzberg, D. Jäger, U. Kneissl, J. Margraf, H. Maser, A. Nord, N. Pietralla, H. H. Pitz, and A. Zilges. *Fragmentation of low-lying dipole strength in the odd-mass nucleus* ^{133}Cs Phys. Rev. C56, 1276 (1997).

[Blac87] J. Blachot and G. Marguier. Nucl. Data Sheets 50, 101 (1987).

[Blac94] J. Blachot and G. Marguier. Nucl. Data Sheets 73, 81 (1994).

[Bohl84] D. Bohle, A. Richter, W. Steffen, A.E.L. Dieperink, N. Lo. Iudice, F. Palumbo, and O. Scholten. *New magnetic dipole excitation mode studied in the heavy deformed nucleus* ^{156}Gd *by inelastic electron scattering* Phys. Lett. B137, 27 (1984).

[Bohr75] A. Bohr and B. Mottelson. *Nuclear Structure*, volume 2. Benjamin, New York, (1975).

[Boot73] E. C. Booth, R. G. Arnold, and W. J. Alston. *Resonance fluorescence studies.* ^{121}Sb *and* ^{123}Sb Phys. Rev. C7, 1500 (1973).

[Bren96] P. von Brentano, J. Eberth, J. Enders, L. Esser, R.-D. Herzberg, N. Huxel, H. Meise, P. von Neumann-Cosel, N. Pietralla N. Nicolay, H. Prade, J. Reif, A. Richter, C. Schlegel, R. Schwenger, S. Skoda, H. G. Thomas, I. Wiedenhöver, G. Winter, and A. Zilges. *First observation of the scissors mode in a* γ*-soft nucleus : The case of* ^{196}Pt Phys. Rev. Lett. 76, 2029 (1996).

[Bren99] P. von Brentano, C. Fransen, A. Linneman, P. Matschinsky, N. Pietralla, V. Werner, J. Enders, P. von Neumann-Cosel, and A. Richter. *High sensitivity photon scattering experiment on* ^{163}Dy Annual report, Suttgart University, 24 (1999).

[Brys99] J. Bryssinck, L. Govor, D. Belic, F. Bauwens, O. Beck, P. von Brentano, D. De Frenne, T. Eckert, C. Fransen, K. Govaert, R.-D. Herzberg, E. Jacobs, U. Kneissl, H. Maser, A. Nord, N. Pietralla, H. H. Pitz, V. Yu. Ponomarev, and V. Werner *Uniform properties of* $J^\pi = 1^-$ *two-phonon states in the semimagic even-even tin isotopes* $^{116,118,120,122,124}Sn$ Phys. Rev. C59, 1930 (1999).

[Brys00a] J. Bryssinck, L. Govor, V. Yu. Ponomarev, F. Bauwens, O. Beck, D. Belic, P. von Brentano, D. De Frenne, T. Eckert, C. Fransen, K. Govaert, R.-D. Herzberg, E. Jacobs, U. Kneissl, H. Maser, A. Nord, N. Pietralla, H. H. Pitz, and V. Werner *Systematic study of electric quadrupole excitations in the stable even mass Sn nuclei* Phys. Rev. C61, 024309 (2000).

[Brys00b] J. Bryssinck, L. Govor, V. Yu. Ponomarev, F. Bauwens, O. Beck, D. Belic, P. von Brentano, D. De Frenne, C. Fransen, R.-D. Herzberg, E. Jacobs, U. Kneissl, H. Maser, A. Nord, N. Pietralla, H. H. Pitz, and V. Werner *Search for the electric dipole excitations to the* $3s_{1/2} \otimes [2_1^+ \otimes 3_1^-]$ *multiplet in* ^{117}Sn Phys. Rev. C62, 014309 (2000).

[Butl73] P. A. Butler, P. E. Carr, L. L. Gadeken, A. N. James, P. J. Nolan, J. F. Sharpey-Schafer, P. J. Twin, and D. A. Viggars. *Construction and use of a three Ge(Li) compton polarimeter* Nucl. Instr. and Meth., 497 (1973).

[Carr93] J. J. Carroll, C. B. Collins, K. Heyde, M. Huber, P. von Neumann-Cosel, V. Yu Ponomarev, D. G. Richmond, A. Richter, C. Schlegel, T. W. Sinor, and K. N. Taylor. *Intermediate structure in the photoexcitation of* ^{77m}Se, ^{79m}Br, *and* ^{137m}Ba Phys. Rev. C48, 2238 (1993).

[Chan91] B. Chand, J. Goswamy, D. Metha, N. Singh, and P. N. Terhan. Can. J. Phys. 69, 90 (1991).

[Cose91] P. von Neumann-Cosel, A. Richter, C. Spieler, W. Ziegler, J. J. Caroll, T. W. Sinor, D. G. Richmond, K. N. Taylor, C. B. Collins, and K. Heyde. *Resonant photoexcitation of isomers.* $^{115}In^m$ *as a test case* Phys. Lett. B266, 9 (1991).

[Cose95] P. von Neumann-Cosel, V. Yu. Ponomarev, A. Richter, and C. Spieler. *The* ^{115}In (γ, γ') *reaction as a test of the quasi-particle phonon model with complex configurations in odd-mass nuclei* Z. Phys. A350, 303 (1995).

[Cose99] P. von Neumann-Cosel, F. Neumeyer, S. Nishizaki, V. Yu. Ponomarev, C. Rangacharyulu, B. Beitz, A. Richter, G. Schreider, D. I. Sober, T. Waindzoch, and J. Wambach. *Spin and orbital magnetic quadrupole resonances in* ^{48}Ca *and* ^{90}Zr *from 180° electron scattering* Phys. Rev. Lett. 82, 1105 (1999).

[Debe88] K. Debertin and R. G. Helmer. *Gamma- and X-ray spectrometry with semiconductor detectors.* North-Holland Amsterdam, (1988).

[Dege90] A. Degener, C. Bläsing, R. D. Heil, A. Jung, U. Kneissl, H. H. Pitz, H. Schacht, S. Schennach, R. Stock, and C. Wesselborg. *Dipole excitations in* ^{48}Ti *studied by nuclear resonance fluorescence* Nucl. Phys. A513, 29 (1990).

[Demi90a] A. M. Demidov and I. V. Mikhailov. Topics in Atom. Sci. & Tech., Ser. Nucl. Const. 4, 24 (1990).

[Demi90b] A. M. Demidov and I. V. Mikhailov. Bull. Acad. Sci. USSR, Phys. Ser. 54 No. 11, 41 (1990).

[Demi91] A. M. Demidov and I. V. Mikhailov. Bull. Acad. Sci. USSR, Phys. Ser., 55 No. 11, 30 (1991).

[Demi92] A. M. Demidov and I. V. Mikhailov. Sov. J. Nucl. Phys., 55 No. 4, 481 (1992).

[Donn66] W. Donner and W. Greiner. *Octupole vibrations of deformed nuclei* Z. Phys. 197, 440 (1966).

[Ecke97] T. Eckert, O. Beck, J. Besserer, P. von Brentano, R. Fischer, R.-D. Herzberg, U. Kneissl, J. Margraf, H. Maser, A. Nord, N. Pietralla, H. H. Pitz, S. W. Yates, and A. Zilges. *Dipole excitations in the transitional nucleus* ^{144}*Nd studied in photon scattering experiments* Phys. Rev. C56, 1256 (1997).

[Ende97] J. Enders, N. Huxel, P. von Neumann-Cosel, and A. Richter. *Where is the scissors mode strength in odd-nuclei ?* Phys. Rev. Lett. 79, 2010 (1997).

[Ende98] J. Enders, P. von Brentano, J. Eberth, R.-D. Herzberg, N. Huxel, H. Lenske, P. von Neumann-Cosel, N. Nicolay, N. Pietralla, H. Prade, J. Reif, A. Richter, C. Schlegel, R. Schwenger, S. Skoda, H. G. Thomas, I. Wiedenhöver, G. Winter, and A. Zilges. *Photon scattering off* ^{52}*Cr: two-phonon E1 strength at the N = 28 shell closure ?* Nucl. Phys. A636, 139 (1998).

[Endt79] P. M. Endt. *Strengths of gamma-ray transitions in A = 45 - 90 nuclei* At. Data and Nucl. Data Tables 23, 547 (1979).

[Endt81] P. M. Endt. *Strengths of gamma-ray transitions in A = 91–150 nuclei* At. Data and Nucl. Data Tables 26, 47 (1981).

[Endt90] P. M. Endt *Energy levels of A = 21–44 nuclei* Nucl. Phys. A521, 1 (1990).

[Fagg59] Lawrence W. Fagg and Stanley S. Hanna. *Polarization measurements on nuclear gamma rays* Rev. Mod. Phys. 31, 711 (1959).

[Fire96] Richard B. Firestone. *Table of isotopes* New York, John Wiley and Sons (1996).

[Fran98] C. Fransen, O. Beck, P. von Brentano, T. Eckert, R.-D. Herzberg, U. Kneissl, H. Maser, A. Nord, N. Pietralla, H. H. Pitz, and A. Zilges. *Systematics of low-lying electric dipole excitations in the* $A \cong 130$*–200 mass region* Phys. Rev. C57, 129 (1998).

[Fran99] C. Fransen, B. Krischock, O. Beck, J. Besserer, P. von Brentano, T. Eckert, R.-D. Herzberg, U. Kneissl, J. Margraf, H. Maser, A. Nord, N. Pietralla, H. H. Pitz, and A. Zilges. *Low-lying dipole excitations in the transitional nuclei* ^{190,192}*Os* Phys. Rev. C59, 2264 (1999).

[Fren94] D. De Frenne and E. Jacobs. Nucl. Data Sheets 71, 1 (1994).

[Fried92] H. Friedrichs, B. Schlitt, J. Margraf, S. Lindenstruth, C. Wesselborg, R. D. Heil, H. H. Pitz, U. Kneissl, P. von Brentano, R. D. Herzberg, A. Zilges, D. Häger, G. Müller, and M. Schumacher. *Evidence for enhanced electric dipole excitations in deformed rare earth nuclei near 2.5 MeV* Phys. Rev. C45, R892 (1992).

[Fried94] H. Friedrichs, D. Häger, P. von Brentano, R. D. Heil, R.-D. Herzberg, U. Kneissl, J. Margraf, G. Müller, H. H. Pitz, B. Schlitt, M. Schumacher, C. Wesselborg, A. Zilges. *Low lying $E1$ and $M1$ strengths in the deformed nucleus ^{160}Gd* Nucl. Phys. A567, 266 (1994).

[Fult69] S. C. Fultz, B. L. Berman, J. T. Caldwell, R. L. Bramblett, and M. A. Kelly. *Photoneutron cross sections for ^{116}Sn, ^{117}Sn, ^{118}Sn, ^{119}Sn, ^{120}Sn, ^{124}Sn and indium* Phys. Rev. 168, 1255 (1969).

[Gacs94] Z. Gacsi and S. Raman. *Decays of ^{116}Sb isomers to levels in ^{116}Sn* Phys. Rev. C49, 2792 (1994).

[Gale88] S. Gales, Ch. Stoyanov, and A. I. Vdovin. Phys. Rep. 166, 125 (1988).

[Garc95] L. M. Garcia-Raffi, J. L. Tain, J. Bea, A. Gadea, L. Palafox, J. Rico, and B. Rubio. *Nonorthogonal gamma-ray compton polarimeters* Nucl. Instr. and Meth. A359, 628 (1995).

[Gate90] R. A. Gatenby, J.R. Vanhoy, E. M. Baum, E. L. Johson, S.W. Yates, T. Belgya, B. Fazekas, A. Veres, and G. Molnár. *Fast E1 transitions and evidence for octupole-octupole and quadrupole-octupole excitations in ^{144}Sm* Phys. Rev. C41, R414 (1990).

[Gate93] R. A. Gatenby, E. L. Johnson, E. M. Baum, S. W. Yates, D. Wang, J. R. Vanhoy, M. T. McEllistrem, T. Belgya, B. Fazekas, and G. Molnar. *Decay properties and lifetimes of states in ^{144}Sm from $(n, n'\gamma)$ reaction studies* Nucl. Phys. A560, 633 (1993).

[Geig94] W. Geiger, Zs. Németh, I. Bauske, P. von Brentano, R. D. Heil, R.-D. Herzberg, U. Kneissl, J. Margraf, H. Maser, N. Pietralla, H. H. Pitz, C. Wesselborg, and A. Zilges. *Low-lying dipole excitations in the isotopes $^{113,114}Cd$* Nucl. Phys. A520, 263 (1994).

[Geor95a] R. Georgii, P. von Neumann-Cosel, T. von Egidy, M. Grinberg, V. A. Khitrov, J. Ott, P. Prokofjevs, A. Richter, W. Schauer, C. Schlegel, R. Schultz, L. J. Simonova, Ch. Stoyanov, A.M. Sukhovoj, and A. V. Vojnov. *Unusual neutron-capture gamma-ray cascade in 124Te : A fingerprint of octupole-coupled multiphonon states* Phys. Lett. B351, 82 (1995).

[Geor95b] R. Georgii, T. von Egidy, J. Klora, H. Lindner, U. Mayerhofer, J. Ott, W. Schauer, P. von Neumann-Cosel, A. Richter, C. Schlegel, R. Schultz, V. A. Khitrov, A.M . Sukhovoj, A. V. Vojnov, J. Berzins, V. Bondarenko, P. Prokofjevs, L.J. Simonova,

M. Grinberg, and Ch. Stoyanov. *Complete level scheme of ^{124}Te up to 3 MeV* Nucl. Phys. A592, 307 (1995).

[Gova94a] K. Govaert, W. Mondelaers, E. Jacobs, D. De Frenne, K. Persyn, S. Pomme, M.-L. Yoneama, S. Lindenstruth, K. Huber, A. Jung, B. Starck, R. Stock, C. Wesselborg, R.-D. Heil, U. Kneissl, and H. H. Pitz. *Polarized bremsstrahlung nuclear resonance fluorescence set-up at the 15 Mev linac in Gent* Nucl. Instr. Meth. Phys. Res. A337, 265 (1994).

[Gova94b] K. Govaert, L. Govor, E. Jacobs, D. De Frenne, W. Mondelaers, K. Persyn, M.-L. Yoneama, U. Kneissl, J. Margraf, H. H. Pitz, K. Huber, S. Lindenstruth, R. Stock, K. Heyde, A. Vdovin, and V. Yu. Ponomarev. *Observation of a 1^- two phonon $(2^+ \otimes 3^-)$ excitation in ^{116}Sn and ^{124}Sn* Phys. Lett. B335, 113 (1994).

[Gova96] K. Govaert. *Nucleaire Resonantie Fluorescentie Metingen aan ^{116}Sn en ^{124}Sn.* PhD thesis, University of Gent, (1996).

[Gova98] K. Govaert, F. Bauwens, J. Bryssinck, D. De Frenne, E. Jacobs, W. Mondelaers, L. Govor, and V. Yu. Ponmomarev. *Dipole excitations to bound states in ^{116}Sn and ^{124}Sn* Phys. Rev. C57, 2229 (1998).

[Govo91b] L. I. Govor, A. M. Demidov, O. K. Zhuravlev, I. V. Mikhailov, and E. Yu. Shkuratova. *Lifetime measurements for excited $^{116-124}Sn$ states in the (n,n'γ) reaction* Sov. J. Nucl. Phys. 54 (2), 196 (1991).

[Grin94] M. Grinberg and Ch. Stoyanov. *Distribution of two-phonon strength in even $N = 82$ nuclei* Nucl. Phys. A573, 231 (1994).

[Hage68] R. S. Hager and E. C. Seltzer. *Particle Parameters* (1968).

[Hamm75b] J. W. Hammer, B. Fisher, H. Hollick, and H. M. Schüpferling. *The SF_6 recovery and storage system of a Dynamitron accelerator* Kerntechnik 17, 471 (1975).

[Hamm79] J. W. Hammer, B. Fisher, H. Hollick, H. P. Trauvetter, K. U. Kettner, C. Rolfs, and M. Wiescher. *Beam properties of the 4 MeV Dynamitron accelerator at Stuttgart* Nucl. Instr. and Meth. 161, 189 (1979).

[Hane81] H. Hanewinkel, Diploma Thesis, Universität zu Köln, Köln, (1981).

[Hart00] T. Hartmann, J. Enders, P. Mohr, K. Vogt, S. Volz, and A. Zilges. *Measurement of the dipole and electric quadrupole strength distributions up to 10 MeV in the doubly magic nuclei ^{40}Ca and ^{48}Ca* Phys. Rev. Lett. 85, 274 (2000).

[Heil88] R. D. Heil, H. H. Pitz, U. E. P. Berg, and U. Kneissl. *Observation of orbital magnetic dipole strength in the actinide nuclei ^{232}Th and ^{238}U* Nucl. Phys. A476, 39 (1988).

[Heil90] R. D. Heil, B. Kasten, W. Scharfe, P.A. Butler, H. Friedrichs, S. D. Hoblit, U. Kneissl, S. Lindenstruth, M. Ludwig, G. Mller, H. H. Pitz, K.W. Rose, M. Schumacher, U. Seemann, J. Simpson, P. von Brentano, Th. Weber, C. Wesselborg, and A. Zilges. *Parity assignments in nuclear resonance fluorescence experiments using compton polarimeters* Nucl. Phys. A506, 223 (1990).

[Herz95a] R.-D. Herzberg, A. Zilges, A. M. Oros, P. von Brentano, U. Kneissl, J. Margraf, H. H. Pitz, and C. Wesselborg. *Observation of dipole transitions to a multiplet in* ^{143}Nd Phys. Rev. C51, 1226 (1995).

[Herz95b] R.-D. Herzberg, I. Bauske, P. von Brentano, Th. Eckert, R. Fischer, W. Geiger, U. Kneissl, J. Margraf, H. Maser, N. Pietralla, H. H. Pitz, and A. Zilges. *Lifetimes of two-phonon* 1^- *states in even* $N = 82$ *nuclei* Nucl. Phys. A592, 211 (1995).

[Herz95c] R.-D. Herzberg, I. Bauske, O. Beck, P. von Brentano, T. Eckert, R. Fischer, D. Jäger, U. Kneissl, J. Margraf, H. Maser, H. H. Pitz, M. Rittner, A. Schiller, and A. Zilges. *Electric and magnetic dipole excitations studied in photon scattering experiments* In W. Andrejtscheff and D. Elenkov, editors, Proceedings of the XII International School on Nuclear Physics, Neutron Physics and Nuclear Energy, Varna, Bulgaria, 27 Sept. - 31 Oct., (1995).

[Herz95d] R.-D. Herzberg. *Untersuchung von gekoppelten Phononenanregungen in Kernen um* $A = 140$. PhD thesis, Universität zu Köln, (1995).

[Herz97] R.-D. Herzberg, P. von Brentano, J. Eberth, J. Enders, R. Fischer, N. Huxel, T. Klemme, P. von Neumann-Cosel, N. Nicolay, N. Pietralla, V. Yu. Ponomarev, J. Reif, A. Richter, C. Schlegel, R. Schwenger, S. Skoda, H.G. Thomas, I. Wiedenhöver, G. Winter, A. Zilges. *Fine structure of the* $E1$ *response in* ^{140}Ce *below the particle threshold* Phys. Lett. B390, 49 (1997).

[Herz99] R.-D. Herzberg, C. Fransen, P. von Brentano, J. Eberth, J. Enders, A. Fitzler, L. Käubler, H. Kaiser, P. von Neumann-Cosel, N. Pietralla, V. Yu. Ponomarev, H. Prade, A. Richter, H. Schnare, R. Schwenger, S. Skoda H. G. Thomas, H. Tiesler, D. Weisshaar, and I. Wiedenhöver. *Resolved dipole strength below the* $E1$ *giant resonance in* ^{138}Ba Phys. Rev. C60, 051307 (1999).

[Heyd97] K. Heyde and C. De Coster. *Electric dipole transitions near the* $Z = 50$ *and* $N = 82$ *closed shells* Phys. Lett. B393, 7 (1997).

[Hamm75a] J. W. Hammer and H. M. Schüpferling. *Beam transport system for a 4 MeV Dynamitron accelerator* Nucl. Instr. and Meth. 128, 409 (1975).

[Hube93] M. Huber, P. von Neumann-Cosel, A. Richter, C. Schlegel, R. Schultz, J. J. Carroll, K. N. Taylor, D. G. Richmond, T. W. Sinor, C. B. Collins, and V. Yu. Ponomarev. *Structure of intermediate states in the photoactivation of the* ^{89}Y *isomer* Nucl. Phys. A559, 253 (1993).

[Huxe92] N. Huxel, W. Ahner, H. Diesener, P. von Neumann-Cosel, C. Rangacharyulu, A. Richter, C. Spieler, W. Ziegler, C. De Coster, and K. Heyde. *Search for low-lying magnetic dipole strength in the heavy odd-mass nucleus* ^{165}Ho Nucl. Phys. A539, 478 (1992).

[Iach85] F. Iachello. *Local versus global isospin symmetry in nuclei* Phys. Lett. B160, 1 (1985).

[Iach87] F. Iachello and A. A. Arima. *The interacting boson model.* Cambridge University press, Cambridge, England, (1987).

[Iach97] F. Iachello. *Mini-workshop on low-lying magnetic and electric dipole excitations in nuclei, darmstadt* unpublished, (1997).

[Isac91] P. V. Isacker, M. A. Nagarajan, and D. D. Warner. *Effect of the neutron skin on collective states of nuclei* Phys. Rev. C45, R13 (1991).

[Iudi78] N. Lo Iudice and F. Palumbo. *New isovector collective modes in deformed nuclei* Phys. Rev. Lett. 41, 1532 (1978).

[Iudi79] N. Lo Iudice and F. Palumbo. *Positive parity isovector collective states in deformed nuclei* Nucl. Phys. A326, 193 (1979).

[Jons81] N.-G. Jonsson, A. Bäcklin, J. Kantele, R. Julin, M. Luontama, and A. Passoja. *Collective states in even Sn nuclei* Nucl. Phys. A371, 333 (1981).

[Jund94] Huo Junde. Nucl. Data Sheets 71, 659 (1994).

[Jung95] A. Jung, B. Starck S. Lindenstruth, H. Schacht, R. Stock, C. Wesselborg, R.-D. Heil, U. Kneissl, J. Margraf, H. H. Pitz, and F. Steiper. *Electric and magnetic dipole excitations to bound states in* $^{70,72,74,76}Ge$ Nucl. Phys. A584, 103 (1995).

[Kaub00] L. Käubler, H. Schnare, R. Schwenger, P. von Brentano, F. Dönau, J. Eberth, J. Enders, A. Fitzler, C. Fransen, M. Grinberg, E. Grosse, R.-D. Herzberg, H. Kaiser, P. von Neumann-Cosel, N. Pietralla, H. Prade, A. Richter, S. Skoda, Ch. Stoyanov, H.-G. Thomas, H. Tiesler, D. Weisshaar, and I. Wiedenhöver. *Is the 4.742 MeV state in* ^{88}Sr *the* 1^- *two-phonon state ?* Eur. Phys. J. A7, 15 (2000).

[Klei82] P. Kleinheinz, J. Styczen, M. Piipqrinen, J. Blomqvist, and M. Kortelahti. *Two-phonon octupole excitation in* ^{147}Gd Phys. Rev. Lett. 48, 1457 (1982).

[Knei93] U. Kneissl, A. Zilges, J. Margraf, I. Bauske, P. von Brentano, H. Friedrichs, R. D. Heil, R.-D. Herzberg, H. H. Pitz, B. Schlitt, and C. Wesselborg. *First experimental evidence for two-phonon octupole-γ-vibrational excitations in deformed nuclei* Phys. Rev. Lett. 71, 2180 (1993).

[Knei96] U. Kneissl, H. H. Pitz, and A. Zilges. *Investigation of nuclear structure by resonance fluorescence scattering* Prog. Part. Nucl. Phys. 37, 349 (1996).

[Knol89] Glenn F. Knoll. *Radiation detection and measurement.* John Wiley & Sons, (1989).

[Kohs00] C. Kohstall et al. *Systematics of dipole excitations in stable Cd isotopes* Annual Report, Stuttgart University, 26 (2000).

[Kran88] Kenneth S. Krane. *Introductory nuclear physics.* John Wiley & Sons, (1988).

[Lehm00] H. Lehmann, A. Nord, A. E. de Almeida Pinto, O. Beck J. Besserer, P. von Brentano, S. Drissi, T. Eckert, R.-D. Herzberg, D. Jäger, J. Jolie, U. Kneissl, J. Margraf, H. Maser, N. Pietralla, and H. H. Pitz. *Dipole excitations in the vibrational nucleus* ^{112}Cd Phys. Rev. C60, 024308 (2000).

[Lepr76] A. Leprêtre, H. Beil, R. Bergère, P. Carlos, A. De Minac, A. Veyssière, and K. Kernbach. *A study of the giant dipole resonance of vibrational nuclei in the* $103 \leq A \leq 133$ *mass region* Nucl. Phys. A219, 39 (1976).

[Lipa66] P. O. Lipas. *Two-phonon quadrupole-octupole vibrations in spherical nuclei* Nucl. Phys. 82, 91 (1966).

[Lore87] A. Lorentz. *Handbook on Nuclear Activation Data.* IAEA (Wien), (1987).

[Luna84] S. Lunardi, P. Kleinheinz, M. Piiparinen, M. Ogawa, M. Lach, and J. Blomqvist. *Single- and double-octupole excitations in* ^{148}Gd Phys. Rev. Lett. 53, 1531 (1984).

[Maie92] U. Maier. *Bestimmung der Polarisationsempfindlichkeit eines Compton-Polarimeters mittels* $(p, p'\gamma)$*-Reaktionen.* Diploma thesis, Institut für Strahlenphysik, Unversität Stuttgart, (1992).

[Marg90] J. Margraf, A. Degener, H. Friedrichs, R. D. Heil, A. Jung, U. Kneissl, S. Lindenstruth, H. H. Pitz, H. Schacht, U. Seemann, R. Stock, and C. Wesselborg. *Photoexcitation of low-lying dipole transitions in* ^{236}U Phys. Rev. C42, 771 (1990).

[Marg93] J. Margraf, R. D. Heil, U. Kneissl, U. Maier, and H. H. Pitz, H. Friedrichs, S. Lindenstruth, B. Schlitt, C. Wesselborg, P. von Brentano, R.-D. Herzberg, and A. Zilges. *Deformation dependence of low lying* $M1$ *strengths in even Nd isotopes* Phys. Rev. C47, 1474 (1993).

[Marg95] J. Margraf, T. Eckert, M. Rittner, I. Bauske, O. Beck, U. Kneissl, H. Maser, H. H. Pitz, A. Schiller, P. von Brentano, R. Fisher, R.-D. Herzberg, N. Pietralla, A. Zilges, and H. Friedrichs. *Systematics of low-lying dipole strengths in odd and even Dy and Gd isotopes* Phys. Rev. C52, 2429 (1995).

[Mase96a] H. Maser, S. Lindenstruth, I. Bauske, O. Beck, P. von Brentano, T. Eckert, H. Friedrichs, R. D. Heil, R.-D. Herzberg, A. Jung, U. Kneissl, J. Margraf, N. Pietralla, H. H. Pitz, C. Wesselborg, and A. Zilges. *Systematics of low-lying*

dipole excitations in the deformed even-even nuclei $^{164,166,168,170}Er$ Phys. Rev. C53, 2749 (1996).

[Mase96b] H. Maser, N. Pietralla, P. von Brentano, R.-D. Herzberg, U. Kneissl, J. Margraf, H. H Pitz, and A. Zilges. *Observation of the* 1^+ *scissors mode in the* γ*-soft nucleus* ^{134}Ba Phys. Rev. C54, R2129 (1996).

[Mase96c] H. Maser, J. Margraf, D. Belic, and H. H. Pitz. *Implementation of the high speed listmode data acquisition system for* γ *spectroscopy* Annual Report, Institut für Strahlenphysik, Universität Stuttgart, 62 (1996).

[Mase98] H. Maser. *Untersuchung niedrigliegender, kollektiver Dipolanregungen der schweren gg-Kerne* ^{168}Er, ^{134}Ba *und* ^{140}Ce. PhD thesis, University of Stuttgart, (1998).

[Mats97] P. Matschinsky et al. Annual Report, Stuttgart University, 8 (1997).

[Metz59] F. R. Metzger. *Resonance fluorescence in nuclei* Prog. in Nucl. Phys. 7, 53 (1959).

[Metz75] F. R. Metzger. *Spin and width of the 4744 kev level of* ^{88}Sr Phys. Rev. C11, 2085 (1975).

[Metz76] F. R. Metzger. *Low-lying E1 transitions in the stable even Sm isotopes* Phys. Rev. C14, 543 (1976).

[Metz78] F. R. Metzger. *Nuclear resonance fluorescence in* ^{142}Nd Phys. Rev. C18, 1603 (1978).

[Mikh89] I. V. Mikhailov and A. M. Demidov. Bull. Acad. Sci. USSR, Phys. Ser. 53 No. 5, 69 (1989).

[Mohr99] P. Mohr, J. Enders, T. Hartmann, H. Kaiser, D. Schiesser, S. Schmitt, S. Volz, F. Wissel, and A. Zilges. *Real photon scattering up to 10 MeV: The improved facility at the Darmstadt electron accelerator S-DALINAC* Nucl. Instr. Meth. Phys. Res. A423, 480 (1999).

[More93] R. Moreh, O. Beck, I. Bauske, W. Geiger, R. D. Heil, U. Kneissl, J. Margraf, H. Maser, and H. H. Pitz. *Precise widths of the 3089 and 3684 keV levels in* ^{13}C Phys. Rev. C48, 2625 (1993).

[Müll88] H.-W. Müller. Nucl. Data Sheets 54, 1 (1988).

[Nord96] A. Nord, A. Schiller, T. Eckert, O. Beck, J. Besserer, P. von Brentano, R. Fischer, R.-D. Herzberg, D. Jäger, U. Kneissl, J. Margraf, H. Maser, N.Pietralla, H. H. Pitz, M. Rittner, and A. Zilges. *Systematic study of the fragmentation of low-lying dipole strength in odd-a rare earth nuclei investigated in nuclear resonance fluorescence experiments* Phys. Rev. C54, 2287 (1996).

[Ohya93] S. Ohya and T. Tamura. Nucl. Data Sheets 70, 557 (1993).

[Oros98] A. M. Oros, K. Heyde, C. De Coster, and B. Decroix. *Local electric dipole strength in heavy nuclei* Phys. Rev. C57, 1 (1998).

[Piet95a] N. Pietralla, I. Bauske, O. Beck, P. von Brentano, W. Geiger, R.-D. Herzberg, U. Kneissl, J. Margraf, H. Maser, H. H. Pitz, and A. Zilges. *Absolute level widths in ^{27}Al below 4 MeV* Phys. Rev. C51, 1021 (1995).

[Piet95b] N. Pietralla, P. von Brentano, R. D. Herzberg, U. Kneissl, J. Margraf, H. Maser, H. H. Pitz, and A. Zilges. *Correlation between low-lying M1 and E2 strength in heavy rare earth nuclei.* Phys. Rev. C52, R2317 (1995).

[Piet97] N. Pietralla, O. Beck, J. Besserer, P. von Brentano, T. Eckert, R. Fischer, C. Fransen, R.-D. Herzberg, D. Jäger, R. V. Jolos, U. Kneissl, B. Kirschok, J. Margraf, H. Maser, A. Nord, H. H. Pitz, M. Rittner, A. Schiller, and A. Zilges. *The scissors mode and other magnetic and electric dipole excitations in the transitional nuclei $^{178,180}Hf$* Nucl. Phys. A618, 141 (1997).

[Piet98b] N. Pietralla, D. Belic, P. von Brentano, C. Fransen, R.-D. Herzberg, U. Kneissl, H. Maser, P. Matschinsky, A. Nord, T. Otsuka, H. H. Pitz, V. Werner, and I. Wiedenhöver. *Isovector quadrupole excitations in the valence shell of the vibrator nucleus ^{136}Ba : Evidence from photon scattering experiments* Phys. Rev. C58, 796 (1998).

[Piet99a] N. Pietralla. *Empirical correlation between two-phonon E1 transition strengths in vibrational nuclei* Phys. Rev. C59, 2941 (1999).

[Piet99b] N. Pietralla, C. Fransen, D. Belic, P. von Brentano, C. Friessner, U. Kneissl, A. Linnemann, A. Nord, H. H. Pitz, T. Otsuka, I. Schneider, V. Werner, and I. Wiedenhöver. *Transition rates between mixed symmetry states : First measurement in ^{94}Mo* Phys. Rev. Lett. 83, 1303 (1999).

[Piip90] M. Piiparinen, P. Kleinheinz, S. Lunardi, M. Ogawa, G. de Angelis, F. Soramel, and W. Meczynski. *Shell model and octupole states in ^{148}Gd from in-beam experiments* Z. Phys. A337, 387 (1990).

[Piip93] M. Piiparinen, P. Kleinheinz, J. Blomqvist, A. Virtanen, A. Atac, D. Müller, J. Nyberg, T. Ramsoy, and G. Sletten. *Two- to one-phonon $E3$ transition strength in ^{148}Gd* Phys. Rev. Lett. 70, 150 (1993).

[Pitz89] H. H. Pitz, U.E.P. Berg, R.D. Heil, U. Kneissl, R. Stock, C. Wesselborg, and P. von Brentano. *Systematic study of low-lying dipole excitations in $^{156,158,160}Gd$ by photon scattering* Nucl. Phys. A492, 411 (1989).

[Pitz90] H. H. Pitz, R. D. Heil, U. Kneissl, S. Lindenstruth, U. Seemann, R. Stock, C. Wesselborg, A. Zilges, P. von Brentano, S. D. Hoblit, and A.M. Nathan. *Low-energy photon scattering off $^{142,146,148,150}Nd$: an investigation in the mass region of a nuclear shape transition* Nucl. Phys. A509, 587 (1990).

[Pono90] V. Yu. Ponomarev, A. P. Dubensky, V. P. Dubensky, and E. A. Boiykova. Journ of Phys. G, Nucl. Part. Phys. 16, 1727 (1990).

[Pono98a] V. Yu. Ponomarev, Ch. Stoyanov, N. Tsoneva, and M. Grinberg. *Boson forbidden low-energy E1-transitions in spherical nuclei* Nucl. Phys. A635, 470 (1998).

[Pono99b] V. Yu. Ponomarev and P. von Neumann-Cosel. *Fragmentation of the two-octupole phonon multiplet in ^{208}Pb* Phys. Rev. Lett. 82, 501 (1999).

[Pono99c] V. Yu. Ponomarev. *Microscopic analysis of a correlation between dipole transitions $1^-_1 \to 0^+_{g.s.}$ and $3^-_1 \to 2^+_1$ in spherical nuclei* Eur. Phys. J. 6, 243 (1999).

[Pono99d] V. Yu. Ponomarev, J. Bryssinck, L. Govor, F. Bauwens, O. Beck, D. Belic, P. von Brentano, D. De Frenne, C. Fransen, R.-D. Herzberg, E. Jacobs, U. Kneissl, H. Maser, A. Nord, N. Pietralla, H. H. Pitz, and V. Werner *Strong fragmentation of low-energy electromagnetic excitation strength in ^{117}Sn* Phys. Rev. Lett. 83, 4029 (1999).

[Radu70] A. Raduta, A. Sandulescu, and P. O. Lipas. *Semi-microscopic theory of two-phonon quadrupole-octupole vibrations in spherical nuclei* Nucl. Phys. A149, 11 (1970).

[Rama91] S. Raman, T. A. Walkiewicz, S. Kahane, E. T. Jurney, J. Sa, Z. Gacsi, J. L. Weil, K. Allaart, G. Bonsignori, and J. F. Shriner Jr. *Nearly complete level scheme of ^{116}Sn below 4.3 MeV* Phys. Rev. C43, 521 (1991).

[Rich83] A. Richter. *Magnetic dipole transitions and other elementary spin excitation modes in nuclei* In Proc. of the Int. Conf. on Nuclear Physics, Florence (Italy), (1983).

[Robi94] S. J. Robinson, J. Jolie, H. G. Börner, P. Schillebeeckx, S. Ulbig, and K. P. Lieb. *E2 and E3 transitions from quadrupole and octupole coupled states in ^{144}Nd* Phys. Rev. Lett. 73, 412 (1994).

[Schi46] L. I. Schiff. *Resonance fluorescence of nuclei* Phys. Rev. 70, 761 (1946).

[Schi95] A. Schiller. *Suche nach der M1-Scheren-Mode im Kern ^{159}Tb* Diploma Thesis, Institut für Strahlenphysik der Universität Stuttgart (1995).

[Schl95] C. Schlegel, P. von Neumann-Cosel, A. Richter and P. Van Isacker. *Unexpected properties of the scissors mode in the odd-mass nucleus ^{167}Er* Phys. Lett. B375, 21 (1995).

[Schl94] B. Schlitt, U. Maier, H. Friedrichs, S. Albers, I. Bauske, P. von Brentano, R. D. Heil, R.-D. Herzberg, U. Kneissl, J. Margraf, H. H. Pitz, C. Wesselborg, and A. Zilges. *A sectored Ge-Compton polarimeter for parity assignments in photon scattering experiments* Nucl. Instr. and Meth. Phys. Res. A 337, 416 (1994).

[Schw97] R. Schwenger, G. Winter, W. Schauer, M. Grinberg, F. Becker, P. von Brentano, J. Eberth, J. Enders, T. von Egidy, R.-D. Herzberg, N. Huxel, L. Käubler, P. von Neumann-Cosel, N. Nicolay, J. Ott, N. Pietralla, H. Prade, S. Raman, J. Reif, A. Richter, C. Schlegel, H. Schnare, T. Servene, S. Skoda, T. Steinhardt, Ch. Stoyanov, H. G. Thomas, I. Wiedenhöver, and A. Zilges. *Two-phonon $J = 1$ states in the even-mass Te isotopes with $A = 122$ - 130* Nucl. Phys. A620, 277 (1997).

[Seel81] W. Seelmann-Eggebert, G. Pfennig, H. Münzel, and H. Klewe-Nebenius. *Chart of nuclides* Kalsruhe, (1981).

[Sieg65] K. Siegbahn. *α, β, γ - Spectroscopy* North-Holland Publishing Company, Amsterdam (1965).

[Simp83] J. Simpson, P. A. Butler, and L. P. Ekström. *Application of a sectored Ge(Li) detector as a Compton polarimeter* Nucl. Instr. Meth. 204, 463 (1983).

[Simp97] J. Simpson. *The euroball spectrometer* Z. Phys. A358, 139 (1997).

[Skor75] S. J. Skorka. *The electromagnetic interaction in nuclear spectroscopy.* North-Holland publishing company, Amsterdam, (1975).

[Solo92] V. G. Soloviev. *Theory of Atomic Nuclei : Quasiparticles and Phonons.* Inst. of Phys. Publ., Bristol and Philadelphia, (1992).

[Spea89a] R. H. Spear. *Reduced electric-octupole transition probabilities for even-even nuclides throughout the periodic table* At. and Nucl. Data Tables 42, 55 (1989).

[Spea89b] R. H. Spear, A. M. Baxter, S. M. Burnett, and C. L. Miller. Austr. Journ. Phys. 42, 41 (1989).

[Stor70] E. Storm and H. I. Israel. At. and Nucl. Data Tables A7, 565 (1970).

[Tamu00] T. Tamura. Nucl. Data Sheets 90, 149 (2000).

[Vett98] K. Vetter, A. O. Macchiavelli, D. Cline, H. Amro, S. J. Asztalos, B. C. Busse, R. M. Clark, M. A. Deleplanque, R. M. Diamond, P. Fallon, R. Gray, R. V. F. Janssens, R. Krücken, I. Y. Lee, R. W. Macleod, E. F. Moore, G. J. Schmid, M. W. Simon, F. S. Stephens, and C. Y. Wu. *Fragmentation of the two-phonon octupole vibrational states in ^{208}Pb* Phys. Rev. C58, R2361 (1998).

[Vdov85] A. I. Vdovin, V. V. Voronov, V. G. Soloviev, and Ch. Stoyanov. Part. Nucl. 16, 245 (1985).

[Voge71] P. Vogel and L. Kocbach. *Low-lying negative parity states in the vibrational nuclei* Nucl. Phys. A176, 33 (1971).

[Voro84] V.V. Voronov, D. T. Khoa, and V. Yu. Ponomarev. Bull. Acad. Sci. USSR, Phys. Ser. 48(9), 190 (1984).

[Waps87] A. H. Wapstra, G. J. Nigh, and R. Van Lieshout. *Nuclear spectroscopy tables* North-Holland Publishing Company, Amsterdam, (1987).

[Weis96] D. Weisshaar. *Die Polarisationsempfindlichkeit des Euroball-Cluster-detektors* Diploma Thesis, Institut für Kernphysik, Unversität zu Köln, (1996).

[Wess88] C. Wesselborg, P. von Brentano, K. O. Zell, R. D. Heil, H. H. Pitz, U. E. P. Berg, U. Kneissl, S. Lindenstruth, U. Seemann, and R. Stock *Photoexcitation of dipole modes in* $^{160,162,164}Dy$ Phys. Lett. B207, 22 (1988).

[Wilh96] M Wilhelm, E. Radermacher, A. Zilges, and P. von Brentano. *Direct proof of the two-phonon character of the dipole excitations in* ^{142}Nd *and* ^{144}Sm *around 3.5 MeV* Phys. Rev. C54, R449 (1996).

[Wilh98] M. Wilhelm, S. Kasemann, G. Pacovici, E. Radermacher, P. von Brentano, and A. Zilges. *Two-phonon character fo the lowest electric dipole excitation in* ^{142}Nd *and in other nuclei near shell closures* Phys. Rev. C57, 577 (1998).

[Wise92] J. E. Wise, J. P. Connelly, F. W. Hersman, J. H. Heisenberg, W. Kim, F. W. Leushner, S. A. Fayans, A. P. Platonov, E. E. Saperstein, and V. Yu. Ponomarev. *Transition densities of collective excitations in* ^{118}Sn Phys. Rev. C45, 2701 (1992).

[Yate86] S. W. Yates, R. Julin, P. Kleinheinz, B. Rubio, L. G. Mann, E. A. Henry, W. Stöffl, D. J. Decman, and J. Blomqvist. *Particle-hole multiplets in* ^{146}Gd *from in-beam studies of non-yrast states* Z. Phys. A324, 417 (1986).

[Yate87] S. W. Yates, L. G. Mann, E. A. Henry, D. J. Decman, R. A. Meyer, R. J. Estep, R. Julin, A. Passoja, J. Kantele, and W. Trzaska. *E0 decays of* 0^+ *states in* ^{146}Gd*: search for two-phonon octupole excitations* Phys. Rev. C36, 2143 (1987).

[Yeh96] Minfang Yeh, P. E. Garrett, C. A. McGrath, S. W. Yates, and T. Belgya. *Two-phonon octupole excitation in* ^{208}Pb Phys. Rev. Lett. 76, 1208 (1996).

[Yeh98] Minfang Yeh, M. Kadi, P. E. Garrett, C. A. McGrath, S. W. Yates, and T. Belgya. *Candidates for two-phonon octupole excitations in* ^{208}Pb Phys. Rev. C57, R2085 (1998).

[Zieg90] W. Ziegler, C. Rangarcharyulu, A. Richter, and C. Spieler. *Orbital magnetic dipole strength in* $^{148,150,152,154}Sm$ *and nuclear deformation* Phys. Rev. Lett. 65, 2515 (1990).

[Zilg90a] A. Zilges, P. von Brentano, A. Richter, R. D. Heil, U. Kneissl, H. H. Pitz, and C. Wesselborg. *Uncommon decay branching ratios of spin-one states in the rare-earth region and evidence for K mixing Phys. Rev.* C42, 1945 (1990).

[Zilg90b] A. Zilges, P. von Brentano, C. Wesselborg, R. D. Heil, U. Kneissl, S. Lindenstruth, H. H. Pitz, U. Seeman and R. Stock. *Observation of low-lying collective dipole transitions in the rare earth nuclei* $^{172,174,176}Yb$ Nucl. Phys. A507, 399 (1990).

[Zilg91] A. Zilges, P. von Brentano, H. Friedrichs, R. D. Heil, U. Kneissl, S. Lindenstruth, H. H. Pitz, and C. Wesselborg. *A survey of* $\Delta K = 0$ *dipole transitions from low lying* $J = 1$ *states in rare earth nuclei* Z. Phys. A340, 155 (1991).

[Zilg93] A. Zilges, R.-D. Herzberg, P. von Brentano, F. Dönau, R. D. Heil, R. V. Jolos, U. Kneissl, J. Margraf, H. H. Pitz, and C. Wesselborg. *First identification of dipole excitations to a* $2^+ \otimes 3^-$ *particle multiplet in an odd A-nucleus* Phys. Rev. Lett. 70, 2880 (1993).